Karlsruhe Institute of Technology

Interplay between Superconductivity and Electronic Orders in $FeSe_{1-x}Te_x$ and AV_3Sb_5

Zur Erlangung des akademischen Grades eines
DOKTORS DER NATURWISSENSCHAFTEN (Dr. rer. nat.)

von der KIT-Fakultät für Physik des
Karlsruher Instituts für Technologie (KIT)
genehmigte

Dissertation
von
M.Sc. Anmol Shukla

Referent:	Prof. Dr. Matthieu Le Tacon
Korreferent:	Prof. Dr. Jörg Schmalian
Betreuer:	Dr. Christoph Meingast
Betreuer:	Dr. Frédéric Hardy

Tag der mündlichen Prüfung: 23.05.2025

Abstract

Quantum materials offer a fertile ground for discovering emergent phenomena that arise from interactions between charge, spin, orbital, and lattice degrees of freedom. Using thermodynamic and transport measurements, this thesis explores two families of such materials: the iron-chalcogenide superconductors $Fe_{1+y}Se_{1-x}Te_x$ and kagome metals AV_3Sb_5 ($A = Cs, Rb, K$).

In $Fe_{1+y}Se_{1-x}Te_x$, bulk thermodynamic measurements establish a phase diagram with two distinct superconducting domes. In the first dome, associated with the nematic phase, heat-capacity data indicate either accidental nodes or strong gap anisotropy, which is progressively lifted with Te substitution. Thermal-expansion measurements further show that orthorhombicity and superconductivity couple cooperatively in this regime, similar to the behavior in Fe(Se,S). In the second dome, where long-range nematic order is absent, the thermodynamic response is dominated by a single electronic band, and the c-axis response becomes strongly enhanced, pointing to substantial changes in the electronic structure. Three-point-bending measurements show a hardening of C_{66} in the superconducting phase for the optimally doped composition, consistent with strong competition between superconductivity and nematic fluctuations. The nemato-elastic effects and the Grüneisen parameter are also discussed.

In kagome AV_3Sb_5 compounds, we performed zero-field calorimetry and transport measurements to characterize the charge-density-wave (CDW) transition, and high-field Shubnikov-de Haas, de Haas-van Alphen, and magnetostriction measurements to probe its impact on the Fermi surface. While KV_3Sb_5 undergoes a continuous CDW transition, RbV_3Sb_5 exhibits a weak first-order transition. Quantum oscillation spectra reveal multiple low-frequency orbits consistent with CDW-induced Fermi-surface reconstruction. The evolution of mid-frequency orbits across the Cs-Rb-K series is consistent with the reported differences between staggered Star-of-David / inverse-Star-of-David (SD/ISD) and mixed SD+ISD superlattices. Finally, comparison of magnetostriction and magnetization data for RbV_3Sb_5 shows that the small elliptical pockets linked to the anomalous Hall effect are only weakly affected by c-axis strain.

Contents

Chapter 1

Introduction

Unlike conventional materials whose properties can often be explained by theories assuming free or nearly free electrons, quantum materials feature pronounced electron correlations and interactions among charge, spin, orbital, and lattice degrees of freedom. This leads to emergent phenomena — collective behaviors not evident from the properties of individual particles, but rather arising spontaneously when many particles interact. Thus, the term *quantum materials* is generally reserved for materials where one must invoke many-body physics to explain their physical properties. Technological aspects aside, quantum materials provide fundamental insights into quantum mechanics at macroscopic scales. Two classes of (quantum) materials are discussed in this thesis: iron-based superconductors $FeSe_{1-x}Te_x$ and the metallic kagome system AV_3Sb_5 ($A = Cs, Rb, K$). Both systems exhibit superconductivity at very low temperatures - 8 K for FeSe and 2.5 K for CsV_3Sb_5. Above its superconducting transition, FeSe undergoes a nematic transition, whereas AV_3Sb_5 exhibits a CDW transition. Section 1.1 provides brief introductions to these two systems (including the crystal structure and the most interesting questions). Following this, Sec. 1.2 and Sec. 1.3 present the fundamentals of electronic phases relevant to these systems (superconductivity and charge density waves) and the basics of quantum oscillations, respectively. Electronic nematicity is not discussed here, and will be introduced directly in relation to Fe-chalcogenides in Chapter 3. Finally, Sec. 1.4 outlines the structure of the thesis.

1.1 Systems studied

1.1.1 Iron-based superconductor: $FeSe_{1-x}Te_x$

Solid-to-solid structural transitions are fairly common in nature. Typically, such transitions are driven by phonons. Iron-based superconductors were first discovered in LaFePO in 2006 [1], and gained widespread attention in 2008 following the report of a high transition temperature ($T_c \approx 26\,\mathrm{K}$) in $LaFeAsO_{1-x}F_x$ [2]. In their normal state, these materials often exhibit a tetragonal-to-orthorhombic structural transition. This transition is often regarded as electronically driven and is commonly referred to as the nematic transition (T_s) [3]. In this nematic phase, a structural distortion develops together with pronounced electronic anisotropy, accompanied by orbital/charge fluctuations and spin fluctuations [4–7]. The presence of these intertwined degrees of freedom, where one can drive or reinforce the others, means it is not straightforward to identify the primary origin of this transition [4].

Iron-based superconductors are characterized by layers of iron atoms coordinated with pnictogen (As, P) or chalcogen (Se, S, Te) atoms, forming a square lattice of iron. The Fe(Se,S,Te) system, often referred to as the "11" family due to its stoichiometry, crystallizes in the PbO-type structure with the space group $P4/nmm$. This simple structure lacks the spacer layers present in other iron-based superconductors, allowing for a more direct investigation of the intrinsic properties of the FeCh layers (see Fig. 1.1A). The superconductivity in these materials is believed to originate from the Fe 3d electrons, with the FePn (pnictogen) or FeCh (chalcogen) layers playing a crucial role. The chalcogen height h and the c/a-ratio are two structural parameters with which the physical properties

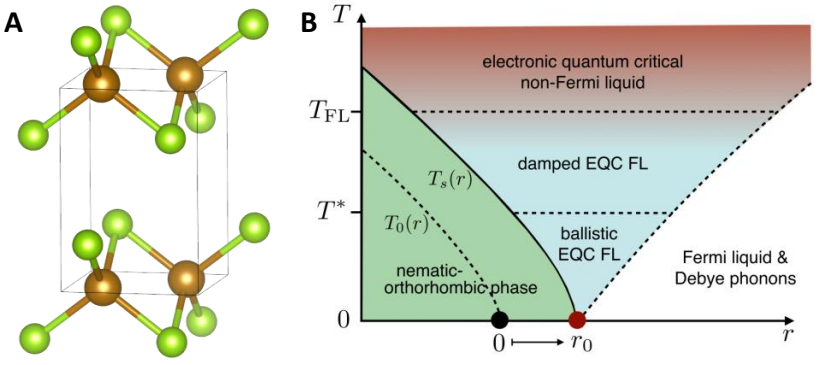

FIGURE 1.1: (A) FeSe(Te) unit cell: golden and green points represent Fe and Se(Te) atoms, (B) shows the theoretical phase diagram for the nematic quantum critical point case in the presence of finite nemato-elastic coupling [(B) Taken from I. Paul and M. Garst, Physical Review Letters 118, 227601 (2017) [8], reprinted with permission from the American Physical Society. Copyright 2017 by the American Physical Society].

often scale in these systems [9, 10]. In iron chalcogenides, the substitution of selenium by tellurium has been shown to enhance electronic correlations [11].

In particular, FeTe exhibits the strongest correlations among the Fe-based superconductors, and the Fe(Te,Se) system thus provides an excellent platform for investigating the evolution of the electronic correlations in Fe-based superconductors [12]. Unlike the iron pnictides, FeSe does not exhibit antiferromagnetic order, making it an attractive system for investigating nematic fluctuations in the absence of magnetic ordering [8, 13–15]. Prior to research on Fe-based superconductors, nematic quantum critical points (QCP) were extensively discussed in the context of cuprates and other correlated electron systems, although experimental evidence remains controversial [16]. What makes iron-based superconductors unique is the presence of significant nemato-elastic coupling, which is expected to shift the nematic quantum critical point away from its intrinsic/bare position (e.g., nominal doping level) to a finite distance in parameter space, as depicted in Fig. 1.1(B). A definitive experimental realization of a pure nematic QCP in FeSe has not yet been achieved. Under applied pressure, FeSe develops magnetic order; substituting S for Se does not enhance the superconducting transition temperature (T_c) at the nematic endpoint; and Te substitution induces phase separation. Recently, however, renewed hope for observing a pure nematic QCP has emerged with advances in single crystal growth of Te-substituted Fe(Se,Te) alloys in the Se-rich regime [15]. These developments continue to stimulate investigation into whether a genuine nematic QCP can be experimentally confirmed in FeSe-based superconductors.

1.1.2 Kagome metals: AV_3Sb_5 ($A = Cs, Rb, K$)

The kagome lattice, characterized by its arrangement of corner-sharing triangles, is also known as the tri-hexagonal tiling. It was introduced into condensed matter physics by Syôzi in 1951 [17]. Structurally, the kagome lattice comprises three distinct sub-lattice sites per unit cell, as illustrated in Fig. 1.2(A).

This lattice structure is primarily of interest due to the interplay among electron-electron correlation effects, band topology, and lattice geometry. This is best exemplified when the band structure of the kagome lattice without any electronic interactions and symmetry-breaking distortions is considered (shown in Fig. 1.2(B)). Even in this case, two vHS, a Dirac cone (DC) and flat bands are obtained. While insulating kagome compounds have been explored for the study of magnetic frustration and spin-liquid states [20], the kagome metals have garnered attention for the large anomalous Hall effect and density waves [21]. Among the kagome metals, the recently discovered AV_3Sb_5 compounds [22]

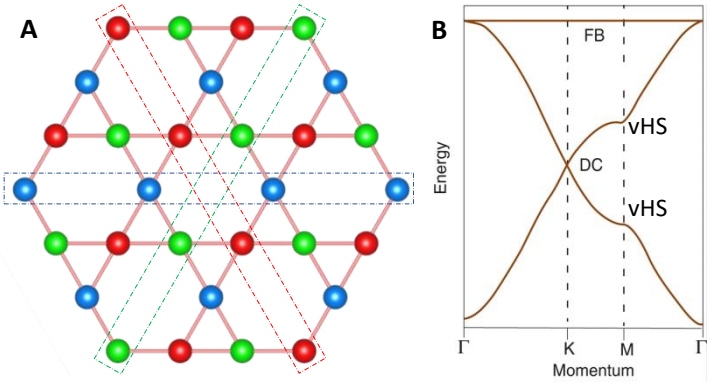

FIGURE 1.2: (A) Structure of the kagome lattice with the three sub-lattices highlighted in different colors. Made using VESTA [18]. (B) Shows the typical band structure of the ideal kagome lattice with no interaction. The two von-Hove singularities (vHS), Dirac cone (DC) and flat band (FB) are labeled. (B) is taken from [19] under the CC BY 4.0.

have sparked interest due to the presence of superconductivity, a charge density wave, and an extraordinarily large anomalous Hall effect [23]. A pair density wave has also been proposed.

The AV_3Sb_5 ($A = Cs, Rb, K$) compounds crystallize into the hexagonal structure with space group $P6/mmm$. The V atoms form a kagome layer and the Sb atoms (Sb_1) occupy the hexagon centers of the V atoms. The alkali atoms sit in a separate plane and are aligned with the Sb_1 sites along the c-axis. A second layer of the Sb atoms (Sb_2) forms a honeycomb structure and sandwiches the V-kagome layer (Fig. 1.3(A,B)).

Upon cooling, all three compounds go through a CDW transition in the range of 75-105 K depending on the alkali atom (A=Cs, Rb, K). The CDW state in AV_3Sb_5 is a so-called $3Q$-state, i.e., the three in-plane wave vectors at the M point of the Brillouin zone condense together - each oriented 120° apart, so their vector sum is zero: $Q_1 + Q_2 + Q_3 = 0$. In addition, there is often a non-zero out-of-plane component at the L point, which results in a superlattice along the crystallographic c-axis (see Fig. 1.3(C, D)). In the simplest scenario, the three in-plane M-point modes define Star-of-David (SoD) or Tri-Hex (TrH)

Distortion	Breathing-mode	$3Q$ mode relation [24]
Star-of-David	breathing-out V1 atoms move away from the center V2 atoms move towards the center	$Q_M^1 = (\pm 1/2, 0)$ $Q_M^2 = (0, \pm 1/2)$ $Q_M^3 = (\mp 1/2, \pm 1/2)$
Inverse-SoD/ tri-Hexagonal	breathing-in V1 atoms move towards the center V2 atoms move away from the center	$Q_M^1 = (\pm 1/2, 0)$ $Q_M^2 = (0, \pm 1/2)$ $Q_M^3 = (\pm 1/2, \mp 1/2)$

TABLE 1.1: Nomenclature of the CDW distortion in AV_3Sb_5 compounds

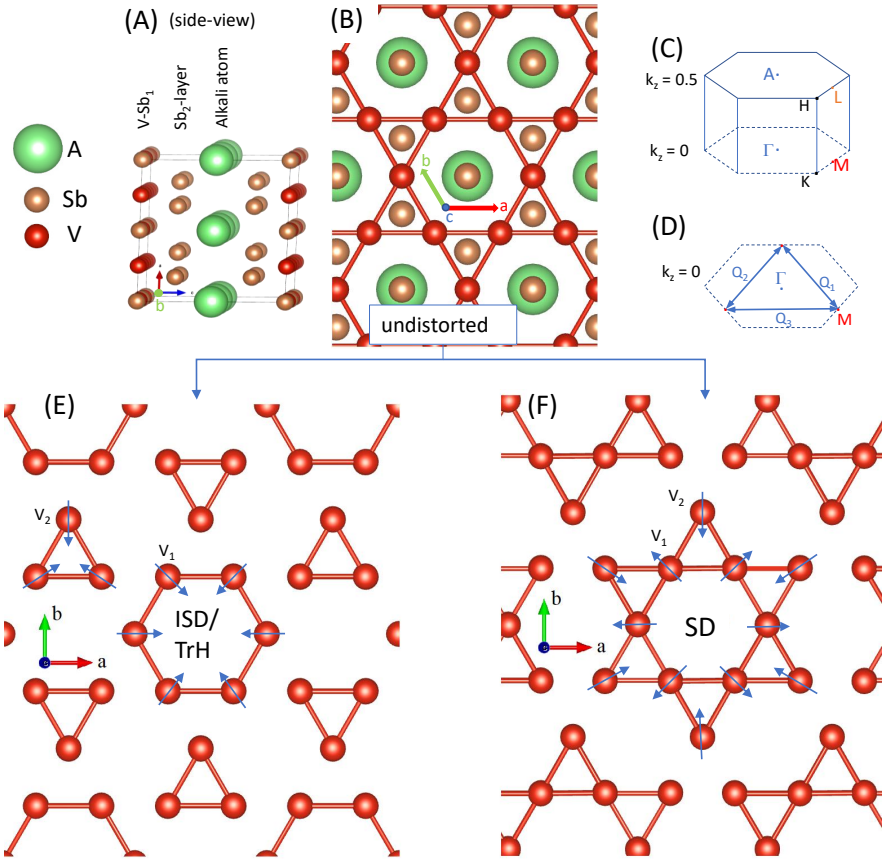

FIGURE 1.3: (A) Side and (B) top-view of the undistorted kagome lattice, with red atoms (V sites) forming a triangular network around the Sb_1 atoms. The alkali atoms sit in a different plane at the same site as Sb_1. (C) Three-dimensional Brillouin zone (BZ) indicating high-symmetry points (Γ, M, K, A, H, etc.). (D) Two-dimensional cut of the BZ at $k_z = 0$, showing the in-plane location of the M points. These zone-edge wave vectors are where CDW instabilities condense. (E, F): Two distorted real-space structures arising from different combinations of those M-point modes: (E) the inverse-star-of-David (ISD) / tri-hex (TrH) distortion, with triangular clusters surrounding a hexagon, and (F) the star-of-David (SD) distortion, where atoms group into a six-pointed star motif. The two nonequivalent V sites, V_1 and V_2, are formed with the motion of V-atoms at these sites defining the breathing -in (ISD) and -out (SD) mode. This motion of the $V_{1,2}$ atoms (in or out) is shown by the arrows in (E,F).
(Made using VESTA [18] and CsV_3Sb_5 cif-file for the sample reported here.)

distortions within each kagome layer, while the out-of-plane wave vector staggers these layers relative to each other (see Fig. 1.3 (E,F)). For K- and Rb-, the common observation is a $3Q$-2×2×2 superlattice [25] that is often referred to as a *staggered Tri-Hex phase* (i.e., each plane has a tri-hexagonal arrangement shifted relative to neighboring planes). CsV_3Sb_5 is more complex and can form alternating SoD and TrH layers exhibiting $2 \times 2 \times 4$ periodicity [25, 26].

At very low temperatures, superconductivity emerges within this CDW state for all the AV_3Sb_5 compounds. The superconducting transition temperature is around 2.5 K

for CsV_3Sb_5 and $\approx 0.8\,\mathrm{K}$ for $(\mathrm{Rb,K})V_3Sb_5$. The superconducting gap structure in these compounds is thoroughly debated, with claims ranging from multiband nodal superconductivity [27–29] to the simple s-wave spin-singlet superconductivity [30]. Table C.1 summarizes the different experiments and their results on the gap structure of the AV_3Sb_5.

1.2 Electronic phases of matter

1.2.1 Superconductivity

Superconductivity is an extraordinary physical phenomenon. It is characterized by the complete disappearance of electrical resistance along with perfect diamagnetism within certain materials when cooled below a critical temperature, known as the superconducting transition temperature. At the microscopic level, superconductivity emerges from electrons forming pairs, called Cooper pairs. The pairing is mediated by the phonons in conventional superconductors and was proposed in 1957 by John Bardeen, Leon Cooper, and Robert Schrieffer (BCS theory) [31]. At the superconducting transition, an energy gap, referred to as the superconducting-gap/ BCS-gap opens up at the Fermi surface. This gap distinguishes the superconducting state from the normal state, in which no such gap exists. The BCS gap equation is a self-consistent equation that quantifies this superconducting gap and is given by [31]:

$$\int_0^{k_B\Theta_D} \frac{1}{\zeta} \tanh\left(\frac{\zeta}{2k_BT}\right) d\epsilon = \frac{1}{N(0)V} \tag{1.1}$$

where Θ_D is the Debye temperature within the Debye model, ζ is the energy required, relative to the paired ground state, to create an electron–hole–mixed quasiparticle excitation, $N(0)$ is the density of states at the Fermi level, and V is the electron-phonon coupling constant. The quasiparticle excitation energy ζ is related to the normal state single-particle energy ϵ and the superconducting gap Δ by:

$$\zeta = \sqrt{\epsilon^2 + \Delta^2(T,\theta)}. \tag{1.2}$$

ζ defines the quasiparticle excitation energy, and the $2\Delta(T)$ is the full energy gap, Δ above and below the Fermi level. Thus, the energy required to break a Cooper pair and create two quasiparticles is 2Δ. At $T = T_c$, the gap $\Delta = 0$, and assuming the weak-coupling

limit, $T_c << \Theta_D$, one gets the expression:

$$ln\left(\frac{2\Theta_D}{1.764 \times T_c}\right) = \frac{1}{N(0)V} \tag{1.3}$$

Equating Eqs. (1.1) and (1.3) and assuming the weak coupling limit, one gets the familiar expression for $T \to 0$:

$$\frac{\Delta(0)}{k_B T_c} = 1.764 \tag{1.4}$$

Thus, the gap equation can be written as:

$$\int_0^{k_B\Theta_D} \frac{1}{\zeta} \tanh\left(\frac{\zeta}{2k_BT}\right) d\epsilon = ln\left(\frac{2\Theta_D}{1.764 \times T_c}\right) = ln\left(\frac{2k_B\Theta_D}{\Delta(0)}\right) \tag{1.5}$$

Equation (1.5) can then be solved self-consistently to obtain the temperature dependence of the superconducting gap. One can define α as:

$$\alpha = \Delta(0)/k_BT_c, \quad \alpha_{BCS} = 1.764, \tag{1.6}$$

then, different values of α correspond to different zero-temperature gaps and one can model the temperature dependence of different superconducting gaps. This forms the basis of the phenomenological α-model [32], which is important to the results in Sec. 3.3.2.

Effects of magnetic field in superconductors:

The upper critical field $H_{c2}(T)$ is defined as the magnetic field at which superconductivity is destroyed at temperature T. The zero-temperature limit, $H_{c2}(0)$, provides crucial information about the superconducting mechanism. Following are the two mechanisms by which application of external magnetic field destroys superconductivity:
(a) Orbital pair breaking - the Lorentz force acts on the charged paired electrons. This gives the orbital limit of superconductivity.
(b) Paramagnetic pair breaking - under a large enough external field, the spins of the two electrons forming the superconducting condensate align due to the Zeeman effect. This is called the Pauli limit (also called the Chandrasekhar-Clogston limit [33]). It is often deemed an upper bound on the H_{c2}, and is given by:

$$\mu_0 H_P(0) = \Delta(0)/(\sqrt{2}\mu_B) = 1.84\,\mathrm{T/K} \times T_c \tag{1.7}$$

for a weak-coupling BCS superconductor. Here, $\Delta(0)$ is the BCS gap and μ_B is the Bohr magneton.

The Werthamer-Helfand-Hohenberg (WHH) theory [34] provides the temperature dependence of $H_{c2}(T)$ for type-II superconductors incorporating both the effects of spin paramagnetism and spin-orbit scattering. Spin-paramagnetism is incorporated through the Maki parameter α. Spin-orbit scattering is introduced using the parameter $\lambda_{SO} = 2\hbar/(3\pi k_B T_c \tau_{SO})$. If there is no spin-paramagnetic effect and $\lambda_{SO} = 0$, the upper critical field is restricted by orbital pair-breaking effects, as described above. In such a case, it can be shown that the orbital limit to the upper critical field is given by:

$$\mu_0 H_{c2}^{\mathrm{orb}}(0) = -0.69 T_c \left(\frac{dH_{c2}}{dT} \right) \Bigg|_{T=T_c} \tag{1.8}$$

The prefactor in Eq. (1.8) depends on the scattering regime, 0.69 in the dirty limit and 0.73 in the clean limit. Indeed in [34] in the clean limit with no spin-paramagnetic considerations and $\lambda_{SO} = 0$, the prefactor obtained is 0.7273 and is in agreement with Gor'kov et al., who made earlier attempts at the same problem [35]. The spin-paramagnetism incorporated through the Maki Parameter α_M is used to represent the relative strength of orbital and spin pair breaking fields $\alpha_M = \sqrt{2} H_{c2}^{\mathrm{orb}}(0)/H_P(0)$.

1.2.2 Charge density wave

The charge density wave (CDW) is a periodic modulation of the electronic charge density ρ in real space ($\vec{r}$), described mathematically as:

$$\rho(r) - \rho_0 = A \cos(\vec{Q} \cdot \vec{r} + \varphi) = \Re(A e^{i\vec{Q}\cdot\vec{r}} e^{i\varphi}) = \Re(\Psi e^{i\vec{Q}\cdot\vec{r}}) \tag{1.9}$$

Here, ρ_0 represents the uniform charge density, $\vec{Q}$ is the ordering wave vector that dictates the periodicity, and A is the amplitude of the *density wave* [36].

The complex quantity $\Psi = Ae^{i\varphi}$ serves as an order parameter for the CDW transition, characterized by amplitude A and phase φ. In practical terms, the gap in the single-particle energy spectrum, $\Delta \approx \Delta_{\mathrm{CDW}}$, provides a useful proxy for the order parameter, analogous to how the superconducting energy gap functions as an order parameter in superconductors.

This electronic rearrangement typically couples strongly with lattice distortions: ions in the crystal lattice shift slightly from their equilibrium positions, reducing the crystal symmetry and creating a new super-lattice structure (see Fig. 1.4). Such distortions cause energy gaps to open at portions of the Fermi surface matched by the ordering wave vector $\vec{Q}$, thereby altering the electronic properties of the material. In one-dimensional systems

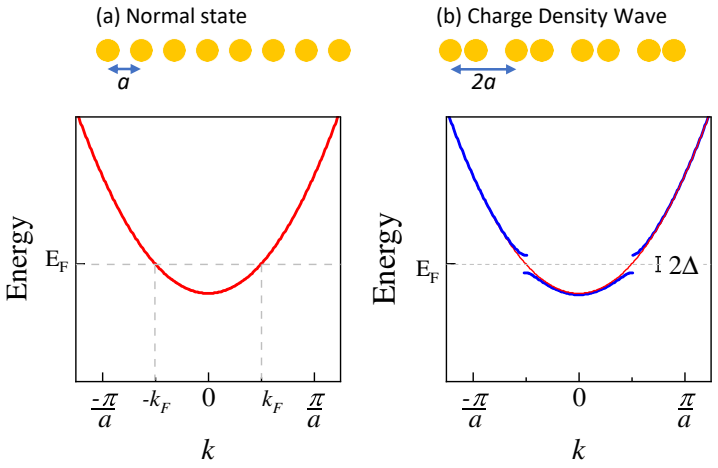

FIGURE 1.4: The idealized 1D Peierls case: Energy dispersion relations illustrating the transition from (a) normal state to (b) (CDW) state. In the normal state, atoms (yellow circles) are uniformly spaced with lattice constant a, resulting in a parabolic energy band (red curve) intersected by the Fermi level (E_F). In the CDW state, atoms undergo periodic lattice distortion with periodicity $2a$, causing an energy gap 2Δ at the $\pm k_F$ on the Fermi surface and splitting the original band into two distinct branches (blue curves).

the problem of stabilization of the lattice was first examined by Rudolf Peierls [36] (shown in Fig. 1.4). In this case, the single-particle energy gap is directly proportional to the amplitude u of the periodic lattice distortion. While such lattice distortions increase the elastic energy proportionally to u^2, they simultaneously reduce the electronic energy, which, for small displacements, scales approximately as $u^2 \ln u$. Thus, at small distortion amplitudes, the combined electron-phonon system exhibits a total energy lower than the undistorted metallic state, stabilizing the CDW phase energetically.

1.3 Quantum oscillations

Quantum oscillations are fundamental phenomena in condensed matter physics, providing direct evidence of the quantized electronic states in crystalline solids. These oscillations are observed predominantly at low temperatures and high magnetic fields, and are powerful tools for probing the electronic structure and Fermi surface (FS) geometry of various materials. Typical manifestations include the de Haas–van Alphen (dHvA) effect, related to magnetization oscillations; the Shubnikov–de Haas (SdH) effect, related to resistivity oscillations.

Under the influence of an external magnetic field B, the allowed electronic states become quantized into discrete cylindrical tubes in reciprocal space, known as Landau tubes.

Electrons are confined to cyclotron orbits perpendicular to the magnetic field direction due to the Lorentz force, $\mathbf{F} = -e(\mathbf{v} \times \mathbf{B})$, while the allowed orbits are quantized by the semiclassical Sommerfeld quantization condition $\oint \mathbf{p}.d\mathbf{r} = (n + \gamma)2\pi\hbar$, where n is the Landau index and γ is the phase offset. For a conventional trivial band with zero Berry phase $\gamma = \frac{1}{2}$ [37, 38]. These Landau tubes have cross-sectional areas proportional to the magnetic field magnitude and satisfy the Onsager–Lifshitz quantization condition [37, 38]:

$$A = \left(n + \frac{1}{2}\right) \frac{2\pi eB}{\hbar}, \quad n = 0, 1, 2, \ldots \tag{1.10}$$

where A is the cross-sectional area in reciprocal space and n is an integer.

As the magnetic field B is varied, the area of these cyclotron orbits changes. Whenever a tube crosses the boundary of the Fermi surface, electrons within that tube become depleted or filled. Consequently, the occupancy of electronic states oscillates periodically in $1/B$, with a frequency proportional to the extremal cross-sectional area A of the FS normal to the magnetic field, expressed through the Onsager relation:

$$F = \frac{\hbar A}{2\pi e} \tag{1.11}$$

This periodic depletion and replenishment of electrons generate distinct oscillations in measurable physical properties, such as magnetization, electrical resistivity, and magnetostriction.

The derivation of these oscillatory behaviors starts from thermodynamic potentials: the grand canonical potential $\Omega(T, B, \mu)$, in the presence of a magnetic field, is given by:

$$\Omega(T, B, \mu) = -k_B T \sum_n g_n \ln\left[1 + e^{-(E_n - \mu)/k_B T}\right], \tag{1.12}$$

where μ is the chemical potential, k_B is Boltzmann's constant, T is temperature. E_n represents the Landau level energies:

$$E_n = \hbar\omega_c \left(n + \frac{1}{2}\right), \quad \omega_c = \frac{eB}{m^*}, \tag{1.13}$$

and g_n denotes the degeneracy of each Landau level, proportional to eB/h per unit area in real space. Lifshitz-Kosevich derived the oscillatory part of the grand canonical potential:

$$\Omega_{\text{osc}} = CB^{5/2} \sum_{\text{orbit,i}} \left|\frac{\partial^2 A_{k,i}}{\partial k_\parallel^2}\right|^{-1/2} \sum_p p^{-5/2} R_T R_D R_S \cos\left(2\pi p\left(\frac{F_i}{B} - \frac{1}{2} + \frac{\Phi_B}{2\pi}\right) + 2\pi\delta_c\right) \tag{1.14}$$

where C is a constant (prefactor), p is the harmonic of a quantum oscillation of frequency F, $\partial^2 A_k/\partial k^2$ is the curvature of the reciprocal-space area A_k relevant to the k-component parallel to the applied magnetic field. Φ_B is the Berry phase, which is zero for conventional metals [38]. The curvature dependent phase factor δ_c varies continuously from 0 for a two-dimensional cylindrical Fermi surface to 1/8 for a three-dimensional surface. The sign of δ_c depends on whether the F_i corresponds to the (+)minimal or (-)maximal extremal cross section [38]. For an ideal two-dimensional cylindrical Fermi surface $A'' = 0$. Then, the leading field and harmonic dependence of $\Omega_{\rm osc}^{\rm 2D}$ is given by $B^2 \sum_p p^{-2} R_T R_D R_S \cos(...)$ [37]. Here, R_T, R_D, and R_S are the temperature damping factor, Dingle factor and spin-splitting factor respectively and are given by:

$$\begin{aligned} &\text{(a)} \qquad R_T = \frac{X}{\sinh X}, \quad \text{where} \quad X = \frac{2\pi^2 p k_B T m^*}{e\hbar B} \\ &\text{(b)} \qquad R_D = \exp\Big(-\frac{2\pi^2 p k_B T_D m^*}{e\hbar B}\Big) \\ &\text{(c)} \qquad R_S = \cos\Big(\frac{\pi p g m^*}{2m_e}\Big) \end{aligned} \tag{1.15}$$

Here, m^* is the effective mass of the quasiparticles, T_D is the so-called Dingle temperature (related to quasiparticle scattering rate) and g is the electron's Landé g-factor. Both temperature effects and electron scattering [Eqs. 1.15(a) and 1.15(b)] contribute significantly to the reduction of oscillation amplitudes. Finite temperature causes a broadening in energy levels, reducing oscillation amplitude (temperature damping factor R_T), while impurity scattering introduces additional damping related to electron relaxation time (τ). A shorter quasiparticle lifetime (larger scattering) increases T_D and thus suppresses oscillations. Except for the Dingle term, the Eq. (1.14) was first derived by Lifshitz and Kosevich and is therefore referred to as LK-formula [37].

Various physical quantities such as magnetization, entropy, strain, and particle number can be derived by appropriate differentiation of the grand canonical potential Ω. The three quantities in which quantum oscillations are studied in this thesis are magnetization, resistivity and length. Below, a brief description of these three is presented.

Quantum oscillations in the magnetization M, known as the de Haas–van Alphen effect, are the most studied among various physical quantities. In the presence of B, the parallel and perpendicular components of M are given by:

$$M_{\parallel} = -\left(\partial\Omega/\partial B\right)_{\mu,T}, \quad \text{and} \quad M_{\perp} = -\frac{1}{B}\left(\partial\Omega/\partial\theta\right)_{\mu,B} \tag{1.16}$$

Here, θ is the angle specifying the orientation relative to the direction of B in the plane in which Ω varies most rapidly with the direction of B. One can then show that the

oscillatory components of the magnetization are given by:

$$M_{\parallel}^{osc} = -\left(\frac{e}{\hbar}\right)^{3/2} \frac{2Fk_BTV}{(2\pi B|A''|)^{1/2}} \sum_{p=1}^{\infty} \left[\frac{\exp\left[-\frac{2\pi^2 p k_B T_D m^*}{e\hbar B}\right] \cos\left(\frac{\pi p g m^*}{2m_e}\right)}{p^{1/2} \sinh\left[\frac{2\pi^2 p k_B T m^*}{e\hbar B}\right]} \times \sin\left(2\pi p\left(\frac{F}{B} - \frac{1}{2} + \frac{\Phi_B}{2\pi}\right) \pm \frac{\pi}{4}\right) \right] \tag{1.17}$$

$$M_{\perp}^{osc} = -\frac{1}{F}\frac{\partial F}{\partial \theta} M_{\parallel}^{osc} \tag{1.18}$$

Similarly, the Shubnikov–de Haas effect arises from oscillations in resistivity due to periodic modulation of the density of states at the Fermi energy E_F. For a single Fermi-surface sheet, the relative amplitude of the oscillatory conductivity is given by [37]:

$$\left|\frac{\delta\sigma_{xx}}{\sigma_{xx}}\right| \sim R_T \left|\frac{\tilde{g}(E_F)}{g_0(E_F)}\right| \tag{1.19}$$

where $g_0(E_F)$ is the non-oscillatory density of states, $\tilde{g}(E_F)$ is its oscillatory part, and R_T is the temperature damping factor. Oscillations occur due to the periodic variation of $g(E)$ with Landau levels crossing μ.

Magnetostriction oscillations are oscillations in the length of the sample. They result from the coupling between electronic states and lattice deformations. The crystal strain ϵ_{ij} can be related directly to changes in Ω under stress σ_{ij}:

$$\epsilon_{ij} = -\frac{\partial \Omega}{\partial \sigma_{ij}} \tag{1.20}$$

which gives,

$$\epsilon_{ij,osc} = -\sum_r \left(\frac{\partial \ln F_r}{\partial \sigma_{ij}}\right) \tilde{M}_r B \tag{1.21}$$

The oscillatory change δl_{osc} of the sample dimension (l) is of the same order of magnitude as the largest component of the strain $\epsilon_{ij,osc}$ and hence the term oscillatory magnetostriction is used for $\epsilon_{ij,osc}$.

In real materials, multiple FS pockets and extremal cross-sectional areas often exist, generating multiple quantum oscillation frequencies. This is shown using the example of the Copper Fermi surface in Fig. 1.5. Fermi surface of Cu was generated from the example files of Ref. [39] and plotted with FermiSurfer [40]. The terms *neck* and *belly* are used to mark the regions on the Fermi surface with minimum and maximum area, respectively. The famous *dog-bone* orbit in Copper spans over multiple Brillouin zones (Fig. 1.5(E)). Apart from this, some frequencies may appear only at specific angle, such as shown in Fig. 1.5(D,E). In Fig. 1.5(F), a cylindrical Fermi surface with modulation in radius along

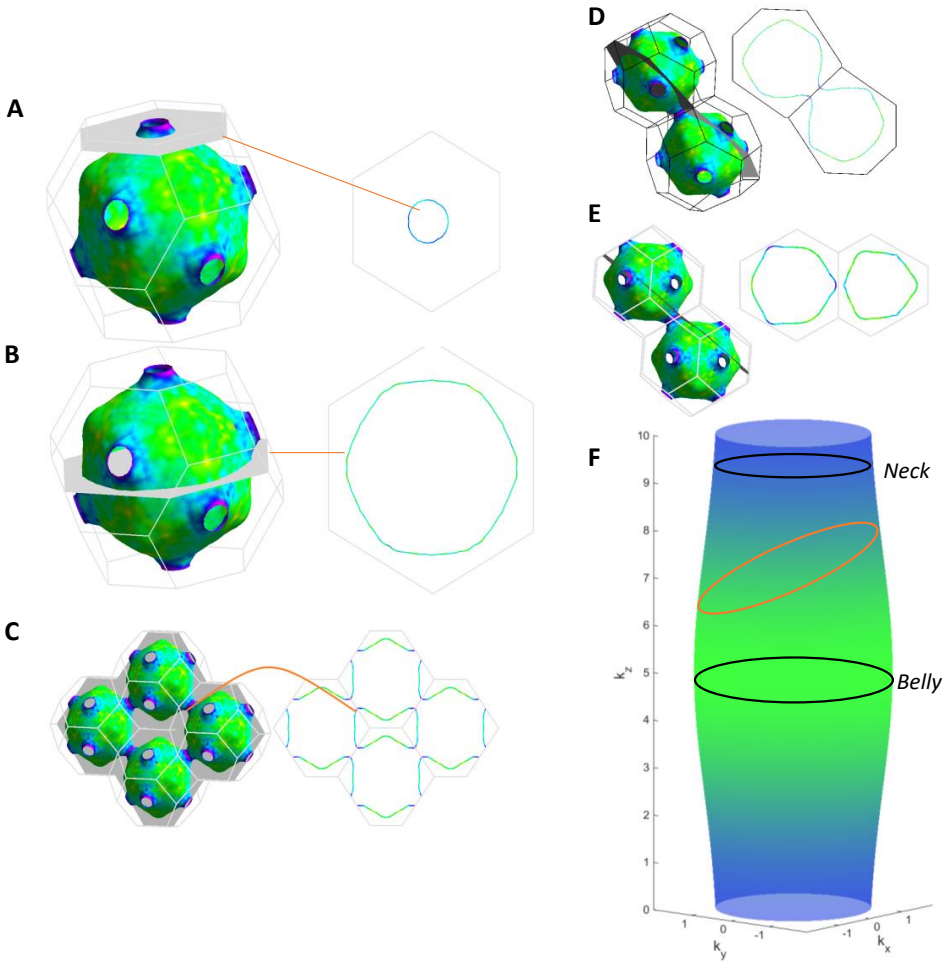

FIGURE 1.5: (A-E) Fermi Surface of Copper: (A, B, C) show the neck, belly and the famous dog-bone orbit for the Cu. (D,E) When B_{ext} is rotated, a high-frequency will appear corresponding to the connected path along the neck as shown in (D), and will disappear for (E). (F) Shows the cylindrical Fermi surface with modulation along the z-axis common to the Fe-based superconductors and many layered compounds. The neck and belly regions are marked corresponding to which the frequencies are observed in the quantum oscillation spectra when B_{ext} is parallel to the length of the cylinder (quantum oscillation frequencies only arise from the extremal orbits). As the B_{ext} is rotated, the frequencies will arise from the curves such as the orange curve. The two frequencies from neck and belly eventually merge at a specific angle called Yamaji angle.

the length is shown. Such a Fermi surface is common to 2D/quasi-2D materials studied in this thesis (iron-based and AV_3Sb_5). While in AV_3Sb_5, numerous small 3D orbits also exist, the majority of the area of the BZ is spanned by hexagonal/hyperbolic cylindrical Fermi sheets. For these cylindrical FS, as the angle of B_{ext} approaches alignment perpendicular to the length of the cylinder, the corresponding F will become larger and larger and will disappear. This is not the case with 3D orbits, say spherical or elliptical pockets. Finally, special cases such as magnetic breakdown may also occur, for example, in Fig. 1.5(E), electrons may tunnel between closely spaced separate Fermi pockets under sufficiently

large magnetic fields (see App. A).

1.4 Outline of the thesis

The experimental, theoretical and data analysis methods are introduced in Chapter 2. In Chapter 3, we first present a more detailed introduction to the Fe(Se,Te) system and its magnetic, orbital and superconducting properties, along with the open questions in the literature. Following this, in Sec. 3.2-3.4, results from different studies are presented. We start with an annealing study of the optimally doped Fe(Se,Te) single crystals, especially how the removal of excess Fe affects the transport and magnetic properties is shown. The role of the $FeTe_m$ layer formation is discussed. Then, a study on the two superconducting domes and possibly distinct mechanisms is presented. Here, we provide evidence from different physical quantities to argue for the different superconducting mechanism in two domes of the Fe(Se,Te) system. In Sec. 3.4, we present the cooperative coupling between the superconductivity and nematicity. Based on this, we argue that the spin-nematic scenario may not fully account for the observed coupling in FeSe. In chapter 4, the nematic-lattice coupling and its effect on the phase diagram is discussed with remarks on the possible quantum criticality in the system.

In Chapter 5, we discuss the reconstruction of the Fermi surface below the CDW and the corresponding signatures in the quantum oscillations for AV_3Sb_5 (A=Cs, Rb, K) compounds. Following this, the details about the electronic structure and compilation of the quantum oscillation studies in the literature are presented. The results are split into two parts. In the first part, Sec. 5.2, we present the zero field thermodynamic and transport study of all the compounds in the series. Similar to the CsV_3Sb_5, the uniaxial pressure derivatives of the T_{CDW} for RbV_3Sb_5 show a highly pronounced response along the c-axis. For all three compounds, we observe a characteristic temperature scale in the resistivity which is likely related to the highly two-dimensional character of the system. In the second part, Sec. 5.3, we present the large study of the quantum oscillations in transport, magnetization and magnetostriction in all three compounds. We relate our results to the reported differences in interlayer modulation upon changing the alkali atom. Finally, by comparing the magnetostriction and magnetization data, we discuss the strain dependence of the small elliptical orbits in RbV_3Sb_5.

Chapter 2

Methods

The chapter begins with a description of the experimental methodologies employed throughout this thesis, including resistivity, magnetization, heat-capacity, and thermal-expansion measurements. How various phase transitions manifest in these measurements is also discussed. Subsequently, an introduction to Landau theory of phase transitions is presented, with emphasis on how to construct the free-energy functional for any system. This has been extensively used in this thesis. A brief overview of density functional theory (DFT) and the procedure for extracting frequencies from DFT calculations is provided. Finally, two programs developed in the course of this thesis are described: one for modeling the heat-capacity measurements within the framework of the α-model, and another for analyzing quantum oscillations.

2.1 Experimental methods

Thermodynamic and transport measurements are indispensable tools for probing fundamental physical phenomena in materials. Transport measurements provide insights into scattering mechanisms and electronic correlations. Magnetization measurements reveal magnetic ordering and transitions between magnetic phases. Heat capacity and thermal expansion measurements, meanwhile, quantify the energetic and structural changes associated with phase transitions, crucial for a complete thermodynamic description.

2.1.1 Resistivity measurements

Resistivity measurements presented in this thesis were conducted using a standard four-point configuration. In this setup, two outer wires serve as current contacts and two inner wires function as voltage contacts. Contacts were made using two-component silver-filled epoxy (EPO-TEK H20E) or silver paint (Welbring 200N), along with gold or platinum wires for connection. The silver paint or epoxy is applied carefully to establish current contact across all sample layers, crucial for eliminating unwanted perpendicular-axis contributions to resistivity [41]. Measurements were carried out using the AC Transport or Electrical Transport Option of the Physical Property Measurement System (PPMS) from Quantum Design. A precision current source supplies an AC drive current, while voltage preamplifiers amplify the sample's voltage response, which is then analyzed by a Digital Signal Processor (DSP). The DSP computes the in-phase and out-of-phase components, as well as second and third harmonics. These higher harmonics serve as an indicator of the *quality* of the measurement; all presented measurements maintained harmonics $< -40\,\mathrm{dB}$.

Electrical transport also provides crucial information about the low-temperature behavior. At very low temperatures, many metals enter the *Fermi-liquid* regime, in which the resistivity often follows: $\rho = \rho_0 + AT^\gamma$, with $\gamma = 2$. In contrast, in a non-Fermi-liquid regime, the resistivity deviates from this quadratic form and is often described by $\gamma < 2$, and for strange metals $\gamma \approx 1$ [42].

2.1.2 Magnetization measurements

Magnetization measurements were performed using the Vibrating Sample Magnetometer (VSM) option of the PPMS (Quantum Design). The VSM operates based on Faraday's Law of Induction. The sample is mounted on a rod driven sinusoidally (typically at 40 Hz) through a gradiometer pickup coil in the VSM puck (Fig. 2.1(a)). Taking z as the

vertical position of the sample, if the sample possesses a magnetic moment, the resulting change in magnetic flux will induce a voltage:

$$V_{\text{coil}} = \frac{d\Phi}{dz}\frac{dz}{dt}, \tag{2.1}$$

where Φ is the magnetic flux enclosed by the pickup coil, and t is the time. A pre-amplifier amplifies this signal. The VSM detection module isolates this voltage signal from the external mechanical and electronic noise.

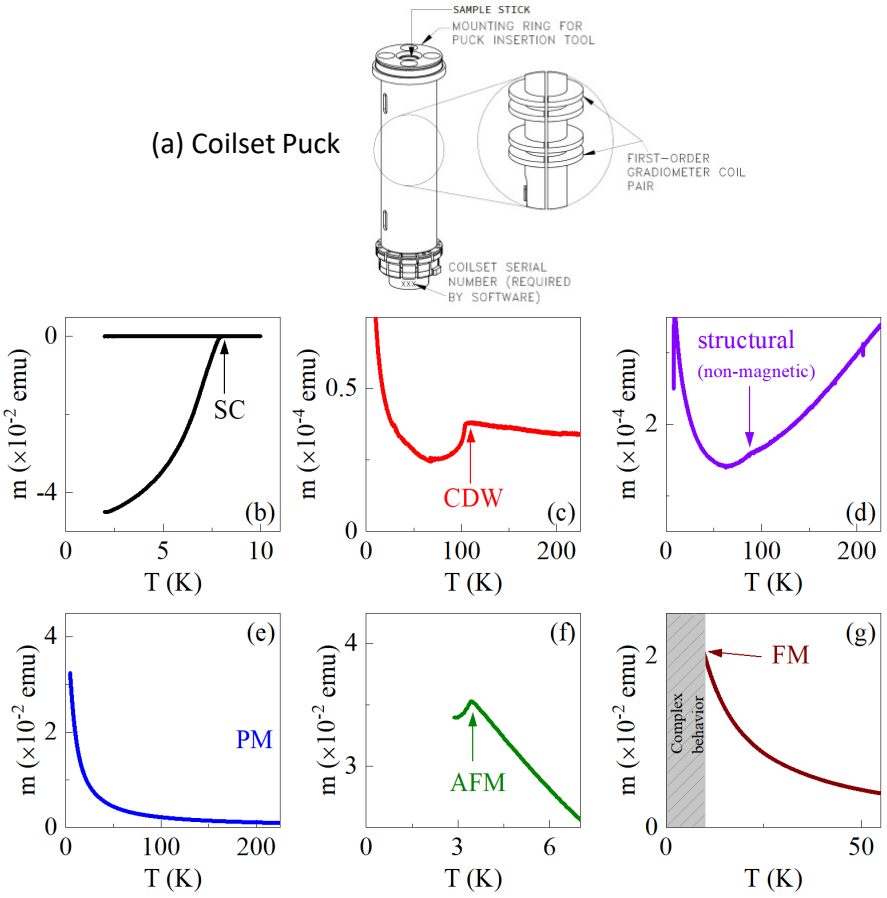

FIGURE 2.1: (a) Schematic of the PPMS coilset puck used for magnetization measurements, highlighting the first-order gradiometer coil pair arrangement (Taken from Quantum Design VSM Manual). (b–g) Moment (m) versus temperature (T) curves obtained from PPMS-VSM measurements, demonstrating characteristic behaviours of various magnetic and electronic states: (b) superconducting (SC) transition, (c) charge density wave (CDW) anomaly, (d) nematic transition indicated by a subtle kink, (e) paramagnetic (PM) state, (f) antiferromagnetic (AFM) transition showing a distinct peak, and (g) ferromagnetic (FM) transition exhibiting complex behavior at lower temperatures (shaded region). In the CDW and nematic transitions shown here, no magnetic order emerges; however, these transitions are detected through magnetization due to the associated changes in the density of states.

The magnetic moment is derived by fitting the measured sinusoidal voltage response to the theoretical form expected for sinusoidal vibrations of the sample with magnetic

moment m, i.e., $V_{\text{coil}} = 2\pi CfmA\sin(2\pi ft)$, where C is a coupling constant, f and A are the frequency and amplitude of the oscillation. The reference position signal comes from the VSM motor module.

2.1.3 Heat-capacity measurements

Heat capacity C quantifies the heat required for a unit temperature change in a material and is fundamental in thermodynamic characterization. In this thesis, heat-capacity measurements utilized the PPMS Heat Capacity option (Quantum Design). The sample is mounted on a calorimeter chip containing an integrated resistive platform heater and thermometer. At low temperatures, Apiezon N grease ensures optimal thermal contact between the sample and the calorimeter platform.

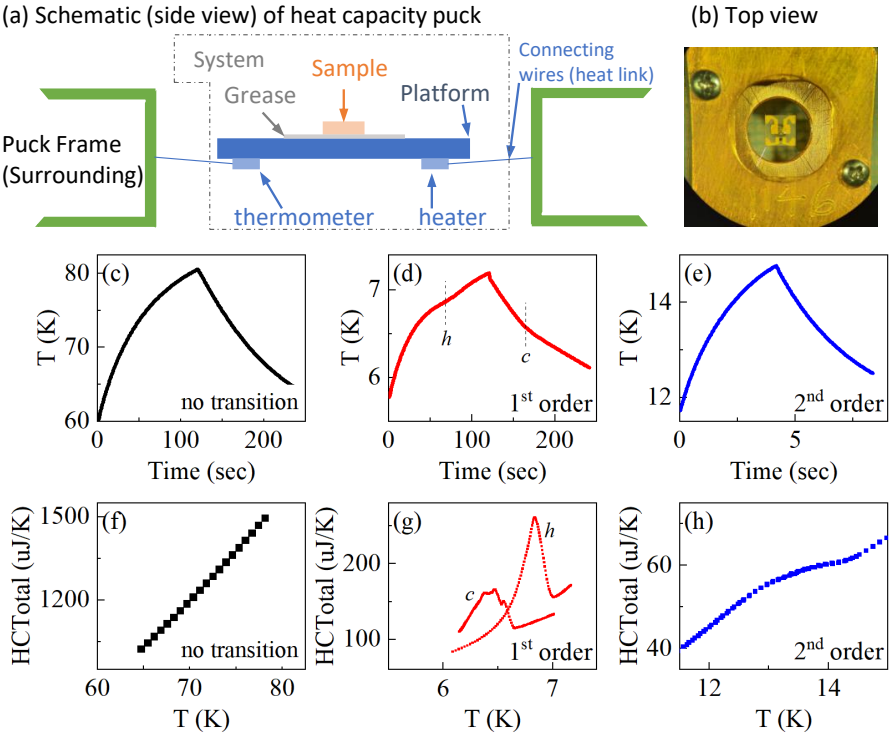

FIGURE 2.2: (a) Schematic side view of the heat capacity measurement puck, showing the sample mounted on a platform connected by grease, with heater and thermometer elements linked by connecting wires to a puck frame. (b) Top-view photograph of the heat capacity puck. (c-e) Temperature versus time curves illustrating heat pulses and cooling periods for: (c) no phase transition, (d) first-order phase transition with clear hysteresis (indicated by heating 'h' and cooling 'c' curves), and (e) second-order phase transition. (f-h) Corresponding total heat capacity (HCTotal) data as a function of temperature, showing (f) a smooth increase for no transition, (g) a sharp discontinuity and a hysteresis loop for a first-order transition, and (h) a continuous change with *extra entropy* characteristic of a second-order transition.

The calorimeter chip is suspended by four or eight wires, providing both electrical connections to the heater and thermometer, as well as thermal links to the puck frame. Here, the puck frame acts as the thermal bath, and the combined sample-platform assembly forms the measurement system.

Measurements employ the thermal relaxation method, applying a heat pulse and recording the heating and cooling responses (see Fig. 2.2(c-e)). The resulting temperature-time data are analyzed with Quantum Design's two-τ model™, which addresses temperature gradients between the sample and platform, based on Ref. [43]. The fitted results yield the sample's specific heat (see Fig. 2.2(f-h)).

2.1.4 Thermal expansion measurements

Thermal expansion describes the dimensional changes of a material with temperature. Although straightforward conceptually, precise measurement is challenging due to minute dimensional variations, typically around 10^{-3} when cooling from room temperature to 5 K. Accurate detection thus requires relative resolutions of at least 10^{-7} [44]. While X-ray diffraction is a common technique, it rarely provides continuous measurements and involves extensive data refinement, introducing uncertainties.

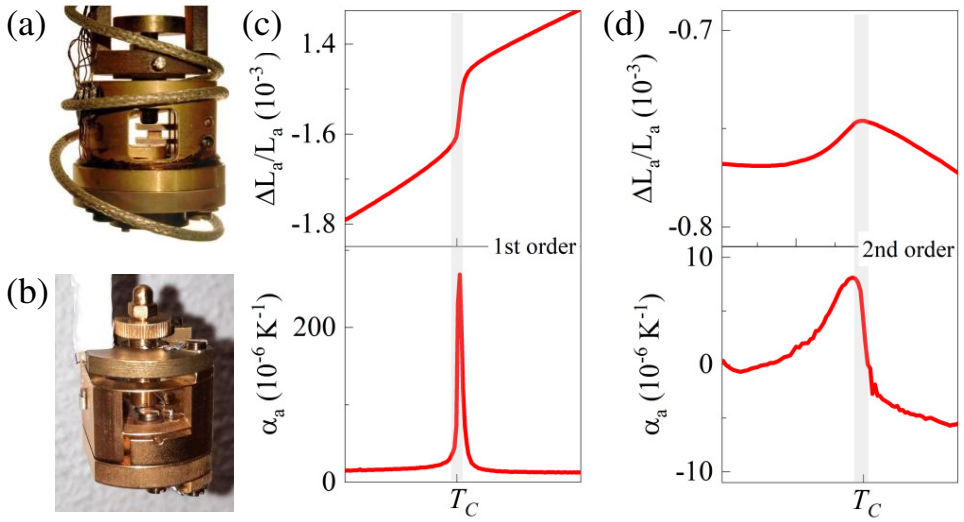

FIGURE 2.3: Photograph of the capacitive dilatometer (a) at Karlsruhe [45] and (b) at Nijmegen [44]. All the zero-field measurements were done in (a) and the high field magnetostriction of $(Cs, Rb)V_3Sb_5$ was done in (b), (c-d) show how a typical first order and second order transitions appear in the relative length change and thermal expansion coefficient $\alpha = (1/L)dL/dT$ respectively. In the first order case, the length change has a discontinuity, and consequently α has a sharp peak. In the second order case, the length change is continuous and has only a slope change; α in this case has a step. The data used are from the CDW transition in AV_3Sb_5.

Capacitance dilatometry addresses these limitations by measuring capacitance changes between two parallel plates sandwiching the sample. One plate remains fixed to the dilatometer frame, while the other plate is movable and connected via parallel springs. The sample is held under a controlled force (approximately 0.2 N in the home-built KIT dilatometer [45], suitable for fragile iron-chalcogenides). Commercial dilatometers (e.g., [44]) may apply higher forces (up to a few newtons), necessitating thicker samples. Capacitance variations are measured precisely using a capacitance bridge, and calibration with a Copper sample corrects for cell expansion and initial capacitor spacing.

At a structural phase transition, such as going from tetragonal to orthorhombic, a material often forms multiple equivalent crystallographic domains (twins) in the reduced symmetry state. *Detwinning* is the process by which these different domain orientations are eliminated or significantly reduced, resulting in a single-domain sample. This is often achieved by applying uniaxial stress or directly during crystal growth.

For the iron-based superconductors, the sample is detwinned in situ by measuring (with an application of small compressive stress) along $[110]_{\text{tet}}$ because it preferentially selects one domain orientation over the other in the orthorhombic phase. In the high-temperature phase, the crystal structure has a four-fold rotational symmetry, and the in-plane lattice parameters are equal. The low temperature orthorhombic phase, C_2, breaks this in-plane symmetry ($a \neq b$), and two equivalent domain orientations (twins) can form, related by a 90-degree rotation: (domain 1) the shorter a_{orth}-axis lies along the original $[110]_{\text{tet}}$ direction, and (domain 2) the longer b_{orth}-axis lies along the original $[110]_{\text{tet}}$ direction. In the absence of external perturbation, both domain orientations are equally favorable. The effect of the strain along different directions is summarized in Table 2.1.

	strain along original $[100]_{\text{tet}}$	strain along original $[110]_{\text{tet}}$
domain 1:	the $[100]_{\text{tet}}$ lies at 45° to both a_{orth}- and b_{orth}-axis	the $[110]_{\text{tet}}$ direction aligns along the shorter a_{orth}-axis.
domain 2:	the $[100]_{\text{tet}}$ lies at 45° to both a_{orth}- and b_{orth}-axis	the $[110]_{\text{tet}}$ direction aligns along the longer b_{orth}-axis
result:	minimal energy difference between domains due to the external strain	external strain favors the domain orientation where the shorter a_{orth}-axis aligns along the direction of the applied strain.

TABLE 2.1: External strain effects on the domain formation. Here we have assumed two-Fe tetragonal notation and that b_{orth}-axis is the longer axis as in Ref. [9] for FeSe.

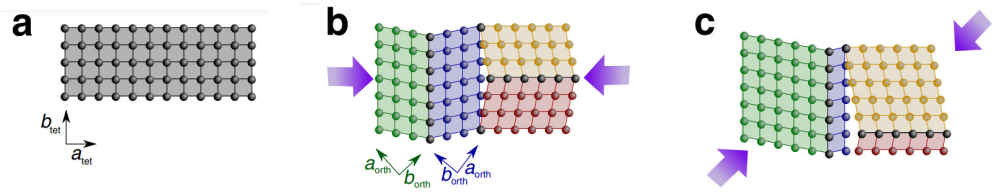

FIGURE 2.4: Adapted from Böhmer et al., Nat. Comm. 6, 7911 (2015) under CC BY 4.0. De-twinning of an iron-pnictide sample in the thermal expansion setup.

2.2 Theoretical and phenomenological methods

2.2.1 Ginzburg-Landau theory

This thesis largely explores phase transitions in iron-based (nematicity and superconductivity) and kagome (CDW and superconductivity) systems and the interplay among phases in these systems. The first step in understanding the physics of phase transitions is usually to discuss their main aspects within the framework of the Landau–Ginzburg theory [46]. Central to it is the concept of an *order parameter*. Assuming a continuous phase transition occurs at $T = T_c$, such that a new phase exists below T_c, the order parameter ϕ differentiates between the two phases in the following way:

$$\begin{aligned} \phi(T) &= 0 \qquad && (T > T_c) \\ \phi(T) &\propto (1 - T/T_c)^{\beta} \qquad && (T < T_c) \end{aligned} \tag{2.2}$$

where β is a critical exponent. The free-energy functional $\mathcal{F}$ is written in terms of this order parameter as

$$\mathcal{F} = \int d^3r \left[\mathcal{F}_0 + A_2\phi^2 + A_3\phi^3 + A_4\phi^4 + \cdots + K(\nabla\phi)^2\right], \tag{2.3}$$

where the coefficients A_i are functions of the thermodynamic variables (p, T, ϵ). In the vicinity of the phase transition, the order parameter ϕ is small and higher-order terms can therefore be neglected; in practice, terms beyond fourth order are usually not considered. In particular, the quadratic coefficient is usually taken in the form: $A_2 = a(T - T_c)$, with $a > 0$, such that the transition occurs at $T = T_c$. Another important constraint comes from the symmetry breaking involved at the phase transition. The free energy should remain analytic with respect to the order parameter and must be invariant under the symmetry operations of the high-temperature phase. In a number of phases, it means that only even terms are permitted. In superconductivity, ϕ is complex; therefore, the free energy must be written in terms that remain real, such as $|\phi|^2$ and $|\phi|^4$. In the Ising model, the presence of $\mathcal{Z}_2$ symmetry requires that $\mathcal{F}(S_i) = \mathcal{F}(-S_i)$, hence, the odd

powers vanish. Using these constraints, the free-energy functional can be written for any system undergoing a phase transition. Other than symmetry, no microscopic quantity explicitly enters the expression for the free energy. Thus, a whole class of phase transitions can give rise to the same Ginzburg-Landau theory. By minimizing the free energy with respect to the order parameter, one can obtain the expressions for the equilibrium free energy, specific heat, and the order parameter itself. In this thesis, the discussion is limited to the spatially uniform limit, since the focus is on bulk phase transitions and their thermodynamic and transport signatures rather than on spatial variations of the order parameter such as domain walls, vortices, or critical fluctuations.

2.2.2 Density functional theory

Density functional theory (DFT) is a computational method that can be used to investigate the electronic structure of many-body systems, for example in condensed matter. The theory uses a functional of the electron density to determine the properties of the system. For $(Cs, Rb)V_3Sb_5$, the DFT calculation using the room-temperature structure was performed by Prof. Amalia Coldea at the University of Oxford using Wien2K [47]. Generalized Gradient Approximation (GGA) was used and a k-mesh of 40000 points was set up. The bxsf file obtained from the calculation was used to determine the quantum oscillation frequencies using the Supercell K-space Extremal Area Finder (SKEAF) software by Rourke and Julian [48]. The plots were prepared using the XCrysden [49] and Fermisurfer [40]. The slices at $k_z = 0, 0.5$ were cut and a Matlab program then plotted and calculated the area of the closed 2D orbits for these slices. This was compared against the result obtained by SKEAF to assign the frequencies to the corresponding orbits.

2.3 Data analysis methods

Here, we describe the two programs constructed: (a) to model heat-capacity data using candidate superconducting gap structures within the framework of the α model, and (b) to analyze quantum oscillations in any physical quantity.

2.3.1 Superconducting gap structure

Despite being phase-insensitive, heat capacity provides crucial information about the gap structure. Below $T < T_c$, the total heat capacity contains both lattice and electronic

contributions, with the electronic part being modified by the onset of superconductivity. To isolate this superconducting contribution, the measured total heat capacity above the superconducting transition can be fitted using a lattice-harmonic approximation

$$C_{\text{fit}} = \gamma T + B_3 T^3 + B_5 T^5 + B_7 T^7 + \dots \tag{2.4}$$

where $C_{\text{lat}} = B_3 T^3 + B_5 T^5 + B_7 T^7$ is the lattice contribution and the γT is the electronic contribution. The T^3 coefficient is related to the Debye temperature T_D by: $B_3 = 12\pi^4 NR/5T_D^3$, where N is the number of atoms per formula unit and R is the molar gas constant. B_5 and B_7 (and higher terms if included) account for higher-order corrections to the simple T^3 behavior. These reflect anharmonic lattice vibrations, additional phonon branches beyond the low-energy (acoustic) modes, or other subtleties in the phonon spectrum. The C_{fit} obtained in this way is extrapolated down to 0 K (to distinguish, let us call it $C_{\text{fit,ext}}$). The superconducting contribution is then:

$$C_e = (C_{\text{measured}} - C_{\text{fit,ext}}) + \gamma T. \tag{2.5}$$

Under BCS theory, exact values and expressions exist to analyze the heat capacity, and in most theoretical frameworks, it is one of the standard quantities that is calculated. Also, unlike Bogoliubov quasiparticle interference imaging (BQPI), angle-resolved photoemission spectroscopy (ARPES), and tunnel-diode-based penetration depth measurements, it is a bulk measurement. In general, for a sufficiently large sample, reliable high-quality data can be obtained for heat capacity, unlike muon spectroscopy, which although is a bulk technique can have very large noise. In the BCS paradigm, the complete expression for heat capacity is:

$$\frac{C_e}{T} = \frac{4N(E_F)}{2\pi k_B T^3}\left[\int_0^\infty \int_0^{2\pi} \frac{e^{\zeta/k_B T}}{(1+e^{\zeta/k_B T})^2} \times \left(\epsilon^2 + \Delta^2(\theta,T) - \frac{T}{2}\frac{d\Delta^2(\theta,T)}{dT}\right) d\theta\, d\epsilon\right] \tag{2.6}$$

This can be evaluated numerically to get the electronic specific heat in the superconducting region. The crucial quantities here are: (a) the upper bound of ϵ and (b) the evaluation of the derivative $d\Delta^2/dT$. To estimate ϵ_{cutoff}, we first discuss the coherence factor (ν_k^2) with respect to ϵ, which is the single-particle energy relative to the Fermi level. The occupation fraction is given by:

$$\nu_k^2 = \frac{1}{2}\left[1 - \frac{\epsilon}{\sqrt{\epsilon^2 + \Delta^2(\theta,T)}}\right] \tag{2.7}$$

It is plotted in Fig. 2.5 for three different values of Δ normalized by $k_B T_c$. The Δ_2 corresponds to the $T = 0$ in BCS theory. In the superconducting state, the single-particle thermal/disorder-induced occupation around the Fermi level in the normal state is replaced

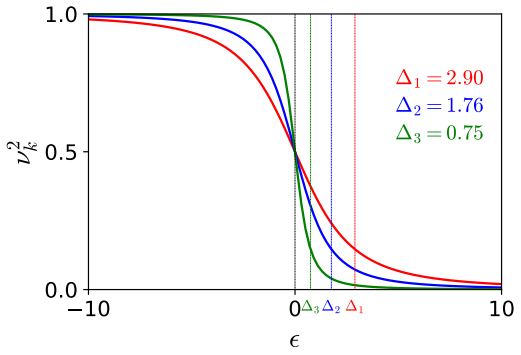

FIGURE 2.5: BCS occupation fraction from Eq. (2.7) for different values of Δ (normalized to $k_B T_c$) against single particle energy ϵ.

by the many-body wave function which is a superposition of various electron occupancy configurations, all linked by fixed phase relationships. The coherence factor ν_k^2 is the pair-occupation probability of this state. At finite temperatures, the actual occupation is further modified by thermally excited quasiparticles, and increasing temperature smears the occupation of states. A larger superconducting gap likewise broadens the energy distribution (see Fig. 2.5), broadening the range over which the transition from occupied to empty states occurs. This is important for setting the upper limit to the integration over the energy spectrum. In principle, it is limited by the Debye value $\hbar\omega_D$, as the BCS pairing is mediated by the electron-phonon coupling. Numerically, it is effectively limited to energies up to a few (say 5-20 times $\Delta(0)$), since contributions from much higher energies become negligible, as shown in Fig. 2.5. The convergence of C_e was verified with respect to this cutoff. Also, setting too large a cutoff can result in numerical overflow at very low temperatures. In contrast, for too small a cutoff, an underestimate of the heat capacity occurs, although the low-temperature behavior may still be correct. (b) Evaluation of the derivative $d\Delta^2/dT$ is done using the finite-difference method: $d\Delta^2/dT = 2 \cdot \Delta \cdot ((\Delta(T + dT) - \Delta(T))/dT)$, where $dT \to 0$. By setting $dT = 10^{-4} - 10^{-6}$ sufficiently small, a good solution can be obtained. To model the superconducting heat capacity, we solve the BCS gap equation in the form of Eq. (1.5) self-consistently and compute the temperature dependence of the specific heat using the gap function $\Delta(T, \theta)$. Certain normalizations of the constants were also made to facilitate the numerical convergence. The modified gap and the resulting changes in the gap equation and the specific heat were directly built into the program for quick analysis. For self consistent solution of the gap equation, an initial guess has to be provided. This was given as the usual temperature dependence in $T \to T_c$ limit:

$$\Delta(T, \theta) = \Delta(T, 0) = \Delta(0)\sqrt{1 - \frac{T}{T_c}} \tag{2.8}$$

In principle, the final solution is immune to the initial guess provided the initial guess itself is not absurd. Several other common functional forms, including the generalized functional form due to Gross [33], were also tested, all of which gave the same result, implying the correctness of the program. Finally, the two-gap model can be incorporated, in which the specific gap contribution of each band is calculated separately and the total heat capacity is given as $C_e = n_1 C_{e1} + n_2 C_{e2}$, where $n_1 + n_2 = 1$ [32]. The single gap and two gap output for standard s, es, $s\pm$, d waves are shown below. For these cases, the angular part of the gap equation is written in the polar form as:

$$\begin{aligned} & \Delta(\theta) = \Delta(\alpha_{10} + \alpha_{11}\cos 2\theta + \alpha_{12}\cos 4\theta + \dots) \\ \textit{alternatively,} \quad & \Delta(\theta) = \Delta_1 + \Delta_2 \cos 2\theta + \Delta_3 \cos 4\theta + \dots \end{aligned} \tag{2.9}$$

where θ is the angle taken from $\Gamma - X$ line.

(a) s-wave:
$\Delta(0) = 1.76 k_B T_c$

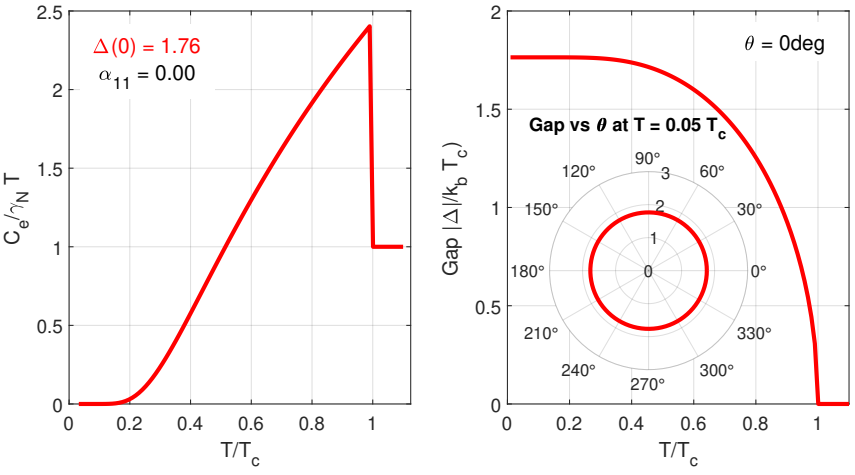

(b) d-wave:
$\Delta = \Delta(0)\cos 2\theta$
$\Delta(0) = 2.14 k_B T_c$

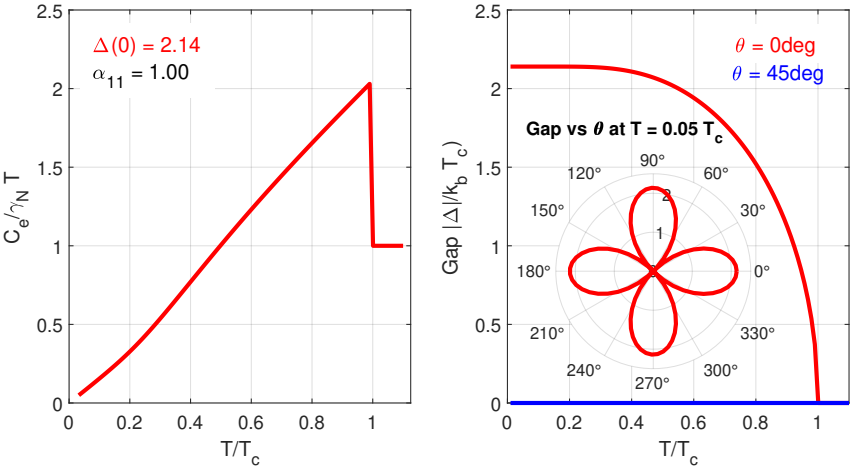

FIGURE 2.6: The heat capacity and the temperature and angular dependence for (a) s-wave and (b) d-wave superconductors with the stated $\Delta(0)$. For the d-wave at very low temperatures $T/T_c < 0.2$, a near-linear behavior occurs; this is the noted T^2 dependence of C_e in the d-wave superconductors.

(c)
$\alpha_{10} = 1$
$\alpha_{11} = 0.45$

(d)
$\alpha_{10} = 1$
$\alpha_{11} = 0.85$

(e)
$\alpha_{10} = 1$
$\alpha_{12} = 0.15$

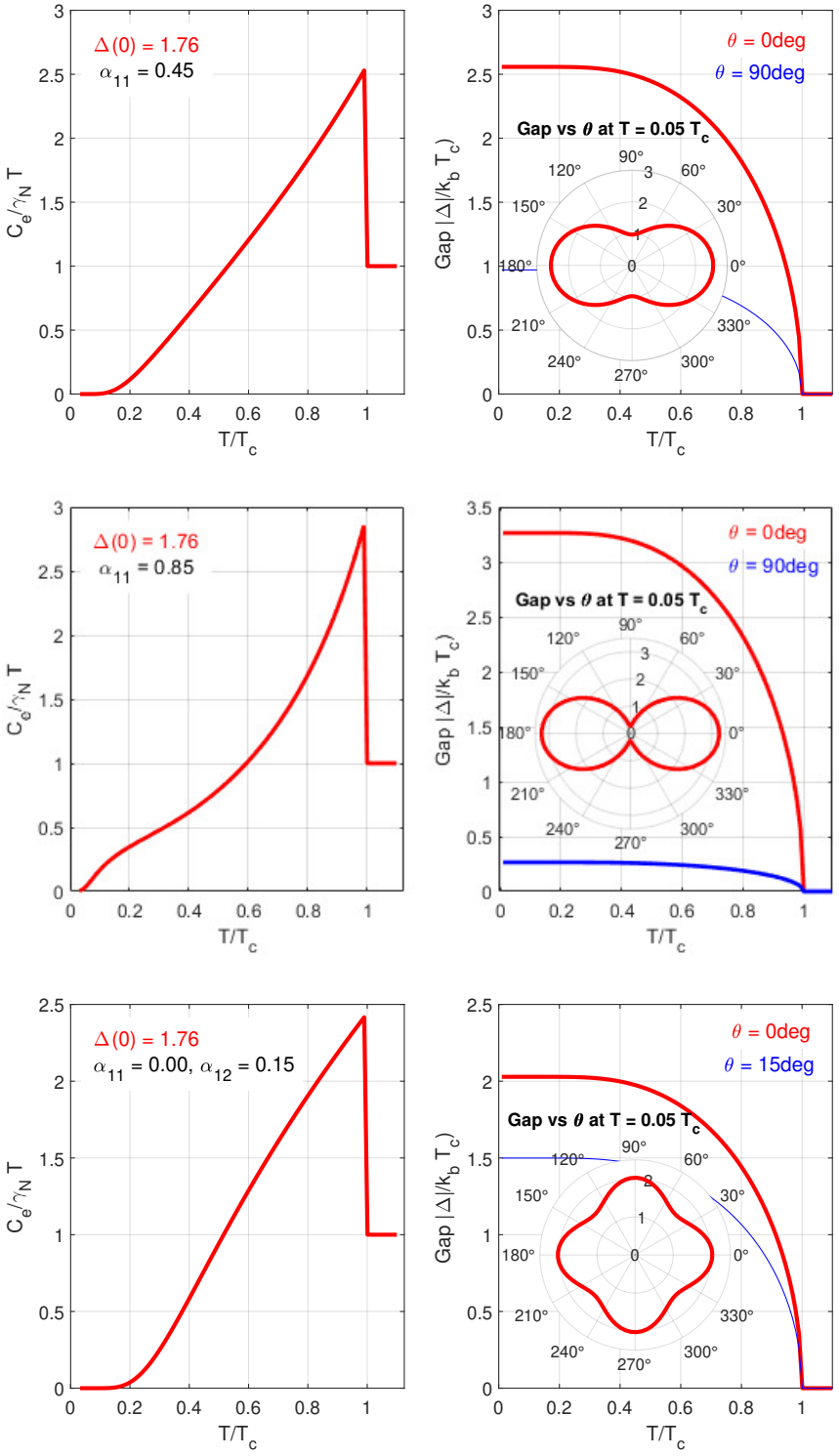

FIGURE 2.7: (c-e) Heat capacity and the temperature and angular dependences for different values of $\alpha_{11,12}$. For FeBS, these contributions emanate from nematicity, and tetragonal phase, respectively.

2.3.2 Analysis of quantum oscillations

To analyze the quantum oscillations, the oscillatory part of the obtained signal in the physical quantity ($R, M, \Delta L \ldots$ vs B) has to be extracted. For this oscillatory signal, the Fast-Fourier transformation is carried out to determine the frequencies. Apart from this, the band-pass filtering, fitting with the Lifshitz-Kosevich equation are also carried out for further analysis. To do this, several programs exist or are offered embedded in software such as Origin, Igor etc. In most of these cases, the smoothing algorithms and windowing functions used are either unknown or available only with limited functionality. The *know-how* of the analysis is thus boxed away.

In the course of this work, a dedicated Python program was written to carry out the background subtraction, FFT, band-pass filtering and the complete fit of the LK-equation to the filtered signal. A Graphic User Interface was created using the wx-utility in Python. The GUI was designed with simplicity to prioritize functionality. Up to five frequencies can be simultaneously fitted together, with control provided for the different parameters.

For the AV_3Sb_5 kagome several frequencies exist in close quarters; the analysis is therefore prone to risks of over-parametrization and spectral leakages, which is one of the reasons for large mismatches in the QO spectra known in these compounds [50–63]. The Py-program offered a faster analysis with control over the methods and functions used. The panel and the generated graph window are shown in Fig. 2.8. Spyder [64] integrated development environment was used for programming in Python. For carrying out the FFT, the following processing of the signal is performed:

1. **Extraction of the oscillatory part** - $\mathcal{Q}_{osc} = \mathcal{Q} - \mathcal{Q}_{st}(B)$. This is usually done by approximating the B dependence of the physical quantity using a low order polynomial. If higher-order polynomials are needed, the low-frequency spectrum needs careful analysis to weed out the artificial frequency arising from the slow moving polynomial background. In case of magnetization M and Hall coefficient Rxy standard functional forms such as Brillouin function for the M can also be used.

2. **Interpolation of the data** to 2^n, where n is an integer - To perform a standard FFT, the data must be sampled at equal intervals in the independent variable, which in the present case is typically $1/B$. FFT-based analysis using NumPy and MATLAB is often most efficient when the number of points is chosen as 2^n [65, 66]. The requirement of equal spacing follows from the discrete Fourier transform (DFT) which is defined as:

$$\mathcal{F}_k = \sum_{n=0}^{N-1} \mathcal{Q}_n e^{-i(2\pi kn)/N} \tag{2.10}$$

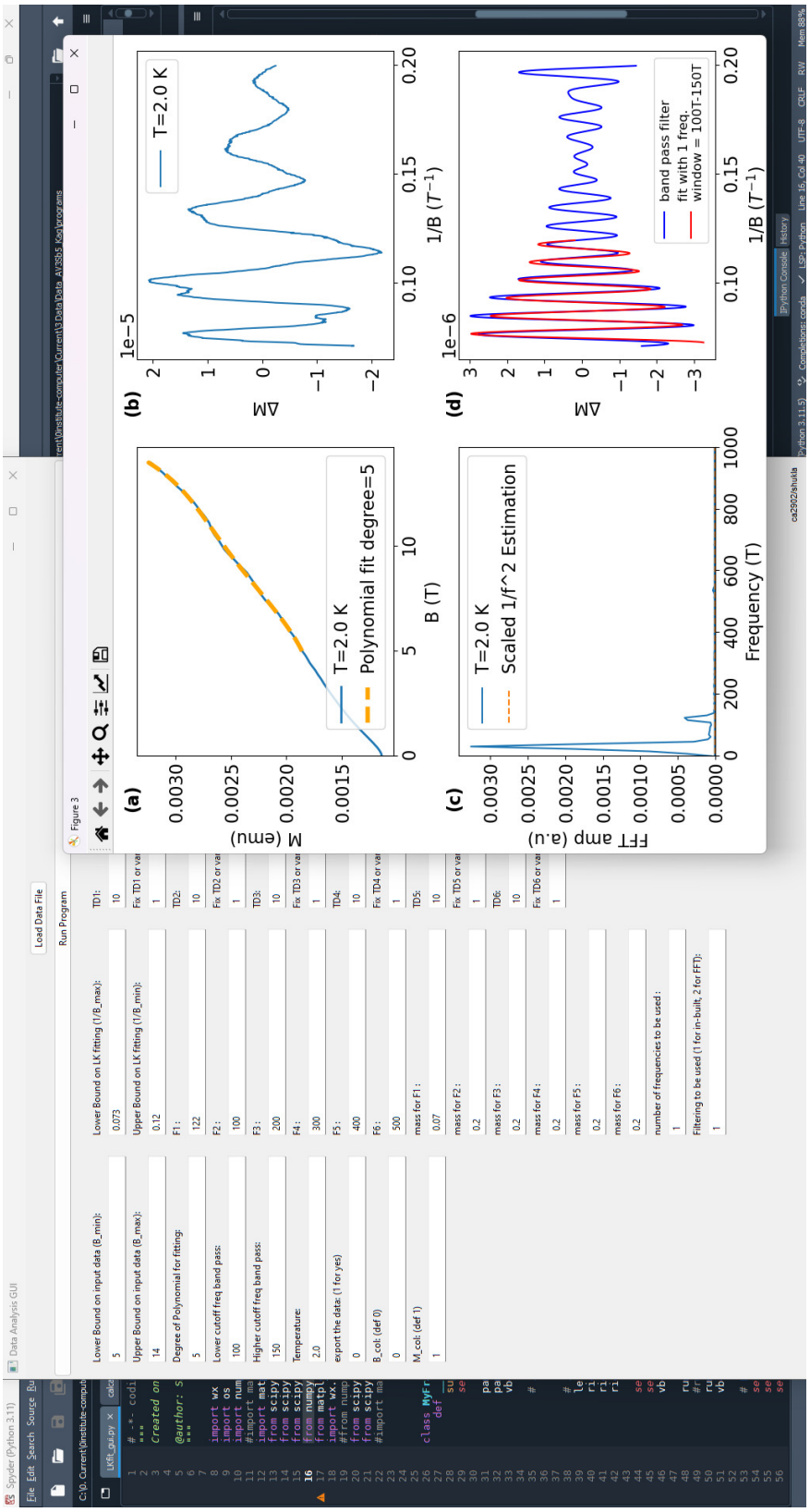

FIGURE 2.8: The constructed GUI based program for Fast-Fourier transformation of the signal and the analysis of multiple frequencies.

here, F_k is the k-th frequency component, Q_n is the n-th data point, N is the total number of data points. Here, it is assumed that the data points Q_n are sampled at regular intervals (i.e., evenly spaced in time or space). The spacing determines the sampling frequency, which directly affects the frequency resolution and range of the transform. The FFT is an efficient algorithm for computing the DFT of data sampled on a uniform grid[1] and is often most efficient when the number of samples is 2^n. When data is evenly spaced, the time (or spatial) interval between samples is constant, so the Fourier transform maps these points to specific, evenly spaced frequencies. This consistency ensures that the frequency components are interpretable in terms of their physical counterparts, like oscillation frequencies (Q_{osc}). Uneven spacing would distort the mapping of data to frequencies, leading to aliasing. The smoothing of the interpolated data is not necessary and is more so discouraged as it can introduce artificial frequencies. If necessary, it should preferably be done using adjacent-averaging.

3. **Multiplication by a Window function**: In FFT, a periodic boundary is assumed. There can be no guarantee that the oscillatory signal in quantum oscillations has an integer number of periods in the field window under consideration. Thus the PBC is not always satisfied and this manifests as additional frequencies in the FFT of the signal. One way to remove this effect is by *windowing* the signal. A window function is any function that is zero-valued outside a certain interval. The oscillatory signal under consideration for the FFT is multiplied by the window function to get the signal which is zero-valued outside the interval. Thus, a signal which is more compatible with the periodic boundary condition assumed in the FFT (signal is viewed through the *window* of the windowing function, hence the name). Some of the most frequently used window functions are [66]:

   Rectangular window (a constant), $= a$, where a is a constant

   Welch window (polynomial type), $= 1 - ((n - N/2)/(N/2))^2$

   Hamming and Hann window (cosine-sum type) $= a_0 - (a_1 \cdot \cos(2\pi n/N))$
   For the Hann window, $a_0 = a_1 = 0.5$.

4. **Zero-padding of the data**: It simply refers to adding zeros at the end of the signal to increase its length. In this way, the N (see Eq. (2.10)) used in the FFT increases, and the spacing of the FFT frequency bins decreases, since for a sampling frequency f_s, the bin spacing is f_s/N. Since zero-padding increases N, the FFT spectrum is sampled more finely. It should be noted, however, that this does **not** improve the

[1]This allows the FFT to achieve a computational complexity of $O(N \log N)$, compared to $O(N^2)$ for DFT.

actual ability to separate two nearby frequencies, since that is controlled by the length of the data for which the signal is nonzero. The main benefit of zero-padding is that it provides a smoother and more finely sampled FFT spectrum, allowing peak positions and amplitudes to be estimated more accurately.

The FFT is then performed on the signal obtained after these modifications. As described in the introduction, a number of frequencies are usually obtained even for simple metals such as Cu, Bi etc. Next step is to derive the effective mass (m^*), Dingle temperature T_D, spin-factor (R_s), and phase Φ_B corresponding to each frequency (orbit). These quantities can be obtained using the LK-formalism described in Sec. 1.3. The best method is to obtain the m^*, T_D from the temperature dependence of the quantum oscillation amplitude whenever possible and then band-pass the particular frequency from the complete $\mathcal{Q}_{osc}$ and fit using the complete LK-equation 1.14. The spin-factor is rather hard to determine and very detailed angle-dependence measurements are often required to evaluate this term [54]. The term in general is absorbed into the amplitude. The band-pass itself can be done by either of the following methods in the developed Python program:

1. **FFT-filtering:** The Fast Fourier Transform (FFT) of the signal is computed to convert it to the frequency domain. Filter Application: A frequency-domain filter H(f) is constructed, such that H(f)=1 between the lowcut and highcut frequencies and H(f) = 0 elsewhere. The filter is applied by multiplying the FFT of the signal by H(f). The final filtered signal is obtained by performing the inverse FFT on the filtered frequency spectrum.
2. **Butterworth bandpass:** A superior signal filter attributed to S. Butterworth [66]. This is created using the butter function from *scipy.signal* in Python, by specifying the lower and upper cutoff frequencies and the filter order. The filter is applied to the residual signal using *sosfiltfilt*, which performs zero-phase filtering by processing the signal in both forward and reverse directions, eliminating phase distortion.

Both methods aim to retain frequencies within the desired range. The result of the band-pass using FFT-filter for a frequency of 122 T in RbV_3Sb_5 is shown in the panel (d) of Fig. 2.8.

Noise or frequency?

To distinguish the noise and frequencies in the quantum oscillations, we calculate two-benchmarks:

1. $1/f^n$ noise: The noise level is determined by analyzing the power spectrum of the obtained FFT of the residual signal. The power spectrum is calculated from the FFT amplitudes, normalized by the total observation time (which is the magnetic field window):
$$P(f) = \frac{|\mathrm{FFT}(f)|^2}{T_{\mathrm{ob}}} \tag{2.11}$$
A fit to the power spectrum by a power-law model is done, typically characterized by $1/f$ behavior, to understand the noise trend: $\log P(f) = -\beta \log f + \log A$, where β is the slope (indicative of the noise type) and A is a scaling factor. The noise spectrum $P_{\mathrm{noise}}(f) = A \cdot f^{-\beta}$ is then overlaid on top of the FFT. The $1/f$-type noise is, by definition, especially crucial in the low-frequency spectra. This is also referred to as the pink noise.

2. Average noise level of the signal-dominated region: An average noise level is estimated by computing the mean of the FFT amplitudes, providing a baseline for the noise floor in the frequency domain and is given by: Average Noise Level = $\langle|\mathrm{FFT}(f)|\rangle$. This helps in distinguishing the signal from the white noise, which occurs with equal intensity across the entire spectrum and is especially important for the high-frequency spectrum.

The high frequencies and the frequencies originating from the background subtraction need further analysis to be labeled as *true* quantum-oscillations frequencies.

Chapter 3

Interplay of superconductivity and nematicity in $FeSe_{1-x}Te_x$

Electronic correlations and nematic fluctuations of $Fe_{1+y}Se_{1-x}Te_x$ are investigated by measuring resistivity, heat capacity, and thermal expansion. Using chemical vapor growth, single crystals in the Se-rich side of the phase diagram were synthesized. An annealing study of an optimally doped sample grown using the Bridgman method is also presented. Two distinct superconducting domes were obtained from the bulk measurements. Based on changes in different physical quantities, we argue that the superconductivity mediation in the second superconducting dome outside the nematic phase is distinct from that centered around FeSe.

3.1 Background and motivation

The Fe(Se,S,Te) family exhibits a rich phase diagram characterized by various electronic phases, including magnetic order, nematicity, and superconductivity. FeSe, FeS, and FeTe, the end members of this system, display markedly different physical properties despite their structural similarities. While the FeSe is nonmagnetic, FeTe displays a double-stripe magnetic order which is unique among the iron-based superconductors. Below Néel temperature $T_N \approx 70\,\mathrm{K}$, FeTe undergoes a first order phase transition to a monoclinic structure accompanied by antiferromagnetic (AFM) order [67, 68]. The magnetic structure is characterized by a double-stripe pattern, where magnetic moments align ferromagnetically along one diagonal direction and antiferromagnetically along the other. This results in a magnetic propagation vector $\mathbf{Q} = (\frac{1}{2}, 0)$ in tetragonal notation, differing from the single-stripe order ($\mathbf{Q} = (\frac{1}{2}, \frac{1}{2})$) observed in iron pnictides. The ordered magnetic moment is approximately $2.0\,\mu_B$ per Fe atom, indicating strong localized magnetism [69]. As stated above, FeSe, despite structural similarities to FeTe, does not exhibit static magnetic order at ambient pressure to the lowest measured temperatures. Over the years, a complex picture has evolved regarding the underlying magnetic fluctuations in FeSe, in which the failure of long-range magnetic order is attributed to magnetic frustration, with multiple collinear magnetic configurations having competing energies [70]. The competing energy scales for different magnetic orders are shown in Fig. 3.1 (see App. B for more details). Inelastic neutron measurements also show that FeSe has spin fluctuations associated with the single-stripe phase, albeit without any long-range order [7, 71]. How the spin fluctuations evolve and their effects on the superconductivity is still an open question [72]. The long range magnetic order is also achieved in the FeSe through application of high pressures (1-2 GPa) [73].

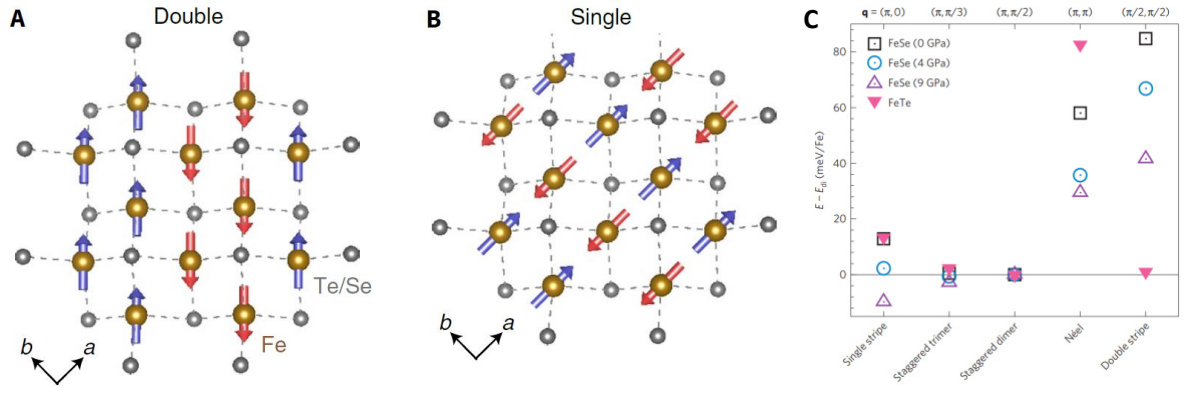

FIGURE 3.1: Taken from [69, 70], reproduced with permission from Springer Nature: (A,B) Double strip and single strip AFM order found in FeTe and FePn respectively. (C) The total calculated DFT energies of different magnetic configurations in Fe(Se,Te) system.

3.1.1 Orbital effects in the Fe(Se,Te)

At the nematic transition in FeSe, an orbital order breaks the symmetry between the d_{xz} and d_{yz} orbitals, leading to orbital polarization [11]. The order parameter associated with this orbital order develops within the nematic phase. Upon incorporating spin-orbit coupling, it has been shown that the spin susceptibility in the nematic state becomes anisotropic. Subsequently, a spin-nematic order parameter develops significantly below the nematic transition, coinciding with the onset of coherence in the d_{xy} orbital. Thus, a spin-orbital intertwined nematicity has been proposed [74]. Nevertheless, orbital ordering occurs first and is considered the driving mechanism for nematicity in FeSe [75, 76]. This zero-momentum orbital order corresponds to a d-wave-type Pomeranchuk instability within the Fermi liquid framework, and is the case in FeSe [77]. Additionally, an orbital-selective Mott phase (OSMP) emerges from the metallic phase when the Se concentration is reduced [12] (Fig. 3.2(a)). In this OSMP, localized and itinerant orbitals coexist. Specifically, in Fe(Se,Te), the coherence of the d_{xy} orbital depends sensitively on temperature and Te substitution level. As the FeTe-rich end is approached, the effective mass associated with the d_{xy} orbital diverges. The resulting (in)coherence of this orbital with temperature change causes a Fermi-surface reconstruction due to changes in hybridization, as depicted in Fig. 3.2(b,c).

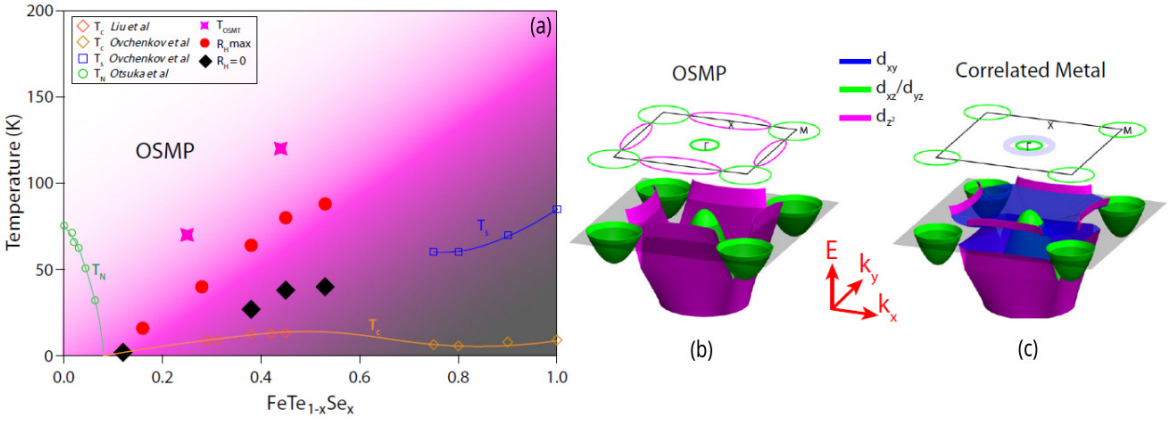

FIGURE 3.2: Taken from [78], under the CC-BY-4.0 license. Orbital effects in Fe(Se,Te): FeTe is the most correlated of the FeBS. The d_{xy} orbital in particular becomes massive as Te is substituted [11]. In the above, the phase diagram where d_{xy} is incoherent (labeled OSMP) and the reconstruction ensuing from the coherence of d_{xy} at low temperature is shown.

3.1.2 Pairing symmetry of the iron-based superconductor

The mechanism by which superconductivity arises in FeSe is highly debated [79, 80]. Determining the symmetry and structure of the superconducting gap function in momentum

space can provide strong constraints to the theoretical framework. Below, the necessary details of the superconducting gap function are introduced. Finally, the experimental findings in the literature for FeSe are summarized.

Assuming the angular part of the pairing interaction to be separable, one can write the superconducting gap as [79]:

$$\Delta(T,\theta) = \Delta(T) \cdot \Delta(\theta) \tag{3.1}$$

The angular symmetry of Δ in momentum space is constrained by the underlying symmetry of the crystal. The iron-based superconductors have a tetragonal lattice, and the physics plays out in the Fe(Pn/Ch)-plane. Thus, the superconducting order parameter should respect this 2D-square symmetry. For a square motif, the relevant group is C_{4v} which has five irreducible representations (irreps). The gap function $\Delta(\theta)$ transforms according to these irreps as given in Table 3.1. The angular gap structure of the superconducting

irrep notation	A_1	B_1	B_2	A_2	E
Basis functions	1	x^2-y^2	xy	$xy(x^2-y^2)$	x,y
'-wave'	s	d	d	g	p

TABLE 3.1: Irreducible representations of C_{4v} and representative lowest-order basis functions (with corresponding gap-symmetry labels).

order parameter should respect these symmetries. Note that the gap structure is not fixed by the symmetry; multiple functional forms can be written for the s-wave as described below. As is shown below, there are multiple functional forms that follow the representation Γ_1. The s-wave symmetry implies that a rotation by 90° shall leave the gap structure equivalent. For the d-wave, a sign change occurs for the similar rotation. The following representative momentum-space basis functions are commonly used to describe superconducting gap symmetries. Along a given Fermi surface, the gap may be parameterized as $\Delta(\theta) \equiv \Delta(\mathbf{k}_F(\theta))$, where θ labels the position on the Fermi surface. In the full Brillouin zone, the corresponding basis functions may be written as

$$\begin{aligned}
&\Delta(\mathbf{k}) \propto 1 && (s\text{-wave, isotropic})\\
&\Delta(\mathbf{k}) \propto \cos k_x + \cos k_y && (\text{extended } s\text{-wave})\\
&\Delta(\mathbf{k}) \propto \cos k_x \cos k_y && (\text{sign-changing } s\pm\text{-wave})\\
&\Delta(\mathbf{k}) \propto \cos k_x - \cos k_y && (d_{x^2-y^2}\text{-wave})\\
&\Delta(\mathbf{k}) \propto \sin k_x \sin k_y && (d_{xy}\text{-wave})\\
&\Delta(\mathbf{k}) \propto (\cos k_x - \cos k_y) + i \sin k_x \sin k_y && (d + id\text{-wave})
\end{aligned} \tag{3.2}$$

These gap structures have been plotted (after normalization) over the complete k-space and shown in Fig. 3.3. The white points in it denote the point where $\Delta(\theta) = 0$ and

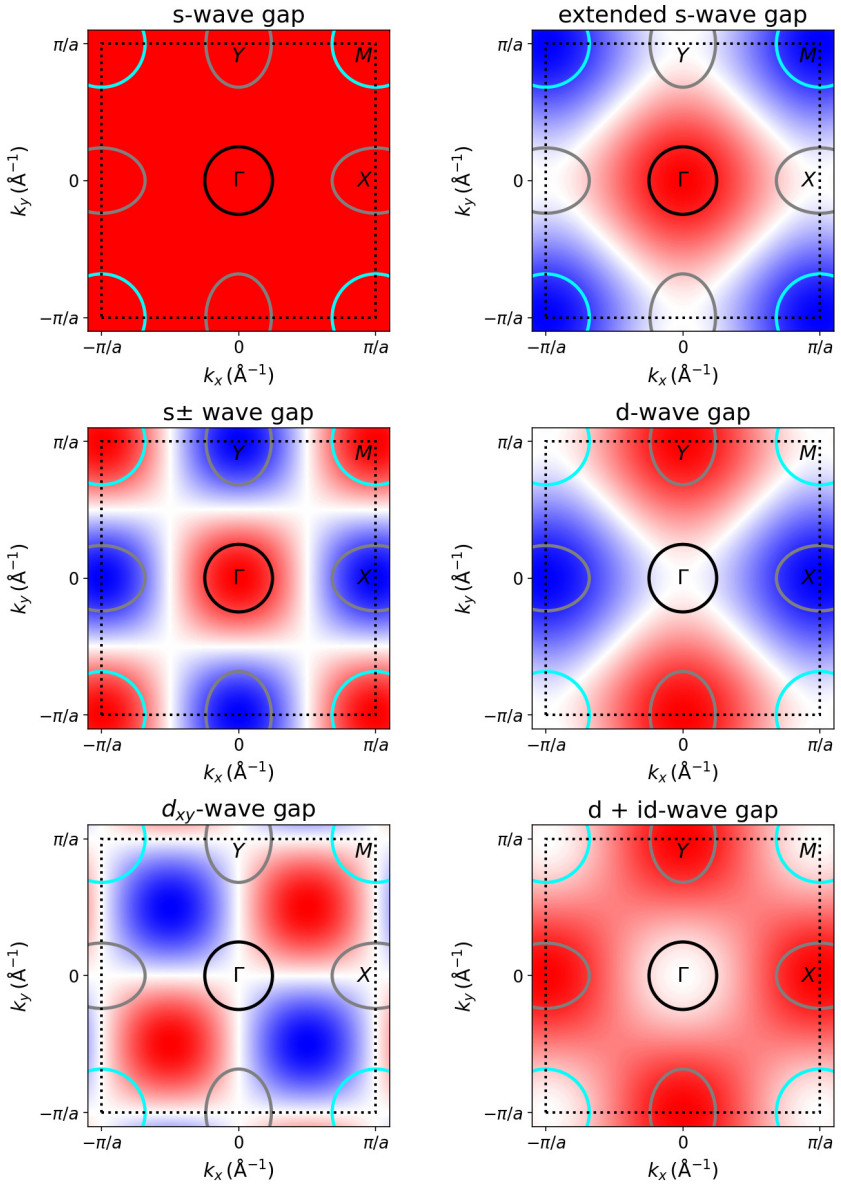

FIGURE 3.3: Different superconducting gap structure. The color here denotes the sign, red(blue) for positive(negative). The white denotes a zero in the gap structure. The black dotted lines denote the 1^{st} Brillouin Zone (one Fe atom/cell) . Note how for the isotropic-s, extended-s and $s\pm$, the symmetry is still s, i.e., rotation by 90° does not change the gap structure, while for the d-types it changes on rotation by 90°. The archetypal Fermi surface of the iron-based superconductors is overlaid on the top and shown by the solid black, gray and cyan lines. The cyan-colored bands are absent in the FeSe, and the evidence of a pocket at Y is also not conclusive. The superconducting gap opens at the Fermi surface and not in the complete k-space; its sign and strength changes, for the standard forms, as shown here. (caveat: For the $d + id$ state, the panel shows the normalized gap magnitude $|\Delta(\mathbf{k})|$; the colors therefore indicate relative amplitude, not sign.)

consequently the gap $\Delta = 0$. These points are referred to as the nodes (when they lie on the Fermi surface). In some cases, such as iron-based superconductors/cuprates, the term

nodal lines is used because the Fermi surface is cylindrical and extends as such along the k_z. The zero-gap points then also extend along the k_z as lines. Because there is no energy gap in the single-particle excitation spectrum at these points, electrons can be excited without the need for additional energy. This results in the presence of low-energy, gapless excitations in such superconductors.

For FeSe, there is already a significant mismatch when it comes to the gap structure. The crucial question is whether nodes exist in the gap structure or not. Modulation of the gap along $\Gamma - Z$ [81] is not even considered due to challenges in the experiments. The list of experiments and their predictions is given below:

nodes	node-less, but deep anisotropy	node-less
STM/STS [82, 83] heat capacity [84]	heat capacity [85] BQPI/STM [86] ARPES [87]	heat capacity [88] thermal conductivity [89] μSR [90], penetration depth [91]

TABLE 3.2: References to the experiments and the predicted gap structure classified into three categories of nodes, a deeply anisotropic gap, or a nodeless superconductivity state in FeSe. The method from which this claim is made is stated.

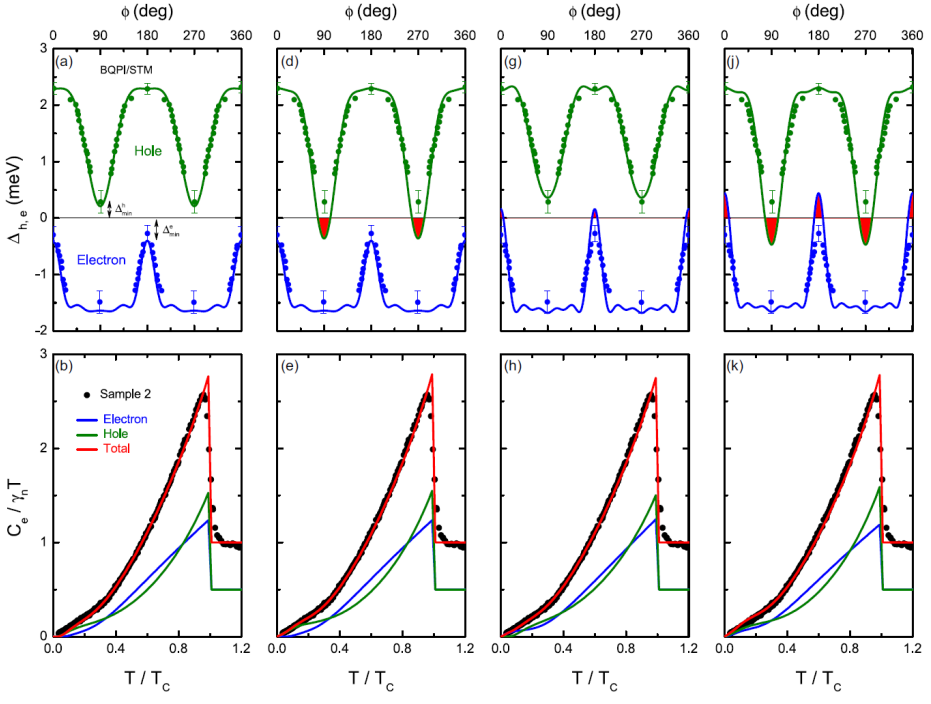

FIGURE 3.4: Taken from F. Hardy et al., Phys. Rev. B 99, 035157 (2019) [84], reprinted with permission from the American Physical Society. Copyright 2019 by the American Physical Society. (a,d,g,j): Angle-resolved superconducting gaps $\Delta_{h,e}(\phi)$ at the hole and electron band as reported by BQPI/STM [86]. Solid lines are fits within the leading angular harmonic approximation using Eq. (2.9). (b,e,h,k) The heat capacity calculated using the gap structures shown in panels above them.

In Fig. 3.4(a,d,g,j), the angle-resolved superconducting gap structure of FeSe as determined using the BQPI is shown along with fits made by [84]. In BQPI, anisotropic but nodeless superconducting gaps are observed in the central hole band and the peanut shaped electron band [86]. Authors in [84] first made fits to the BQPI data and then calculated the heat capacity using this gap structure. They found that the nodes are necessary in order to obtain good fits at low temperatures (see Fig. 3.4(b,e,h,k)).

3.1.3 Phase-separation in the Fe(Se,Te) and this study

The phase separation for $0.2 < x < 0.4$ in the Bridgman-grown crystals meant that the Se-rich side of the phase diagram was less studied. This also left the nature of the nematic critical point, evolution of the orbital selectivity and the magnetic fluctuations and their impact on the full phase diagram open to questions. Using the chemical vapor transport method, high-quality single crystals in the aforementioned composition range have also become possible [92, 93]. Since then, the evolution of nematicity and superconductivity has become clearer. While T_s decreases monotonically with Te substitution, T_c shows a small but conspicuous dip in the value before increasing around $x \sim 0.35$ (see Fig. 3.5). Such a peculiar evolution is rather unknown, at least in the pnictides. The elasto-resistivity coefficient m_{66}, which measures how resistivity changes under in-plane shear strain, also shows a peak around $x \sim 0.3$ [15]. This, along with the momentum-dependent gap in FeSe in calorimetric [84] and STM studies, but nodeless in the optimally doped region in STM studies, has led to the proposal of *two distinct superconducting regimes* in Fe(Se,Te) and the superconducting dome around the optimally doped region being independent of the superconductivity of FeSe [94]. The disappearance of the nematic order with Te doping coincides with the maximization of T_c to 14 K [95], which has been interpreted as a pure nematic quantum critical point [94].

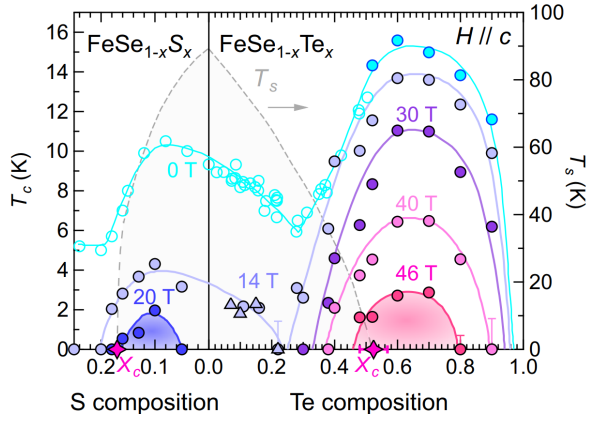

FIGURE 3.5: Taken from [94] under the CC BY 4.0 license: Evolution of H_{c2} and the proposed complete phase diagram of the Fe(Se,S,Te) system.

3.2 Results I: annealing study of $x = 0.5$

Excess iron is known to affect the properties of the Fe(Se,Te) system drastically [96]. The moments at the excess iron site break Cooper pairs, leading to an absence of bulk superconductivity. The localization of charge carriers and the destruction of surface states are also well-known. Numerous methods have been proposed to remove excess Fe, such as oxygen annealing, nitrogen annealing, vacuum annealing, and elemental vapor annealing (Te, Se, I, etc.) [96]. Of these, the N_2 annealing and vacuum annealing are known to be ineffective and the effects seen are due to the oxygen contamination in the annealing ampules. Among element-based vapor annealing methods, Te vapor annealing has been known to produce the best results in terms of the superconducting volume fraction [92, 97] with nearly 100% superconducting volume fraction in the annealed samples. In this process, Te vapor reacts with excess Fe to form FeTe complexes ($FeTe_m$). These FeTe complexes have a lower magnetic moment ($\leq 0.2\mu_B$), leading to a reduction in magnetic scattering. Thus, the scattering due to free magnetic ions is reduced in the annealed samples.

On account of these positives associated with Te vapor annealing, we have chosen this method to remove excess Fe from Bridgman-grown samples of $x = 0.5$. For this, a Te : Crystal :: 1 : 10 ratio was taken and the annealing was carried out over 400 h and 600 h at 400°C. Of these two batches (B1, B2), more than 15 samples were measured with heat capacity to check for bulk superconductivity. Of these, ten samples were bulk superconducting ($\approx 100\%$), four were non-SC, and one had a low volume fraction. Such variation can occur because the surface area of the crystals exposed to Te vapor is not the same or due to the difference in the excess iron content.

In Fig. 3.6, the (a) electrical transport and (b) heat capacity of the annealed samples and the as-grown samples have been shown. In the resistivity, the as-grown samples exhibit an upward trend, implying additional scattering stemming from the non-quenched magnetic moments in the sample (excess Fe). The resistivity value is in the bad-metal region throughout the temperature scale. Among the many annealed samples, the sample (#TW946_B2-6A) showing no bulk superconductivity was also measured in the transport. The resistivity value in this case is much smaller than for the unannealed sample. It also exhibits a pronounced dip in resistivity before increasing, which is typical of Kondo-like/localization behavior. For the annealed sample, the resistivity value drops further and is similar in magnitude to what is reported in [92] for the best samples. In the corresponding specific heat, plotted as (b) C/T vs. T, the superconducting transition can be clearly seen in the annealed samples around $T_c = 12-14$ K. The jump height varies from sample to sample, but the low-temperature behavior for all samples for $T < 0.9T_c$ is nearly

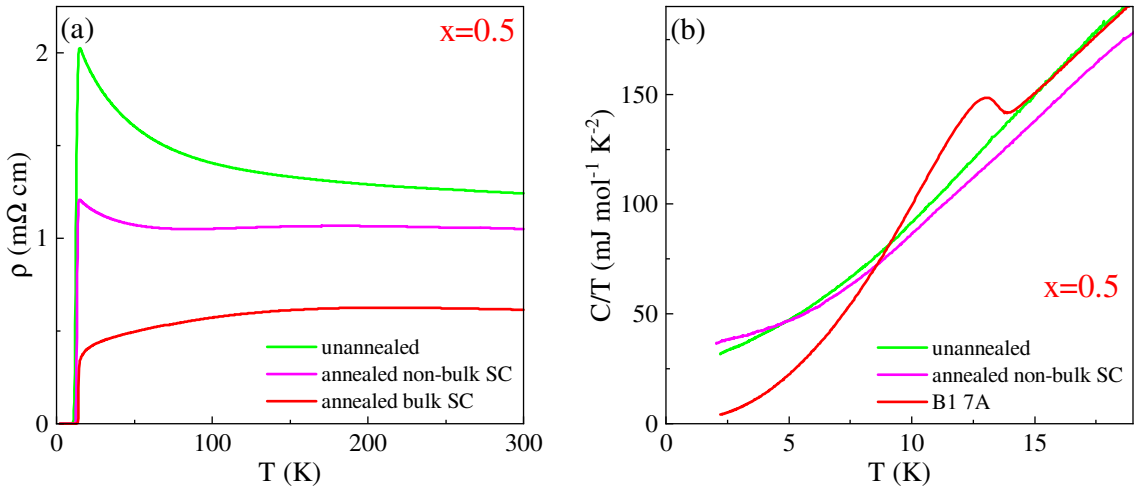

FIGURE 3.6: (a) In-plane resistivity vs temperature at 0 T for unannealed, partially annealed and annealed samples of $FeSe_{0.5}Te_{0.5}$, (b) the corresponding heat capacity of plotted as C/T against temperature. B1 7A corresponds to the annealed bulk SC sample shown in (a). The heat capacity of several annealed samples was checked to select the best samples for further measurement.

identical. As described before, the jump height and shape (2 peak-like or smeared) can vary on account of the possibility of different excess Fe present in the sample/ difference in exposure to the Te-vapor.

In disordered metallic systems, multiple mechanisms can induce an insulating-like upturn in resistivity at low temperatures. To identify the dominant mechanism in our annealed sample, we measured the field dependence of its resistivity (Fig. 3.7). A linear, positive magnetoresistance of about 1% is observed, which is inconsistent with standard weak localization (WL), since WL typically manifests as negative magnetoresistance.

Both weak (anti)localization and the Kondo effect can introduce logarithmic corrections to resistivity at low temperatures[1]. In WL, quantum interference leads to a pronounced resistivity increase upon cooling if the phase coherence length (l_{coh}) significantly exceeds the mean free path (l_{mean}). However, because WL usually shows negative magnetoresistance, the observed positive magnetoresistance (Fig. 3.7(a)) suggests WL is not the primary cause of the low-temperature behavior in this sample.

[1]Localization effects arise due to quantum interference when the phase coherence length l_{coh} significantly exceeds the mean free path l_{mean}. The coherence length l_{coh} is governed by inelastic scattering processes, while the mean free path l_{mean} is determined primarily by elastic scattering events. When $l_{coh} \gg l_{mean}$, electron wavefunctions maintain their phase coherence despite frequent scattering, characterizing a quantum diffusive regime of electronic transport. In contrast, the opposite limit of negligible scattering defines the ballistic transport regime. Weak localization (WL) occurs when constructive interference arises from electron paths and their time-reversed counterparts; conversely, destructive interference characterizes weak anti-localization (WAL). WL manifests experimentally as an increase in resistivity at low temperatures due to enhanced backscattering.

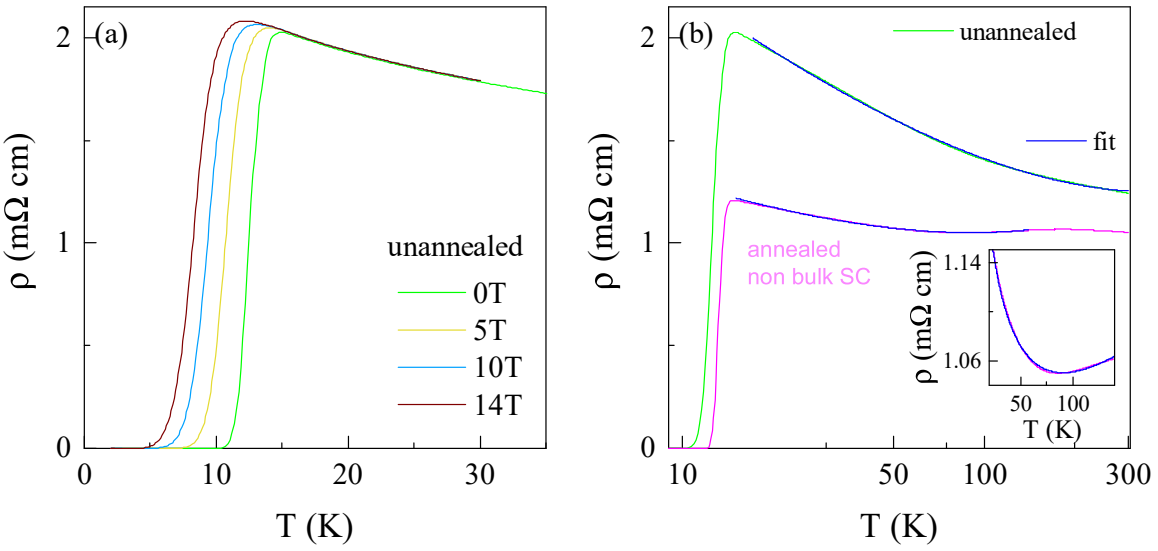

FIGURE 3.7: (a) In-plane resistivity vs temperature at different external magnetic fields parallel to c-axis for as-grown samples of $Fe_{1+y}Se_{0.5}Te_{0.5}$, and (b) resistivity for as-grown and partially annealed (B2-6A) fitted using Kondo contribution (purple solid line as fit). (annealed non-SC implies no bulk SC)

We next consider the Kondo effect. The Kondo effect occurs when magnetic impurities are present in the sample (excess Fe in this case). The hallmark of the Kondo effect is the appearance of a minimum in the electrical resistance at a specific temperature (T_{min}). Below T_{min}, the resistance increases as the temperature decreases, due to enhanced scattering of conduction electrons off the magnetic impurities. In the case of partially annealed B2_6A, this dip can be clearly seen in the in-plane resistivity. The resistivity plotted against a log-T scale shows linear increase at low temperatures. For the Kondo case, the electronic transport can be fitted using:

$$\rho(T) = (\rho_0 + AT^n) + (\rho_k \; ln(T_K/T)) \tag{3.3}$$

where T_K is the Kondo temperature. This represents the characteristic temperature below which the magnetic impurity and the conduction electrons start to form a Kondo singlet, leading to the characteristic increase in resistivity at lower temperatures. Usually, this is slightly higher than T_{min}.

The fit result is shown in Fig. 3.7(b). A good fit is only achieved (inset) when T_K is rather large ($\sim 300\,\text{K}$). This value is also much larger than T_{min}. The large value of T_K may represent that the Kondo effect dominates over other scattering mechanisms across a broad temperature range. However, the value being very far from T_{min}, implies that this complex behavior cannot be described only by Kondo physics. The transport study, thus, supports a more complex interplay of localization effects stemming from the disorder in

the sample and the Kondo effect from excess Fe. Thus, the system can best be described as a dilute magnetic system with disorder. This is also supported by the magnetization measurements carried out on the annealed superconducting samples, shown in Fig. 3.8(a).

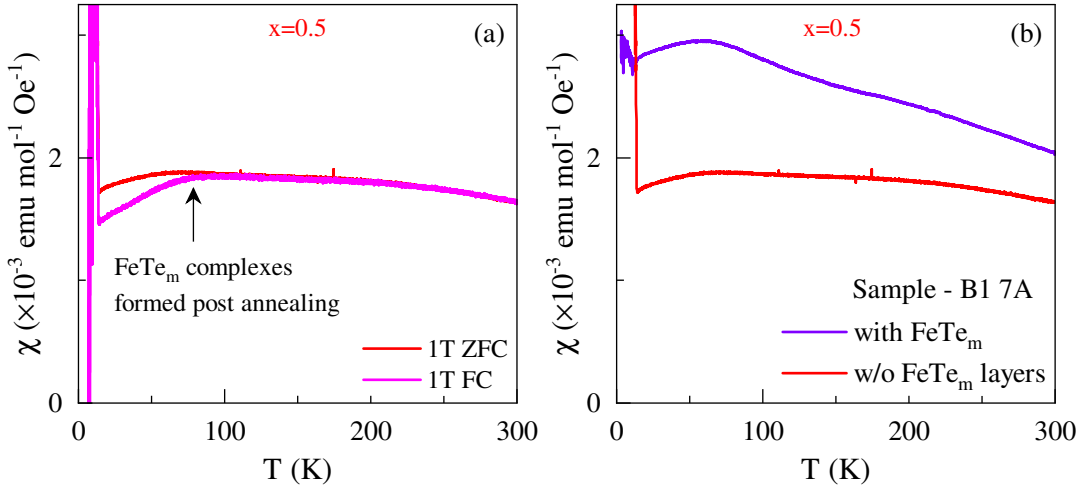

FIGURE 3.8: (a) Zero-field-cool and field-cooled magnetization at a 1 T external magnetic field, the bifurcation around the 100 K relates to the FeTe complexes formed post-annealing, (b) shows a reduction in the susceptibility value after removing the top layer containing the most FeTe complexes. (Sample-B1 7A)

The zero field and field-cooled curves for the annealed superconducting sample ($x = 0.5$) bifurcate below 150 K. This is akin to the magnetization reported in $FeTe_2$ single crystals. During Te-vapor annealing, the excess Fe reacts with the Te-vapor to form complexes of $FeTe_m$. As the $FeTe_m$ complexes are deposited on the surface of the sample, removal of the surface layer should reduce this *extra magnetization*. This indeed can be reduced by removing the top surface of the annealed samples. The difference in the two measurements (with and without layer) is shown in Fig. 3.8(b). A significant drop in the absolute values can be clearly seen.

In conclusion, the combined transport and magnetization results strongly suggest that the low-temperature resistivity upturn is governed by magnetic impurity (Kondo) scattering and disorder-induced localization effects. The formation of $FeTe_m$ complexes is primarily on the sample surface and can be removed by polishing (scratching) the sample surface.

3.3 Results II: Two superconducting domes with two different mechanisms

The in-plane resistance normalized to room temperature is shown in Fig. 3.9 (a). Resistance vs. temperature measurements were performed using the 4-probe method. All vapor-grown samples ($x = 0, 0.06, 0.12, 0.33, 0.35, 0.45$) show a metallic resistivity and a clear nematic transition T_s (identified as a kink in resistivity). The normalized resistance derivative $dR/R_{300}/dT$ shown in App. B.1 shows a pronounced jump or a dip at the nematic transition. For FeSe and low value of Te substitution, a minimum occurs at the nematic transition, whereas for $x \geq 0.33$ a maximum is observed in the derivative at the nematic transition. Although there is a change in the concavity, the transition retains a mean-field character. FeTe data ($x = 1$) is taken from [72] and is shown for completeness. For FeTe, the sharp drop in the resistivity at 67 K corresponds to the antiferromagnetic transition. For $x = 0.5$, the Te-vapor annealed sample with metallic character is presented. The low-temperature normalized resistance, highlighting the superconducting transition temperature (T_c), is shown in Fig. 3.9(c). Unlike the nematic transition, T_c does not exhibit monotonic behavior; it initially decreases with Te substitution, reaching a minimum near $x = 0.33$, consistent with previous studies and then increases in the putative second superconducting dome [93, 94]. For FeSe and samples with low Te concentration, the resistivity at low temperatures displays linear temperature dependence (indicative of a strange metal state; see [98]), whereas higher Te substitutions exhibit bad metallic behavior. Around the minima of T_c (e.g., $x = 0.33, 0.35$), the resistivity follows a T^2 dependence.

For the annealed sample at $x = 0.5$, an absolute resistivity value of approximately $1\, m\Omega\, cm$ was measured, corresponding to a Drude mean free path (0.3 nm) comparable to the in-plane lattice parameter. This resistivity represents the upper bound of scattering—the Mott-Ioffe-Regel (MIR) limit [99]. At this limit, coherent quasiparticle transport transitions into a regime where quasiparticle lifetime diminishes until quasiparticles become ill-defined. Importantly, this phenomenon differs from the incoherence of the d_{xy} orbital at higher temperatures, discussed separately later in this work. For the $x = 0.33$, the susceptibility shows a very small superconducting volume fraction (see Fig. 3.9(c)). Additionally, single-crystal X-ray diffraction (XRD) for this sample does not indicate any detectable excess Fe (see Fig. B.7).

Fig. 3.9(d) shows C/T vs T for different compositions at 0 T at low temperatures, plotted as C/T to highlight the electronic part. The curves have been shifted for clarity. The superconducting transitions can be clearly seen. For x=0.33 and 0.35, no superconducting

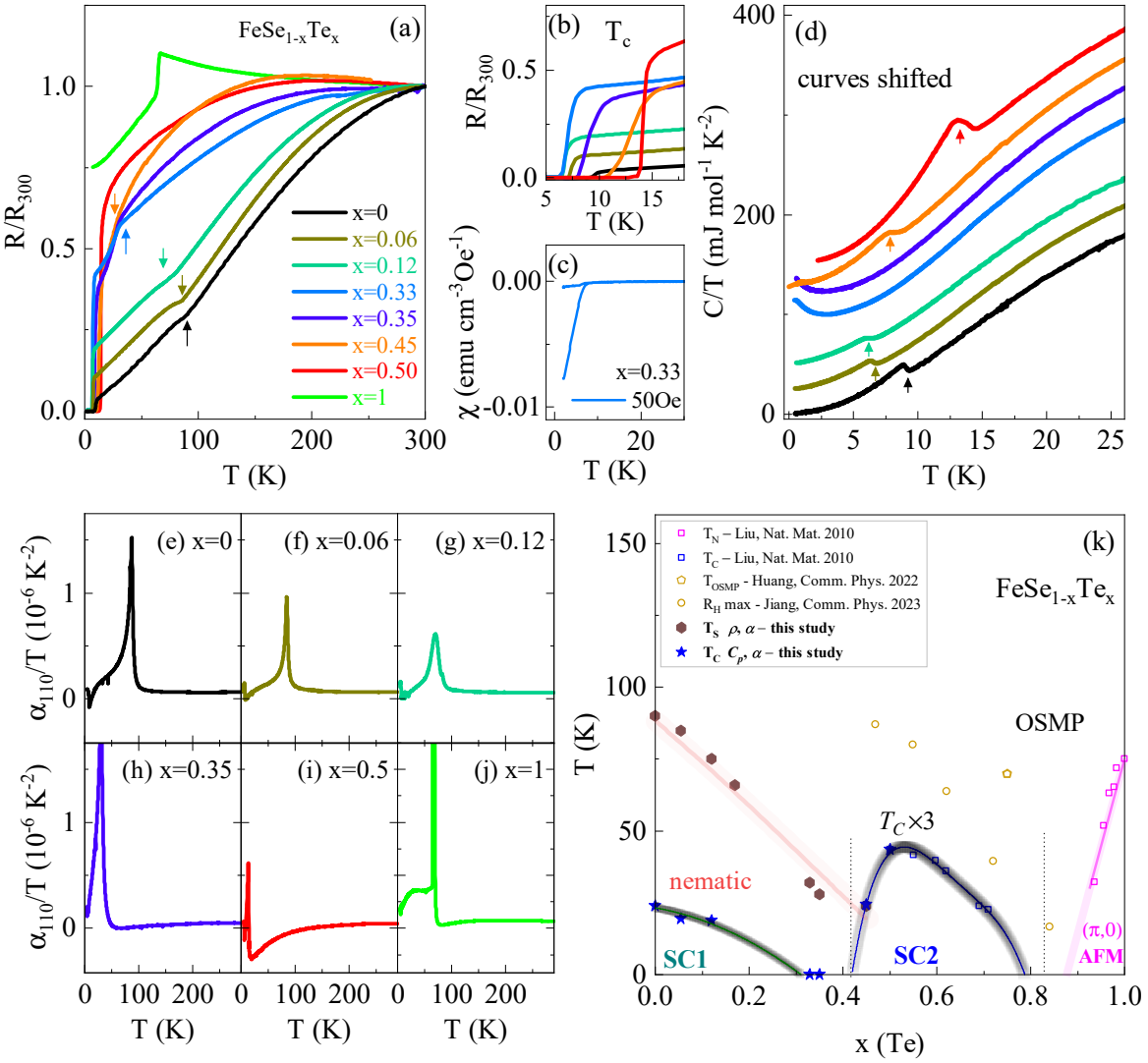

FIGURE 3.9: (a) In-plane normalized resistance vs temperature at 0 T for various composition in $FeSe_{1-x}Te_x$, the nematic transitions are marked by arrows. (b) The zoomed-in low-temperature part showing the superconducting transition. (c) The magnetization (ZFC/FC) at 50 Oe external field for the x=0.33 (composition with lowest T_c in transport), implies a low superconducting volume fraction. (d) Heat capacity plotted as C/T vs T for different compositions. Curves have been shifted for clarity. (x=0: [9]). Arrows mark the T_C. (e-j) Thermal expansion coefficient for different compositions, along the detwinned [110] direction. For x=0.35, no superconducting transition is seen in thermal expansion as well (x=0: [9]). (k) Phase Diagram for Fe(Se,Te) made using the bulk C_p and α probes ($T_c \times 3$ for clarity).

anomaly is seen in the heat capacity. The upturn below 2 K in these compositions is likely a Schottky anomaly. This absence of superconductivity cannot be attributed to the presence of excess Fe, as is the case for as-grown samples $x = 0.5$, since neither single-crystal XRD nor EDX show the presence of any excess Fe. The resistivity is also metallic and significantly smaller than what it is for samples containing excess Fe, which suggests that the superconductivity in $x = 0.33$ is spurious/ filamentary in nature. The heat

capacity anomaly ($\Delta C/T_c$) at T_c decreases with Te substitution and is absent for $x \sim 0.3$. The absence implies two disconnected superconducting domes in Fe(Se,Te). At first, the absence might be an indication of the recently postulated unconventional Sommerfeld coefficient behavior due to the interaction between the electron and hole pocket [100]. However, in [100], a hump associated with superconductivity still exists but is shifted to $T/T_c \sim 0.8$. Annealing the sample to induce T_c risks altering the Se–Te stoichiometry, as XRD shows no excess Fe and EDX reveals no Fe-rich regions. Furthermore, at $x = 0.33$, the transport transition broadens significantly. Mukasa et al., using high-field transport have marked this composition range ($0.2 < x < 0.4$) as the range where there is a change in superconducting mechanism [94]. The m_{66} also reaches a peak in this composition range before declining, although maintaining a Curie-Weiss behavior [15, 101]. The fact that T_c goes to zero in this composition range, despite the clear nematic transition, strengthens the case of two distinct domes in the Te-substituted FeSe.

As the nematic transition breaks the tetragonal symmetry, it is most pronounced in the thermal expansion [6, 9, 10]. Thermal-expansion measurements were performed by the author, Dr. Wang, and Dr. Meingast. The x=0, 1 data is from Dr. Böhmer [9] and shown here for completeness. In Fig. 3.9(e-j), the thermal expansion coefficients plotted as α/T to highlight the electronic contribution, along the detwinned [110] direction are shown. The nematic transition manifests as a sharp anomaly for x=0, 0.06, 0.12, 0.35. Here also, no superconducting transition is observed for x=0.35. For x=0.5, no nematic transition is observed; rather a highly electronic α emerges which is negative from 100 K down to the superconducting transition. This composition is also where the nematic quantum criticality has been postulated. The aspects of nematic quantum criticality are discussed later in detail in Sec. 4.3.2. For x=1, the sharp first-order jump corresponds to the antiferromagnetic transition.

Finally in Fig. 3.9(k) the phase diagram derived using the thermodynamic probes C_p and α is presented. The T_{OSMP} and the $T(\mathrm{R_H(max)})$ denote the orbital selectivity and the maxima in the Hall resistance and are taken from [12] and [101] respectively, while the T_c and T_N in the high Te concentration are from [72]. Two distinct domes of superconductivity are observed here. The transport phase diagram [94] that sees these two distinct domes only at sufficiently high external B actually exists at 0 T when the bulk superconductivity is measured.

In the following section, we argue that these two domes have two distinct superconducting mechanisms. We present evidence from three physical quantities, (a) upper critical field, (b) superconducting gap structure, and (c) pressure derivative of the superconducting transition.

3.3.1 Upper critical field - $H_{c2}^{orb}, H_P, H_{c2}$

Resistance vs. temperature measurements were carried out for all samples with an external magnetic field up to 14 T, parallel to the c-axis, and are shown in Fig. 3.10 [2]. Linear magnetoresistance $\propto (R_{xx}(H) - R_{xx}(0))$ decreases with Te substitution and becomes almost negligible as $x = 0.33$ is approached, whereas it is gigantic for FeSe [102]. The derivative for x = 0.33 in the zero field and 13 T is shown in the appendix Fig. B.2. The near-perfect overlap for the two fields (0 T and 13 T) implying zero magnetoresistance, can also be seen in this comparison of $d\rho/dT$. The slope of the linear magnetoresistance for Fe(Se,Te) is known to evolve from positive to negative as the Te concentration is increased.

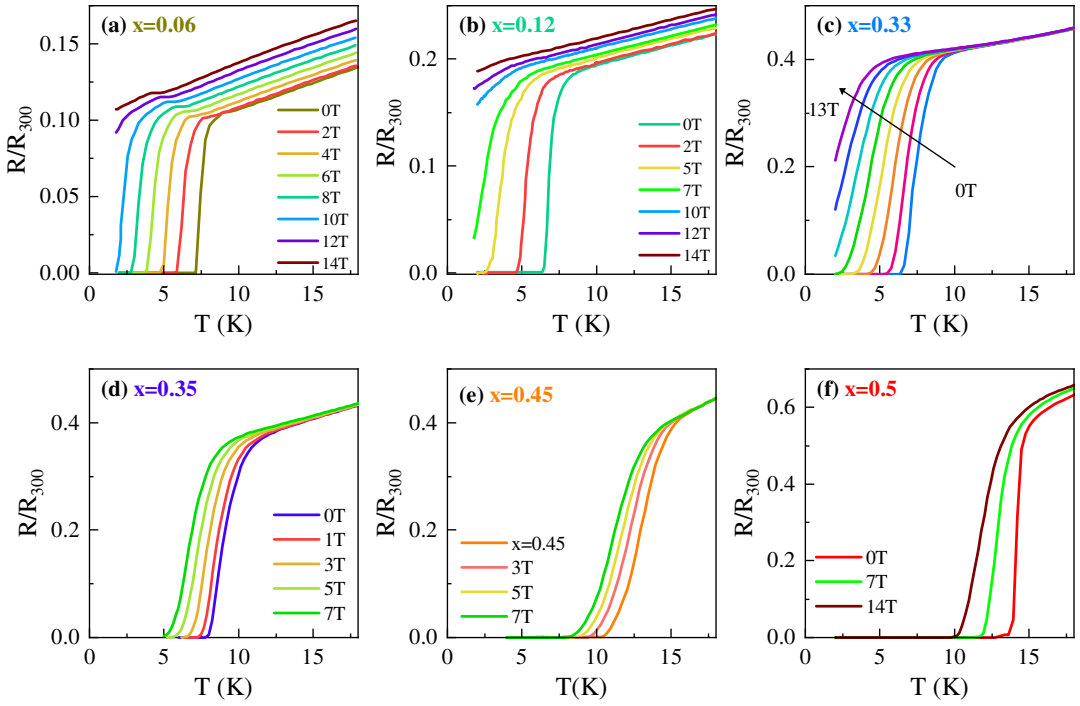

FIGURE 3.10: (a-f) In-plane normalized resistivity vs temperature at different external magnetic fields for various compositions. The field direction is always parallel to $c-$axis. A reduction in the normal state magnetoresistance above the T_c can be clearly seen and is attributed to the increasing bad metallicity in the system.

In the transport measurement, the superconducting transition is marked by a sharp drop to zero resistance. The drop itself can range from rather abrupt (0.01 K) to broad (a few Kelvins). The different regions mark different phenomena; see Fig. 3.11(a):

1. when the resistance becomes zero (marked by T_M) - vortex melting,

[2] For x=0.06, a small hump is seen, which is due to contribution of the c-axis resistivity. This was overcome in the other sample by painting the sides of the sample completely with silver paint, so the contribution from all the layers is read

2. when the resistance is *dropping* from the normal state to the zero resistance state (points between T_M and T_{cross}) - condensation of Cooper pairs (labeled flux flow state - only when $H \neq 0$),
3. when the resistance starts to drop (T_{cross}) - the onset of the superconducting state.

The melting temperature at different magnetic fields and the superconducting transition temperatures were obtained for all compositions. These are shown in Fig. 3.11(b) and 3.11(c), respectively. The color code is the same for both figures. For all compositions, the *melting points* and the *superconducting transitions* display linear behavior.

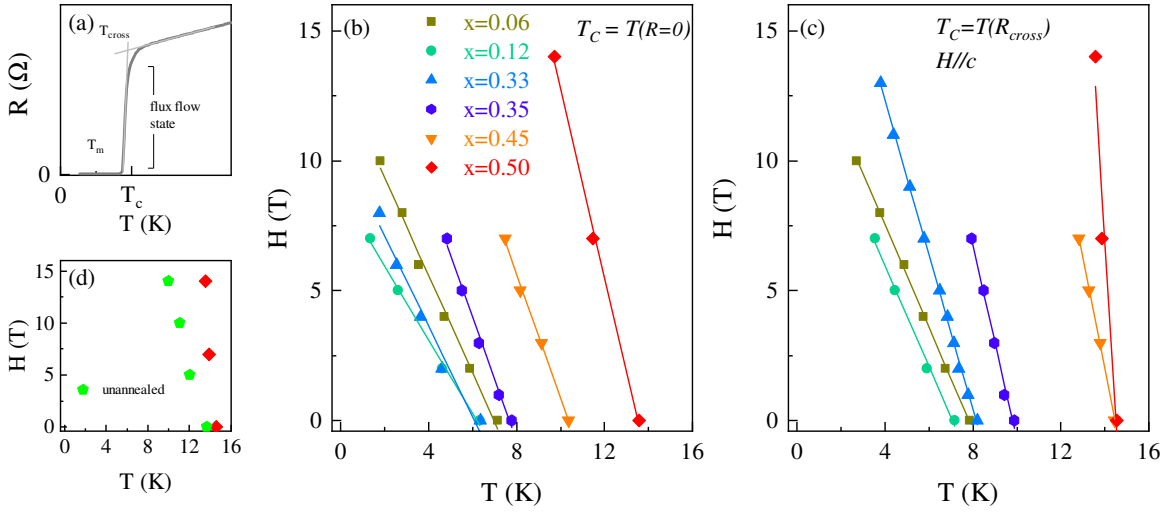

FIGURE 3.11: (a-d, clockwise from top left): (a) A generic superconducting transition highlighting the T_M, T_{cross} and flux-flow state (only in $H \neq 0$), (b,c) the H vs T for different composition using T_M and T_{cross} respectively. The linear lines are fitted to extract the $(dH_{c2}/dT)|_{T=T_c}$. (d) Shows the T_{cross} for unannealed and annealed $x = 0.5$.

The initial slope obtained for the superconducting transition ($T = T(R_{\text{cross}})$) in Fig. 3.11(c) of the H-T diagram is presented in Table 3.3, along with the zero-field critical temperature and the zero-temperature magnetic field at which the vortex lattice melts, i.e., T_M and H_{melting}. The Pauli limiting field $H_P(0)$, calculated using the BCS gap and $T_c(0)$, is also tabulated. For FeSe, the data are taken from [103]. The calculated value of $H_P(0)$ for FeSe is significantly lower than the actual value of 26.5 T, found by fitting the high-field H-T diagram where T_c is completely suppressed. In particular, $H_P^{calc}(0) < H_{c2}^{\text{orb}}(0)$, which is inconsistent with the weak-coupling picture. This suggests that Pauli de-pairing plays a significant role in FeSe.

With increasing Te substitution, both H_{c2}^{orb} and T_c, and hence H_P, decrease. However, beyond x=0.35, $|H'_{c2}|$ increases, and for optimal doping $x = 0.5$, it reaches -13.96 T/K, leading to an extraordinarily high $H_{c2}^{\text{orb}}(0) = 146$ T. In contrast, $H_P(0) = 27$ T, which is about five times smaller than the $H_{c2}^{\text{orb}}(0)$ value. It is noteworthy that the modifying

Eq. (1.7) using the gap energy for Fe(Se, Te) (calculated in Sec. 3.3.2) provides a value of $H_p(0) \approx 40\,\mathrm{T}$. Thus, the system may be characterized as a strongly coupled superconductor with a larger gap; however, it does not yet capture the complete mechanism of *how* the magnetic field destroys superconductivity. Since $H_{c2}^{orb}(0)$ is inversely proportional to Fermi velocity and mean free path, the modification of the Pauli-limiting effects in the optimally doped sample should stem from either of the following two reasons:

(a) scattering effects, which modify the mean free path, or
(b) changes in the density of states, leading to a change in the Fermi velocity.

Using Drude model, the calculated mean free path (l_{mfp}) for the optimally doped annealed sample is 0.3 nm. The Ginzburg-Landau coherence length $\xi = \sqrt{(\Phi_0/(2\pi H_{c2}))}$ calculated using $H_{c2} = 48\,\mathrm{T}$ from the high-field experiments is 2.62 nm. Here $\Phi_0 = h/2e \approx 2.07 \times 10^{-15}\,\mathrm{Wb}$ is the quantum magnetic flux. The condition $l_{\mathrm{mfp}} << \xi$ implies that the system is in the dirty limit.

x (Te)	T_M (K)	$H^{\mathrm{linear}}_{\mathrm{melting}}$ (T)	$(dH_{c2}/dT)\|_{T=T_c}$ T/K	T_c (K)	H_{c2}^{orb} (T)	$H_P(0)$ (T)	ΔT (K)
0[103]			-3	9.1	19.85	16.926	
0.06	7.14	13.09	-1.97	7.83	11.24	14.56	0.69
0.12	6.34	8.75	-1.94	7.17	10.11	13.34	0.83
0.33	6.35	10.61	-2.96	8.20	17.66	15.25	1.85
0.35	7.79	18.25	-3.72	9.88	26.73	18.38	2.09
0.45	10.36	24.79	-4.32	14.43	45.35	26.84	4.07
0.50	13.56	49.13	-13.86	14.53	146.46	27.03	0.97

TABLE 3.3: Listed here for various compositions: the upper bound to the vortex-lattice melting temperature T_M and field H_{melting} estimated from the linear fit to the $R = 0$; the slope $(dH_{c2}/dT)|_{T=T_c}$ calculated using T_c defined by the onset of superconductivity; the orbital critical field and coherence length calculated as described in the text[3]. ΔT is the superconducting transition width. The $H_P(0)$ values in red indicate the physically unfeasible condition of $H_{c2}^{\mathrm{orb}} >> H_p(0)$.

For FeSe, $\xi = 3.5\,\mathrm{nm}$, thus the decrease in ξ alone is not sufficient to explain the seven-fold increase in H_{c2}^{orb}. Also, as shown in Fig. 3.11(d), the $|H'_{c2}|$ increases with annealing. Since annealing increases the mean free path (as evidenced by the reduction in the absolute value of ρ), the change in the density of states probably plays a dominant role in the Pauli limiting effects in the optimally doped FeSe. Indeed from the density functional theory, it

[3]We use the clean-limit WHH prefactor 0.727 for consistency; using the dirty-limit value 0.69 changes the H_{c2}^{orb} by only about 5%.

has been shown that removing the excess Fe in FeSe induces additional states near the Fermi level [104]. The decline in the linear magnetoresistance to complete absence at x=0.3 has also been related with the presence of Dirac states [105] around this composition.

Figs. 3.12(a-d) show the magnetic field ($H//c$) dependence of C/T for x=0.12, 0.33, 0.45, 0.5 respectively. Using this, the $H-T$ diagram was constructed and presented in Fig. 3.12(e). Similar to the upper critical field derived from the transport, a giant enhancement occurs for x = 0.5, $H_{c2}(C_p) = 123\,\mathrm{T}$.

The enhanced Pauli limiting effects derived using transport and heat capacity support the idea that the superconductivity beyond $x > 0.35$ has a *different origin*.

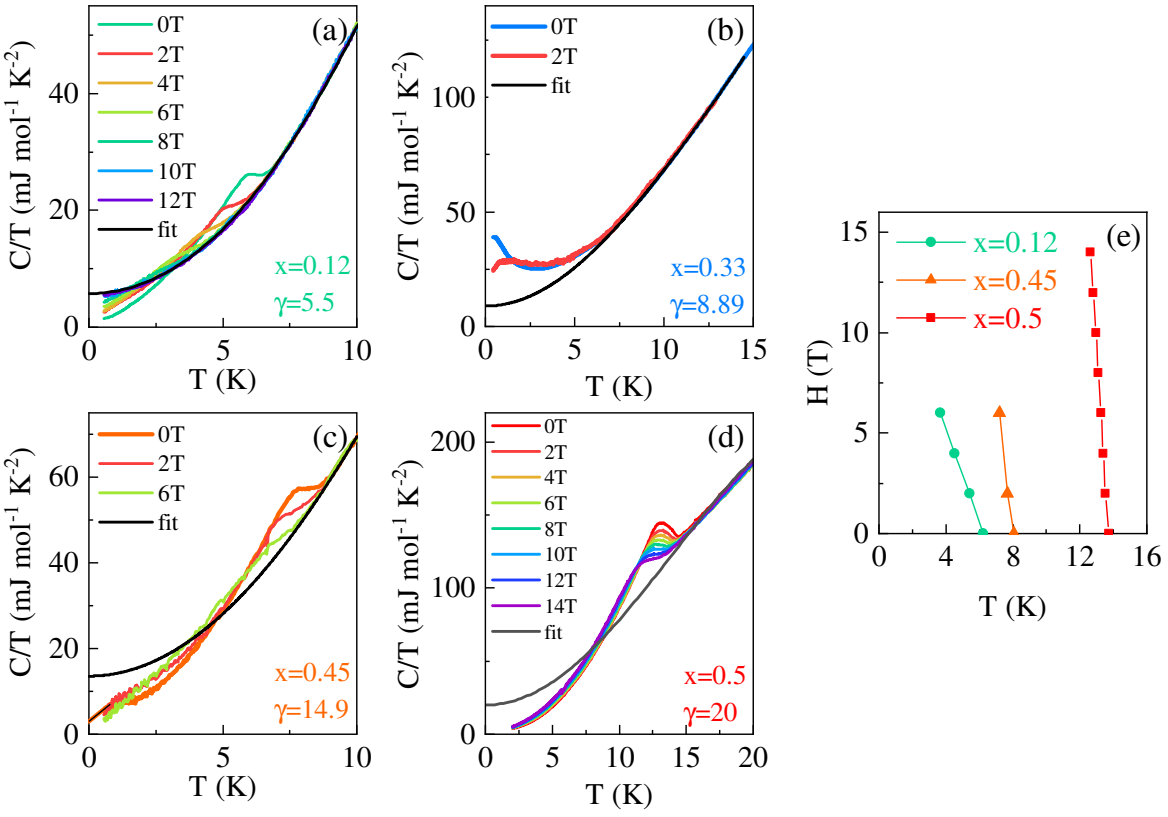

FIGURE 3.12: (a-d) The magnetic field dependence of heat capacity plotted as C/T for x=0.12, 0.33, 0.45, 0.5. The black solid line represents fits made in the normal-state data, using which the electronic contributions and the Sommerfeld coefficients are determined. (e) Shows the H vs. T graph using heat capacity for different compositions. Field is always parallel to c-axis.

3.3.2 Electronic specific heat in superconducting phase

If there is a change in the superconducting mechanism across $0.2 < x < 0.4$, it should be captured in the electronic heat capacity, C_e/T, of the SC region. For this, the phonon

part of the heat capacity is extracted by fitting the experimental data above T_c, such that entropy conservation follows for the superconducting transitions. The usual method of fitting the high temperature heat capacity or using an unannealed sample as background for optimally doped Fe(Se,Te) leads to an excess entropy and an overestimation of γ_N. Fig. 3.13(a-f) shows C_e/T plotted against T and shows a clear difference in qualitative behavior between $x = 0$ and $x = 0.5$.

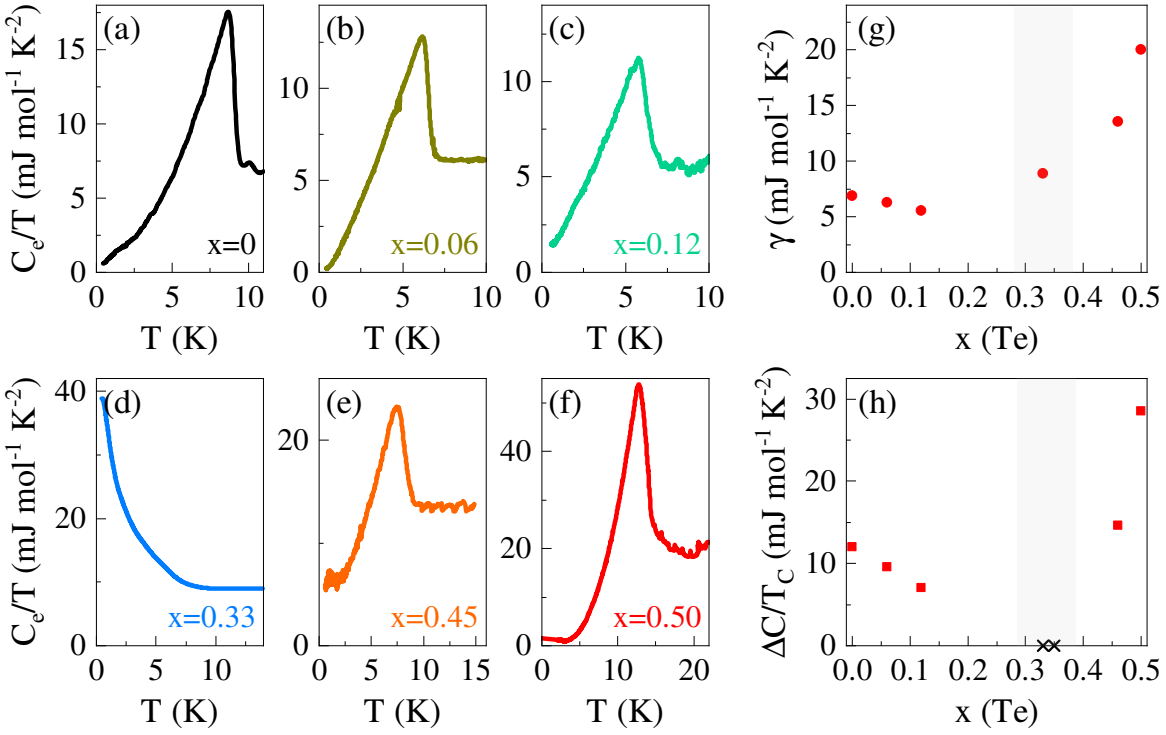

FIGURE 3.13: (a-f) Electronic specific heat plotted as C_e/T vs. T for different compositions. For x=0.33, no bulk superconducting transition is detected. (g) Sommerfeld coefficient and (h) $\Delta C/T_c$ show a clear distinction for higher substitution ($x = 0.45, 0.5$).

The residual heat capacity is very small for all the compositions, except for $x = 0.45$, indicating the high quality of our samples. The bulk transition is absent for $x = 0.33$, but the data have been shown here for completeness. In Fig. 3.13(g), the Sommerfeld coefficient derived from the phonon fits (see black lines in Fig. 3.12) has been plotted. The fit procedure is detailed in Sec. 2.3.1. The Sommerfeld coefficient is directly proportional to the density of states at the Fermi level ($\gamma = \pi^2 k_B^2 N(E_F)/3$). The significant enhancement in the second dome is related to the additional density of states coming from the d_{xy} orbital becoming coherent [106]. The $\Delta C/T_c$, which is a measure of the superconducting pairing strength, also jumps in the second superconducting dome, as shown in Fig. 3.13(h), hinting at a change in the mechanism.

Fig. 3.14 shows the electronic heat capacity for the superconducting samples, normalized by the Sommerfeld coefficient plotted against T/T_c. The heat capacity data can provide

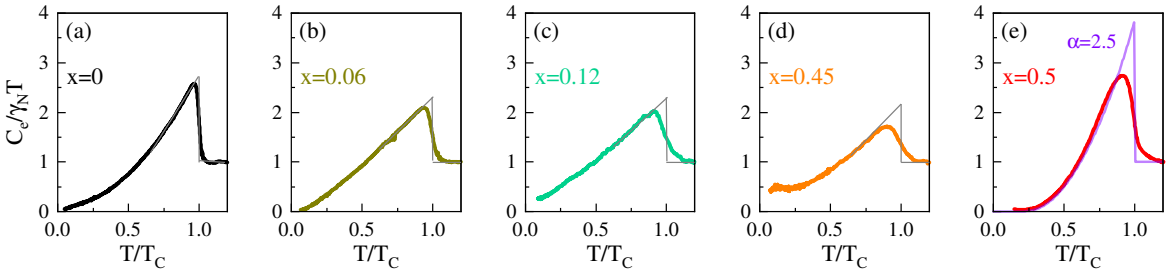

FIGURE 3.14: Electronic specific heat normalized by the Sommerfeld coefficient γ_N plotted against temperature normalized by superconducting transition temperatures, T/T_c for $x = 0, 0.06, 0.12, 0.45, 0.5$. Superconducting volume fraction for all except $x = 0.45$ composition is more than 80%. Thin gray lines indicate the idealized jump. Data for $x = 0$ is from [84].

useful information about the gap structure [6, 84, 107, 108]. Hence, a change in the superconducting mechanism, might be reflected in the heat capacity in the superconducting state. As detailed in the introduction, there is a significant debate around FeSe's gap structure in the experimental literature (Table 3.2). In the following, we detail the method for modeling the electronic specific heat in terms of candidate gap structures within the existing theoretical framework.

The basic aspects of superconducting gap structure and their manifestations in heat capacity measurements were introduced in Sec. 2.3.1. Additionally, the superconducting gap structure relevant to iron-based superconductors (FeBS) was discussed in Sec. 3.1.2. Building upon these discussions, we note that the nematic phase reduces the symmetry from tetragonal (C_4) to orthorhombic (C_2), resulting in a mixing of isotropic and anisotropic (two-fold symmetric) gap components. Consequently, the SC gap of the hole pocket (at center) of the Brillouin zone (BZ) can be described by the following gap function [81, 86, 87]:

$$\Delta = \Delta_h(1 + \alpha_{11}\cos 2\theta + \alpha_{12}\cos 4\theta) \tag{3.4}$$

where $\cos 2\theta$ is induced by nematicity and $\cos 4\theta$ is the C_4 symmetric term coming from the tetragonal phase [81]. The sign of α_{11} depends on the details of the nematic order. The gap structure at the electron pocket for the FeSe at X/Y is given by:

$$\Delta = -\Delta_h\gamma_{X/Y}(1 - \alpha_{21}\cos 2\theta_{X/Y} \pm \mathcal{O}(n\theta)) \tag{3.5}$$

where the terms with higher harmonics are sufficiently large (see [79] and the references within) and a nodal or deeply anisotropic gap structure at the X/Y appears.

For pure FeSe ($x = 0$), the fits to the heat capacity using the BQPI / STM data [86] have been made in [84, 85]. In both [85, 88] the heat capacity at low temperatures shows a

hump identified as a second superconducting transition or related to the Schottky effect. No such second superconducting transition exists for fully superconducting samples with minimal impurities [84]. In this case, the low temperature heat capacity can only be explained by introducing nodes at either Δ_e or Δ_h. To show this, the angular dependence of the gaps is obtained from the fit to the BQPI/STM data. For Te-doped samples, BQPI experiments have not been reported. Hence, we use a deduction method to obtain the best fit:

- Start by assuming the gap form in the leading order of the nematic order parameter:

  $\Delta_e = \Delta_e(1 + \alpha_{21} \cos 2\theta)$, where $\alpha_{21} \to 1$ and

  Δ_h given by Eq. (3.4) with $\alpha_{11} \sim 0.65$ and $\alpha_{12} \sim 0.1$,

- decrease the α_{21} in steps of say 0.1,

- allow higher harmonic terms $n\theta$, set the order of these higher harmonics to the limit $\mathcal{O}(\alpha_{21}^2)$ [13, 109] and then to the limit $\mathcal{O}(\alpha_{21})$ [79], thus allowing for large enough contribution necessary for systems like FeSe.

The whole sequence was then parallelized to take advantage of full computing power, and the complete iteration can be completed in a few hours. Using the method described above, the normalized heat capacity for all superconducting samples was obtained. A remarkable feature for $x = 0$ is that the α_{ij} parameters obtained are close to the one obtained from the fit to the BQPI/STM. Moreover, the behavior of the low temperature heat capacity is mimicked only when the electron gap (Δ_e) becomes deeply anisotropic (nodal). This is shown in Fig. 3.15. In addition to the case shown here, the normalized heat capacity obtained from the two-band model is also close for one set of α_{ij}, where $\alpha_{21} \approx 0.9$. However, in this case, the obtained Δ_e at $\theta = 0$ is too large (positive). Also, the jump height at the superconducting transition mismatches. Based on the other experiments [87], this has been discarded. For Te substituted $x = 0.06$, the $C_e/\gamma T$ vs. T/T_c along with the heat capacity calculated in the two-band model is shown in Fig. 3.16. The angle-averaged part of the superconducting gap at the hole and the electron bands are $\Delta_h = 1.03\,\text{meV}$ and $\Delta_e = 0.82\,\text{meV}$, respectively. Since the angular dependence of the superconducting gap on the hole pocket does not deviate much for the S substitution, we assume the same for $x = 0.06$ also. The first observation from the obtained $\Delta_e(\theta)$ is that it is no longer deeply anisotropic in this case. This disappearance of nodes implies that the nodes, if present in FeSe are likely *accidental*, since the nodes arising due to symmetry compulsion (say in a d-wave) are also protected against perturbations.

For $x = 0.12$, there is a slight residual. Thus, achieving a complete fit is rather difficult. For the $T/T_c > 0.2$ region, several fits were attempted and are shown in Fig. B.3. The $\Delta_{h,e}$

decreases further in line with the decrease in the $\Delta C_e/T$ in the superconducting transition. Two results follow from the attempted fits (a) single band fits are not possible (Fig. B.3(f,g)), (b) reasonably good fits are obtained for the cases when the Δ_h develops deep anisotropy (Fig. B.3(c,d)) or even sign-changing nodes (Fig. B.3(b,h)). Such a gap structure is possible if the orthorhombicity α_{21} becomes smaller and/or the tetragonal anisotropic contribution (α_{22}) increases. The $\cos 4\theta$ term arises from spin orbit coupling or due to the influence of high energy Fermions on the low energy properties through virtual excitations [76, 110]. Te $5p$ orbitals increase the spin orbit coupling and the orbital overlap, leading to an increase in the contribution C_4. The Te substitution is also known to alter the density of states at energies away from the Fermi level (high energy Fermions), and these changes can modify the effective pairing interaction $V_{\rm sf}(\mathbf{q}) = \frac{3}{2}U^2\chi(\mathbf{q}, \omega \approx 0)$ mediated by spin fluctuations. Such a sign-changing gap with accidental nodes in $FeSe_{0.88}Te_{0.12}$ is similar to the ultra-nodal state observed in Fe(Se,S) at the nematic end point [111, 112]. However, here it results from a complex interaction due to modifications in the C_4 contribution with respect to the contribution induced by nematicity.

Bulk superconductivity reappears in the putative second superconducting dome. For $x = 0.45$, a large residual remains (Fig. 3.14(d)). No fit attempts were made because of this

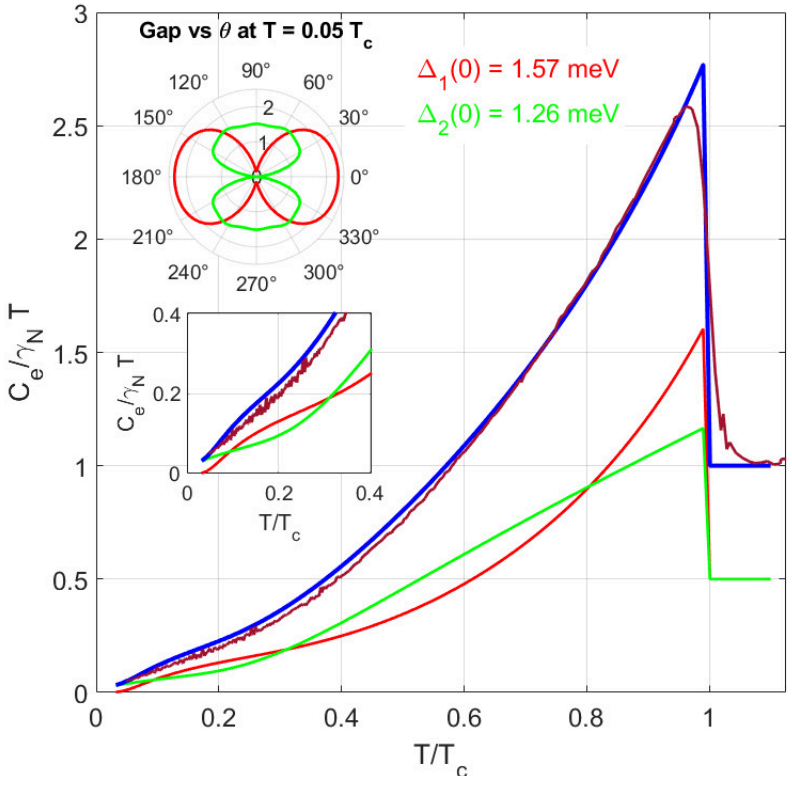

FIGURE 3.15: $x = 0$: Normalized heat capacity for FeSe along with the contribution from the two bands and their sum for the case when the higher harmonic contributions are permitted to be large enough.

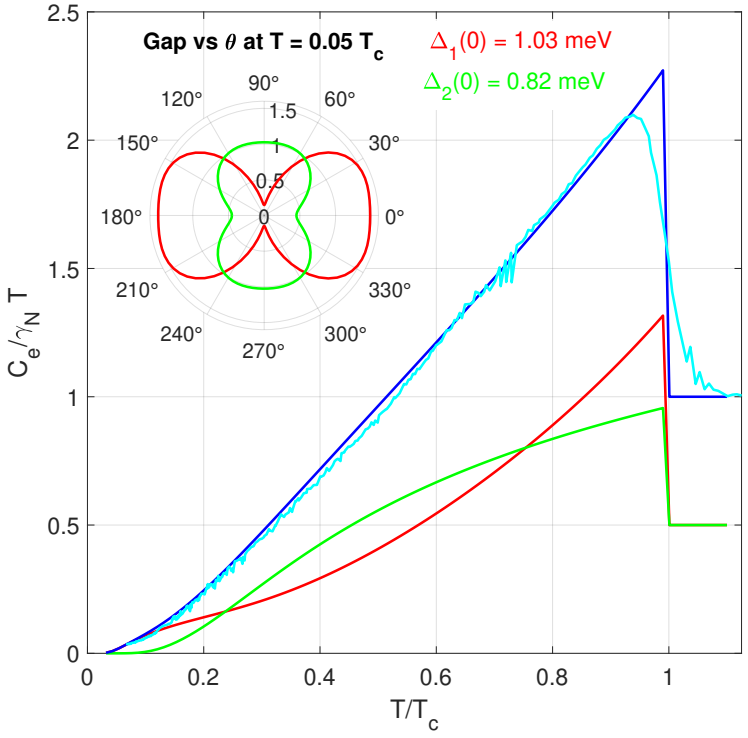

FIGURE 3.16: $x = 0.06$: Normalized heat capacity for Te substituted FeSe. The gap at the Γ is assumed to be the same as for the pure FeSe [87]. The Δ_e does not have a deep anisotropy/node.

large residual. For the annealed $x = 0.5$, the $\Delta C_e/(\gamma_N T_c) = 1.9 > 1.43$(BCS), the BCS value. The calculated $C_e/(\gamma T_c)$ vs. T/T_c, shown in Fig. B.4, requires a much larger gap $\Delta_{h/e}$ to accurately reproduce the experimental curve. The ARPES and penetration depth studies in this region of the phase diagram put $\Delta > 2\,\text{meV}$ [113]. Here, the calculated heat capacity suggests that the thermodynamics is dominated by the single isotropic gap (probably the hole band [113]). Adding the contribution from the electron band improves the fit (Fig. B.4(a-d,g,h)). The electron band has C_4 anisotropy, but no nodes [109, 114]. The large values of $\Delta_{h,e}$, suggest that the superconductivity is in a strong coupling regime and the pairing mediation is likely different from the FeSe. The strong coupling is marked by the possibility of a BCS-BEC regime. The Cooper pairs in the BCS theory are highly delocalized, whereas in the strong-coupling case, electrons can form tightly bound pairs that behave like bosons. In such a case, the coherence length (ξ_0), which is related to the *size of Cooper pairs*, is small and approaches the interparticle spacing, thus implying a large orbital critical field H_{c2}^{orb} as obtained in transport measurements ($= 140\,\text{T}$). For the gap $\Delta_h \approx 3.1\,\text{meV}$, the Pauli limit, $H_P = \frac{\Delta(0)}{\sqrt{2}\mu_B} = 38\,\text{T}$, significantly larger than the value obtained using the BCS gap, which is 27 T (see Table 3.3). The large fitted gap, together with the large inferred H_{c2}^{orb}, and H_P are compatible with the system being in the BCS-BEC crossover regime [113].

3.3.3 Pressure dependence of T_c - development of c-axis anisotropy

Thermal expansion is an ideal measurement for probing the uniaxial strain dependence of phase transitions. The high-resolution thermal expansion was measured in the capacitive dilatometer [45]. A very small force of $\sim$ 0.2 N [6] is applied to the sample on the dilatometer. This is crucial for measuring the thermal expansion of Fe-chalcogenide systems as they are extremely soft. A large force will bend the sample and induce mechanical strain and deformation, leading to strain-induced contributions to the measurement.

The low-temperature region highlighting the superconducting anomalies is shown in Fig. 3.17(a-d). The superconducting jumps along the detwinned $a-$ axis, the twinned [100] and c-axis are shown for $x = 0, 0.06, 0.12$. For optimally doped $x = 0.5$, the [100] direction is shown since there is no structural transition and the effect of the applied strain of the dilatometer on the thermal expansion is lesser compared to [110].

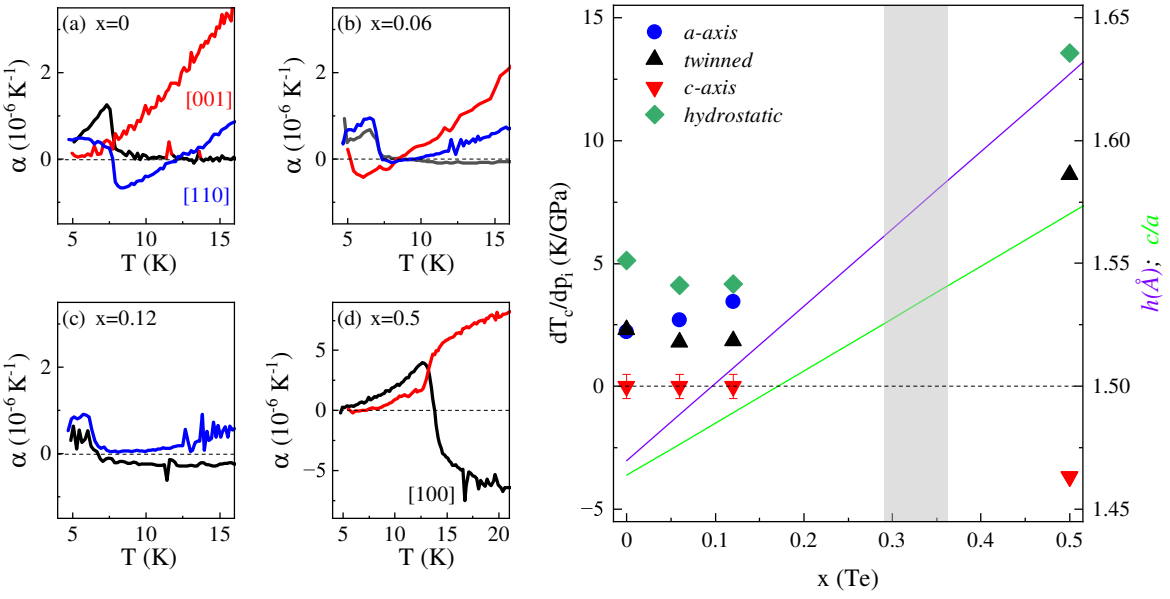

FIGURE 3.17: Left (a-d) thermal expansion coefficient α for $x = 0, 0.06, 0.12, 0.5$ along [100], [110] and [001]. Right: hydrostatic pressure dependence of the SC transition along with the c/a ratio and h, the chalcogen height. For $x = 0, 0.06, 0.12$, α[110](=detwin) was used and for $x = 0.5$- α[100] was used for calculation. (x=0: [9]: Dr. Böhmer)

The superconducting anomalies along the c-axis are not well resolved for $x = 0$, 0.06, 0.12, but are clearly distinguishable in the optimally doped system. For this composition, $x = 0.5$, there is a large anisotropy in the superconducting transition for the in-plane and c-axis response, where $\Delta\alpha_{in-plane}$ is positive like FeSe and $\Delta\alpha_c$ is negative. Like the heat capacity, the superconducting transition is also not resolved in the thermal expansion for $x = 0.35$ down to 5 K while the nematic transition is clearly visible; see Fig. 3.23(d). The uniaxial and hydrostatic response for all superconducting samples are

summarized in Fig. 3.17(e). For the c-axis in low compositions, $\Delta\alpha_c \to 0$, consequently, $dT_c/dp_c = 0(\pm 0.5)$ K/GPa. For the in-plane, the dT_c/dp for the detwinned a -axis increases with x, while the twinned response decreases. The overall hydrostatic response decreases marginally with x in the first SC dome from 5.1 K/GPa for FeSe to 4.57 K/GPa for $FeSe_{0.88}Te_{0.12}$. The in-plane response $\Delta\alpha$ is plotted for completeness in Fig. 3.25. The $\Delta C/T_c$ are taken from the specific heat measurements discussed earlier (see Fig. 3.13). The values obtained for $dT_c/dp_h = 4.5 - 5$ K/GPa here in the first SC dome ($x = 0,\ 0.06,\ 0.12$) are very close to the ones computed using the initial slope from the PT phase diagram $dT_c/dp_h = 4 - 6$ K/GPa [73, 93, 115].

In FeSe, the isoelectronic substitution of a larger (smaller) Te (S) atom is expected to exert a negative (positive) internal pressure [5]. Since $dT_c/dp_h > 0$, T_c of FeSe should decrease with Te substitution and increase with S. Thus, in the first dome the Te/S substitution mimics the hydrostatic effect. It is important to stress that the $dT_c/dp_{i/h}$ obtained from the thermal expansion / heat capacity is under limiting pressure $p \to 0$.

Comparison with $BaFe_2As_2$

In iron-pnictides, the c/a ratio serves as a tuning parameter for the phase diagram [10]. The c/a ratio is related to the interplane interactions and changes in Fermi surface sheets. Increasing pressure in these materials changes the c/a ratio, enhancing interlayer hopping and distorting the cylindrical Fermi surfaces. This distortion reduces the nesting conditions between hole and electron pockets, suppresses spin-density wave (SDW) order, and favors superconductivity [116–118].

In contrast to the pnictides, which contain FeAs layers separated by spacer layers, FeSe exhibits a highly two-dimensional crystal structure where the charge neutral Fe layers are held together primarily by van der Waals forces, and superconductivity is dominated by in-plane electronic interactions. Consequently, two main orbital interactions arise due to the presence of chalcogen atoms: (a) intralayer Fe-chalcogen (pd) interactions, and (b) interlayer chalcogen-chalcogen (pp) interactions. As chalcogen atoms are not coplanar with Fe atoms (see Fig. 3.18(A,B)) and the c-axis is significantly longer than the a-axis, applying uniaxial pressure along the c-axis minimally affects the Fe–Se bond lengths or bond angles critical for superconductivity. Thus, for low Te/S substitutions, $dT_c/dp_c \to 0$.

Another tuning parameter is the chalcogen height, defined as the vertical displacement between the Fe plane and the chalcogen atom. The chalcogen height (h) also increases with substitution similar to c/a ratio, and is not an effective universal tuning parameter for the entire Fe(Se,Te) phase diagram (see Fig. 3.17(e); [93, 106, 120]).

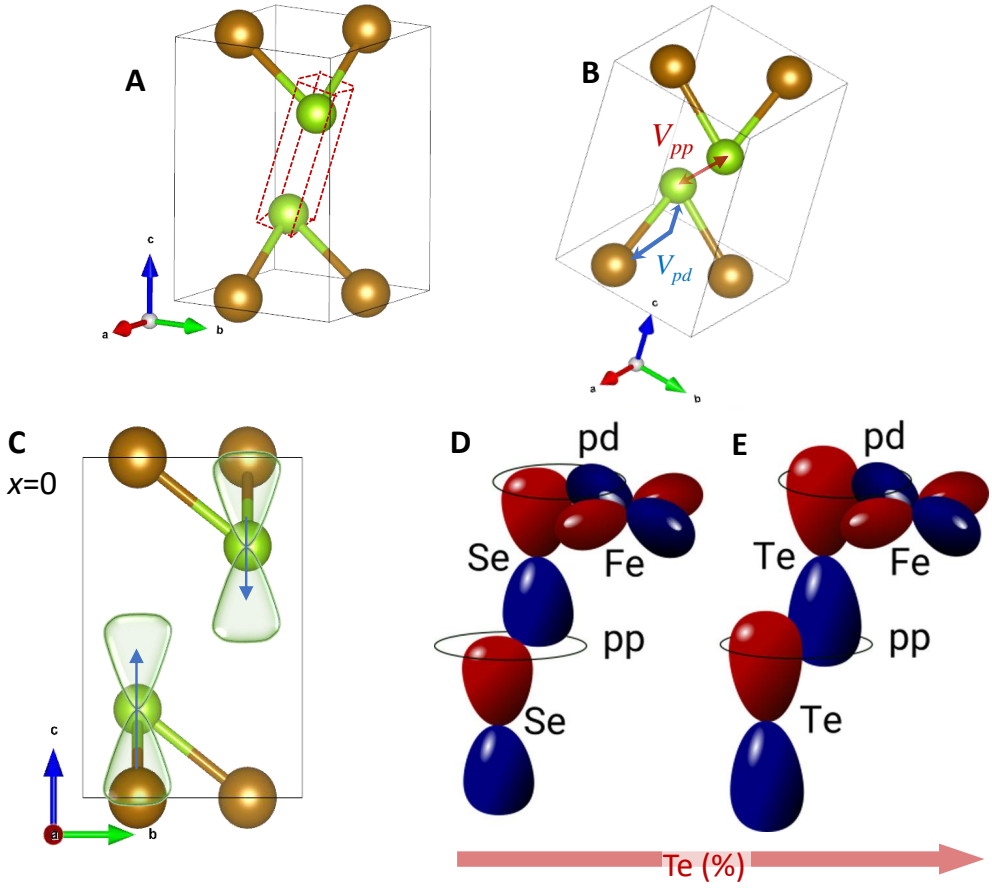

FIGURE 3.18: Crystal structure highlighting orbital interactions in Fe-Ch (Ch = Se, Te) compounds: (A) Unit cell representation, with Fe atoms in golden and chalcogen atoms (Ch) in green. The dashed red box emphasizes two distinct chalcogen positions. (B) Arrow indicates the *pp* and *pd* orbital interaction (V_{pp}, red arrow; V_{pd}, blue arrow) between relevant chalcogen-chalcogen and chalcogen-iron atoms. (C-E) From SC dome 1 to SC dome 2: The orbitals overlap evolution as Se is substituted with Te. On substituting Te in (C) FeSe, the chalcogen atom shifts up, indicated by the blue arrows in (C) at Se site. Beyond a critical composition, the larger Te p_z orbitals lead to enhanced V_{pp} interaction. We correlate the appearance of three-dimensionality in the system to *pp* overlap becoming large enough. (D, E) are taken from Lars Lauke et al., Phys. Rev. B 102, 054209 (2020) [119], reprinted with permission from the American Physical Society. Copyright 2020 by the American Physical Society.

Based on the above discussion, we conclude that the orbital effects, in particular, how the p_z orbital of the chalcogen atom interacts with the d orbitals of Fe and the resulting effects on the superconducting gap, are most crucial for understanding the FeSe (Te/S) phase diagram [80, 120]. *Obtaining a simple structural tuning parameter like c/a or h for the complete phase diagram may not be possible in the Fe(Se,Te).*

Development of the c-axis anisotropy

For $x = 0.5$, we obtained a heat capacity jump at T_c of $\Delta C_p/T_c = 28.5$ mJ mol^{-1} K^{-2}

and molar volume $V_m = 25.96$ cm^3 mol^{-1}. The in-plane thermal expansion coefficient change, $\Delta\alpha_a = 9.5 \times 10^{-6}$ K^{-1}, gives a positive $dT_c/dp_a = +8.6$ K/GPa. Conversely, along the c-axis, a negative thermal expansion change, $\Delta\alpha_c = -4 \times 10^{-6}$ K^{-1}, results in a negative pressure dependence, $dT_c/dp_c = -3.67$ K/GPa. The opposite signs of dT_c/dp_i indicate that in-plane compression enhances superconductivity, whereas c-axis compression suppresses it. Similar opposite anisotropy is reported in overdoped $BaFe_2As_2$ [6, 10]. The calculated hydrostatic pressure dependence, $dT_c/dp_h = +13.5$ K/GPa, exceeds previously reported direct pressure measurements (6 K/GPa; [93]). For low Te substitution, the c-axis expansion anomaly at T_c remains unresolved [9], contrasting the well-defined change at $x = 0.5$, highlighting substantial alterations in superconducting mechanisms and the normal-state electronic structure.

Te substitution significantly influences intralayer (pd) and interlayer (pp) hopping. In particular Te's larger spatially extended $5p$ orbitals, compared to Se's $4p$ orbitals, increase Fe–Te bond lengths and chalcogen height h. Up until a critical composition, the net effect is the reduction in the intralayer Fe-$3d$ and Te-$5p$ orbital overlap, leading to a decrease in intralayer hopping and density of states at the Fermi level. Above a critical Te concentration, enhanced interlayer (pp) orbital overlap due to larger Te orbitals and the increased chalcogen height take over, inducing three-dimensionality in the system [119]. Thus, interlayer hybridization increases and modifies the band structure and electronic correlations. Indeed, at optimal doping ($FeSe_{0.5}Te_{0.5}$), ARPES studies reveal the d_{xy} orbital moving closer to the Fermi level, exhibiting significant dispersion and band inversion at the Z point [120]. *Enhanced three-dimensionality manifests as the anomalous c-axis anisotropic response observed in the second superconducting dome.*

Finally, the changes in orbital overlap influence the bandwidth which is further enhanced by the Hund's orbital blocking mechanism [11]. This has an overall effect on the electronic correlations U, which modifies the spin-susceptibility $\chi(\mathbf{q},\omega) = \frac{\chi_0(\mathbf{q},\omega)}{1-U\chi_0(\mathbf{q},\omega)}$, where χ_0 is the bare spin susceptibility. In this line of reasoning, beyond a critical composition, substituting with Te can lead to significant modifications (enhancement) in spin susceptibility which can be conducive to superconductivity if a static magnetic order doesn't develop.

We conclude that the observed anisotropic c-axis response at $x = 0.5$ is likely related to the changes in band topology and orbital hybridization effects in Fe(Se,Te).

3.4 Results III: Coupling between superconductivity and orthorhombicity

In this section, we discuss the interplay between superconductivity and orthorhombicity in the Fe(Se,Te). We first show the pressure dependence of the T_{nem} is same as that derived from the direct pressure measurement. This is crucial to make the comparison to the pressure measurements and the conclusions presented in this study.

Fig. 3.19 shows the $\Delta L_i/L_{i,0}$ for $x = 0, 0.06, 0.12, 0.35, 0.50, 1$ measured along the twinned and detwinned directions. The shorter $a-$axis is labeled [110] for Iron-chalcogenides [9, 121]. The twinned thermal expansion corresponds to the in-plane average $(a+b)/2$. Thus, the b-axis thermal expansion is obtained by: $2 \cdot \frac{\Delta L_{[twin]}}{L_{[twin],0}} - \frac{\Delta L_{[110]}}{L_{[110],0}}$. The nematic transition manifests itself as a second-order tetragonal-to-orthorhombic transition (for FeSe at 90 K). A bifurcation occurs in the a and inferred b-axis at this point (Fig. 3.19(a-d)).

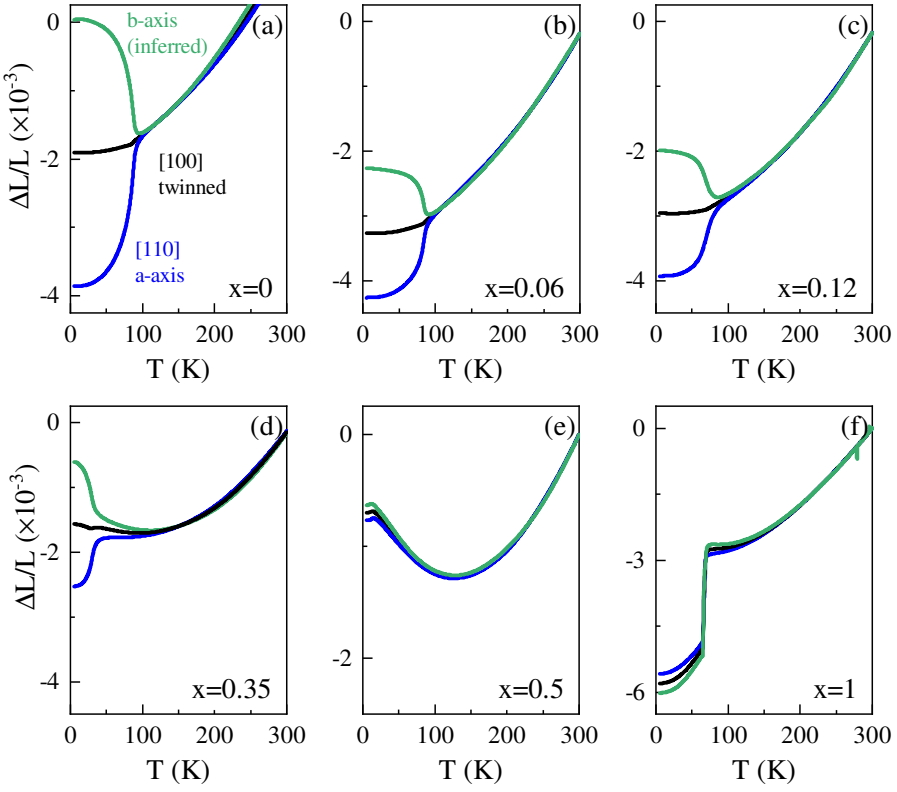

FIGURE 3.19: (a-f) $\Delta L/L$ plotted against temperature for different compositions. The $x = 0$ data is from [9]. The nematic transition breaks the tetragonal symmetry seen as the bifurcation in the a and b-axis data. The b-axis is inferred using the detwinned (a-axis) and twinned ($a+b$). For $x = 1$ (FeTe) the sharp drop corresponds to the AFM transition. The color legend follows for all the plots.

At the nematic transition, unlike the iron pnictides, FeSe does not develop a magnetic order, and there is no *second* discernible transition after substitution with Te. For the optimally

doped $x = 0.5$, no nematic transition is observed. At the superconducting transition T_c, the in-plane lattice constants show a sharp change in slope and are best visible in the case of the optimally doped sample Fig. 3.19(e). For FeTe ($x = 1$), the simultaneous tetragonal-to-monoclinic structural transition and bicollinear antiferromagnetic transition develop at 67 K (Fig. 3.19(f)). This is seen as an abrupt change in the $\Delta L/L$, implying a first-order transition [67, 68].

3.4.1 Pressure dependence of T_{nem}

To obtain information on the volumetric strain dependence of the phase transitions, the uniaxial thermal expansion coefficients $\alpha_i = \frac{1}{L_i}\frac{dL_i}{dT}$ were calculated. The α_i divided by the temperature to emphasize the electronic part is shown in Figs. 3.23 and 3.24 for $i = [100], [001]$ and $i = [110]$, respectively. From this, the volumetric thermal expansion $\beta = \alpha_a + \alpha_b + \alpha_c$ was determined. The uniaxial pressure derivative of the transition temperature for a second order transition is given by the Ehrenfest relation:

$$\frac{dT_{nem}}{dp_h} = \sum_i \frac{dT_{nem}}{dp_i} = \frac{V_m}{\Delta C_p/T_{nem}} \sum_i \Delta\alpha_i \tag{3.6}$$

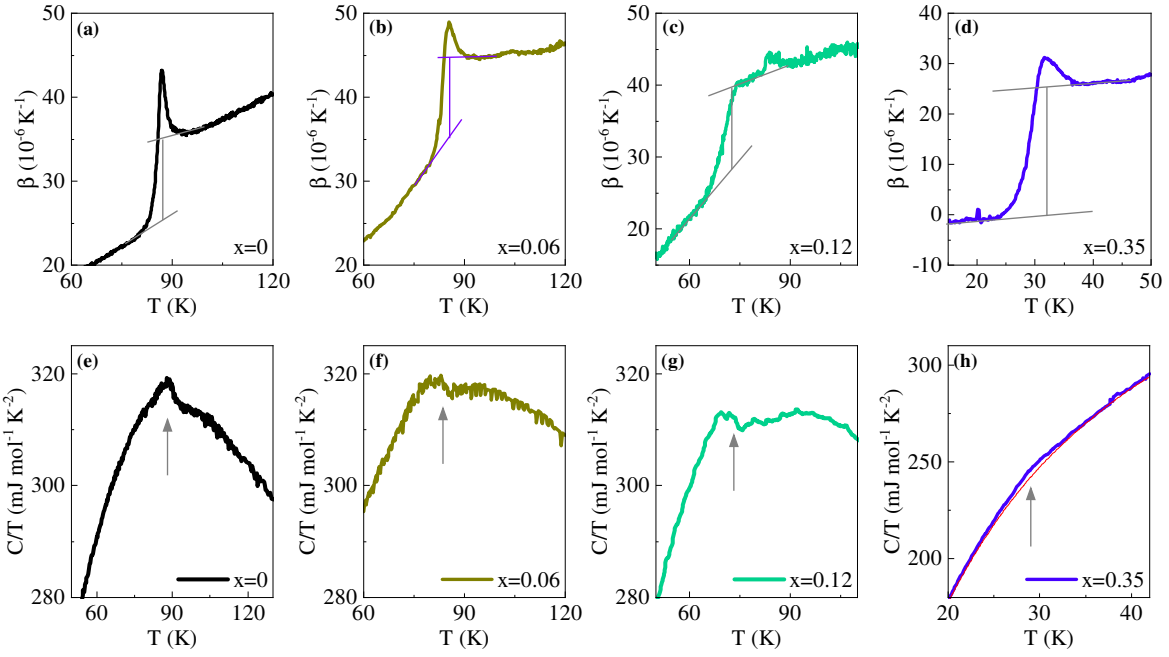

FIGURE 3.20: (a-d) Volumetric thermal expansion β vs T for $x = 0, 0.06, 0.12, 0.35$ highlighting the nematic transition. (e-h) show the corresponding heat capacity anomaly.

Here, i is the crystallographic axis, and V_m is the molar volume. Using Eq. (3.6), the pressure dependence of $T_{s,c}$ can be calculated using the change in thermal expansion $(\alpha_{LT} - \alpha_{HT})$ and heat capacity at transition [122].

The volumetric thermal expansion β for x = 0, 0.06, 0.12 at the nematic transition is shown in Fig. 3.20. Thin solid gray lines represent the idealized jumps. The $\Delta\beta \approx -10 \times 10^{-6}\,\mathrm{K}^{-1}$ remains constant for the three compositions. Since the molar volume doesn't increase drastically with composition, and the transitions in the heat-capacity are $\Delta C/T_s \sim 5$ mJ mol^{-1} K^{-2} also constant, the hydrostatic pressure dependence, $dT_s/dp_h \sim -40$ K/GPa for FeSe remains almost in this range (35-50 K/GPa) with Te substitution. This strong hydrostatic-pressure-dependence is also seen in direct hydrostatic pressure measurements, although the value is almost halved there [93] because the pressure steps in such measurements are often large (1 GPa), whereas the thermal expansion measures the pressure dependence in the limit of $p \to 0$.

3.4.2 Orthorhombic distortion

For the tetragonal-to-orthorhombic transition, the orthorhombic distortion serves as an order parameter. For small relative length changes $\Delta L_i/L_{300\,\mathrm{K}} \sim 10^{-3}$, the orthorhombic distortion is given by $\delta = |b-a|/(b+a) \approx (|\Delta L_a - \Delta L_b|/2L_{300\,\mathrm{K}})$ [9]. Fig. 3.21(a) shows the orthorhombicity for $x = 0, 0.06, 0.12$. The nematic transition, which is a second-order phase transition, manifests itself with a typical rising-arch behavior in the order parameter δ (and a corresponding peak in the derivative $d\delta/dT$, see Fig. 3.21(b)). The tail in δ above the transition is related to the finite strain applied in the dilatometer. This finite strain is necessary for de-twinning the samples. The effect is larger for thinner and smaller samples, and therefore maximum for $x = 0.35$. The jump below T_s can be fitted using $\delta = A(T_s - T)^\beta$, where $\beta = 1/2$ is the critical exponent of a mean-field transition.

The coupling of the superconducting transition and the orthorhombic transition can be inferred from these data. The zoomed-in δ and $d\delta/dT$ around the T_c are shown in Fig. 3.21(c,d) panels, respectively. For $x = 0, 0.06, 0.12$, δ has a very small kink-like anomaly at T_c resulting from the in-plane anisotropy in the thermal expansion associated with superconductivity. Consequently, $d\delta/dT$ has a peak feature at T_c, indicating that δ is larger in the superconducting state than in the normal state. This is seen in the extrapolated δ from the normal state for $x = 0.06$ and 0.12. There is no indication of competition between orthorhombicity and superconductivity in these low-Te-substituted compositions. Even for the case of $x = 0.06$, where a step is observed, the absolute values δ associated with SC remain in the same order 10^{-6}. For low x, the δ decreases on

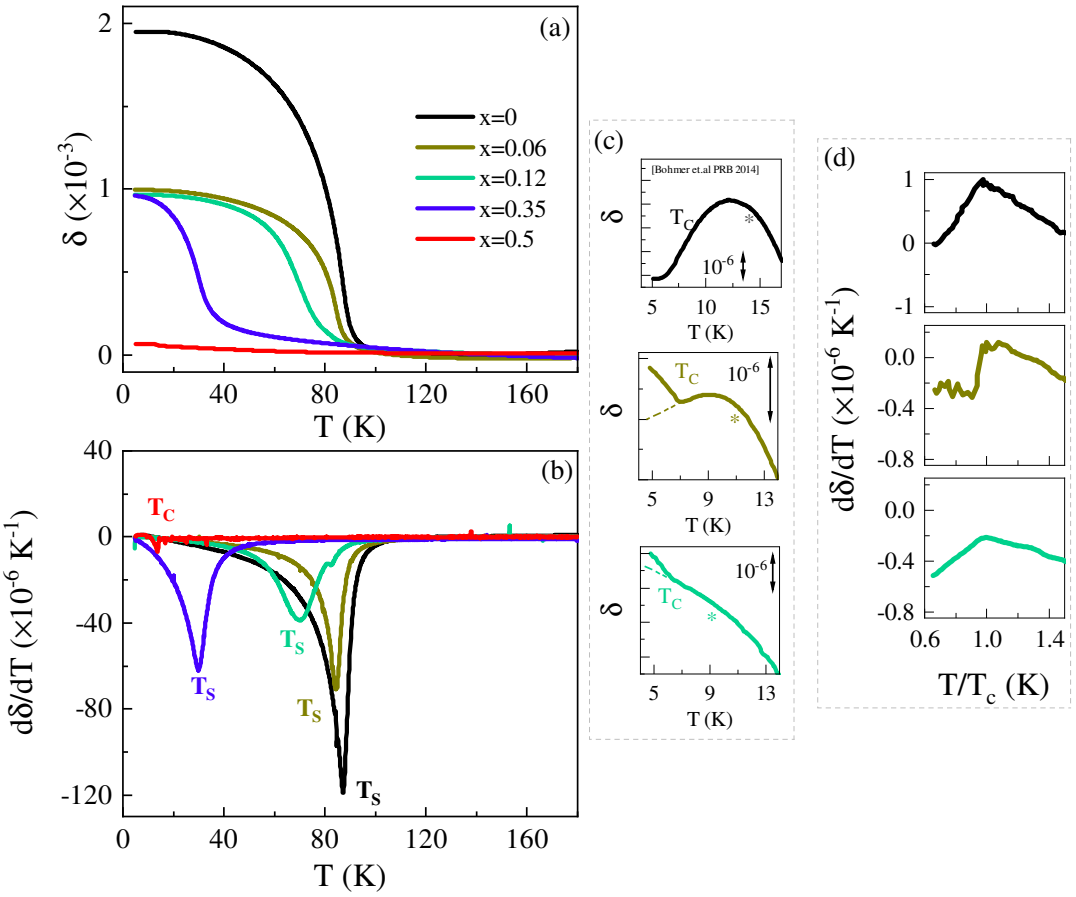

FIGURE 3.21: (a) Orthorhombic distortion and its (b) derivative for different compositions of $FeSe_{1-x}Te_x$. Panels (c) and (d) show the zoomed in δ and its derivative around the superconducting transition temperature respectively for different compositions.

approaching the superconducting transition below T^*, which can be related to either the superconducting fluctuations or a non-Fermi liquid behavior, and increases slightly at the T_c. However, the overall effect is rather benign.

3.4.3 Discussion

Since there is no magnetic ordering, the effective Landau free energy in terms of the superconducting order parameter (as described in the introduction, the superconducting energy gap (Δ) or the Cooper pair density (ψ) serves as the superconducting order parameter) (ψ_{sc}) and the orthorhombic order parameter (δ) is:

$$\mathcal{F}_1(\Phi_{sc}, \delta) = -\frac{a}{2}\delta^2 + \frac{b}{4}\delta^4 - \frac{\alpha}{2}|\psi_{sc}|^2 + \frac{\beta}{4}|\psi_{sc}|^4 - \frac{g}{2}|\psi_{sc}|^2\delta^2 \tag{3.7}$$

where g is the coupling coefficient between δ and ψ_{sc}. Since the nonzero orthorhombic order parameter equates to breaking of the C_4 symmetry at low temperatures, the linear quadratic term ($\delta \cdot |\psi_{\rm sc}|^2$) is not permitted, and only a quadratic coupling term occurs. The energy minimization with respect to these two order parameters, δ and ψ gives:

$$\delta^2 = +\frac{a}{b} + \frac{g\psi_{sc}^2}{b} \qquad \text{and} \qquad \psi_{sc}^2 = +\frac{\alpha}{\beta} + \frac{g\delta^2}{\beta} \tag{3.8}$$

In absence of any orthorhombic-superconductivity coupling, $g = 0$, $\delta^2 = a/b$ and $\psi_{sc}^2 = \alpha/\beta$. The effect of $g < 0$ ($g > 0$) is to decrease (increase) the δ below the superconducting transition. Physically, it implies that for the case of $g < 0$, superconductivity and orthorhombicity compete, while for $g > 0$, the two are mutually enhancing or cooperative. For low x, as discussed earlier, the change in δ at the superconducting transition is small (10^{-6}), two orders smaller than doped $BaFe_2As_2$ [10]. Hence, the coupling constant g is small but positive in the low Te substituted samples. Similar positive feedback between the two (δ and ψ_{sc}) was recently reported in the S-substituted FeSe as well [121, 123]. Therefore, the nematic state in FeSe(Te/S) couples weakly but cooperatively to the superconductivity, *implying that the nematic transition does not gap out the states responsible for the superconductivity.*

In the spin-nematic scenario [4, 9], the origin of this coupling (g) is attributed to the magneto-elastic coupling. The magnetic spin fluctuations give rise to electronic (in-plane) anisotropy because of the staggered magnetism of (π, π) character, which in turn induces orthorhombic distortion via magnetoelastic coupling. This *spin-nematic scenario* is the accepted argument for the iron-pnictides. The same is also observed for FeSe under hydrostatic pressure, where the coupling of the distinct structural and magnetic transitions is observed above 1 GPa pressure, with transitions merging into a single phase line of first order above 1.7 GPa similar to the $BaFe_2As_2$. This is taken as support for the argument for spin-nematic mediation in FeSe as well. However, for Te substitution, no magnetic transition emerges, nor does any hint of an extraordinary enhancement in the δ-ψ_{sc} coupling occur. A similar dissociated behavior is observed with the S-substitution [121]. This puts the spin-nematic scenario at odds with the experimental observations made here, suggesting that the spin-nematic scenario may not fully account for the nematic behavior in these materials.

Competition in the orthorhombicity and superconductivity for $x = 0.5$

In Fig. 3.22(a), the thermal expansion of the $x = 0.5$ sample is presented at different strains. For this the room temperature capacitance gap value is changed slightly. A

smaller gap value then means a larger strain on the sample. The sample was mounted with the $L//[110]$ direction. With an increase in the strain, broadening in the superconducting transition is seen. The width of the transition is marked on the color plot as upward and downward triangles. The larger strain enhances the orthorhombicity. The strong competition is evidenced by the desire of $\alpha \to 0$ as the superconducting gap evolves below the T_c.

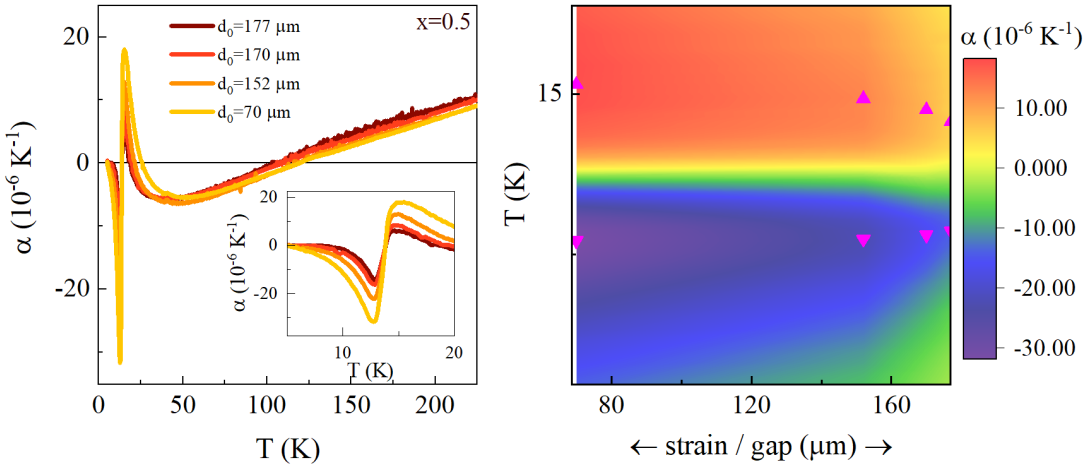

FIGURE 3.22: Competing orthorhombicity and superconducting state in $x = 0.5$: (left) α vs T at different strain, here, larger gap corresponds to smaller strain. The increase in the strain results in the broadening of the transition (color plot in the right panel).

Summary of Sec. 3.4:

We do not find any evidence of magnetism in the orthorhombic distortion. Much like in Fe(Se,S), orthorhombicity and superconductivity couple cooperatively, in the first superconducting dome of Fe(Se,Te). While in the second dome there is no nematic transition, the nematic fluctuations strongly compete with the SC opposite to the first dome where there is a cooperative coupling. The lack of magnetism on Te substitution is at odds with the spin-nematic scenario proposed using the hydrostatic-pressure studies for the FeSe. While counterintuitive, this is similar to the interplay between antiferromagnetism and superconductivity in cuprates and iron pnictides, where static magnetic order is not conducive to superconductivity, but fluctuations mediate superconductivity.

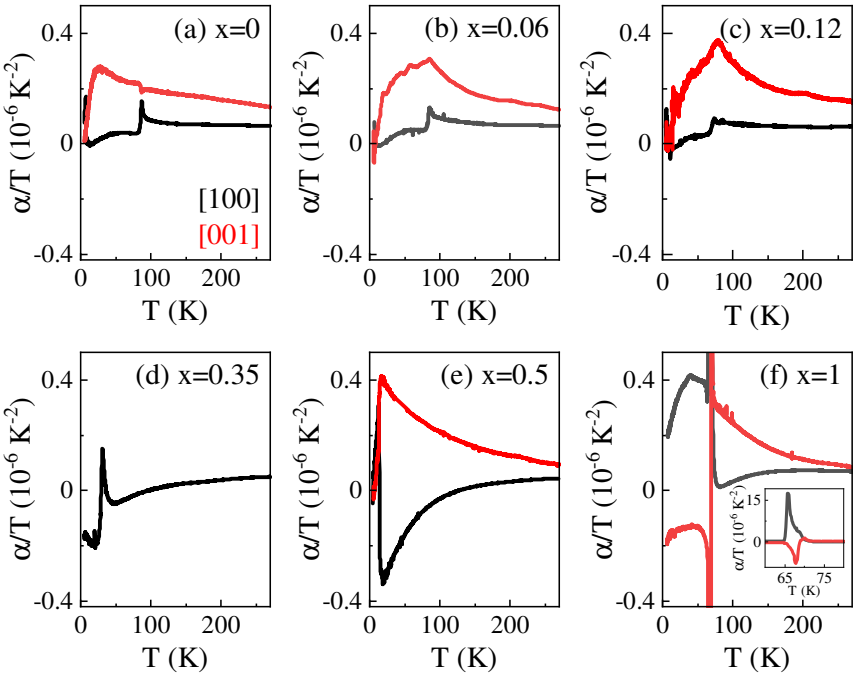

FIGURE 3.23: (a-f) Thermal expansion coefficient for different compositions, along the twinned direction [100] and c-axis, plotted as α/T against T, highlighting the electronic part.

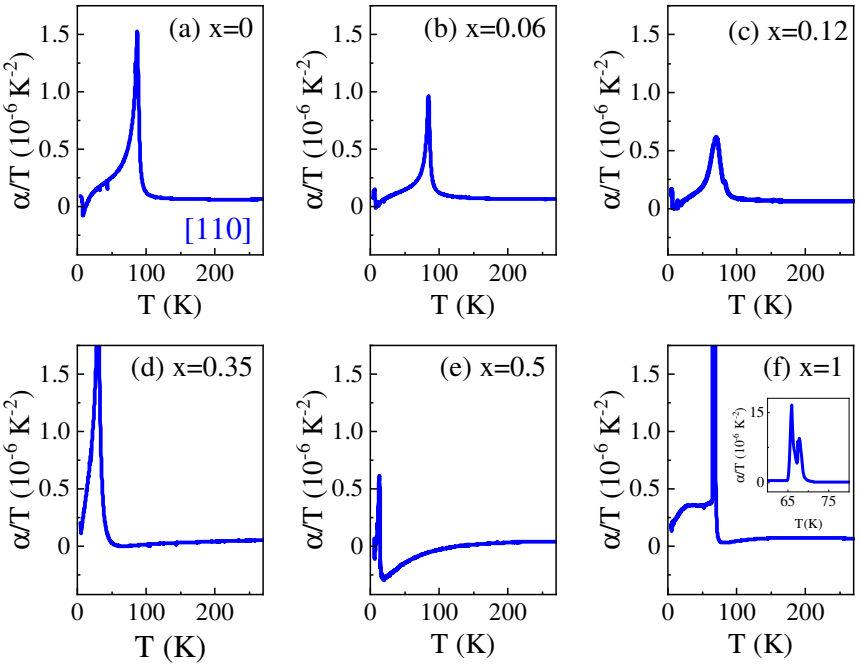

FIGURE 3.24: (a-f) Thermal expansion coefficient for different compositions, along the detwinned [110] direction. Inset for (f) $x = 1$ shows the giant change accompanying antiferromagnetic transition.

3.5 Conclusion

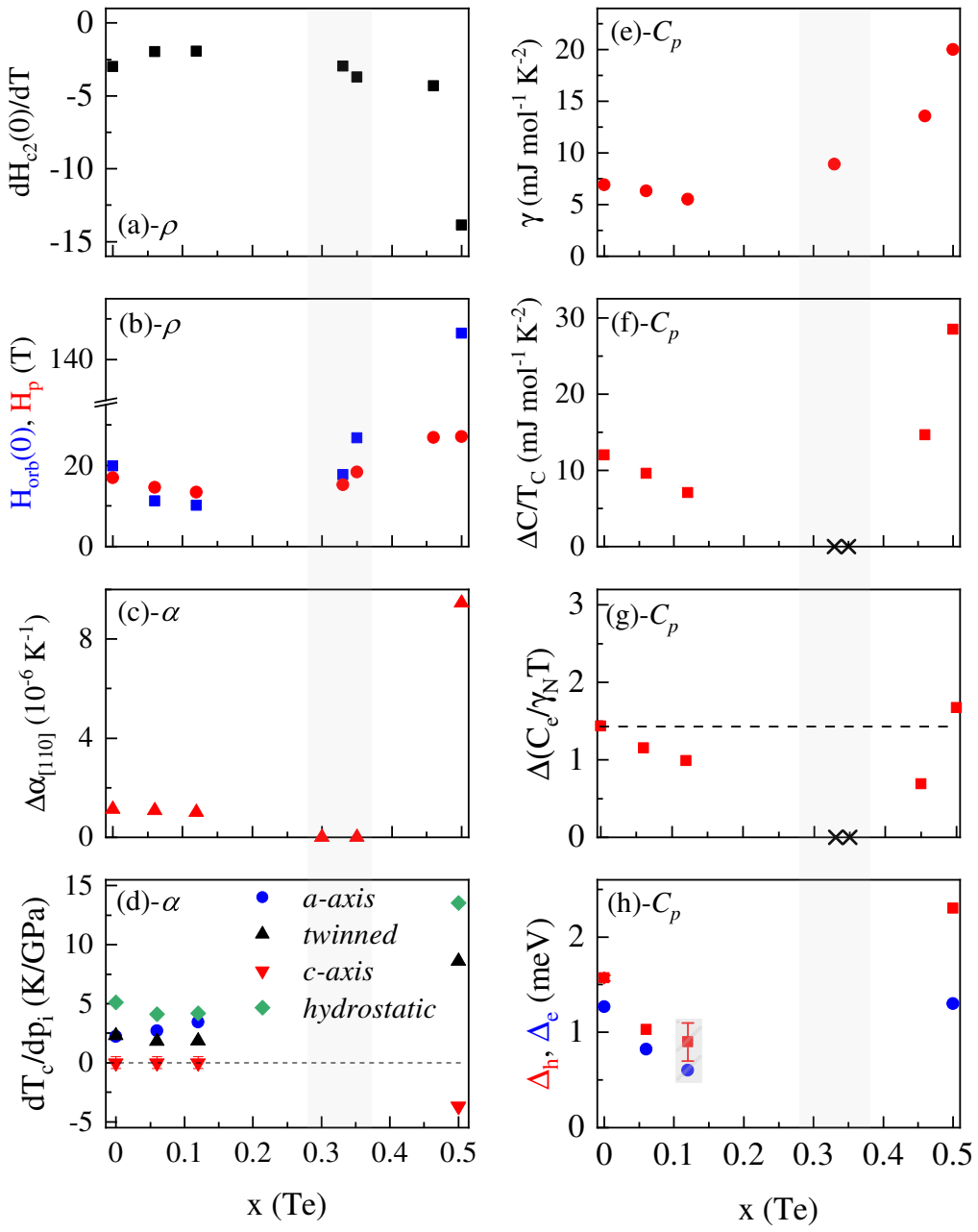

FIGURE 3.25: (a-g) Variation of different physical quantities related to the superconducting transition computed in this study for Fe(Se,Te). (g) For $x = 0.12$, a concrete proportional determination of the $\Delta_{h,e}$ cannot be made as discussed in the text, the same is represented as an overlaid bar. The probe from which the quantity was obtained is written next to the label in each subplot. Two domes in the phase diagram are separated by the gray bar for guide.

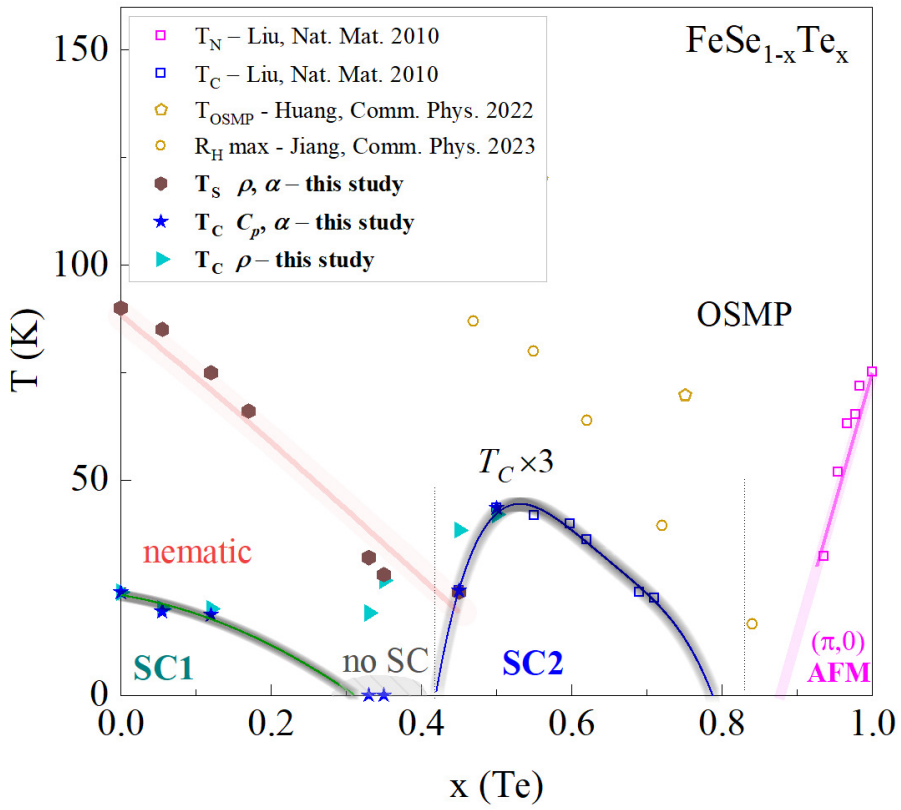

FIGURE 3.26: Phase diagram for Fe(Se,Te) constructed using the bulk C_p and α probes. The T_{OSMP} and the $T(R_H(max))$ are taken from [12] and [101] respectively, while the T_c and T_N in the high Te concentration are from [72]. The T_c values have been multiplied by 3 for clarity.

The variations of different physical quantities related to the superconducting transition computed in this study for Fe(Se,Te) are presented in Fig. 3.25(a-g). The phase diagram drawn using the thermodynamic bulk probes along with the OSMP values of [12] is shown in Fig. 3.26. The results can be summarized as:

- Two distinct domes of superconductivity exist in Fe(Se,Te). The transport phase diagram that sees these two distinct domes only at sufficiently high external B actually exists at 0 T when the bulk superconductivity is measured.
- Significant changes in the physical quantities when compared to the FeSe and low Te substitution values compared to that in the second dome, suggest changes in the superconducting mechanisms.
- In the first SC dome, from the modeling of electronic heat capacity, we detail how the accidental nodes or deep anisotropy weaken with Te substitution, with the possibility of deep minima then developing for $x = 0.12$ similar to the development of the ultra-nodal state in Fe(Se,S).

- In the second SC dome, the heat-capacity behavior is consistent with a larger, mostly isotropic strong-coupling gap, implying a different pairing regime from FeSe.
- From the thermal expansion study, we show that the effects of chalcogen substitution in small amounts on the superconducting state in FeSe are similar to the application of hydrostatic pressure.
- Unlike pnictides, orthorhombicity, and superconductivity do not compete in the first superconducting dome.
- The anisotropic response of the c-axis for $x = 0.5$ is the macroscopic manifestation of the changes in the band topology in Fe(Se,Te), specifically, the modest electronic correlations in the FeSe evolve into a highly correlated state.

Chapter 4

Lattice effects on nematicity and aspects of quantum criticality in Fe(Se,Te)

Nemato-elastic coupling in $Fe_{1+y}Se_{1-x}Te_x$ is investigated by measuring Young's modulus. At the optimal composition $x = 0.5$, the nemato-elastic coupling strength is the largest among all iron-based superconductors. The observed hardening of C_{66} and possible back-bending features are discussed in relation with the presence of nematic instability and diverging nematic correlation length. An alternative scenario where these effects can arise from the antiferromagnetic fluctuations is also presented. Finally, the question of pure nematic quantum criticality is explored using the Grüneisen parameter. We observe a logarithmic divergence here as opposed to $1/T$ expected for the Ising nematic QCP. Whether the highly electronic thermal expansion can also stem from the orbital selectivity is also discussed.

4.1 Background

A phase transition such as ice $\longleftrightarrow$ water is driven by thermal motion of the interacting molecules. A phase transition driven by quantum fluctuations associated with Heisenberg's uncertainty principle is called a *quantum phase transition*. The best known example of a quantum phase transition is observed in solid helium, which is so delicate that it requires pressure to maintain its crystal lattice even at absolute zero. When the pressure is removed, quantum fluctuations cause the crystal to melt. The search and understanding of quantum phase transitions has been a constant theme in condensed matter physics in the last three decades. While most quantum phase transitions involve magnetism in metals, another *type* of quantum phase transition occurs in the correlated electronic systems in which the rotational symmetry is spontaneously broken - nematic quantum phase transition. The nematic quantum criticality was introduced in Chapter 1 and is one of the main motivations for the study of Fe(Se,Te) [15, 94]. The enhancement of T_c at the nematic end point in the Fe(Se,Te) would be the first case of the nonmagnetic QCP of electronic nematic order that is conducive to the superconductivity. The phase diagram made using the m_{66} coefficient for (S/Te)-substituted FeSe is shown in Fig. 4.1. The enhancement of T_c coincides with an increase in the m_{66} coefficient which also shows a stronger temperature dependence compared to the B_{1g} nematic susceptibility, implying an Ising nematic quantum criticality. Here, we examine these by directly probing the

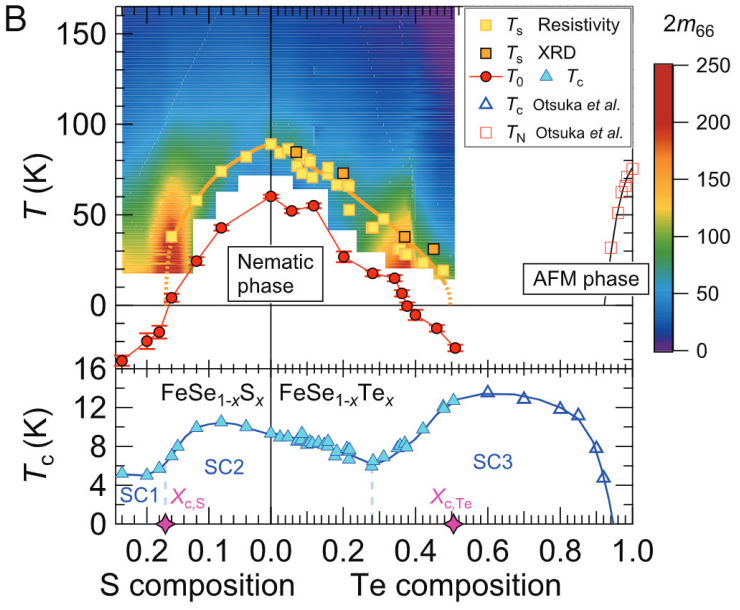

FIGURE 4.1: Taken from [15] under the CC BY-NC-ND 4.0. Fe(Se,S,Te) phase diagram made using the m_{66} coefficient derived from elasto-resistance study.

Young's modulus which is proportional to the C_{66} for iron-based superconductors (see succeeding Sec. 4.2 and [6, 10, 124]) and the Grüneisen parameter [125].

4.2 Elastic constants relevant to iron-based superconductors

Elastic constants are fundamental parameters that describe how a material deforms under applied stress. Within elastic limits, Hooke's Law relates stress (σ) and strain (ε) tensors:

$$\sigma_i = C_{ij}\varepsilon_j \tag{4.1}$$

where σ_i are stress tensor components, ε_j are strain tensor components, C_{ij} are the components of the stiffness tensor in the Voigt notation [1]. In many strongly correlated materials, the coupling between the lattice (atomic arrangement) and the electronic states is often significant. Elastic constants help quantify this coupling by describing how lattice deformations affect electronic properties. For example, in piezoelectric materials, mechanical strain can induce electric polarisation and vice versa. Elastic constants are also directly related to phonon spectra. Below, using free energy arguments, we show the relevant elastic coefficients for the iron-based superconductors, which undergo a tetragonal to orthorhombic transition and have a layered structure. The elastic free energy for a tetragonal symmetry (common to FeBS) is given by [126]:

$$\begin{aligned} F_{elastic} =& \frac{C_{11}}{2}(\epsilon_{xx}^2 + \epsilon_{yy}^2) + C_{12}\epsilon_{xx}\epsilon_{yy} + \frac{C_{33}}{2}\epsilon_{zz}^2 \dots \\ & \dots + C_{13}\epsilon_{zz}(\epsilon_{xx} + \epsilon_{yy}) + 2C_{66}\epsilon_{xy}^2 + 2C_{44}(\epsilon_{zx}^2 + \epsilon_{yz}^2) \end{aligned} \tag{4.2}$$

In terms of the symmetric and antisymmetric strain components, $2\epsilon_A = \epsilon_{xx} + \epsilon_{yy}$ and $2\epsilon_B = \epsilon_{xx} - \epsilon_{yy}$ respectively, the $F_{elastic}$ is written as:

$$F_{elastic} = (C_{11} + C_{12})\epsilon_A^2 + (C_{11} - C_{12})\epsilon_B^2 + 2C_{66}\epsilon_{xy}^2 + \dots \tag{4.3}$$

As stated in Eq. (3.7) the electronic nematic free energy F_{nem} can be expressed in terms of the nematic order parameter ϕ is: $F_{nem} = \frac{a}{2}\phi^2 + \frac{b}{4}\phi^4$, where ϕ is the electronic nematic order parameter. The coupling energy between different components of the strain tensor (ϵ_{ij}) and the nematic order ϕ is dictated by the symmetry considerations in the following way:

- Linear coupling with the shear strain: $-(2\lambda)\phi\epsilon_{xy}$
  In the rotated system, one gets equivalently linear coupling with the orthorhombic strain: $-\bar{\lambda}_1\phi\epsilon_B$

[1] Voigt Notation: $\epsilon_1 = \epsilon_{xx}, \epsilon_2 = \epsilon_{yy}, \epsilon_3 = \epsilon_{zz}, \epsilon_4 = 2\epsilon_{yz}, \epsilon_5 = 2\epsilon_{xz}, \epsilon_6 = 2\epsilon_{xy}$. $\epsilon_{1,2,3}$ represent the normal strain along x, y, z and $\epsilon_{4,5,6}$ represent the shear strain in the yz, xz, xy planes, respectively

- Quadratic coupling with the out-of-plane shear strain: $-\bar{\lambda}_2\phi^2(\epsilon_{xz}^2+\epsilon_{yz}^2)$
- Quadratic coupling with the in-plane strain: $-\bar{\lambda}_3\phi^2(\epsilon_{xx}+\epsilon_{yy})$.
  The in-plane strain here represents a uniform (isotropic) expansion or contraction of the lattice in the xy-plane and is invariant under 90° rotation, consequently a linear coupling term would not be invariant.
- For the out-of-plane strain ϵ_{zz}, a linear coupling to ϕ is forbidden by symmetry, while quadratic coupling terms are allowed. Their effect on the elastic response associated with C_{33} is expected to be small in layered iron-based superconductors.
- Similarly, cross-term $\epsilon_{zz}(\epsilon_{xx}+\epsilon_{yy})$, associated with C_{13}, is allowed. Its coupling to nematic order is allowed only at even order in ϕ and is negligible.

The total free energy is then given by:

$$F = F_{elastic} + F_{nem} + F_{coupling}$$

$$\begin{aligned} F = {} & \frac{C_{11}}{2}\left(\epsilon_{xx}^2+\epsilon_{yy}^2\right) + C_{12}\epsilon_{xx}\epsilon_{yy} + \frac{C_{33}}{2}\epsilon_{zz}^2 + C_{13}\epsilon_{zz}\left(\epsilon_{xx}+\epsilon_{yy}\right) \\ & + 2C_{66}\epsilon_{xy}^2 - 2\lambda\phi\epsilon_{xy} + 2C_{44}\left(\epsilon_{xz}^2+\epsilon_{yz}^2\right) - \bar{\lambda}_2\phi^2\left(\epsilon_{xz}^2+\epsilon_{yz}^2\right) \\ & - \bar{\lambda}_3\phi^2\left(\epsilon_{xx}+\epsilon_{yy}\right) + \frac{a}{2}\phi^2 + \frac{b}{4}\phi^4. \end{aligned} \tag{4.4}$$

Since, quadratic coupling effects are much smaller, from the free-energy point, one can expect the most significant effect in the symmetry-matched shear channel. In the present convention this corresponds to C_{66}, while in the rotated convention it is equivalently expressed through $(C_{11}-C_{12})/2$. For iron-based superconductors, experiments are commonly discussed in terms of the softening of C_{66} [127, 128]. The term *softening* refers to a reduction in the elastic constant, meaning that the material becomes more susceptible to deformation in response to strain. The elastic coefficients are given by the (see Eq. (4.1)):

$$C = \frac{d^2F}{d\epsilon^2} = \frac{\partial^2F}{\partial\epsilon^2} - \left(\frac{\partial^2F}{\partial\epsilon\partial\phi}\right)^2\left(\frac{\partial^2F}{\partial\phi^2}\right)^{-1} \tag{4.5}$$

The complete derivation of the above equation, along with the effect of the strain-nematic coupling on C_{66} and the temperature dependence, is given in App. B. The final result for the C_{66} is given below:

$$\bar{C}_{66}/C_{66} = \frac{T-T_S^{CW}}{T-T_S^b} \qquad \text{where } T_S^{CW} = \lambda^2\chi_0/C_{66} + T_S^b \tag{4.6}$$

where T_S^b is the bare nematic transition, i.e., $1/\chi_N \to 0$ as T_S is approached. Due to the finite coupling (λ) of strain (ϵ) and the nematic transition ϕ, the nematic transition occurs

at T_S^{CW} instead of T_S^b. To measure the C_{ij}, few direct methods exist namely, resonant ultrasound spectroscopy, Brillouin scattering spectroscopy. For iron-based superconductors, the $Y_{[110]} \propto C_{66}$ as the other elastic constant is too large and has weak temperature dependence [10, 124, 127]. The $Y_{[110]}$ can be reliably obtained for iron-based superconductors by using the 3-point bending measurement [6, 10, 75, 129]. These measurements are inspired by bending measurements performed in the domain of structural engineering and applied mechanics, where the behavior of a thin object under an external force perpendicular to the long axis of the object is studied and referred to as *bending (or flexure)*. The Young's modulus along [110] is proportional to the stiffness of the sample in the three-point bending, $k_s(T) = F(T)/(d^0(T) - d^1(T))$, where $F(T)$ is the force acting on the sample and $d^0(T)$, $d^1(T)$ are the capacitor gap changes in zero-force state and in the 3-point bending configuration.

4.3 Results:

4.3.1 Nemato-elastic coupling

To obtain Young's modulus, 3-point bending measurements were performed in a capacitive dilatometer [6, 10]. For iron-based superconductors and many compounds, it has been shown that the shear modulus $C_{66} \propto Y_{[110]}$ and can be reliably extracted from these measurements [129]. The ΔL of the 3-point bending along [110] for $x = 0.06$ and $x = 0.5$ is shown in Fig. 4.2 (a,b), respectively.

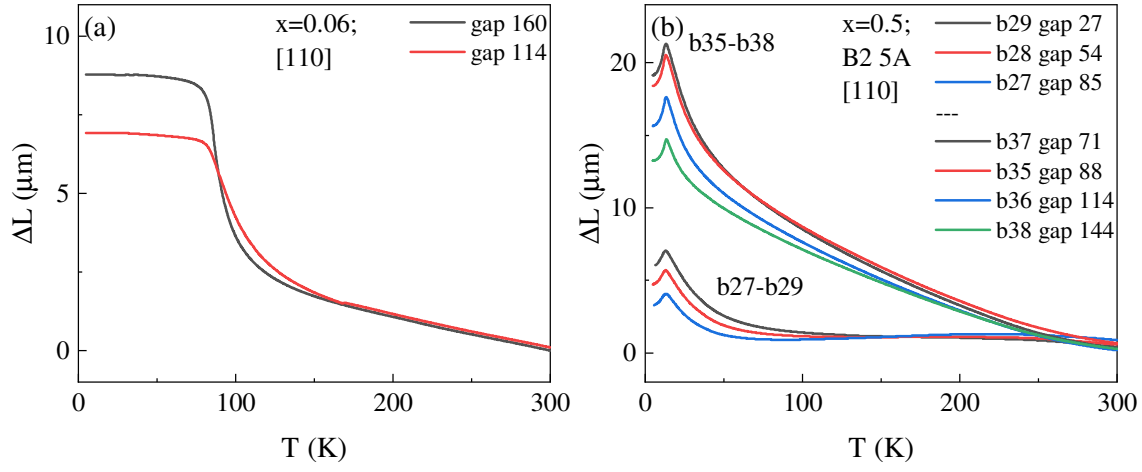

FIGURE 4.2: Raw data for the [110] direction for (a)$x = 0.06$ and (b) 0.5 obtained from 3-point bending. In (b) legend indicates the dataset label (b27-b29) forms one set and (b35-b38) second set at different gaps (strains).

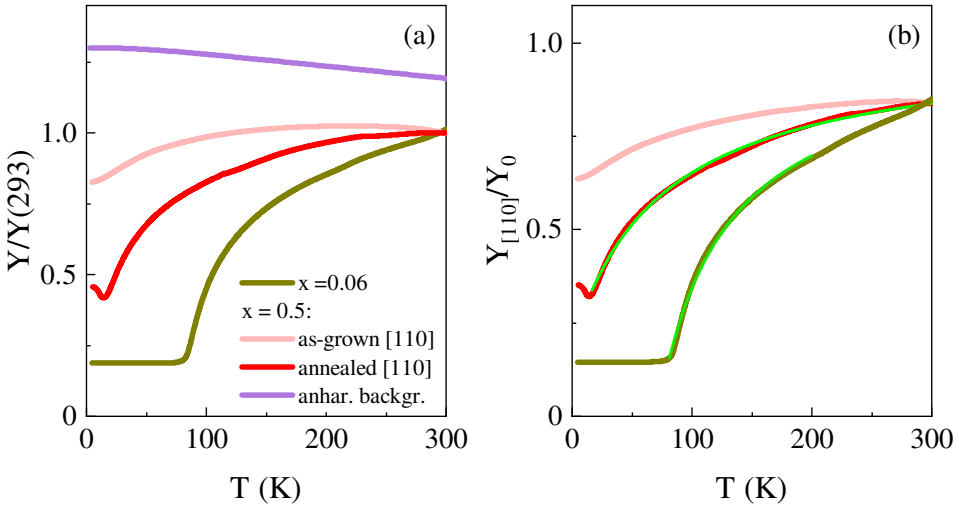

FIGURE 4.3: (a) Young's modulus normalized by its room temperature value for $x = 0.06$, and $x = 0.5$ (as-grown and annealed), (b) shows the $Y_{[110]}$ normalized by the non-critical contribution, the dotted line represents the Curie-Weiss fit.

The ΔL shows a sharp jump at the structural transition beyond which a minimal change is observed, much like the Co-doped $BaFe_2As_2$. For $x = 0.5$ a sharp change in ΔL is recorded at the superconducting transition. The Young modulus along [110] and [100] normalized by the room temperature value (Y/Y_{RT}) is calculated from these data and is shown in Fig. 4.3(a). The $x = 0.06$, much like FeSe, shows softening as the nematic transition is approached. As orthorhombicity sets in, Y has a near-temperature independent behavior. However, the superconducting transition is not resolvable in this case, which can be accounted using the Ehrenfest relation [129]:

$$\begin{aligned} dT_c/dp_i = \Delta(1/Y_i)/\Delta\alpha_i = V_m\Delta\alpha_i/(\Delta C_p/T_c); \\ \implies \Delta Y_i/Y_i \approx -Y_i\Delta(1/Y_i) = -Y_i(\Delta\alpha_i)(dT_c/dp_i) \end{aligned} \tag{4.7}$$

In FeSe, ΔY is shown to soften by a minuscule value of 8.5×10^{-6} [75]. Since both dT_c/dp_i and $\Delta\alpha_i$ decrease upon Te substitution (see Figs. 3.25(c, d)), $\Delta Y|_{T=T_c}$ decreases further. Thermodynamically, this is the same result as in thermal expansion - *for low Te substitutions, much like FeSe, the orthorhombicity and superconductivity continue to coexist without competition.* This is in contrast to the iron pnictides where an anomalous hardening $\sim 4 \times 10^{-3}$ below T_c occurs [124, 130].

For $x = 0.5$, both the annealed and unannealed samples were measured to understand the effects of the bulk superconductivity on the nematic fluctuation. The Y for the unannealed sample (shown in light red in Fig. 4.3) shows a weak temperature dependence, and no superconductivity is seen. In the heat capacity measurements, shown in Fig. 3.6(b), there

is also no T_c. On annealing, the bulk superconductivity is accompanied by lattice softening in the normal state, implying that *the bulk superconductivity and nematic fluctuations are intertwined in this compound*. The extracted $Y_{[110]}/Y_0 \propto C_{66}/C_{66,0}$ is shown in Fig. 4.3(b). The phonon background used here is the same as in FeSe [75, 129]. The thin solid green lines show the Curie-Weiss fit from Eq. (4.6). The unannealed sample is also plotted for completeness. A large softening similar to the $Ba(Fe,Co)_2As_2$ can be seen. The $T_S^{CW} - T_S^b = \lambda^2/AC_{66,0}$, where $A = 1/\chi_0$, which gives the energy scale characterizing the nemato-elastic coupling as determined by the Curie-Weiss fit and is 56 K for $x = 0.06$ and 61 K for $x = 0.5$. For FeSe, it is ~ 40 K from [75]. These values are highest among the reported iron-based superconductors [75, 129]. For the quantum critical Co-doped $BaFe_2As_2$, the value is 35 K [6]. The softening in the [100] direction is rather benign, indicating that the critical behavior is restricted or enhanced along the [110] direction [131].

This giant lattice softening has been postulated to shift the quantum critical point (or nematic end point) in the composition space [132]. This can be inferred by comparing the bare nematic transition, T_S^b with the T_S^{CW}. The two temperatures are plotted in Fig. 4.4. The x_0 denotes the effect of the nemato-elastic coupling on the composition space. It implies that in the absence of nemato-elastic coupling the nematic phase would have been limited to $x \sim 0.2$. This is intricately related to the nemato-elastic energy scale $\lambda^2/AC_{66,0}$, shown along the $y-$axis. The strength of nemato-elastic coupling on an energy scale is given by $r = (\lambda^2/AC_{66,0})/T_F$, where T_F is the Fermi temperature [15]. The Fermi energy for the Fe(Se,Te) is $4 - 20$ meV and varies over the composition space and the momentum space. Within the paradigm of [132], the large r implies that the enhancement of the T_c is not related to the nematic quantum fluctuations. An enhancement is postulated only when the nematic pairing interaction is either sufficiently large or the magnetic pairing interactions are sufficiently small. Moreover, such an enhancement may also occur if the spin fluctuations are enhanced in the second superconducting dome. Indeed for the optimally doped superconducting samples, a spin fluctuation spectrum dominated by two-dimensional spin excitations extending to energies greater than 250 meV has been observed [72]. Earlier, while discussing the $c - axis$ response evolution we have also postulated the possibility of spin-susceptibility enhancement.

A sharp hardening ($d(Y/Y_{293})/dT = 0.2\,\mathrm{K}^{-1}$) can be clearly seen at the T_c for $x = 0.5$, similar to the Co-doped $BaFe_2As_2$, beyond the nematic composition. If the system is in the vicinity of a nematic instability and the nematic correlation length is sufficiently large, the exact expression describing the variation of the shear moduli below the superconducting

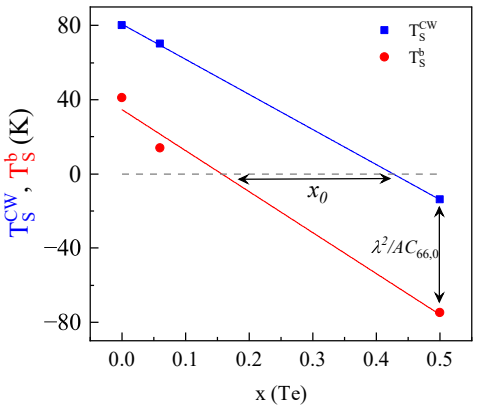

FIGURE 4.4: Effect of nemato-elastic coupling: T_S^{CW} and T_S^b calculated using the 3-point bending measurements. x_0 denotes the effect of the nemato elastic coupling on the control parameter (composition) tuning the nematic transition, $\lambda^2/AC_{66,0}$ is the characteristic energy scale of the nemato-elastic coupling. (FeSe data is from [75])

transition has been derived by Labat et al. in [133] and is given by:

$$\begin{aligned} c_s(T)/c_0 &= 1 - a_0 P(T)/[1 - b_0 P(T)] \\ \text{and,} \qquad P(T \leq T_c) &= \frac{1}{(\frac{T}{T_c}\frac{T_c}{\lambda} + \frac{T_1}{\lambda})} - t_2(1 - \frac{T}{T_c}) \end{aligned} \tag{4.8}$$

where $a_0 \equiv \alpha^2 N_F/c_0$ and $b_0 \equiv gN_F$ are constants, and $P(T)$ is the dimensionless bare nematic polarization. In the superconducting phase the bare polarization has an additional term proportional to $\lambda_0\Delta(T)^2$. The λ_0 is the coupling of the shear strain to the superconducting transition. The large change and the hardening of $c_s = C_{66}$ can be obtained if the system is near a nematic instability and if the λ_0 is sufficiently large, respectively. If the $\lambda_0 < 0$, then a softening ensues. But the change $\delta C_{66}|T = T_c$ is still large (~ 0.1). This implies that for the $x = 0.5$, the $\lambda_0 > 0$ and the large change in the C_{66} below T_c is the direct result of the system being in the vicinity of the nematic instability, with a strong competition between the nematic instability and the superconducting phase.

Bending of T_s: Within the theoretical formulation by Labat et al. in [133], a back-bending has also been proposed if the system is near nematic instability and $\lambda > 0$. We include the T_s^{CW} estimated from the 3-point bending method for $x = 0.5$ in the phase diagram to check this proposition. The resulting phase diagram shown in Fig. 4.5 indeed hints at such a possibility. The *bending* in the T_s is not as strong as in the pnictides [133], nevertheless the T_s^{CW} shows a back-bending. Note that the T_s^{CW} is slightly lower than the actual T_s on account of the finite stiffness [10] in the orthorhombic phase implying that the effect may be weaker than what is seen here.

Alternatively, it has been theoretically shown that if antiferromagnetic fluctuations are

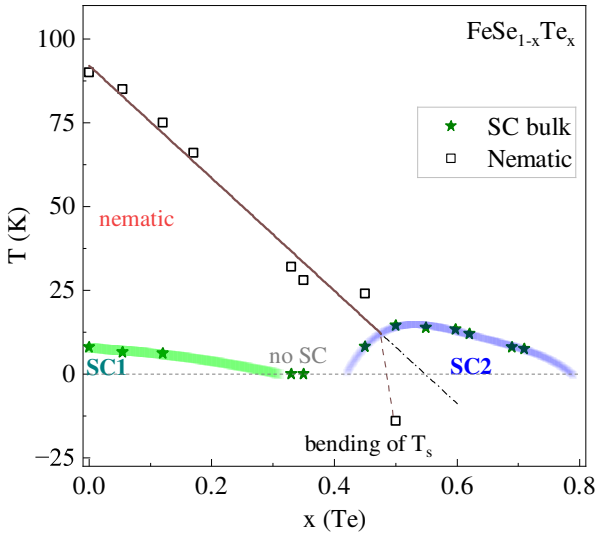

FIGURE 4.5: Back-bending of the T_s near the nematic instability in Fe(Se,Te).

present which can enhance nematic correlation then lattice hardening at T_c can also occur. For the case of iron-pnictides using resonant ultrasound spectroscopy and shear modulus study [10, 124, 130] the hardening in C_{66} is explained in this paradigm. In the iron-pnictides the magnetic fluctuations are clearly present. The magnetic fluctuations of (π, π) character are known to occur for high Te concentration [72, 134]. Thus, the result can be explained either way by assuming the presence of AFM fluctuations enhancing nematic correlation or simply the presence of the nematic instability (which is expected in this scenario!). The *missing data* is the enhancement in the spin-relaxation rate, $1/T_1T$ in the Nuclear Magnetic Resonance measurements. In [135] for $FeSe_{0.42}Te_{0.58}$, there is no such softening, which has been interpreted as the lack or faint presence of magnetic fluctuations. However, the $1/T_1T$ does scale with the local spin susceptibility (indicating magnetic impurities - local Kondo effects) and there is orthorhombic transition at 40 K in an identical sample in neutron data [136]. The diverging behavior in spin-relaxation in NMR has been observed for $FeSe_{0.33}Te_{0.67}$. Hence, NMR measurements around this composition, which can quantify the spin-fluctuation strength, can provide the necessary constraint. Finally, this change in C_{66} behavior at FeSe and low Te substitution against the $x = 0.5$ can be interpreted as compatible with a Lifshitz transition. As argued extensively throughout this study, significant electronic reconstruction occurs as system transitions into the second superconducting dome [120, 137]. Since, Te substitution maintains the charge neutrality in the system, and no *new* structural transitions in the normal state occur, the changes in the superconducting-mechanism should stem from a continuous evolution of the Fermi surface. Finally, the enhancement of T_c cannot be ascribed to the giant nemato-elastic coupling until the presence of magnetic fluctuations is ruled out in the second dome [132], which casts doubt over the existence of the postulated *pure*

nematic critical point.

4.3.2 Nematic quantum criticality or orbital selectivity?

Nematic QCP: It has been shown that near a quantum critical point, the thermal expansion response is more remarkable than the specific heat [138, 139]. The divergent response extends to low temperatures for $x = 0.5$ until it encounters the superconducting transition, indicating that the system may be in the vicinity of the postulated nematic quantum critical point [93, 94]. Ample discussion in the literature has been done on the quantum criticality in the optimally doped Fe(Se,Te), with claims ranging from the pure nematic criticality to the nematic criticality with added magnetic fluctuations enhancing the superconductivity. However, the nature of criticality remains elusive. The critical/ electronic part of the Grüneisen parameter provides a way to *judge* this. The Grüneisen parameter is defined as:

$$\begin{aligned} \Gamma &= -\frac{1}{V_m T}\frac{\partial S/\partial p}{\partial S/\partial T} \\ \Gamma &= \beta/C_p \end{aligned} \tag{4.9}$$

where β is the volumetric thermal expansion coefficient, and C_p is the heat capacity at constant pressure. For a tetragonal system such as optimally doped system ($x = 0.5$) under consideration: $\beta = 2\alpha_a + \alpha_c$. The above is true if the control parameter of the quantum phase transition is *pressure*. In case it is an external magnetic field H, then,

$$\begin{aligned} \Gamma &= -\frac{1}{T}\frac{(\partial S/\partial H)_T}{(\partial S/\partial T)_H} \\ \Gamma &\propto \text{magnetocaloric effect} \end{aligned} \tag{4.10}$$

For a nematic quantum critical point, the uniaxial stress couples directly and linearly to the nematic order parameter, allowing it to influence the free energy landscape effectively (see the detailed coupling explanations in Sec. 4.2). For the uniaxial stress σ, the Landau free-energy expansion of the nematic system is

$$F(\phi, \sigma) = F_0 + \frac{a}{2}\phi^2 + \frac{b}{4}\phi^4 - \sigma\phi, \tag{4.11}$$

where F_0 is the free energy of the symmetric phase, a and b are coefficients (with $b > 0$ for stability). The term $-\sigma\phi$ represents the linear coupling between uniaxial stress and the nematic order parameter. The minimization of the free energy gives

$$\frac{\partial F}{\partial \phi} = a\phi + b\phi^3 - \sigma = 0. \tag{4.12}$$

This equation shows that even when $a > 0$, a sufficiently large σ can induce a non-zero ϕ, effectively driving the system into the nematic phase. In contrast, hydrostatic pressure is isotropic and preserves rotational symmetry, so it does not couple linearly (directly) to the nematic order parameter ϕ_{nem} that breaks the rotational symmetry. It may effect by the coefficient $a = a(P)$, but since a linear coupling is forbidden, it serves as a poor parameter for direct tuning of the nematic phase transition.

Similar to other QCPs, nematic critical fluctuations should lead to diverging correlation lengths and times. Using the arguments as described in [138], close to the nematic QCP, the correlation length ξ shall diverge as $\xi \sim |r|^{-\nu}$, where $r = r(a)$ is the control parameter (distance from criticality), ν is the correlation-length exponent. The corresponding correlation time ξ_τ diverges as: $\xi_\tau \sim \xi^z \sim |r|^{-\nu z}$, where z is the dynamical critical exponent. Following the [138], the critical part of the Grüneisen parameter is then given by:

$$\Gamma_{cr} = -G \cdot T^{-1/\nu z} \tag{4.13}$$

Since for the optimal composition $x = 0.5$, the uniaxial thermal expansion is highly electronic, the critical part of the uniaxial Grüneisen parameter is estimated by $\Gamma_{cr} = \alpha/C_p$, where the specific heat is dominated by a noncritical contribution $C_p = \gamma_N T$. This is shown in Fig. 4.6(a).

For the 2D Ising nematic quantum critical point [140] the critical exponents are $\nu = 0.5 \pm 0.1$ and $z = 2.0 \pm 0.3$. Hence, $\nu z \in [0.68, 1.4]$. The near maxima, minima and the $\nu z = 1$ (Ising-qcp case) are fitted for the optimally doped $x = 0.5$ and shown in Fig. 4.6(b) using Eq. (4.13) plus an additive constant. None of these cases yields a good fit. However, as shown in Fig. 4.6(c) the Γ_{cr} diverges logarithmically. The logarithmic fits $\Gamma_{cr} = -A + B \ln T$ were performed in the diverging part of Γ for different strains and are shown as black lines in Fig. 4.6(b). Phenomenologically, note that a very weak power-law dependence can mimic a logarithmic variation over a temperature interval. Formally, for large νz:

$$\begin{aligned} \Gamma_{cr} &= -G \cdot e^{[\ln T^{-(1/\nu z)}]} = -G \cdot e^{[-(\ln T)/(\nu z)]} \\ \Gamma_{cr} &= -G \cdot \left(1 - \frac{\ln T}{\nu z} + \frac{(\ln T)^2}{(\nu z)^2 \cdot 2!} - \frac{(\ln T)^3}{(\nu z)^3 \cdot 3!} + \dots\right) \end{aligned} \tag{4.14}$$

For νz is sufficiently large, the higher order terms in the expansion $\mathcal{O}(2, 3, \dots) \to 0$: (become small), then,

$$\begin{aligned} \Gamma_{cr} &= -G \left(1 - \left(\frac{1}{\nu z}\right) \ln T + \mathcal{O}(2) + \dots\right) \\ \Gamma_{cr} &= -A + B \ln T \end{aligned} \tag{4.15}$$

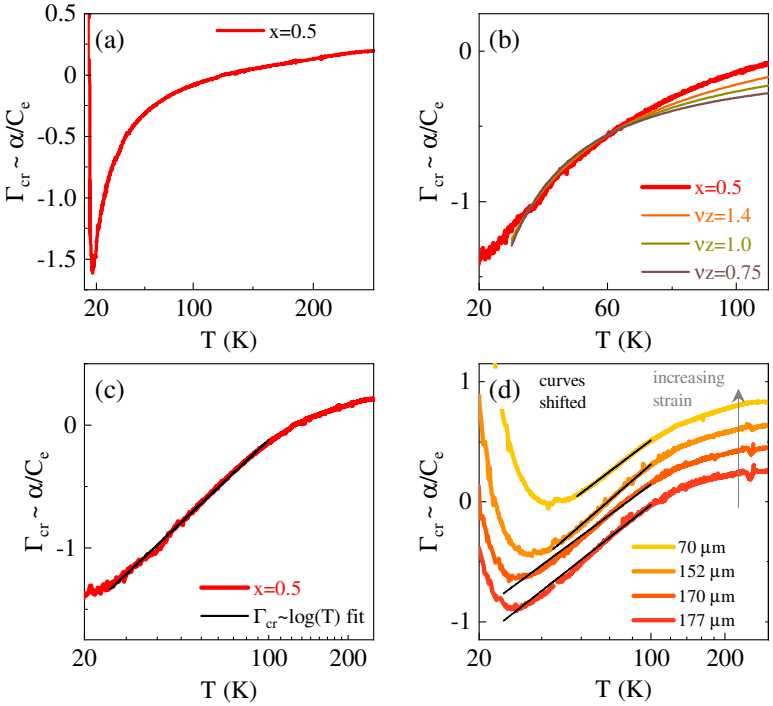

FIGURE 4.6: (a-d) Estimated critical component of the uniaxial Grüneisen parameter and its fit above the T_c using (b) Eq. (4.13) where $\nu z = 0.75$, 1, 1.4 and (c) Eq. (4.15). For (c) the temperature scale is in log(T) to highlight this. (d) Shows the evolution of the uniaxial Grüneisen parameter with strain. The strain is given by the different capacitor gaps, lower value indicates higher strain. On increasing strain the critical region shrinks.

Note that the $A \neq G$ as the higher order terms still contribute finitely, even though small. Physically, the log-divergence implies that either the correlation lengths become very large near the criticality *or* the time scales involved in the critical fluctuations become very long compared to the spatial scales. The interpretation of large correlation lengths will be in line with the nematic instability related earlier to the hardening of C_{66} (see section 4.3.1, [133]).

Orbital Selective Mott Phase:

Alternatively, the logarithmic-like behavior can be explained assuming the electronic contribution to the thermal expansion originates from the coherence of the d_{xy} orbital at low temperature as discussed before. Whether a true nematic-QCP exists or the OSMP is responsible for the logarithmic divergence cannot be conclusively determined using the experiments. However, our results provide a strong constraint for the modeling of the Fe(Se,Te) system. Any complete theoretical model for the iron-chalcogenides should be able to produce the logarithmically diverging Grüneisen parameter at the nematic end point. The $\alpha_{in-plane}/T$ becomes highly electronic in the second putative superconducting dome (x = 0.5) compared to the superconducting dome centered around FeSe [94]. This

enhancement of the electronic behavior at low temperatures below $\sim$ 100 K (T^*) is highlighted when the in-plane thermal expansion $\alpha_{[110]/T}$ of the bulk superconducting and non-superconducting samples are compared (Fig. 4.7(a)). The volumetric thermal expansion β/T diverges below 60 K and becomes completely negative. Note that for the non-superconducting sample, β remains positive for the entire temperature range. This enhanced *electronic response* at low temperatures (T^*) correlates with the d_{xy} orbital becoming coherent around this temperature. Using Hall effect measurements, a sign change in the Hall coefficient in this temperature range has been reported and interpreted as evidence for the existence of an orbital selective Mott phase above the said temperature [12, 92, 101].

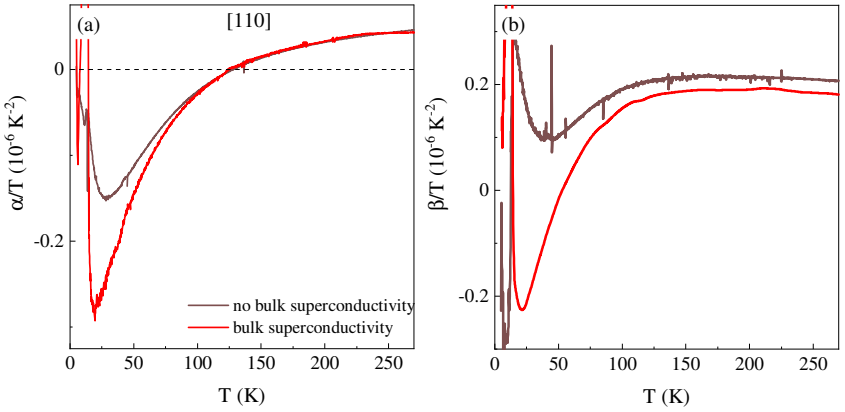

FIGURE 4.7: Comparison of (a) α/T and (b) β/T vs T between non-superconducting and superconducting samples highlighting the strong enhancement of the electronic behavior in bulk superconducting samples for the optimally doped composition $x = 0.5$.

4.4 Conclusion

- The nemato-elastic coupling strength for Fe(Se,Te) is the largest among the reported iron-based superconductors, and the nematic end point is accompanied by an enhancement of T_c in the second dome.
- The hardening of C_{66} for $x = 0.5$ in the second superconducting dome is likely related to the competition between the nematic instability and superconductivity, hinting at large nematic correlation lengths.
- If a nematic quantum critical point exists in Fe(Se,Te), it appears to be highly unconventional. A *log*-divergence is seen in the critical Grüneisen parameter over a limited temperature window.

Chapter 5

Study of the CDW state and quantum oscillations in AV_3Sb_5

The CDW state and superconductivity in AV_3Sb_5 compounds are investigated using a combination of thermodynamic and transport probes. Using the heat capacity data and the McMillan formula, we estimated that the values of the electron-phonon coupling in these systems are moderate to weak. The CDW transition in RbV_3Sb_5 is a weak first-order transition with highly anisotropic pressure dependence, which is five times larger along the c-axis. Measurements in magnetic field show quantum oscillations in magnetization, transport and magnetostriction. Quantum oscillation frequencies in between 250-1000 T can be related to the proposed SD/ISD and SD+ISD reconstruction in $(Rb, K)V_3Sb_5$ and CsV_3Sb_5 respectively. Finally, the strain response of the small elliptical orbits in Rb- is calculated using the magnetostriction and magnetization data.

5.1 Background and motivation

The details of the kagome lattice and the AV_3Sb_5 system were introduced in Ch. 1. We continue from there and discuss the reconstruction of the Fermi surface below the CDW and its signatures in the quantum oscillations. The AV_3Sb_5 group of compounds displays a rich spectrum of quantum oscillations [50–63], which is readily divided into three parts: (a) low-frequency spectra ($< 250\,\mathrm{T}$), (b) mid-frequency spectra ($250 - 1000\,\mathrm{T}$), and (c) high-frequency spectra ($> 1000\,\mathrm{T}$). Below we discuss these frequency windows in detail.

Low-frequency spectra ($< 250\,\mathrm{T}$) - Small elliptical V-orbits: Up to four low-frequency orbits are known to occur in AV_3Sb_5. Most of them have been predicted to be topologically non-trivial using the Landau level index plots [55]. Recent quantum-oscillations measurements using focused ion beam to create micron-sized samples have shown that these low frequency orbits are three-dimensional in nature [141]. These small orbits are introduced as a direct result of the band reconstruction at CDW transition. The 2D cylindrical orbital (originating from V d-band) [50, 141] breaks into a large cylindrical orbit and several small elliptical induced V d-orbits (see Fig. 5.1(A,B)). These three-dimensional ellipsoidal pockets are also observed in the ARPES measurements (see Fig. 5.1(C)) [142]. Apart from this, the quantum oscillation studies and ARPES measurements on the bulk crystals also confirm the quasi-2D nature of the larger vanadium bands (see the blue reconstructed orbit in Fig. 5.1(A) and [50, 142].

Mid-Frequency Spectra ($250-1000\,\mathrm{T}$) - Signature CDW Orbits: The mid-frequency range (250–1000 T) of quantum oscillation spectra in the kagome superconductor family AV_3Sb_5 (A = K, Rb, Cs) provides information about the electronic structure reconstruction associated with the CDW state. Density functional theory (DFT) calculations indicate that CDW-induced structural distortions significantly alter the electronic bands derived from vanadium d orbitals [50, 143]. In the pristine kagome structure, these orbitals form triangular orbits at the K points of the Brillouin zone, yielding a single frequency around 600 T (DFT calculations using the pristine structure are also presented later in the results).

The TrH/ISD and SoD/SD distortions in the kagome lattice were introduced in Sec. 1.1.2. Upon transitioning into the CDW phase, two distinct distortion types, the Star-of-David (SD) and inverse Star-of-David (ISD), can emerge. Both fragment the original large V-derived orbit at the $k_z = 0$ plane into multiple smaller pockets and create additional triangular orbits at the K points (see Sec. 1.1.2 and Fig. 5.2). Consequently, theoretical analyses predict the presence of at least two prominent quantum oscillation frequencies within the mid-frequency region (approximately 250–1000 T), if only SD or ISD distortion is present. However, the presence of SD+ISD can yield six to seven frequencies in this

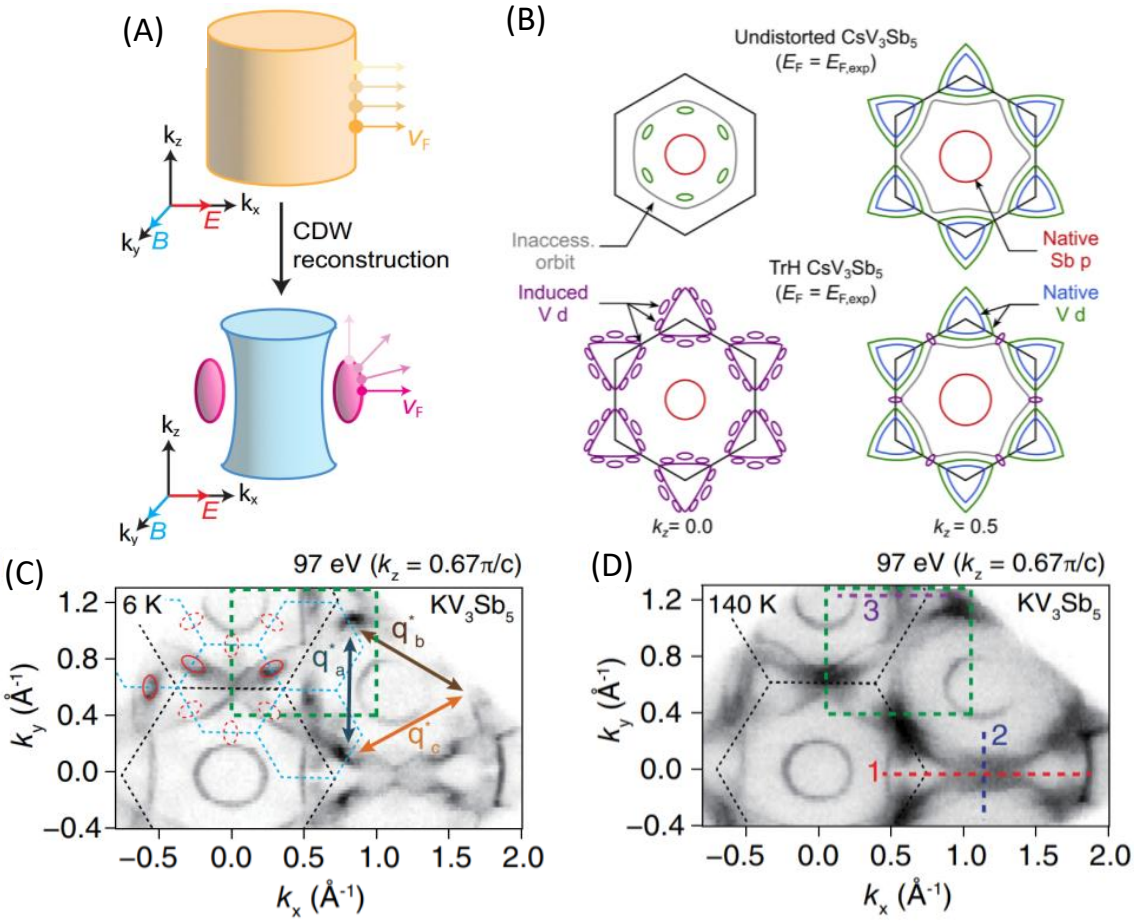

FIGURE 5.1: Taken from [141] (arXiv version)-(A), [50]-(B), and [142]-(C,D) under the CC BY 4.0 license. Band reconstruction at the CDW transition and the induced small 3D V orbitals in AV_3Sb_5: (A, B) Show the schematic of how small 3D V orbits are induced at the CDW transition in CsV_3Sb_5. (C,D) Show the reconstruction in KV_3Sb_5 from ARPES - the blue dashed hexagons represent the Brillouin zone in CDW phase. The reconstructed elliptical Fermi pockets are shown as red ellipses in (C).

region [143]. Therefore, how the CDW-induced structural changes reshape the Fermi surface can be studied by analyzing the quantum oscillation spectrum in this frequency range.

At low temperatures, CDW-induced distortions vary distinctly among the AV_3Sb_5 compounds. KV_3Sb_5 and RbV_3Sb_5 primarily display a staggered Tri-Hexagonal (TrH) distortion pattern (Fig. 5.2(b,c)), whereas CsV_3Sb_5 exhibits a more complex modulation of TrH and Star-of-David (SoD) layers (Fig. 5.2(d-g)). Consequently, in Cs-, more than two quantum oscillation frequencies should be observed if a SD+ISD structure does exist in the compound, whereas, only two should be observed in the case of Rb- and K- where only ISD/TrH exists [144]. For the KV_3Sb_5, the XRD data can also be closely fitted using the staggered SD structure; the staggered ISD yields a slightly better fit (R_1(SD)=6.31 vs R_1(ISD)=6.22, where R_1 is the measure of the disagreement between the crystallographic

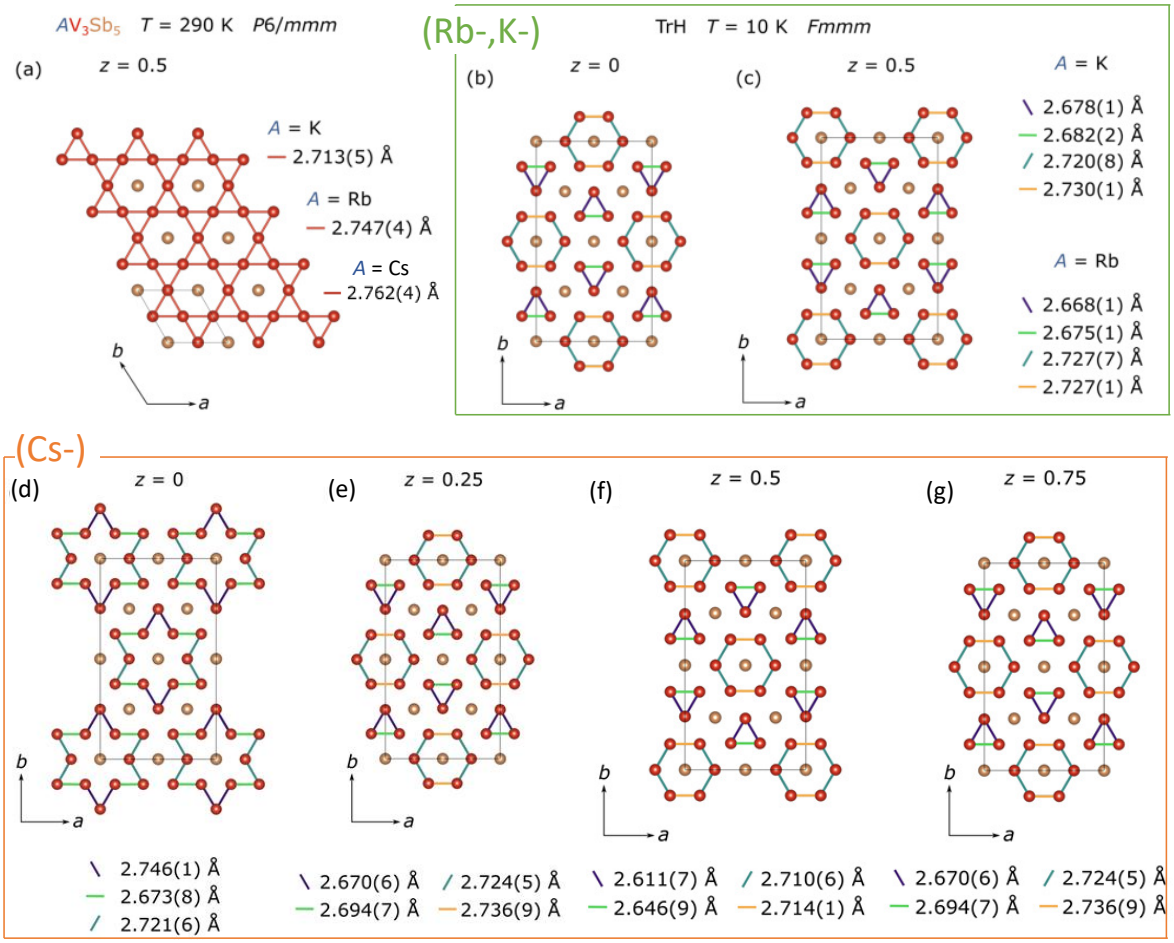

FIGURE 5.2: Taken from [25](arXiv version) under CC BY 4.0. Structural models for AV_3Sb_5 as obtained from synchrotron-XRD. (a) Shows the z=0.5 layer comprised of V and Sb atoms at the room temperature structure of AV_3Sb_5 in the P6/mmm group. (b,c) Shows the TrH model for the 2×2×2 superstructure in the orthogonal space group Fmmm obtained for RbV_3Sb_5. (d-g) Shows the TrH+SD model for the 2x2x4 superstructure for the CsV_3Sb_5.

model and the experimental X-ray diffraction data, implies that lower value is better) [25]. In the CsV_3Sb_5, different kinds of CDW structures have been reported, namely staggered ISD, and SD+ISD. Appearance of only staggered ISD is related to the quality of the samples and the thermal history [145, 146]. In the SD+ISD, 1 ISD layer is followed by 3 SD layers (see Fig. 5.2(d-g)) [50]. A compilation of these terminologies and expectation/observations are given in Table 5.1, along with the number of frequencies expected in the quantum oscillations spectra in the 250-1000 T range. *Therefore, understanding the quantum oscillation spectra in this range can provide direct information about the CDW ordering in AV_3Sb_5 materials.* An alternative has also been presented in [54], where this mid-band in CsV_3Sb_5 is ascribed to magnetic breakdown (see Sec. A for details about magnetic breakdown) between the triangular V orbit and smaller reconstructed V d-orbitals discussed above (80 T).

CDW Structure	interlayer modulation	Compounds (A) in which configuration is observed [25, 145, 146]	Number of QO frequencies in 250-1000 T (DFT [50, 143])
SD	None - 2×2×1	None	2
Staggered SD	2×2×2	K- [25]	2
ISD	None - 2×2×1	None	2
Staggered ISD	2×2×2	Rb-,K-,Cs-	2
SD+ISD	2×2×4 (1 ISD) + (3 SD)	Cs-	6

TABLE 5.1: Summary of possible CDW structures in AV_3Sb_5, with associated interlayer modulations, observed compounds, and the number of quantum oscillation (QO) frequencies (250–1000 T) predicted by DFT.

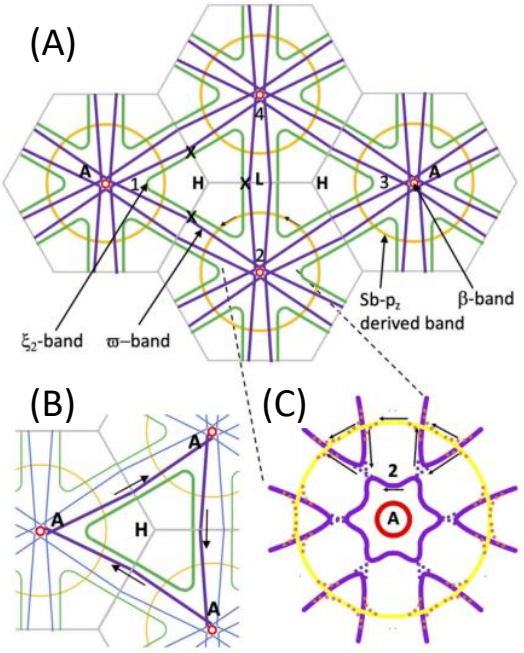

FIGURE 5.3: Taken from [55](arXiv version) under CC BY 4.0. (A, B) Shows the schematic of the band reconstruction at the CDW transition in CsV_3Sb_5 and the folded Fermi surface across multiple Brillouin zones. The two large triangular FS sheets are marked as ξ_2 and $\bar{\omega}$. (C) Shows the likely points of magnetic breakdown from the interaction of the triangular Fermi sheet with the reconstructed hyperbolic hexagonal orbit (purple) at the Γ point.

High Frequency Spectra (>1000 T) - Magnetic Breakdown: Frequencies higher than 1000 T originate from the reconstructed large triangular FS sheets marked by $\bar{\omega}$, $F_{\bar{\omega}} \approx 1900$ T in Fig. 5.3 and the magnetic breakdown between $\bar{\omega}$ and ξ_2-band. Magnetic breakdown arises when two extremal orbits on different sheets of the Fermi surface are

close enough that carriers can tunnel from one to another. Here, the tunneling event occurs at the X points where the two orbits are closest in the $k-$space. Using this, the large number of frequencies observed in high-field measurements have been reconciled as either the harmonics of this frequency or as the breakdown between $\bar{\omega}$ and other orbits.

Quantum oscillation measurements of AV_3Sb_5 reveal substantial variations in observed frequencies and cyclotron masses. Tables 5.2, 5.3, and 5.4 list the reported frequencies in K-, Rb-, and Cs-based compounds, along with the experimental techniques used. Although technique-specific sensitivities and intrinsic crystal variations may contribute to these discrepancies, they do not fully account for the wide range of frequencies reported. In many cases, such discrepancies may stem from superficial data analysis or an inclination to report a larger number of frequencies. Two key issues are, (a) one low-frequency branch (50–100 T) consistently appears in Shubnikov–de Haas (SdH) measurements on CsV_3Sb_5 but is notably absent in de Haas–van Alphen (dHvA) data, (b) QO frequencies observed in the *middle band* are inconsistent across different studies and in many cases cannot be reconciled with the previously discussed CDW structures.

To clarify these issues, we investigated the Fermi surface of AV_3Sb_5 using multiple experimental techniques—transport (SdH), magnetization (dHvA), and magnetostriction (dHvA)—on the same samples. Our primary focus is on the *mid-freq. spectra*, previously identified as a signature range for the CDW reconstruction. We compare our findings with density functional theory (DFT)-based Fermi surface reconstructions reported in the literature [143] and with additional room-temperature calculations performed in this study.

S. Y. Yang et al., [60] transport		K. Shrestha et al., [61] torque		Z. Wang et al., [62] transport 80 nm flake	
F (T)	m^*	F (T)	m^*	F (T)	m^*
33	0.125	33	0.032	18	
148		119	0.043	35	
		194	0.056	60	0.71
		285		115	0.74
		454		148	0.67
		2001		237	
		2149		285	
				308	
				385	
				502	
				1000	
				1304	
				1480	
				1601	
				1879	
				2202	

TABLE 5.2: Compilation of frequencies (F in Tesla) and the corresponding effective mass (m^*) from different studies for KV_3Sb_5 along with the measurement method used.

Y. Wang et al., [56] transport		K. Shrestha et al., [57] torque		L. Wang et al., [58] transport		Q. Yin et al., [59] transport	
F (T)	m^*	F (T)	m^*	F (T)	m^*	F (T)	m^*
7.6	0.032			17	0.06		
30.5	0.043	32		34	0.08	33	0.09
122	0.056	155	0.71	121	0.09	117	
		355	0.74	91	0.11		
		438	0.67	178			
		989		322			
		1294		461			
		2620		525			
		2846	0.42	716			
		2941		856			
				1370			
				1461			
				2235			

TABLE 5.3: Compilation of frequencies (F in Tesla) and the corresponding effective mass (m^*) from different studies for RbV_3Sb_5 along with the measurement method.

B.R. Ortiz, et al., [50] transport		Y. Fu, et al., [51] transport		K. Shrestha, et al., [52] torque		D. Chen, et al., [53] thermoelectric	
F (T)	m^*	F (T)	m^*	F (T)	m^*	F (T)	m^*
11	0.06			18	0.160	18	0.039
28	0.08	27	0.127			28	0.043
73	0.09	73	0.142			72	0.058
90	0.11			102	0.346	91	0.054
580				239	0.327		
		727	0.54				
		786	0.55	788	0.302		
860				865	0.312		
1370							
1700				1605	0.240		
1930				2135	0.233		

TABLE 5.4: Compilation of frequencies (F in Tesla) and the corresponding effective mass (m^*) from different studies for CsV_3Sb_5 along with the measurement method.

5.2 Characterization

5.2.1 Experimental results

Figure 5.4(a-c) compares the specific heat (C_p) for the $(Cs, Rb, K)V_3Sb_5$ samples. Fig. 5.4(d-f) shows the entropy plotted as S/T to highlight the CDW transition. The T_{CDW} = 95, 103, and 78 K for Cs-, Rb-, K- respectively. The entropy change across the CDW manifests itself as a step for Cs- and a slope change for K-, implying that the transition is second order for K- as opposed to first order

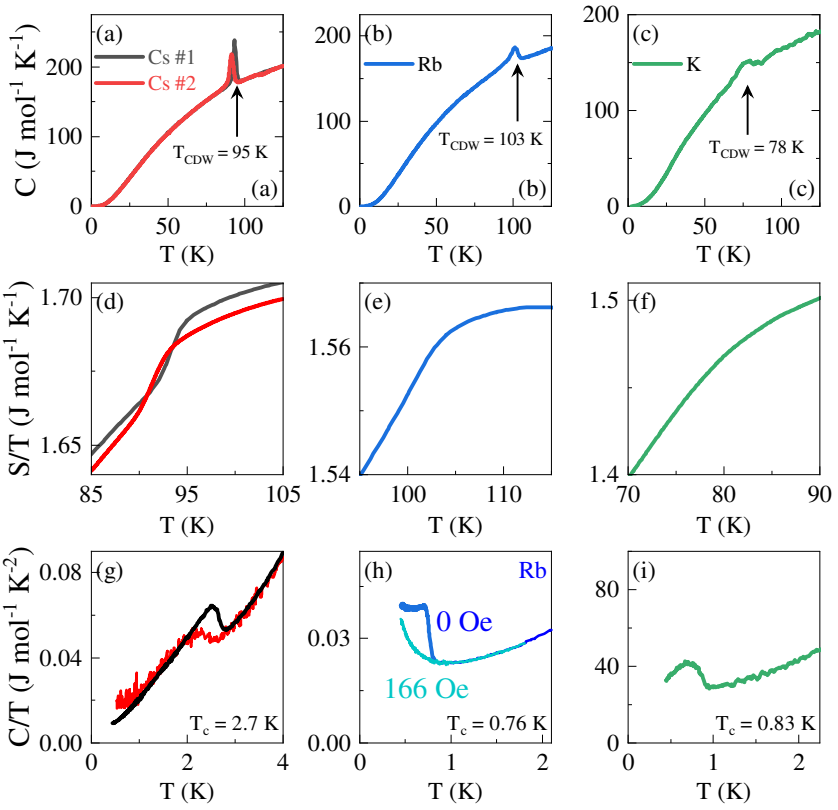

FIGURE 5.4: (a–c) Heat capacity C versus temperature T for CsV_3Sb_5, RbV_3Sb_5, and KV_3Sb_5, respectively, showing sharp anomalies at the CDW transition temperatures T_{CDW}. Both CsV_3Sb_5 samples (labeled #1 (China) and #2 (Karlsruhe)) exhibit $T_{CDW} \approx 95$ K, RbV_3Sb_5 displays a transition near 103 K and KV_3Sb_5 near 78 K. (d–f) Entropy S divided by T in the vicinity of the CDW transition for the same three compounds, highlighting the change in order of T_{CDW} from 1st to 2nd as the A goes from Cs- to K-. The case of Rb- cannot be concluded. (g–i) Low-temperature heat capacity data, plotted as C/T vs T, revealing superconducting transitions at $T_c \approx 2.7$ K for CsV_3Sb_5 (g), $T_c \approx 0.76$ K for RbV_3Sb_5 (h), and $T_c \approx 0.83$ K for KV_3Sb_5 (i). Different magnetic fields (0 Oe and 166 Oe) are shown for RbV_3Sb_5 in panel (h).

for Cs- [147]. The transition in Rb- appears intermediate, that is, either a very weak first order or a second order. (For Cs-, #1 was grown by M. He, Chongqing U., China and #2

was grown by A. Haghighirad, KIT, Germany. C of #1 was measured by L. Wang at KIT and reported in [147]).

The low-temperature heat capacity, plotted as C/T vs. T, to highlight the electronic part is shown in Fig. 5.4(g-i). The bulk superconducting transition is visible for all three samples. The C/T above the superconducting transition was fitted using the lattice-harmonic approximation,

$$C = \gamma T + B_3 T^3 + B_5 T^5 + B_7 T^7 + \dots \tag{5.1}$$

where $C_{lat} = B_3 T^3 + B_5 T^5 + B_7 T^7$ is the lattice contribution and γT is the electronic contribution. The T^3 coefficient is related to the Debye temperature T_D by: $B_3 = 12\pi^4 NR/5T_D^3$, where N is the number of atoms per formula unit and R is the molar gas constant. Using these fits, γ and T_D were determined. From T_D and T_c, the electron-phonon coupling strength λ_{e-ph} can also be determined using the McMillan formula [148] given by,

$$T_c = \frac{\Theta_D}{1.45} \exp\left(-\frac{1.04(1+\lambda)}{\lambda - \mu^*(1+0.62\lambda)}\right) \tag{5.2}$$

where μ^* is a dimensionless parameter that quantifies the repulsive screened Coulomb interaction between electrons in the context of superconductivity. It ranges between 0.11-0.15 and is taken here as 0.13 [149]. The obtained values of transition temperature, γ, B_3, T_D and λ_{e-ph} are summarized below in Table 5.5. The values of λ_{e-ph} imply that all the three lie in the weak-coupling limit, with Cs- being marginally in the intermediate coupling limit. For comparison, Aluminum and Niobium have $\lambda_{e-ph} = 0.44, 1.0$ respectively. The value obtained here for λ_{e-ph} are close to the ones reported using DFT+DMFT+SOC ($m^*/m_{DFT} \approx 1.7$) [150] and twice as large as the one obtained using DFT+SOC [149].

Compound	T_{CDW} (K)	T_c (K)	γ (mJ mol^{-1}K^{-2})	B_3 (mJ mol^{-1}K^{-4})	T_D (K)	λ_{e-ph}
CsV_3Sb_5	95	2.67	16.94	4.38	158	0.64
RbV_3Sb_5	103	0.75	18.36	3.17	176	0.47
KV_3Sb_5	78	0.86	22.84	4.84	153	0.49

TABLE 5.5: Summary of transition temperatures along with Sommerfeld coefficients and Debye temperature as obtained from heat capacity.

Figure 5.5(a) shows the relative length change, $\Delta L/L$, for RbV_3Sb_5 as a function of temperature. The T_{CDW} manifests as an abrupt change in $\Delta L/L$, see Fig. 5.5(b,c), in which it is more prominent along the c-axis (measured by Dr. L. Wang). Both $\Delta L/L$ and thermal expansion, $\alpha = 1/L(dL/dT)$, (Fig. 5.5(d)) indicate a much weaker first-order phase transition at the CDW transition ($T_{\mathrm{CDW}} = 105\,\mathrm{K}$) compared to CsV_3Sb_5 [147].

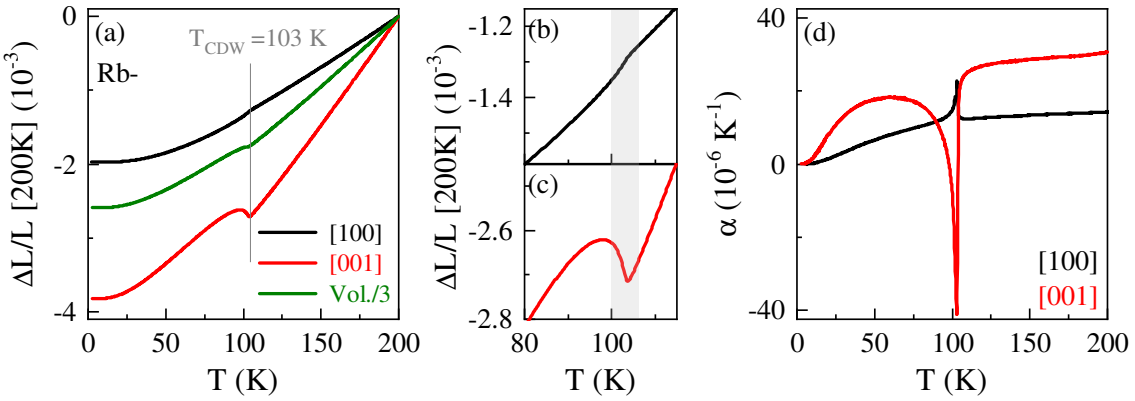

FIGURE 5.5: (a) Relative length change $\Delta L/L$ for the crystallographic directions $i = [100], [001]$ for the RbV3Sb5, along with one-third of the volumetric expansion. A pronounced anomaly appears at CDW transition $T_{\mathrm{CDW}} \approx 103\,\mathrm{K}$. (b,c) Magnified views near the CDW transition, highlighting the abrupt length changes in [100] and [001] expansions, respectively. (d) The corresponding linear thermal expansion coefficients $\alpha(T)$ along [100] and [001]. The sharp discontinuity in $\alpha(T)$ at T_{CDW} implies a (very) weak first-order transition.

From the thermal expansion coefficient and heat capacity, the uniaxial pressure dependence of the T_{CDW} can be calculated by applying the Clausius-Clapeyron relation (Eq. (A.3)) for the first-order phase transition. Table 5.6 summarizes both the anisotropic and hydrostatic pressure dependence of the CDW transition temperature T_{CDW} in $(\mathrm{Cs,Rb})V_3Sb_5$ obtained using the heat capacity and thermal expansion data presented here. Similar to the CsV_3Sb_5

Compound	$d\ln T_{\mathrm{CDW}}/dp_i$ (GPa^{-1})			
	a	c	$Volume$	hydrost. studies
Cs- [147]	+0.24	-1.3	-0.81	-0.85 [151]
Rb-	+0.12	-0.62	-0.38	-0.34 [152]

TABLE 5.6: Summary of the anisotropic and hydrostatic pressure dependencies of the charge-density-wave transition temperature T_{CDW} in $(\mathrm{Cs,Rb})V_3Sb_5$ as obtained from combination of thermal expansion and heat capacity using Eq. (A.3) and compared to hydrostatic studies [151, 152]

[147], the uniaxial compression along the c-axis strongly lowers T_{CDW}, as reflected in the large negative value, $\mathrm{d}\ln T_{\mathrm{CDW}}/\mathrm{d}p_c \approx -0.61$ for RbV_3Sb_5. This suppression of the CDW is primarily due to structural effects, where shortening of V–V distances leads to increased bonding interactions that must be balanced by vertical displacements of adjacent Sb2 atoms away from the kagome planes (see Fig. 1.3 and [153]). Under increased c-axis compression, however, these Sb displacements become energetically less favorable, directly destabilizing the CDW state.

Compressive stress along the a axis increases T_{CDW}, reflecting a pronounced anisotropic response of the CDW to lattice compression. Consequently, although hydrostatic pressure systematically suppresses T_{CDW} in CsV_3Sb_5 [151], chemical substitution with the smaller Rb ion does not simply replicate this uniform pressure effect. Instead, the Cs-to-Rb substitution induces structural adjustments such as partial expansion along the a axis (see the low temperature data in Fig. 5.2(b-g), [25]) and subtle shifts of Sb atoms, collectively enhancing the stability of the CDW, thus increasing T_{CDW} in RbV_3Sb_5. Further replacement with K likely then affects the apical Sb atoms such that it destabilizes the CDW state in KV_3Sb_5.

The in-plane resistance R normalized by its room temperature value for $(\mathrm{Cs, Rb, K})V_3Sb_5$ are shown in Fig. 5.6 (a-c) respectively. The CDW manifests as a kink in the electrical transport and appear in the derivative as a sharp peak for Cs- and as a jump for Rb-, K-.

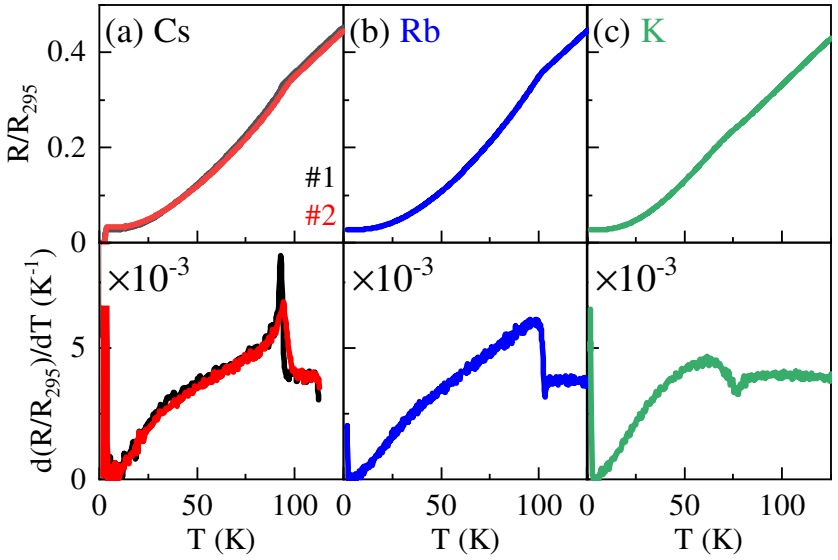

FIGURE 5.6: Room-temperature normalized resistance $R_n = R/R_{300}$ vs T for AV_3Sb_5 single crystals and their corresponding derivative dR_n/dT. CDW transition manifests as a kink in the resistivity and correspondingly as sharp peaks in the derivative.

In agreement with the specific heat and thermal expansion, the CDW transition is first order (sharp peak in derivative) for Cs- and second order for K-. For Rb- the transition here appears to be second order. However, this can also be related to the fact that the in-plane lattice change is much less abrupt compared to that along the c-axis (see Fig. 5.5). Also, the resistivity might change more smoothly if multiple conduction channels average out the transition.

5.2.2 Electrical transport below $T^* \sim 30\,\mathrm{K}$

The changes in the scattering mechanism can be tracked by observing $1/T(dR/dT)$. For all three compounds, a noticeable hump-like feature appears in the $1/T(dR/dT)$ around 30 K. This is not accompanied by any phase transition, as observed from the heat capacity, thermal expansion and the resistivity. This is also not related to the electro-magneto chiral effect [154] observed in these compounds as the measurements shown here are at 0 Tesla [155].

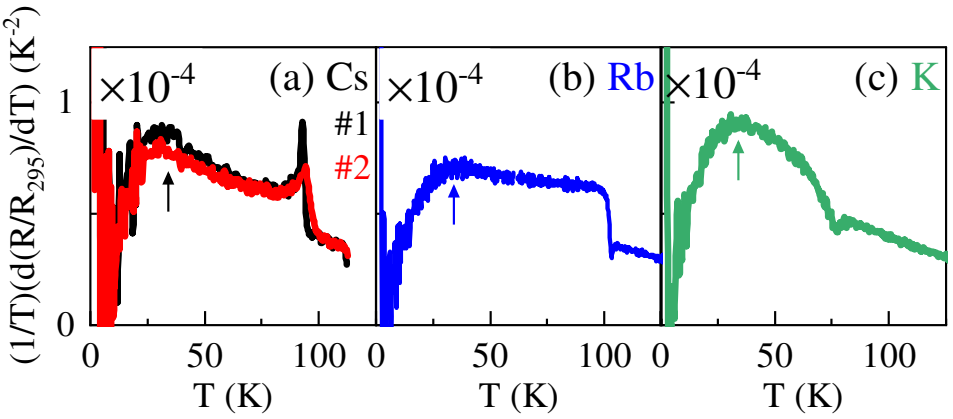

FIGURE 5.7: The temperature scaled derivative of the normalized resistivity for $(Cs,Rb,K)V_3Sb_5$. An anomaly around $\sim 30\,\mathrm{K}$ is observed. This is not accompanied by any signatures of a phase transition.

The linear decrease here implies a T^3-like behavior in resistivity. In the absence of a phase transition, the changes in the resistivity behavior can be typically traced to the changes in the scattering mechanism. Going from T^2 at higher temperatures to T^3-like at lower temperatures indicates a decrease in scattering strength as the system moves into the lower-temperature regime (since the resistivity vanishes more quickly). We ascribe this behavior to the highly two-dimensional character of the AV_3Sb_5. The $\rho_c/\rho_{ab} \sim 30$ [141, 156] is a large value, indicating pronounced quasi-two-dimensional transport in these bulk kagome metals. Landau's Fermi-liquid theory in 3D states that the electron–electron scattering rate $\tau_{\text{e-e}}^{-1}$ near the Fermi surface scales like $\sim T^2$. A standard result from perturbation theory for a clean 2D Fermi liquid is that the quasiparticle scattering rate may still show a leading T^2 term but with an additional logarithmic correction factor - $\rho(T) \sim AT^2 \ln(T_F/T)$ [157].

Below $T^* \sim 30\,\mathrm{K}$, the resistivity changes in a way that it supports the idea of enhanced conduction. Impurity scattering will have an opposite effect on the resistivity. While the residual resistivity ratio (RRR) for our samples is around 30-40, samples reported in the literature, such as [158], have much higher RRR(=140). This suggests that impurity

scattering alone is not responsible for this. Thus, the $T^* \approx 30\,\mathrm{K}$ anomaly appears to be universally present in the AV_3Sb_5 compounds and cannot be ascribed to a real phase transition, rather its origin likely lies in the quasi 2D transport and/or modification in the phonon spectra.

Evidence from measurements by other groups:

From [159]: In Fig. 5.8(a-b), the normalized resistivity data from Ref. [159] has been reproduced. Figures 5.8(a) and (b) show the normalized resistivity for a pristine and distorted CsV_3Sb_5 sample respectively. The corresponding temperature scaled derivative is shown in Fig. 5.8(c, d). Here also, the peak around 25-30 K is observed in the scaled derivative. Most importantly, the anomaly is present in the pristine sample S1 where the authors [159] report no $C2$-symmetry breaking, implying the said behavior is intrinsic to the system and cannot be ascribed to the widely reported time reversal symmetry breaking in these compounds [160].

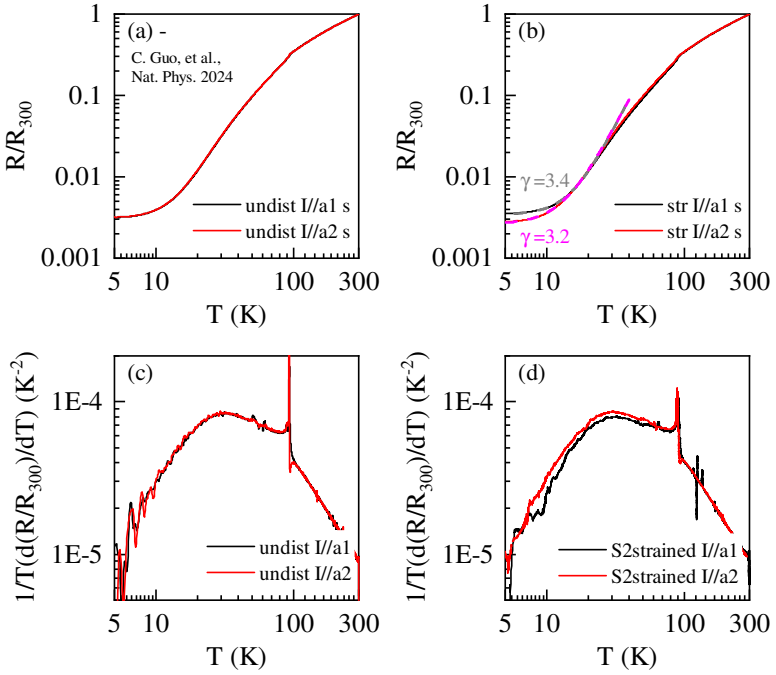

FIGURE 5.8: [Data taken from [159] and replotted/analyzed under the CC BY 4.0 license; changes were made]. Room-temperature normalized resistance $R_n = R/R_{300}$ vs T for CsV_3Sb_5 single crystals and their corresponding scaled derivative $(1/T)(dR_n/dT)$ for pristine and distorted samples plotted on a log-log scale. CDW transition manifests as a kink in the resistivity and correspondingly as sharp peaks in the scaled derivative, similar to our study. The low-temperature fits with $R = R_0 + AT^\gamma$ give $\gamma = 3.4, 3.2$ for the pristine and distorted case.

From [158]: In [158], where no nematic transition is observed, the R vs T has a $T^{2.91}$, similar to our result. This is reproduced in Fig. 5.9 from their publication. It should be

noted these samples have a much higher RRR=141 compared to our case. Therefore, the said effect cannot be ascribed to impurities as well.

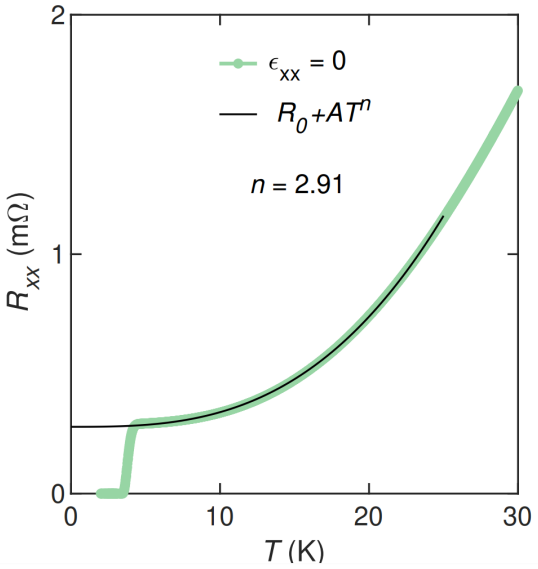

FIGURE 5.9: [Taken from [158]] under the CC BY 4.0 license: Resistance vs temperature with fit showing a $T^{2.91}$ dependence below 25 K.

5.3 Quantum oscillations in electrical transport and magnetization

In this study, the Fermiology of $(Cs, Rb, K)V_3Sb_5$ compounds has been investigated using quantum oscillations in electrical transport and magnetization. We have measured the SdH- and dHvA-oscillations using high-quality single crystals of $(Cs, Rb, K)V_3Sb_5$ compounds. Magnetization measurements were performed using a vibrating sample magnetometer (VSM) utility of the physical property measurement system (PPMS, Quantum Design) in magnetic fields up to 14 T. The magneto-transport measurements were carried using the electrical transport option (ETO) in the four-probe method. The electrical contacts were prepared with platinum wires and silver paint.

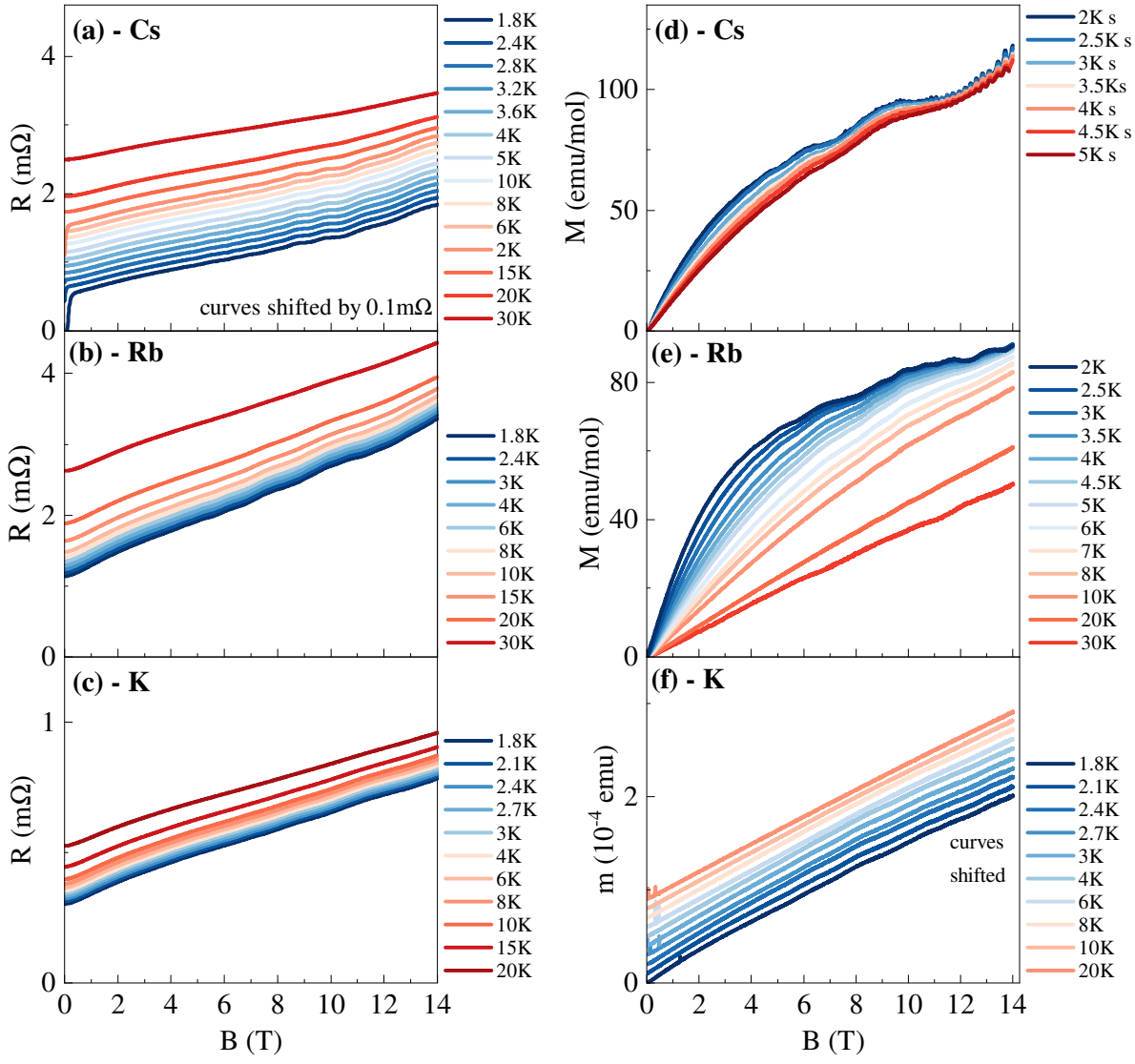

FIGURE 5.10: Quantum Oscillations in (a-c) electrical transport and (d-f) magnetization for $(Cs,Rb,K)V_3Sb_5$.

For the VSM measurements, the samples were glued using the GE-varnish to a non-magnetic stick. A fairly small amount of the varnish is used as the samples are non-magnetic and a larger amount obscures the signal and may also put anomalous strain on the sample. The R_{xx}-vs. B and M-vs. B are presented in Fig. 5.10(a-c) and (d-f) respectively for all the samples. The magnetic field is parallel to the c-axis in these measurements. Feeble oscillations are observed in transport up to T=30 K - a testament to the high quality of the samples. The oscillatory part of the signal was obtained by subtracting a smooth polynomial. Since quantum oscillations are periodic in the inverse of magnetic field, the fast Fourier transformation is performed on the signal $\Delta R/\Delta M$ plotted against $1/B$. The complete procedure is described in Sec. 2.3.2.

As discussed earlier, large mismatches exist in the QO spectra of these compounds in the literature, partly stemming from the superficial treatment of the complicated spectra. As explained in Sec. 2.3.2, the windowing function used and the subtraction procedure etc. can all induce artifacts. To overcome this, we use three benchmarks to establish a frequency as a *true* quantum oscillation frequency. We first employ the so-called derivative method - we have taken the lowest temperature ($T = 1.8$ K) resistance vs magnetic field curve and performed first and second derivatives on it, see Fig. C.7(a). The fast Fourier transform (FFT) of R, dR/dB and d^2R/dB^2 is then performed in different windows. This is shown in Fig. C.7(b,c). To understand how the derivative modifies the FFT spectra, assume a signal Q_{osc} and its corresponding FFT $\mathcal{F}(Q_{osc})$:

$$\begin{aligned} \mathcal{F}\{Q(B)\} &= \int_{-\infty}^{\infty} Q(B) e^{-i\omega B} dB \\ \frac{dQ(B)}{dB} &\longleftrightarrow i\omega \cdot \mathcal{F}\{Q(B)\} \\ \frac{d^2Q(B)}{dB^2} &\longleftrightarrow (i\omega)^2 \cdot \mathcal{F}\{Q(B)\} = -\omega^2 \cdot \mathcal{F}\{Q(B)\} \end{aligned} \tag{5.3}$$

In the above for a simple analysis we have considered the continuous Fourier transformation of the signal. In practice we do a discrete Fourier transformation. The net result here is that the high-frequency components enhanced for the derivatives. The white noise will also amplify then. We have systematically performed the FFT of the signal, derivatives and double derivatives to identify the quantum oscillation frequencies. Apart from this, power spectrum of the signal, given by $1/f^2$, is calculated and the standard deviation of the signal-dominated region (up to 2000 Tesla here) is also calculated as described in Sec. 2.3.2 at the end. Only the frequencies above these noise floors are considered.

We now present the results of the large set of quantum-oscillation measurements using the transport and magnetization. The study is split into two parts to discuss low-frequency and mid-frequency spectra separately.

5.3.1 Quantum oscillation frequencies $F < 250\,\mathrm{T}$

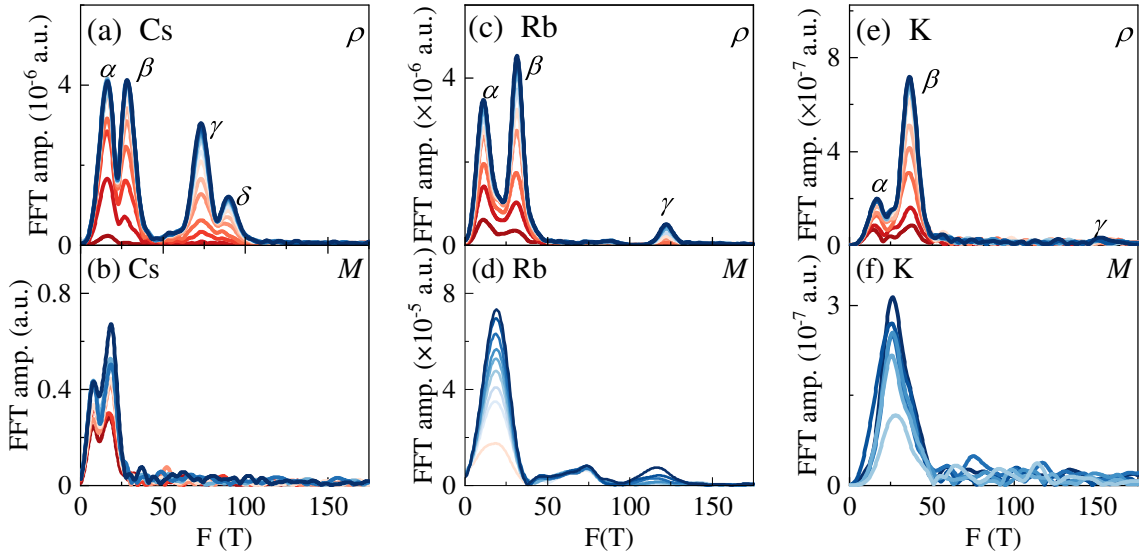

FIGURE 5.11: Summary of quantum oscillation spectra highlighting the low frequency part in *electrical transport* and *magnetization* for AV_3Sb_5. The sample (C/Rb/K), the magnetic field window (B_m) used, and the measurement method (transport ρ or magnetization M) are stated in the top corner. Color code corresponds to the same temperature as in the raw data (see Fig. 5.10).

CsV_3Sb_5			RbV_3Sb_5			KV_3Sb_5		
F	R	M	F	R	M	F	R	M
α	17	[9, 18]	α	11	19	α	17	26
β	28		β	32		β	36	
γ	72			85*	79			
δ	90	97	γ	122	121	γ	151	

TABLE 5.7: Tabulation of different quantum oscillation frequencies (in Tesla) obtained in resistivity and magnetization for $(Cs, Rb, K)V_3Sb_5$ compounds. The [9,18] and star marked frequencies reflect the unreliability in assignment due to limits of frequency resolution in magnetization and the frequency being below noise level in the transport data respectively.

At first glance, an apparent mismatch is seen in the low frequency region $< 150\,\mathrm{T}$ between SdH and dHvA results. These mismatches have been extensively reported in the literature. We show below that at least for the case of Rb- and K-, the said discrepancy can be ascribed

to the number of periods of a particular frequency in the quantum oscillation spectra, i.e., frequency resolution is not sufficient. After this, the case for Cs- is discussed in detail. Finally, how the aspects of reconstruction below CDW manifest in these low-frequencies is presented.

Case for Rb- and K-:

The ΔM and ΔR for Rb- and K- are shown in Fig. 5.12. The oscillations in the magnetization are not resolved below $B^{-1} = 0.17\,\mathrm{T}^{-1}$ for RbV_3Sb_5 and $B^{-1} = 0.1\,\mathrm{T}^{-1}$ for KV_3Sb_5. We see only 2–3 oscillation cycles of these low frequencies from 4 T to 14 T, making them difficult to resolve. This is related to the frequency resolution in the FFT which is given by,

$$F_{res} = \left(\frac{1}{B_{min}} - \frac{1}{B_{max}}\right)^{-1} \tag{5.4}$$

where B_{min} and B_{max} are the field intervals considered for the FFT. For the case of Rb- and K- the quantum oscillations in magnetization are not resolved below 5 Tesla, thereby small frequencies cannot be resolved in M as consistently as they are from transport measurements. The general mathematical details are given in App. C.

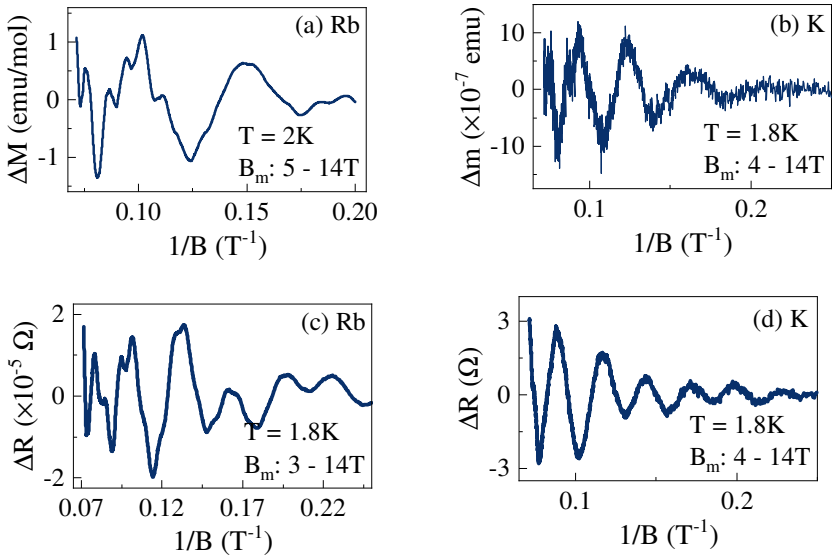

FIGURE 5.12: Quantum oscillation data for $(Rb, K)V_3Sb_5$, plotted as the oscillatory components of (a,b) magnetization ΔM and (c,d) resistance ΔR versus the inverse magnetic field $1/B$. The lowest measured temperature (1.8-2 K) and the widest field window in which quantum oscillations are present is shown.

Case for Cs-:

Within the low frequency spectrum of Cs-, the absence of 72 T frequency in the dHvA-oscillations cannot be ascribed to the windowing effects discussed above. A careful look at the other published studies shows that only one frequency is observed between 50-100 T in the dHvA- measurements. While slight differences in the observed frequencies can easily occur due to choice of the subtracted polynomial, an absence is surprising in

	SdH (transport, Seebeck, AHE)								dHvA (torque)		TDO		this study	
	[161]	[162]	[51]	[50]	[53]	[163]	[141]	[54]	[54]	[52]	[144]	[55]	ρ	M
F_1	11	18	–	11	18	12	18	–	–	18	–	–	16	11*
F_2	18	36	27	28	28	24	27	20	20	–	28	–	28	18
F_3	72	72	73	73	72	73	72	–	–	–	74	79	73	–
F_4	88	90	–	90	91	88	90	80	80	102	85	–	89	97

TABLE 5.8: Quantum oscillation frequencies (in Tesla) for CsV_3Sb_5 from different probes classified into SdH and dHvA-class and compared to this study. Tunnel diode oscillator (TDO) can be sensitive to both dHvA- [164] and SdH- [165] oscillations[1]. For AV_3Sb_5 compounds, it is more susceptible to SdH due to high σ and small moment $0.2\,\mu_B$.

the least. At the same time, all four frequencies have been consistently seen in nearly all the SdH measurements, and in this study as well. Table 5.8 presents a summary of the quantum oscillation frequencies in the low-frequency domain < 150 T, classified by the type of oscillation (SdH or dHvA).

Quantum interference in $\mathbf{CsV_3Sb_5}$: Given that the observed frequency cannot be attributed to instrumental artifacts or data-analysis errors, its appearance in the SdH signal and absence in the dHvA raises the possibility of quantum interference (QI) [37]. QI frequencies originate from multiple quasiparticle trajectories connected via magnetic-breakdown junctions, leading to a difference frequency in the SdH spectra. A schematic adopted from Shoenberg is shown in Fig. 5.13. Since $72 \approx 89 - 16$, the $F_{QI} = F_4 - F_1$ is satisfied, this frequency may arise from quantum interference.

However, quantum interference (QI) appears only at specific orientations of the sample relative to the magnetic field. This is due to the dephasing mechanism similar to that in the de Haas–van Alphen (dHvA) effect: only those electron orbits with extremal

[1] If f_0 is the resonant frequency of the TDO circuit, then the signal = shift in the frequency, $\Delta f/f_0 \propto \chi$ (magnetic susceptibility) and $\propto \Delta\rho$ (change in the resistivity).

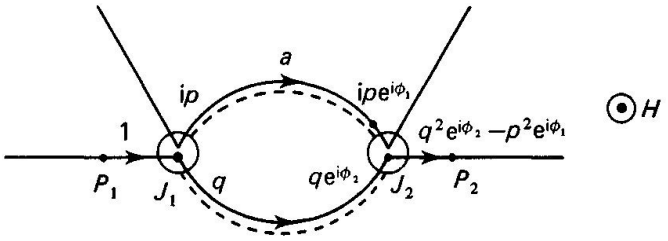

FIGURE 5.13: Taken from [37]. Copyright Cambridge University Press 1984. Reproduced with permission of Cambridge University Press through PLSclear: Principle of the Stark Quantum Interference effect between two paths a and b. Electron can proceed along an open orbit by two alternative paths a or b whose relative probabilities depend on magnetic breakdown at the junctions J_1 and J_2.

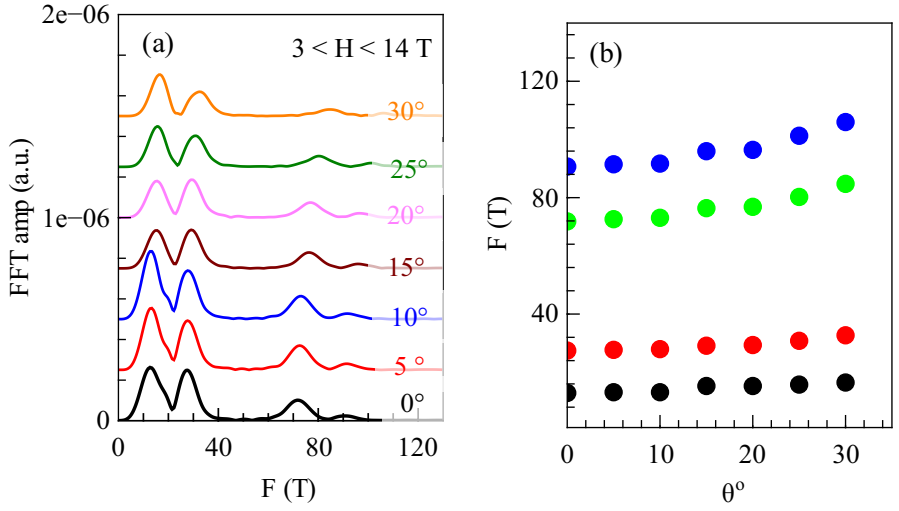

FIGURE 5.14: (a) Fast Fourier transform (FFT) amplitude of the quantum oscillations measured in the resistivity (transport) as a function of frequency F, for different tilt angles, over the magnetic-field window $3 < H < 14\,\mathrm{T}$ (curves offset vertically for clarity). (b) Extracted fundamental frequencies F versus tilt angle θ, illustrating the angular dependence of all four frequencies.

cross-sectional areas contribute to the observed oscillations. As a result, the phenomenon exhibits a pronounced angle dependence [37]. In Fig. 5.14, the angle dependence of all four observed frequencies (up to 150 T) has been shown (measurement and analysis by Dr. F. Hardy). All four frequencies follow a $\cos^n\theta$ behavior (see Fig. 5.14 and [50, 141]), which is *inconsistent* with the pronounced angular variation expected for the quantum interference. Therefore, QI can be ruled out as the cause of the absence of 73 T frequency in dHvA data.

Interband Scattering in $\mathbf{CsV_3Sb_5}$: The small three-dimensional (3D) orbitals in CsV_3Sb_5 arise from the CDW reconstruction of V d orbitals [50, 141]. ARPES detects one such band crossing in the range 50–100 T [142], whereas the observed $\sim 18\,\mathrm{T}$ frequency is too small ($A \approx 0.0015\,\mathrm{\AA}^{-2}$) to be resolved by photoemission. Since, as discussed above, QI

is not a possible mechanism, we explore the proposition of interband scattering between these Vanadium orbits. Within the theory of difference-frequency quantum oscillations [166, 167], a nonlinear interband coupling (say impurity scattering) can give rise to such quantum oscillation frequencies which have no thermodynamic counterpart. A cartoon depicting such a process is shown in Fig. 5.15. Here, the intraband scattering shown by

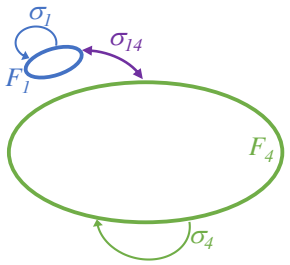

FIGURE 5.15: Schematic shows the intraband (σ_i) and interband ($\sigma_{1,4}$) coupling between orbits $F_{1,4}$.

$\sigma_{1,4}$ refers to the scattering of quasiparticles between different parts of the same band $F_{1,4}$ respectively, whereas the interband scattering refers to the quasiparticle scattering between orbits from different bands. This leads to the possible forbidden quantum oscillation frequencies in the SdH spectra. For the dHvA, up to second order, the effect cancels out. Since such a difference frequency $F_4 - F_1$ does not have a direct thermodynamic origin, it can continue to occur at much higher temperature than the underpinning frequencies F_1 and F_4. A defect-assisted intraband scattering between the small Fermi pocket of 89 T (V) is known to occur from the ARPES and STM measurements [142]. It leads to dispersive wave vectors in SI-STM measurements, and has been also held responsible for the *nematicity* in these compounds [168]. Since these effects originate from defects and are *limited* to the defect rich regions of the sample they are not observed in the thermodynamic measurements [147, 158]. The frequency of 16 T is too small (A=0.0015 Å^{-2}) to be resolved in ARPES. A defect assisted interband scattering between 89 T and 16 T band will then explain the missing frequency 73 T =89 − 16 T in dHvA.

Fermi Surface Reconstruction below CDW

The three/four frequencies in the low temperature experiments against single frequency in the DFT calculations with undistorted structure is taken as an evidence of reconstruction in the CDW phase [143]. This is highlighted in the room temperature DFT shown in Fig. 5.16 and 5.17 for RbV_3Sb_5 and CsV_3Sb_5 respectively. Here, no choice of the Fermi level is able to reproduce the three/four frequencies in the spectra for either of the compound. Apart from this, a strong interlayer dependence is seen especially between $k_z = 0$ and $k_z = 0.5$. The reconstructed Fermi surface for the Cs- (Taken from [143]) is also presented in Fig. 5.18 for completeness.

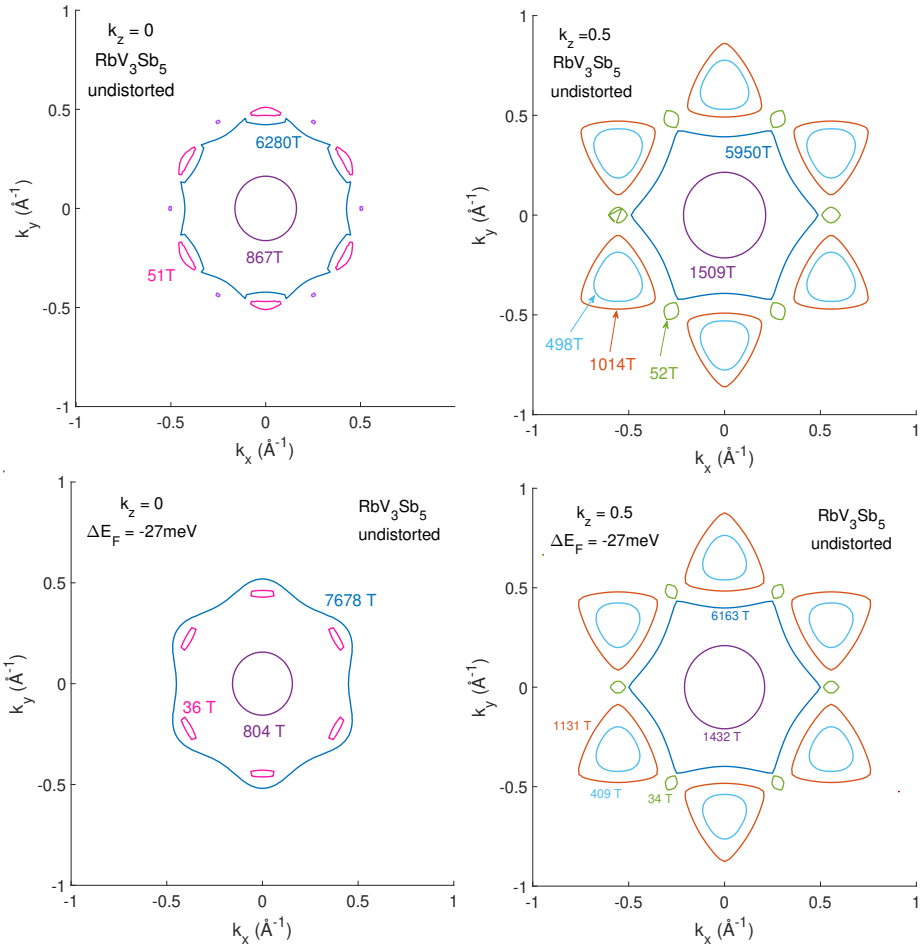

FIGURE 5.16: DFT for the RbV_3Sb_5 for the undistorted case showing cuts at $k_z = 0$, 0.5. The case of $E_F = E_F(\text{exp})$ and E_F shifted by -27 meV are shown to highlight the presence of the low-frequency orbits.

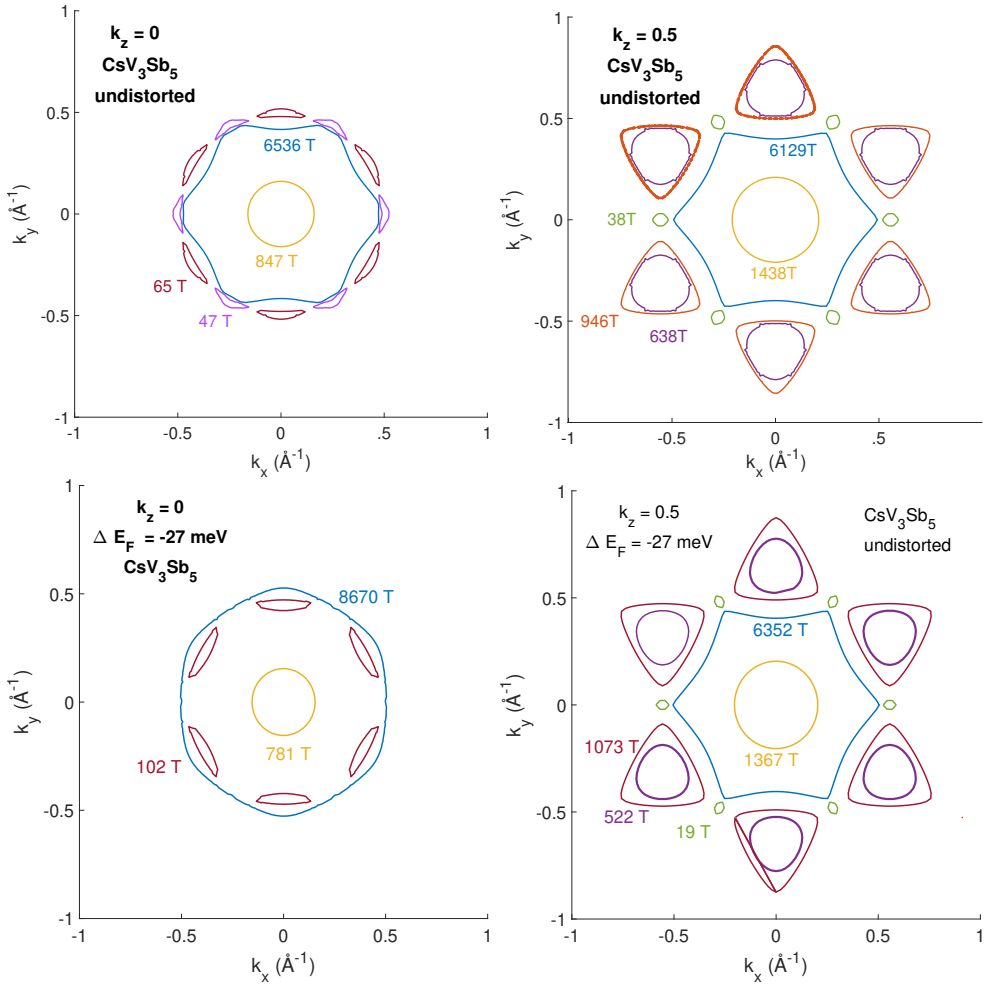

FIGURE 5.17: DFT for the CsV_3Sb_5 for the undistorted case showing cuts at $k_z = 0$, 0.5. The case of $E_F = E_F(\text{exp})$ and E_F shifted by -27 meV are shown to highlight the presence of the low-frequency orbits and strong dependence on the *choice* of Fermi level.

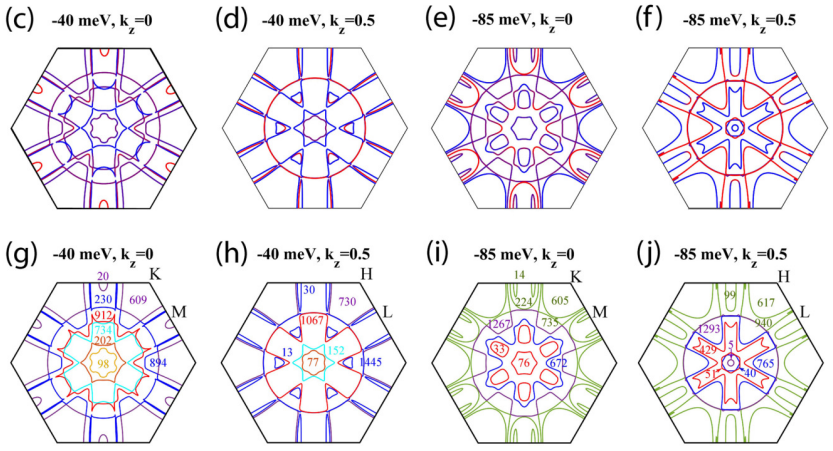

FIGURE 5.18: Taken from [143] under the CC BY 4.0 license. 2x2x2 CDW reconstruction in CsV_3Sb_5: The open Fermi surfaces at the BZ boundary extend to neighboring BZs and form closed Fermi pockets [55]. The cyclotron frequencies (in T) of the corresponding Fermi surfaces is labeled next to them.

5.3.2 Quantum oscillation frequencies $250 < F < 1000$ T

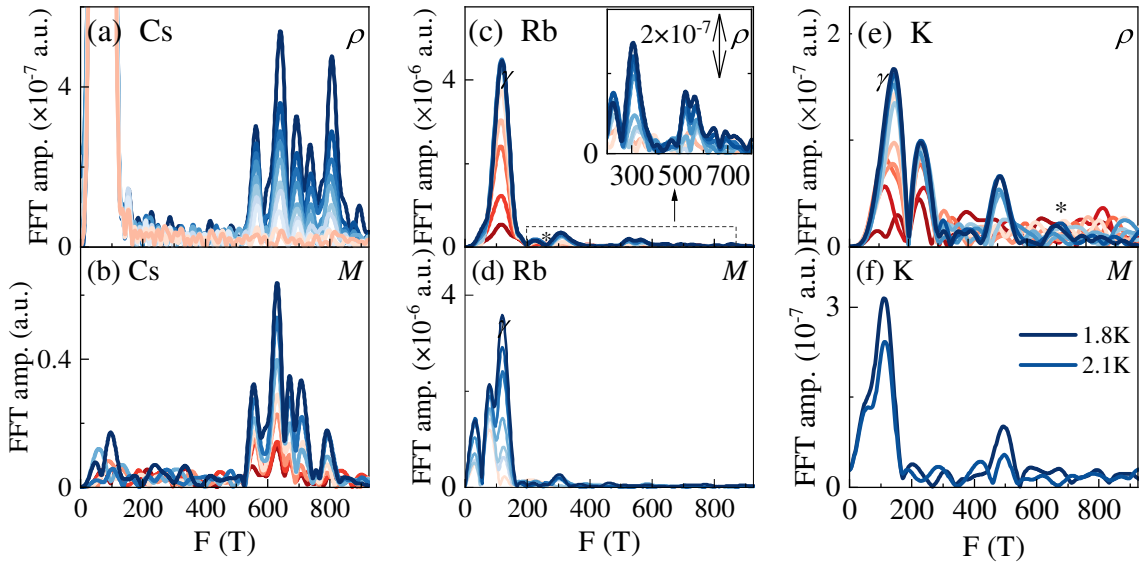

FIGURE 5.19: Summary of quantum oscillation spectra highlighting the mid-frequency part in *electrical transport* and *magnetization* for AV_3Sb_5. The sample (C/Rb/K), the magnetic field window (B_m) used, and the measurement method (transport ρ or magnetization M) are stated in the top corner. Color code corresponds to the same temperature as in the raw data (see Fig. 5.10).

CsV_3Sb_5			RbV_3Sb_5			KV_3Sb_5		
F	R	M	F	R	M	F	R	M
ϵ_1	561	553	ϵ_1	308	301	ϵ_1	245	
ϵ_2	640	631				ϵ_2	510	498
ϵ_3	692	670						
ϵ_4	738	708	ϵ_2					
ϵ_5	805	790	ϵ_3					
	894*							

TABLE 5.9: Tabulation of different quantum oscillation frequencies (in Tesla) obtained in resistivity and magnetization for $(Cs, Rb, K)V_3Sb_5$ compounds.

The mid-frequency FFT spectra ($250 - 1000$ T) for all three compounds (Cs-, Rb-, K-) as derived from transport and magnetization are shown in Fig. 5.19. A systematic decline is observed in the richness of the quantum oscillation spectra in this region with lighter alkali atom. The Cs- shows six frequencies in both transport and magnetization measurements. Rb- and K- show only two frequencies in the middle-band. For the Cs- it has been proposed that these six frequencies originate from either the magnetic breakdown [54], or interlayer modulation [143, 144]. We observe these frequencies in both dHvA and

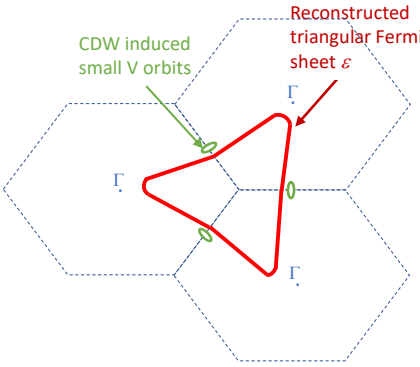

FIGURE 5.20: Illustration of the triangular pocket and the elliptical pocket at a fixed k_z for AV_3Sb_5 [142, 169].

SdH oscillations in fields up to 14 T. Prior to this work, these frequencies have only been observed in very high field measurements (∼35 T) [54, 144].

The magnetic breakdown has been proposed on the basis that the tunneling occurs across the large reconstructed triangular orbit and the smaller reconstructed orbits. A schematic of the two orbits is shown in Fig. 5.20. However, as discussed before, these small elliptical orbits are three-dimensional in nature and don't extend in the k_z space [141, 142]. For the KV_3Sb_5, they are only observed at the $k_z = 0$ and are completely absent at $k_z \approx \pi$ [169]. Also, we see these frequencies at rather low fields up to 14 T. The probability of magnetic breakdown is given by $P = e^{-H_0/H}$, where $H_0 \propto \epsilon_g^2/E_F$, is the characteristic breakdown field. Here, ϵ_g, E_F are the energy gap at the zone boundary and Fermi energy respectively. The probability of breakdown orbit is substantial only above this breakdown field. Often, if some of these frequencies were purely due to magnetic breakdown, one might see them only at higher fields, above the breakdown field. If they appear consistently across low-to-moderate as well as high-field windows, that leans toward them being fundamental orbits. The fact that we see them at much lower fields weakens (but does not refute) the argument for the magnetic breakdown.

We now explore the argument of interlayer modulation between 3 layers of star-of-David (SoD) and 1 layer of inverse-star-of-David (ISD) configurations [50]. The DFT calculations incorporating the SD and ISD ordering predict 6-7 frequencies in this frequency domain, against only two frequencies when only one (SD or ISD) distortion is considered [143, 163]. For the CsV_3Sb_5, XRD [50, 145], Raman [170], NQR [30] all support this $2 \times 2 \times 4$ modulation of the SoD and ISD. However, for $(Rb, K)V_3Sb_5$ only $2\times2\times2$ ISD configuration has been reported [171, 172]. This fits well within our data, where we observe six frequencies in the mid-band (250-1000 T) for the CsV_3Sb_5, but only two for the Rb- and K-.

Since these frequencies are observed consistently across the ρ and M, arguments that these frequencies are related to the oxidation of the surface, which can affect E_F and influence the spectra, are not applicable. Although they may be responsible for the differences in the temperature dependence.

5.4 Quantum oscillations in magnetostriction

Next, we explore quantum oscillations in magnetostrictive coefficient (λ). We have measured λ_c for $(Cs, Rb)V_3Sb_5$ in magnetic fields $H \parallel c$. The magnetostriction is another *dHvA-class* physical quantity and is related directly to the stress dependence of magnetization. The oscillatory magnetostrictive coefficient ($\bar{\lambda}$) is given by:

$$\lambda_{ijk} = \frac{1}{V}\frac{\partial M_k}{\partial \sigma_{ij}} \tag{5.5}$$

To measure the quantum oscillations in these compounds, a stack of crystals was made by gluing small crystals with GE7031 varnish [147]. The measurements were performed at the High Field Magnet Laboratory, Nijmegen using Küchler's cell [44] by the author, F. Hardy, T. Ottenbros and S. Wiedmann. For temperature dependence, magnetic field was set parallel to the c-axis and ΔL_c was measured. The relative length change for $(Cs, Rb)V_3Sb_5$ is shown in Fig. 5.21(a,b) respectively.

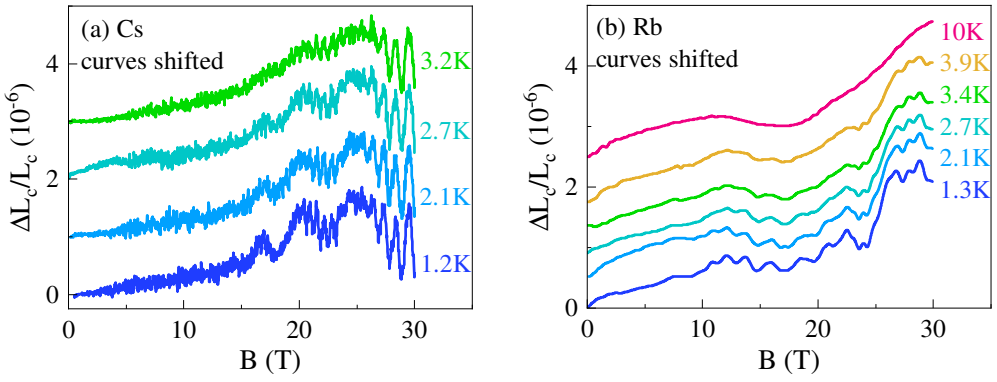

FIGURE 5.21: Magnetic-field dependence of the relative change in the c-axis length, $\Delta L_c/L_c$, measured using Küchler's cell for (a) CsV_3Sb_5 and (b) RbV_3Sb_5. Quantum Oscillations are well resolved in both cases for temperatures up to 4 K. Curves are vertically shifted for clarity.

For the CsV_3Sb_5, the ΔL^c_{osc} vs $1/B$ and the FFT along with comparison with magnetization are shown in Fig. 5.22. Quantum Oscillations can be seen in magnetic fields above 14 Tesla in this case. In the low frequency domain, one dominant frequency around 95 T is observed, same as in M, as shown in Fig. 5.22(b,c). The 6 frequencies observed in M

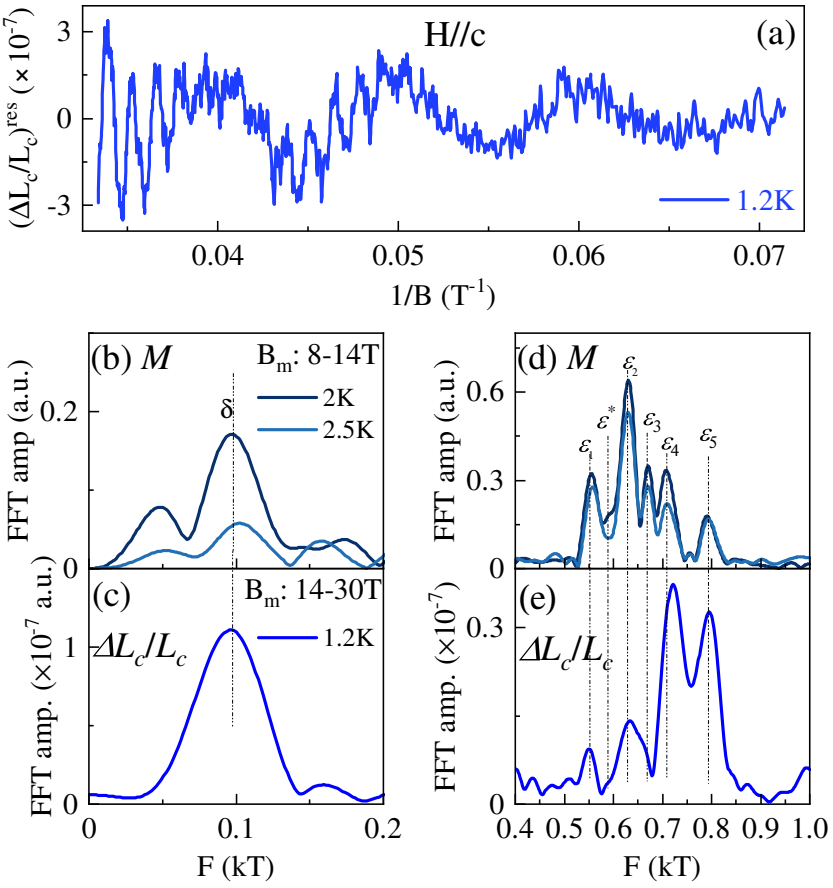

FIGURE 5.22: (a) Oscillatory component of the relative length change, $\Delta L_c/L_c$, plotted against inverse magnetic field $1/B$ at $T = 1.2\,\mathrm{K}$ with $\mathbf{H} \parallel c$. (b) Fast Fourier transform (FFT) spectra of the magnetization M in the field window $B_m = 8$–$14\,\mathrm{T}$ at $T = 2\,\mathrm{K}$ (black) and $T = 2.5\,\mathrm{K}$ (red). (c) Corresponding FFT amplitude of ΔL_{osc} for $B_m = 14$–$29\,\mathrm{T}$. (d) FFT spectra of M and (e) of ΔL_{osc} over the same field range, with vertical dashed lines marking the quantum-oscillation frequencies observed in both the experiments.

in the mid-frequency domain are also observed in ΔL_{osc} precisely at the same points. The enhancement in the amplitude is dictated by the strain response of the particular orbit $\partial F_i/\partial\epsilon$. All six frequencies (555, 590*, 631, 670, 705, 788 T) cannot be reconciled using any breakdown assignment, contrary to the claim of [54]. In general, frequencies arising from smaller *necks* are much more sensitive to stress than large free electron-like extrema. Thus, the corresponding low frequencies show up relatively more strongly than the high frequencies in the magnetostriction oscillations as compared to the magnetization oscillations [37]. Since in the middle band, the larger frequencies get amplified more compared to the smaller frequencies, it implies that these frequencies emerge from different parts of the Fermi surface. Indeed in the reconstructed picture for Cs-, the frequencies contributing to the middle band (250-1000 T) arise from both the center of the BZ as well as the larger triangular section spanning multiple BZs [143].

For the RbV_3Sb_5, the temperature dependence of λ_c vs B and its FFT are plotted in Fig. 5.23(a) and (b), respectively. Quantum Oscillations are observed up to 4 K, although their amplitude falls considerably. Unlike CsV_3Sb_5, only two frequencies are obtained in the mid-frequency band at 695 and 849 T, in expectation with the presence of only ISD (or SD) distortion.

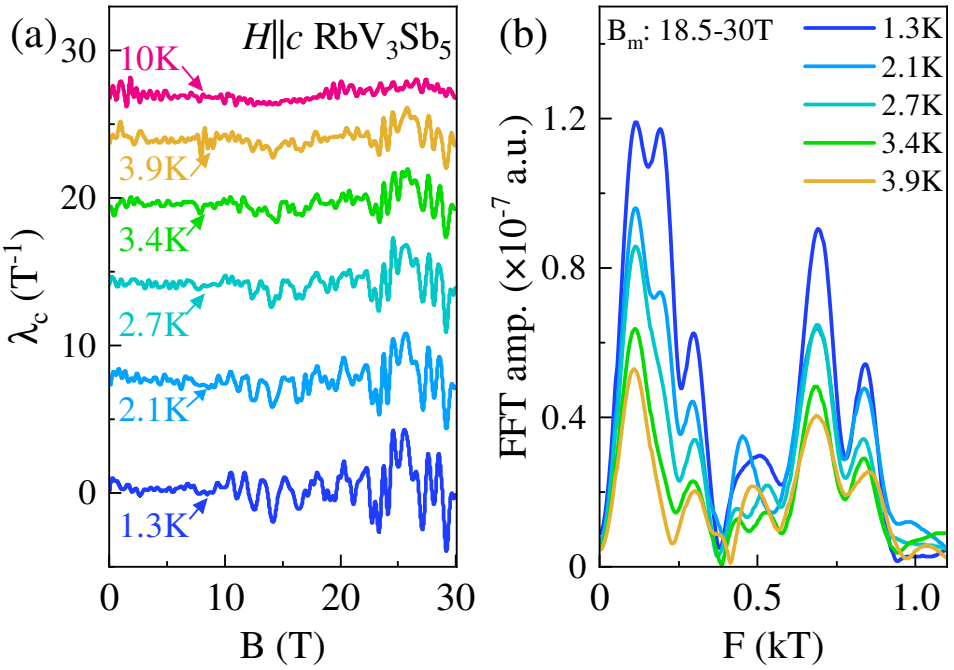

FIGURE 5.23: (a) Magnetic field dependence of the c-axis response of the magnetostrictive coefficient $\lambda_c(B)$ in RbV_3Sb_5 with $\mathbf{H} \parallel c$, measured at various temperatures from 1.3 K to 10 K (offset vertically for clarity). (b) Corresponding fast Fourier transform (FFT) amplitude of $\lambda_c(B)$ over the field range B_m = 18.5–30 T. The shaded region indicates the standard deviation at T = 1.3 K.

Thus, our quantum oscillation data in magnetostriction strongly indicates that the SD + ISD interlayer ordering effects occur exclusively in CsV_3Sb_5, while the spectra for $(Rb, K)V_3Sb_5$ can be well explained using only the SD or ISD distortion.

5.4.1 Strain dependence of the small elliptical orbit

Since the quantum oscillations are well resolved for the RbV_3Sb_5 even at 14 T (Fig. 5.23(a)), we can use this data to estimate the strain response along c-axis of the low frequency elliptical orbit (122 T). To do this, the amplitude of the oscillations in magnetization and the magnetostriction are required in the same field window. The relevant quantity in this case is not λ but rather $\Delta L/L_0$. While a clear beating between 89 T and 122 T is observed, the FFT spectrum is dominated by a single frequency in the field window (see

Fig. 5.19 for Rb-, 9-14 T window). A filtered signal has been compared and shown in App. C. The equation connecting the strain tensor to the oscillatory magnetization ΔM is [37]:

$$\bar{\epsilon_{ik}} \approx \Delta L/L = -\left(\frac{\partial ln F}{\partial \sigma_{ik}}\right) \cdot \Delta M \cdot H \tag{5.6}$$

where $(\partial \ln F/\partial \sigma_{ik})$ is the stress dependence of the particular frequency and the largest component of $\bar{\epsilon_{ik}} \approx \Delta L/L$ - the magnetostriction. The oscillatory part of the magnetization ΔM and the magnetostriction $\Delta L_c/L_c$ for $H \parallel c$ are plotted together in absolute units in Fig. 5.24. The observed shift (from 120 T in M to 108 T in λ) is small.

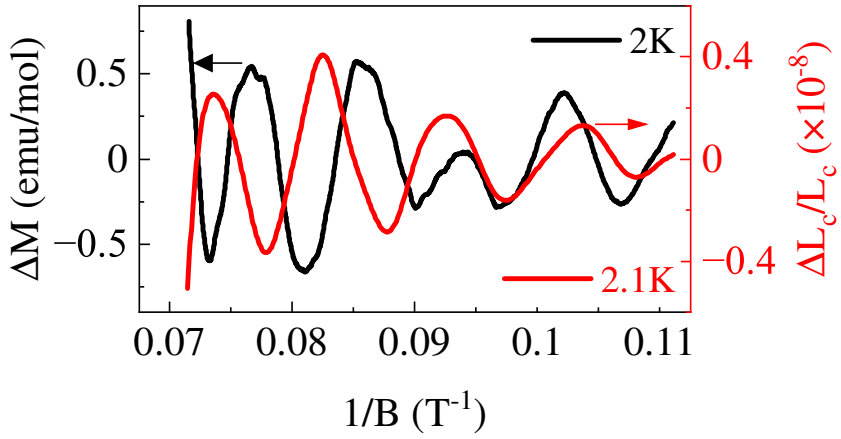

FIGURE 5.24: Oscillatory magnetization ΔM (black curve, left axis) and c-axis magnetostriction $\Delta L_c/L_c$ (red curve, right axis) in RbV_3Sb_5, measured at $T = 2$ K and 2.1 K, respectively, as functions of the inverse magnetic field $1/B$.

Using Eq. (5.6), we obtain $(\partial \ln F)/(\partial \sigma_{zz}) \approx 1.04 \times 10^{-13}$ cm^2/dyne $\approx 1.04 \times 10^{-12}$ Pa^{-1}, where ΔM is converted from emu/mol to Gauss using the cell volume and molar mass. Although this sensitivity leads to a measurable frequency change in magnetostriction, its magnitude is small. This fairly small value is comparable to the value of the $(\partial \ln F)/(\partial \sigma_{zz})$ for the *belly* in the noble metals [173]. As discussed earlier, these small elliptical orbits originate from the V d-bands [50], and have been proposed to play an important role in the low-temperature magnetotransport [141]. Crucially, this small strain response implies that only chemical doping or substitution that substantially changes in-plane bond lengths (with respect to c-axis) or modifies the electron count near the V d-bands may produce significant shifts in these Fermi-surface pockets and the uniaxial strain along the c-axis is unlikely to strongly tune the low-temperature transport properties governed by this FS pocket.

CsV_3Sb_5				RbV_3Sb_5				KV_3Sb_5		
F	R	M	λ	F	R	M	λ	F	R	M
α	17	[9, 18]*		α	11	19		α	17	26
β	28			β	32			β	36	
γ	72				85*	79				
δ	90	97	95	γ	122	121	108	γ	151	
ϵ_1	561	553	555	ϵ_1	308	301	296	ϵ_1	245	
ϵ_2	596	593	591							
ϵ_3	640	631	635					ϵ_2	510	498
ϵ_4	692	670	666							
ϵ_5	738	708	724	ϵ_2			695			
ϵ_6	805	790	798	ϵ_3			849			

TABLE 5.10: Summary of different quantum oscillation frequencies (in Tesla) obtained in resistivity, magnetization and magnetostriction for $(Cs, Rb, K)V_3Sb_5$ compounds. The labels for frequencies used in the text are also given. As discussed in the text, for RbV_3Sb_5, the frequencies 9, 18 T cannot be reliably assigned due to limits of frequency resolution.

5.5 Conclusion

The results of our thermodynamics, transport and quantum oscillations study in the AV_3Sb_5 compounds are summarized below:

- The CDW phase transition is second-order in KV_3Sb_5, as opposed to being weakly first-order in $(Cs, Rb)V_3Sb_5$.
- Similar to CsV_3Sb_5, the CDW transition for Rb- also shows a highly anisotropic pressure response, with a giant effect along the c-axis. The hydrostatic pressure dependence derived from the Clausius-Clapeyron closely matches the value obtained from direct pressure studies.
- From the transport data, we uncover a new temperature scale $T^* \sim 30\,\mathrm{K}$ for all three compounds. This is not accompanied by any phase transition. We relate this to the two-dimensionality of the system and/or presence of the van-Hove singularity.
- Quantum oscillations are observed in both resistivity and magnetization for the Cs-, Rb-, and K-based compounds. Some of the noted differences in the quantum oscillation (QO) frequencies can be reconciled as arising from windowing effects. For CsV_3Sb_5, we postulate that interband scattering [142] may explain the absence of one frequency in all the reported dHvA spectra [52, 54].

- We attribute the *rich middle band* (250–1000 T) in quantum oscillation spectra of CsV_3Sb_5 to ISD+SD interlayer modulation [144] as opposed to magnetic breakdown [54]. This rich spectrum is absent in our data for the Rb- and K-based compounds, which exhibit modulation in SD or ISD structure only [25].
- Additional evidence comes from magnetostrictive oscillations, in which the amplitude variations cannot be reconciled if the spectrum were to originate solely from magnetic breakdown (enhancement in the relative amplitude is larger for the higher frequencies).
- The *c*-axis strain dependence of the small elliptical orbits for RbV_3Sb_5, which are linked to the anomalous Hall effect [141], is derived using the magnetostriction and magnetization data. The small value obtained indicates that these orbits remain essentially unperturbed by *c*-axis strain. This result has important implications for tuning the magnetotransport properties of AV_3Sb_5. To achieve substantial tuning, modifying the electron count is likely to be more effective than structural perturbations (e.g., chemical substitutions). For structural perturbations, the disorder-driven effects may become more dominant.

Chapter 6

Summary and perspectives

In this thesis, I have focused on the study of two superconductors - Fe(Se,Te) and AV_3Sb_5, and their normal states through thermodynamics and transport measurements. I investigated the behavior of various physical quantities related to the superconducting transition in Fe(Se,Te) by combining thermodynamic bulk probes and electrical transport. This approach revealed a phase diagram comprising two distinct superconducting domes, which, crucially, remain observable even at zero magnetic field once bulk superconductivity is considered. A comparison of physical properties from the FeSe and the low-Te substitutions with those of the second superconducting dome indicates notable differences in the superconducting gaps and interactions.

An important observation arises from the evolution of the electronic heat-capacity data in the first superconducting dome: accidental nodes or pronounced gap anisotropies at one pocket seem to be progressively lifted with increasing Te substitution. In the second dome, the single band dominates the thermodynamic properties. The thermal-expansion measurements show that for modest Te substitution in FeSe the orthorhombicity and superconductivity couple weakly but in a cooperative way. This contrasts with many pnictide systems, in which orthorhombic order and superconductivity often compete strongly. Furthermore, the anisotropic response of the c-axis observed in crystals with $x = 0.5$ reflects significant changes in the electronic structure, where modest electronic correlations in FeSe evolve into a more strongly correlated regime in Fe(Se,Te). In conjunction with these findings, I established that the nemato-elastic coupling in Fe(Se,Te) is the largest among iron-based superconductors, and that the end of the nematic phase is accompanied by an enhancement of T_c in the second superconducting dome. The conspicuous hardening of C_{66} in this dome likely arises from the interplay of the nematic instability and superconductivity, and hints at substantial nematic correlations in the vicinity of the transition. Whether these observations can be explained by nematic quantum

criticality, orbital selectivity, or an alternative mechanism remains a vital question for future research.

For the AV_3Sb_5 ($A = Cs, Rb, K$), I carried out a comprehensive study of the thermodynamics, transport, and quantum oscillations, to understand the CDW transition and the subsequent low-temperature ground states. The zero-field thermodynamic and transport measurements confirmed that while KV_3Sb_5 undergoes a second-order CDW transition, RbV_3Sb_5 displays a weak first-order transition. The anisotropic pressure response of the T_{CDW} is similar to that of CsV_3Sb_5, with the c-axis response being five times larger than the in-plane response. Furthermore, all three compounds exhibit a characteristic temperature scale, $T^* \approx 30\,K$, around which no clear phase transition is detected. I connect this temperature to two-dimensional aspects of the electronic structure.

Quantum oscillations were observed in both resistivity and magnetization for the Cs-, Rb-, and K-based crystals. These measurements suggest that many of the variations in the quantum oscillation spectra reported in the literature may be explained by windowing (for Rb-, K-) or by interband scattering effects (for Cs-). The presence of multiple quantum oscillation frequencies in the low-frequency domain is the first sign of CDW reconstruction, as only one frequency is obtained from the pristine structure in this frequency range ($F < 200\,T$). Differences in the middle band for the different members (Cs, Rb, K) are consistent with the differences in the modulated structures, particularly the SD+ISD modulation reported for CsV_3Sb_5 against only staggered-SD/ISD for RbV_3Sb_5 and KV_3Sb_5. Quantum oscillations in magnetostriction data further reinforce the conclusion that the *rich middle band* in the quantum-oscillation spectra of CsV_3Sb_5 arises more naturally from the interlayer modulation than from magnetic breakdown. Moreover, the subtle strain dependence of the small elliptical orbits associated with the anomalous Hall effect implies that these orbits in RbV_3Sb_5 remain largely unaffected by c-axis strain, underscoring the importance of tuning the electronic density near the V *d*-bands over purely structural modifications when attempting to tailor magnetotransport properties.

Appendix A

Fundamentals

Thermodynamic Relations

The thermodynamic state of a system is described by thermodynamic variables such as temperature T, pressure P, volume V, entropy S, internal energy U, and chemical potential μ. The relationships among these variables are governed by the first $dU = TdS - PdV + \mu dN$ and second $\delta Q = TdS$ law of the thermodynamics, and related via Maxwell's thermodynamic relations:

$$\begin{aligned}
\left(\frac{\partial T}{\partial V}\right)_S &= -\left(\frac{\partial P}{\partial S}\right)_V = \frac{\partial^2 U}{\partial S\,\partial V} \\
\left(\frac{\partial T}{\partial P}\right)_S &= +\left(\frac{\partial V}{\partial S}\right)_P = \frac{\partial^2 H}{\partial S\,\partial P} \\
\left(\frac{\partial S}{\partial V}\right)_T &= +\left(\frac{\partial P}{\partial T}\right)_V = -\frac{\partial^2 F}{\partial T\,\partial V} \\
-\left(\frac{\partial S}{\partial P}\right)_T &= +\left(\frac{\partial V}{\partial T}\right)_P = \frac{\partial^2 G}{\partial T\,\partial P}
\end{aligned} \tag{A.1}$$

Changes in these thermodynamic parameters (T, p, V) directly affect measurable material properties, which are probed experimentally to reveal underlying physical mechanisms. From these, the specific heat and coefficient of (volumetric) thermal expansion can be written as derivatives of entropy with respect to pressure and temperature, respectively:

$$\begin{aligned}
\beta = \frac{1}{V}\frac{\partial V}{\partial T} &= -\frac{1}{V}\left(\frac{dS}{dp}\right)_T \\
dQ = C_p dT = TdS \implies \frac{C_p}{T} &= \left(\frac{dS}{dT}\right)_p
\end{aligned} \tag{A.2}$$

Thermodynamic measurements are particularly important for identifying and characterizing phase transitions. At a first-order phase transition, entropy S changes discontinuously with temperature, associated with latent heat $T\Delta S$, and sample dimensions also undergo abrupt changes. Consequently, specific heat C_p and uniaxial thermal expansion (α_i), where $\beta = \sum_i \alpha_i$, exhibit pronounced peaks. The pressure dependence of the transition temperature for a first-order transition is expressed by the Clausius–Clapeyron relation:

$$\frac{dT_c}{dp_i} = V\frac{\Delta L_i/L_i}{\Delta S}, \tag{A.3}$$

where ΔS and $\Delta L_i/L_i$ represent entropy and relative length change along the direction i at the transition. In contrast, second-order (continuous) transitions show no latent heat and involve continuous but sharp changes in thermodynamic variables. These transitions exhibit distinct anomalies in specific heat C_p and thermal expansion coefficient α_i. Specifically, at a second-order transition, discontinuities in heat capacity ΔC_p and thermal expansion $\Delta\alpha_i$ are observed, which correspond to a continuous but slope-changing entropy. The Ehrenfest relation describes the pressure dependence of the transition temperature in second-order transitions:

$$\frac{dT_c}{dp_i} = V_m\frac{\Delta\alpha_i}{\Delta C_p/T}, \tag{A.4}$$

where V_m is the molar volume of the material. According to convention, positive ΔC_p indicates an increase in specific heat when temperature decreases through the transition, and the sign of dT_c/dp_i matches that of the thermal expansion anomaly $\Delta\alpha_i$. Different phases such as superconductivity, (anti)ferromagnetism, density waves, structural transitions, coupled magneto-structural transitions, also produce distinct features in the thermodynamic measurements.

Magnetic Breakdown

Magnetic breakdown arises when two extremal orbits on different sheets of the Fermi surface are close enough that carriers can tunnel from one orbit to another orbit (see Fig. A.1). The probability of the magnetic breakdown is given by:

$$P = e^{-H_0/H} \tag{A.5}$$

where H_0 is the breakdown field and H is the applied magnetic field. The problem of magnetic breakdown was worked out in detail by R.G. Chambers [174], in which he showed

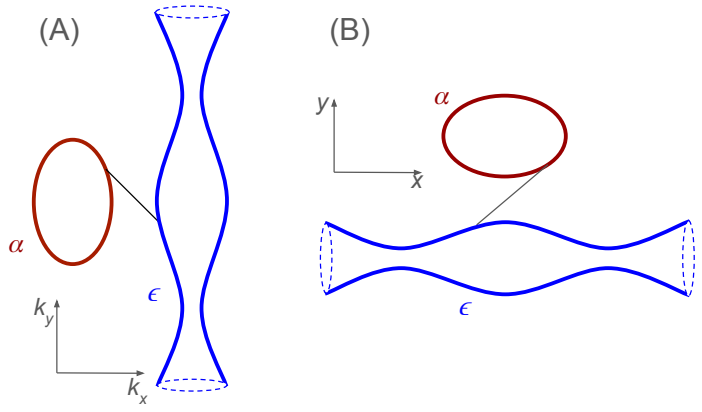

FIGURE A.1: Modeled after [174]. The breakdown region between two orbits (blue and brown - similar to 2D orbits and elliptical in the AV_3Sb_5 respectively). (A) in k space, and (B) in real space. Based on Eq. (A.6), the probability for a carrier to tunnel from orbit α to orbit ϵ is lower for the path shown by thin black line.

that the breakdown field H_0 depends solely on the local geometry of the Fermi surface in the breakdown region. For the Fermi surface (FS) sketched schematically in Fig. A.1, H_0 is given by:

$$H_0 = \frac{\pi\hbar c}{e}\left(\frac{k_g^3}{a+b}\right)^{1/2}, \tag{A.6}$$

where $1/a$ and $1/b$ are the radii of curvature of the two FS sections at points 1 and 2, respectively, and k_g is their separation.

Landau Level Index Plot

The Landau level index plot is a standard approach in which integer or half-integer indices (n) are assigned to minima or maxima of quantum oscillation signals measured versus inverse magnetic field $1/B$. The Landau level index plot emerges naturally from the quantization of electron orbits in a magnetic field. As discussed in the introduction (Ch. 1, Sec. 1.3), in an external magnetic field B, electrons form discrete quantized energy levels known as Landau levels (LLs), where the quantization condition is given by the Onsager relation:

$$A\frac{\hbar}{eB} = 2\pi\left(n+\gamma-\delta\right); \quad \Longrightarrow \quad \frac{A}{B} = \frac{2\pi e}{\hbar}(n+\gamma-\delta) \tag{A.7}$$

where A denotes the cross-sectional area of the electron orbit in momentum space, n is an integer (0, 1, 2, ...), indexing the Landau levels, and γ is a phase factor related directly to the Berry phase accumulated by electrons traversing closed orbits in reciprocal space. The additional term δ arises from the curvature of the Fermi surface in the direction parallel to

the magnetic field. Specifically, the curvature-dependent phase shift δ varies continuously from 0 for an ideal quasi-two-dimensional cylindrical Fermi surface to approximately $\pm 1/8$ for a three-dimensional surface.

When the integer index n is plotted against the inverse magnetic field $1/B$, the resulting plot is called a Landau-level index plot and is linear. The slope of this line yields the frequency F of quantum oscillations, while the intercept contains information about the overall phase offset and therefore can provide information regarding the Berry phase. The assignment of the index is convention dependent. For example, if the peak of the SdH oscillations (R_{osc}) is assigned integer indices and the valley as half indices, then, for quasi-two dimensional cylindrical Fermi surface ($\delta = 0$) an intercept of integer in transport corresponds to a nontrivial Berry phase of π, indicative of relativistic Dirac fermions characteristic of systems such as graphene or topological insulators. And the intercepts approaching half-integer values ($\gamma \approx 1/2$) corresponds to trivial electronic bands (conventional metallic behavior) [38].

Appendix B

Supplemental to $FeSe_{1-x}Te_x$

Comments on magnetism in FeSe

The absence of magnetic order in FeSe is attributed to magnetic frustration arising from competing exchange interactions: (a) nearest-neighbor (NN) exchange (J_1): Fe–Fe interactions along the edges of the square lattice, (b) next-nearest-neighbor (NNN) exchange (J_2): Fe–Fe interactions along the diagonals of the square Fe lattice, and (c) third nearest neighbor exchange (J_3). The J_1-J_2 Heisenberg model on a square lattice fails to produce the double-stripe configuration in FeTe. In [70], the three-neighbor Heisenberg model along with the nearest-neighbor biquadratic exchange interaction $K(S_i \cdot S_j)^2$ (known as J1–J2–J3–K model) produces a FeTe ground state. Together with ab initio calculation, it has been shown that FeSe has a highly frustrated magnetic ground state. Furthermore, magnetic frustration acts in a way that suppresses the magnetic but not the nematic order; resulting in the ferro-orbital order in the nematic phase in FeSe [95].

Temperature derivative of the resistivity

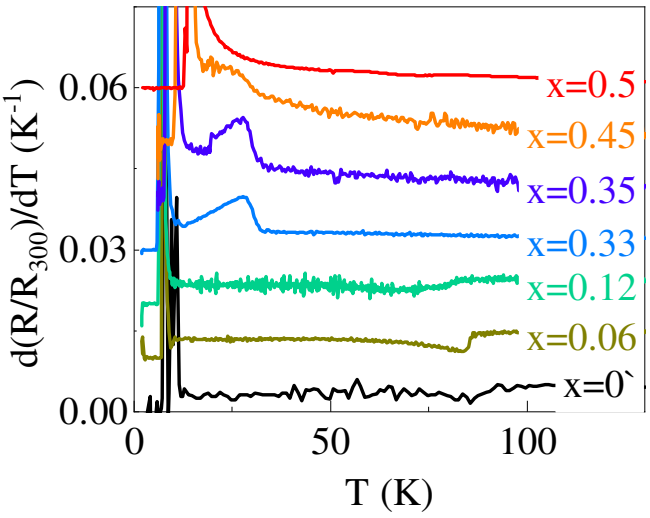

FIGURE B.1: (a) $d(R/R_{300})/dT$ vs. T for all the samples presented in Fig. 3.9

Transport for x=0.33

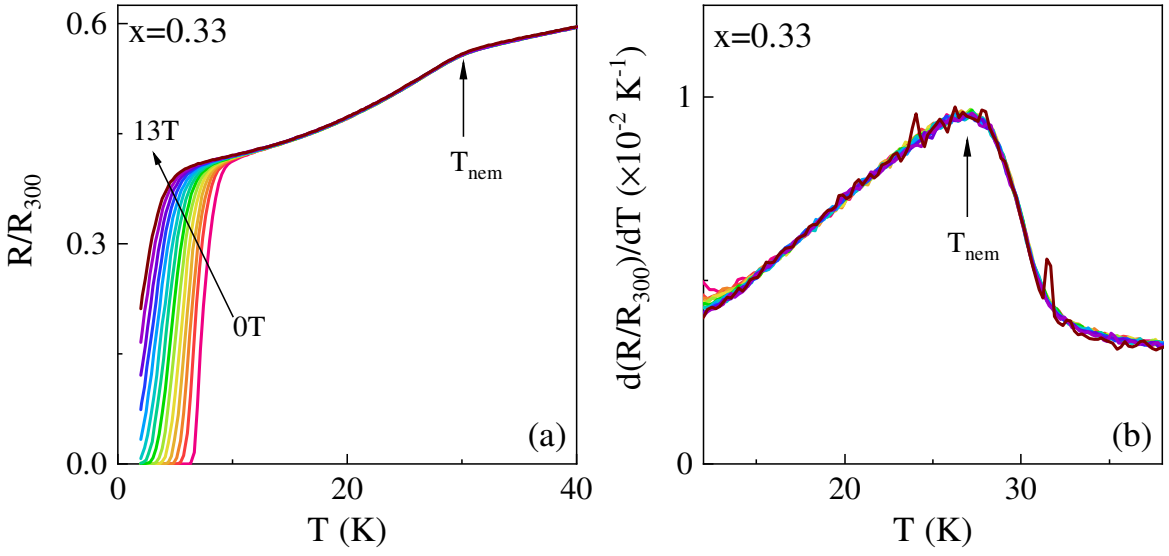

FIGURE B.2: (a) R vs. T for all the external fields (0 to 13 T) up to 40 K and (b) dR/dT for the same indicating near-zero linear magnetoresistance.

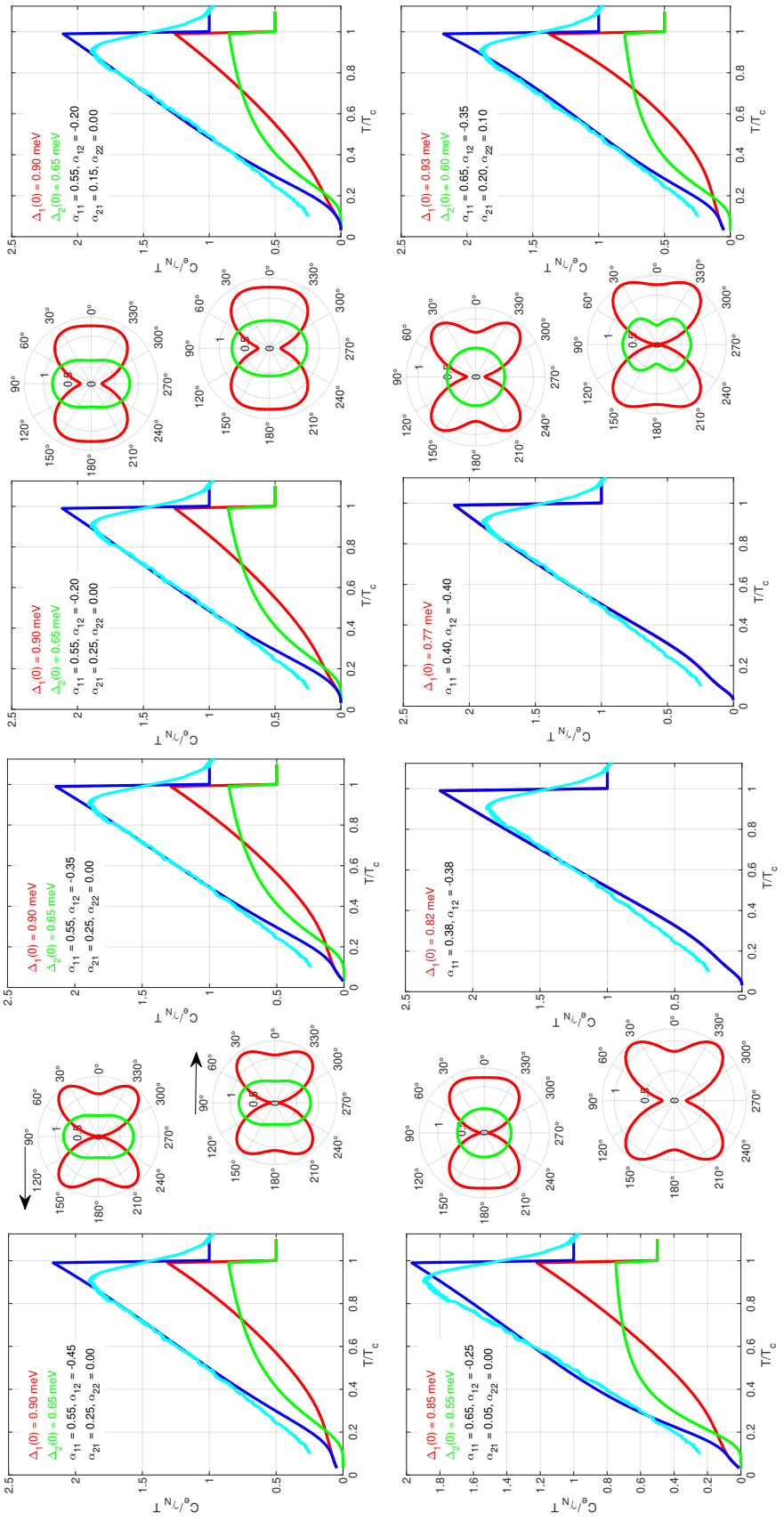

FIGURE B.3: $x = 0.12$: Calculated $C_e\gamma/T$ for different parameters

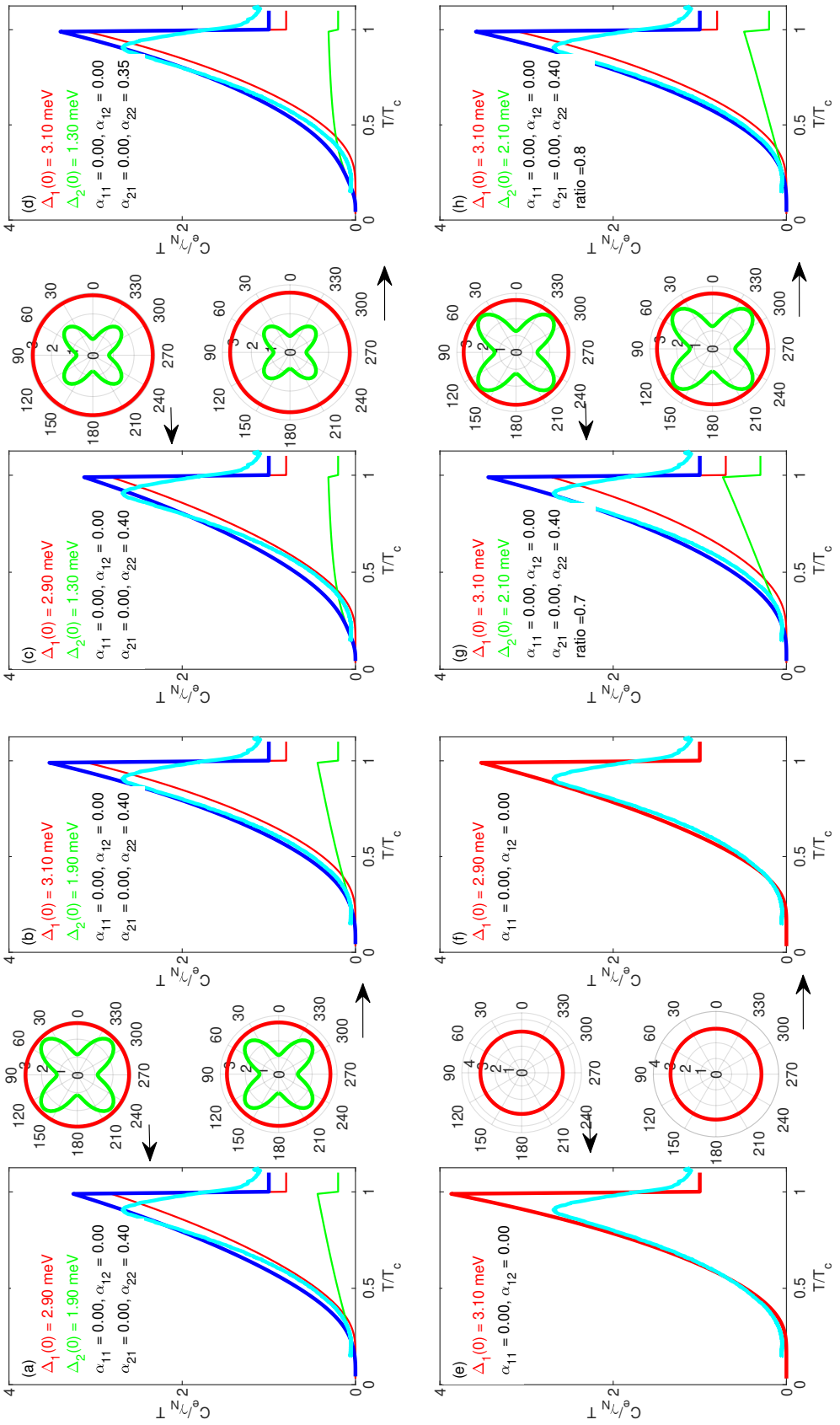

FIGURE B.4: $x = 0.5$: Calculated $C_e\gamma/T$ for different parameters

Various free-energy couplings

One can write the following three free-energy functionals (all strains in Voigt notation as well - note the change in normalization of coefficients as well) for the different couplings between $\mathcal{F}_2$ and the strain-superconductivity coupling $\mathcal{F}_3$:

$$\begin{aligned}
\mathcal{F}_{\text{nemato-elastic}}(\epsilon,\phi) &= \frac{a}{2}\phi^2 + \frac{b}{4}\phi^4 + \frac{C_{66}}{2}\epsilon_6^2 - g_1\epsilon_6\phi \\
\mathcal{F}_{\text{nemato-sc}}(\Delta,\phi) &= \frac{a}{2}\phi^2 + \frac{b}{4}\phi^4 + \frac{\alpha}{2}|\Delta|^2 + \frac{\beta}{4}|\Delta|^4 + \frac{g_2}{2}|\Delta|^2\phi^2 \\
\mathcal{F}_{\text{elastic-sc}}(\Delta,\epsilon) &= \frac{C_s}{2}\epsilon_s^2 + \frac{\alpha}{2}|\Delta|^2 + \frac{\beta}{4}|\Delta|^4 + \frac{g_3}{2}|\Delta|^2\epsilon_s^2
\end{aligned} \tag{B.1}$$

The shear strain ϵ_6 and the orthorhombic order parameter δ both can serve as the nematic order parameter under some conditions. The resistivity anisotropy $\eta = (\rho_b - \rho_a)/2$ may also serve as the nematic order parameter.

Derivation for $d^2F/d\epsilon^2$

$$\frac{d^2F}{d\epsilon^2} = \frac{\partial^2 F}{\partial\epsilon^2} - \left(\frac{\partial^2 F}{\partial\epsilon\partial\phi}\right)^2 \left(\frac{\partial^2 F}{\partial\phi^2}\right)^{-1} \tag{B.2}$$

Since $F = F(\epsilon,\phi)$ and $\phi = \phi(\epsilon)$, one gets:

$$\frac{dF}{d\epsilon} = \frac{\partial F}{\partial\epsilon} + \frac{\partial F}{\partial\phi}\frac{d\phi}{d\epsilon} \tag{B.3}$$

But at equilibrium, $\frac{\partial F}{\partial\phi} = 0$ (from the minimization condition). Therefore:

$$\frac{dF}{d\epsilon} = \frac{\partial F}{\partial\epsilon} \tag{B.4}$$

Then the required second derivative of F is:

$$\begin{aligned}
\frac{d^2F}{d\epsilon^2} &= \frac{d}{d\epsilon}\left(\frac{dF}{d\epsilon}\right) = \frac{d}{d\epsilon}\left(\frac{\partial F}{\partial\epsilon}\right) \\
\frac{d^2F}{d\epsilon^2} &= \frac{\partial^2 F}{\partial\epsilon^2} + \frac{\partial^2 F}{\partial\epsilon\partial\phi}\frac{d\phi}{d\epsilon}
\end{aligned} \tag{B.5}$$

The term $d\phi/d\epsilon$ can be found using the implicit function theorem based on the equilibrium condition:

$$\begin{aligned} & \frac{\partial F}{\partial \phi} = 0 \\ \text{differentiating w.r.t. } \epsilon: \quad & \frac{d}{d\epsilon}\left(\frac{\partial F}{\partial \phi}\right) = 0 \\ \text{apply chain rule:} \quad & \frac{\partial^2 F}{\partial \epsilon \partial \phi} + \frac{\partial^2 F}{\partial \phi^2}\frac{d\phi}{d\epsilon} = 0 \implies \frac{d\phi}{d\epsilon} = -\left(\frac{\partial^2 F}{\partial \epsilon \partial \phi}\right)\left(\frac{\partial^2 F}{\partial \phi^2}\right)^{-1} \end{aligned} \tag{B.6}$$

Substituting this into the expression for $\frac{d^2F}{d\epsilon^2}$:

$$\begin{aligned} \frac{d^2F}{d\epsilon^2} &= \frac{\partial^2 F}{\partial \epsilon^2} + \frac{\partial^2 F}{\partial \epsilon \partial \phi}\left(-\left(\frac{\partial^2 F}{\partial \epsilon \partial \phi}\right)\left(\frac{\partial^2 F}{\partial \phi^2}\right)^{-1}\right) \\ \frac{d^2F}{d\epsilon^2} &= \frac{\partial^2 F}{\partial \epsilon^2} - \left(\frac{\partial^2 F}{\partial \epsilon \partial \phi}\right)^2\left(\frac{\partial^2 F}{\partial \phi^2}\right)^{-1} \end{aligned} \tag{B.7}$$

Nematic susceptibility and the resulting temperature dependence of C_{66}:

The susceptibility χ_N measures how the order parameter ϕ responds to an external field h that couples linearly to the nematic order. Thus, the total *nematic* free energy including the external field is: $F_{nem} = \frac{a}{2}\phi^2 + \frac{b}{4}\phi^4 - h\phi$. Then at equilibrium, the component of the free energy is minimum with respect to the order parameter:

$$\begin{aligned} \frac{dF_{nem}}{d\phi} &= a\phi + b\phi^3 - h = 0 \\ \text{in linear response limit, } & a\phi = h \\ \text{nematic susceptibility, } \chi_N &= \frac{d\phi}{dh} = \frac{1}{a} = \frac{1}{a_0(T - T_S^b)} \end{aligned} \tag{B.8}$$

where $a = a_0(T - T_S^b)$ (see Sec. 2.2.1). For the bilinearly coupled nemato-elastic problem, Eq. (4.4) can be written as:

$$F = F_0 + 2C_{66}\epsilon_{xy}^2 - 2\lambda\phi\epsilon_{xy} + \frac{a}{2}\phi^2 + \frac{b}{4}\phi^4 \tag{B.9}$$

with $a = 1/\chi_N$ as discussed above. Following [129], the temperature dependence of C_{66} above the transition (in tetragonal phase) is then given by:

$$\begin{aligned} \bar{C}_{66} &= C_{66} - \lambda^2\chi_0/(T - T_S^b) \\ \bar{C}_{66}/C_{66} = \frac{T - T_S^{CW}}{T - T_S^b} \quad & \text{and} \quad T_S^{CW} = \lambda^2\chi_0/C_{66} + T_S^b \end{aligned} \tag{B.10}$$

Confirmation for the bending measurements being in the elastic regime

The relationship between the applied force F and deflection u of the material in the elastic regime is governed by Hooke's Law:

$$F = k_s u \tag{B.11}$$

where k_s is the stiffness of the material. Stiffness is a constant determined by both the material properties and the geometry of the sample under study.

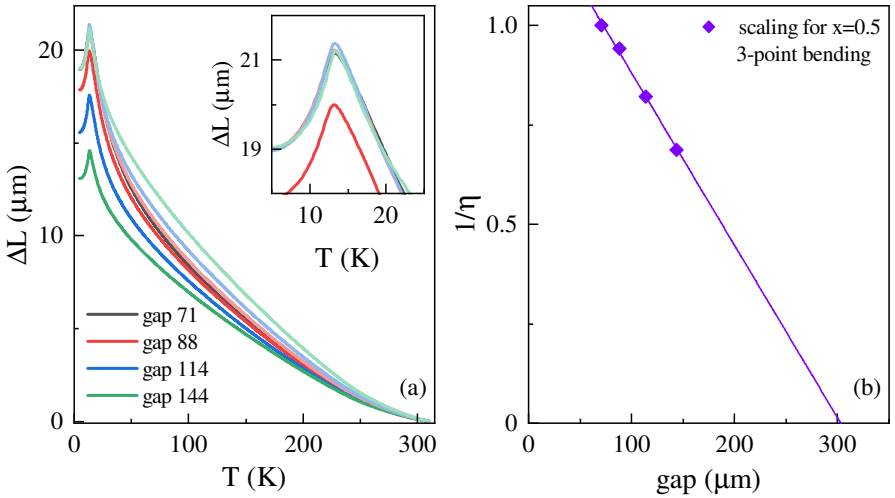

FIGURE B.5: Check for whether 3-point-bending measurements are within elastic regime or not (a) measurements at different gaps, inset: scaled curves overlap well in the hardening regime at low temperatures, (b) inverse of the scaling used to scale the curves.

In the elastic regime, the deflection u is directly proportional to the applied force. As the force increases, the deflection increases proportionally:

$$u \propto F \tag{B.12}$$

For two different applied forces, F_{test} (a test force, higher gap values (88, 114, 144)) and F_{max} (the maximum applied force, corresponding to gap 71 in Fig. B.5, the corresponding deflections u_{test} and u_{max} satisfy the following relationship:

$$\frac{u_{\text{test}}}{u_{\text{max}}} = \frac{F_{\text{test}}}{F_{\text{max}}} \tag{B.13}$$

Scaling Factor η: To compare deflection curves at different forces, a scaling factor η is introduced. The scaling factor η is defined as the factor by which the deflection curve

at a lower test force F_{test} needs to be multiplied in order to align with the deflection curve for the maximum force F_{max}. This is performed in the low-temperature regime, where hardening occurs due to superconducting temperature. At low temperatures, the stiffness is highest, so the scaling is done to *match* in the low-temperature region, i.e., $u_{\text{test}} \times \eta = u_{\text{max}}$.

Since deflection is proportional to force in the elastic regime, the scaling factor η can be written as:

$$\eta \propto \frac{F_{\text{max}}}{F_{\text{test}}} \tag{B.14}$$

Thus, the plot of $\frac{1}{\eta}$ versus F_{test} forms a straight line Fig. B.5(b), as long as the measurements are within the elastic regime.

Case for diverging nematic correlation lengths: $\nu z \to \infty$

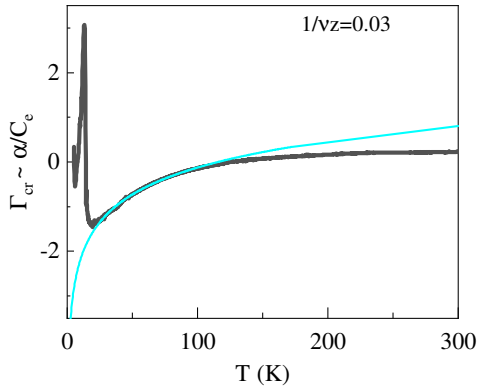

FIGURE B.6: Case for $\nu z \to \infty$ (a value of 30) discussed in the logarithmic estimation of QCP

B.1 XRD data for $FeSe_{1-x}Te_x$

	$FeSe_{1-x}Te_x$	$x = 0$	$x = 0.339(13)$	$x = 0.483(9)$	$x = 0.516(8)$
	a (Å)	3.7688(7)	3.7922(7)	3.7913(7)	3.7948(2)
	c (Å)	5.520(1)	5.8422(14)	5.945(3)	5.986(1)
	c/a	1.465	1.541	1.568	1.577
Fe1	U_{11} (Å^2)	0.0108(5)	0.0135(6)	0.0096(2)	0.0106(1)
	U_{33} (Å^2)	0.0226(6)	0.0313(13)	0.0184(5)	0.0187(2)
Se/Te	z	0.26680(9)	0.27155(18)	0.27794(9)	0.27984(7)
	U_{11} (Å^2)	0.0138(4)	0.0172(3)	0.0126(1)	0.0129(1)
	U_{33} (Å^2)	0.0184(4)	0.0392(8)	0.0365(4)	0.0368(2)
Fe2	z	–	-	0.6969(16)	0.6991(9)
	U_{iso} (Å^2)	–	-	0.0111(21)	0.0134(12)
	SOF	–	-	0.080(4)	0.105(3)
	wR_2 (%)	4.67	4.01	2.70	3.56
	R_1 (%)	1.92	2.08	1.49	1.53

TABLE B.1: Refined structural parameters for $FeSe_{1-x}Te_x$ at $x = 0$, $x = 0.34$, $x = 0.48$, and $x = 0.51$. Listed are the lattice parameters a and c, relative atomic coordinates (z), isotropic (U_{iso}) or anisotropic (U_{11}, U_{33}) displacement parameters, site occupancy factors (SOF), and final refinement residuals wR_2 and R_1. Statistical errors are given in parentheses. [119] - Dr. M. Merz (IQMT)

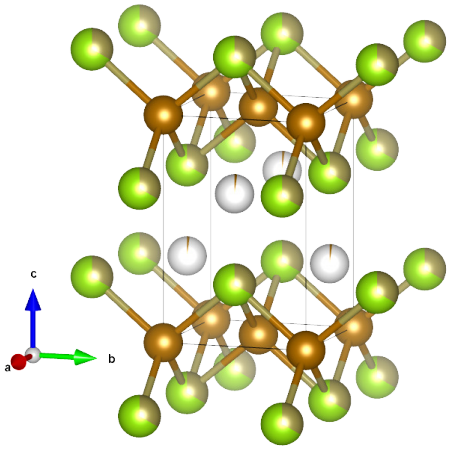

FIGURE B.7: Crystal-structure from XRD for x=0.33 showing near-zero occupancy of interstitial Fe sites - Dr. M. Merz (IQMT)

Appendix C

Supplemental to AV_3Sb_5

Predicted superconducting gap structure

Even in the experiments where s-wave nodeless superconductivity is predicted [175] in AV_3Sb_5, multi-gap features have been observed (two isotropic s-wave gaps). However, the origin of these multi-band effects or gap anisotropy has been contested [160, 176]. Aside from the gap structure, the interplay between superconductivity and charge order has also been extensively studied, especially using STM [26]. Distinct effects are recorded in the superconducting state for $(Rb,K)V_3Sb_5$ compared to Cs- when the charge order is suppressed using pressure or doping. For the latter, a two dome structure is observed in $(x/P, T_c)$ whereas in (Rb-, K-), a single dome is observed in T_c.

singlet	triplet	nodal/ deep anisotropy	nodeless
NMR/ NQR [30]	Coh. length & Josephson J^n -[177]	STM (K-) [179]	NMR/NQR [30]
transport & I-V [175]	transport [178]	STM [180]	penetration depth and sp. heat [182]
	transport [156]	thermal conductivity [27]	sp. heat (K-) [183]
		STM [28]	ARPES[2] [184]
		STM[1] [29]	
		μSR (Rb-, K-) [181]	

TABLE C.1: References and experimental methods used to predict the superconducting gap structure of different members of AV_3Sb_5.

[1]In Ref. [29] multiband behavior is predicted, however, distinction is not made whether a deep anisotropy or nodes exist.

[2]In Ref. [184], the measurements are done in Ta and Nb-substituted CsV_3Sb_5 when CDW is suppressed.

Multi-Q Ginzburg-Landau theory

Here, we provide details of the Ginzburg-Landau (GL) formalism used to describe the multi-**Q** charge density wave (CDW) in AV_3Sb_5. We define three order parameters, $\Delta_1, \Delta_2, \Delta_3$, corresponding to density modulations at wave vectors $\mathbf{Q}_1, \mathbf{Q}_2, \mathbf{Q}_3$. By symmetry, when $\mathbf{Q}_1 + \mathbf{Q}_2 + \mathbf{Q}_3 = 0$, a trilinear (cubic) term in the free energy is permitted. For simplicity, we treat Δ_i as real scalar amplitudes. Near T_{CDW}, the relevant GL free energy can be expressed as

$$\mathcal{F} = \frac{a}{2}\sum_{i=1}^{3}\Delta_i^2 + \frac{w}{3}\Delta_1\Delta_2\Delta_3 + \frac{u_1}{4}\sum_{i=1}^{3}\Delta_i^4 + \frac{u_2}{4}\sum_{i\neq j}\Delta_i^2\Delta_j^2, \tag{C.1}$$

where a is proportional to $(T - T_{\mathrm{CDW}})$ and changes sign at the transition. The quartic terms $u_1, u_2 > 0$ stabilize the ordered phase. A large $|w|$ (typically associated with strong electron-phonon coupling) can tilt the free energy, favoring a *first-order* transition by creating a local minimum at nonzero Δ_i even when $a > 0$.

At the CDW transition, electronic modulations at wavevector **Q** couple strongly to lattice distortions, making the lattice distortion (δ) practically proportional to the electronic order parameter (Ψ). The primary instability originates electronically (Fermi-surface nesting or electron correlations), with electron–phonon coupling causing the lattice distortion. Thus, while the true order parameter is electronic density modulation, lattice distortion provides a measurable proxy. In AV_3Sb_5, the lattice energy vs. distortion δ is not simply a symmetric (even) function, but has a tilt (odd component) favoring the positive distortion [149]. In the CDW free energy expression, this is related to the cubic term (odd term). Microscopically, the amplitude of this tilt depends on how strongly the lattice distortion pays off in energy once the electrons form a CDW. The electron-phonon coupling relates the lattice distortion to the density modulation. Thus, one can state that the energy payoff due to asymmetric lattice distortion maybe influenced by the electron–phonon coupling [150].

Implications for $(Cs, Rb)V_3Sb_5$**:** Although CsV_3Sb_5 shows a stronger first-order transition, RbV_3Sb_5 achieves a higher T_{CDW}, reflecting the fact that $\lambda_{e\text{-ph}}$ is not the sole factor determining the transition temperature. Band-structure effects, correlation physics, and structural effects (subtle Sb apical atoms displacement [147]) can all raise or lower T_{CDW}, leading to a complex interplay between the first-order nature and the actual value of T_{CDW}.

Transport anomaly at 30 K in field

The effect of the orbital flux phase will also be opposite to the enhanced conduction. The orbital flux phase is characterized by spontaneous bond currents that form patterns of loop currents. While no finite flux/charge order exists below T_{CDW} at zero magnetic fields [154, 185] and is induced only for finite fields, enhanced skew-scattering due to the magnetic fluctuations in the triangular cluster formed by V moments may still occur and can provide an additional scattering mechanism. Application of finite magnetic field can induce loop currents in the system [185] and is associated with the large AHE in these systems [160, 186]. The application of magnetic field on the normalized transport of CsV_3Sb_5 is shown in Fig. C.1(a). While the large AHE is well reproduced, the effects in the temperature dependence are not particularly strong (C.1(c, d)).

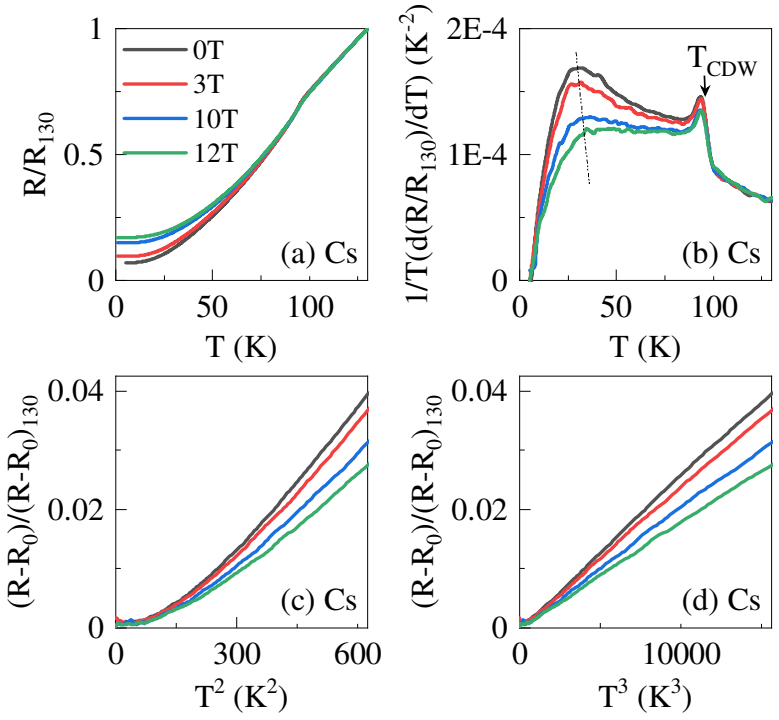

FIGURE C.1: (a) Normalized resistance vs temperature curves for CsV_3Sb_5 in different external magnetic fields parallel to c-axis, (b) shows the corresponding scaled derivative ($(1/T)(dR_{130}/dT)$). The dotted line (guide to the eye) shows the T^*. At temperatures above T^* and below T_{CDW}, with the increase in field, curves shift to T^2 trend. (c,d) Show the normalized resistance vs temperature curves post residual subtraction. Comparison of (c) T^2 and (d) T^3 dependence showcasing the low temperature behavior and its *robustness* to the magnetic field. The color code is same for all the graphs.

Largest expected QO frequency from the *size* of BZ

Compound	Lattice constant a(Å)	Area of undistorted BZ, $A_{undist.}(\text{Å}^{-2}) = \frac{8\pi^2}{\sqrt{3}a^2}$	Area of BZ in CDW, $A_{\text{CDW}} = A_{undist.}/4$	Freq. F (T)
CsV_3Sb_5	5.5236(7)	1.494	0.3735	3921
RbV_3Sb_5	5.4941(7)	1.510	0.3775	3963
KV_3Sb_5	5.4260(9)	1.548	0.3870	4063

TABLE C.2: Lattice parameter taken from [25] and estimation of the fictitious frequency corresponding to the complete BZ using Onsager's formula 1.11 for AV_3Sb_5.

Estimation of change of c-axis in $(Cs, K)V_3Sb_5$ relative to RbV_3Sb_5:

Compound	Lattice constant		c/a	$\frac{(c-c_{\text{Rb}})}{c_{\text{Rb}}}$
	a(Å)	c(Å)		
CsV_3Sb_5	5.5236(7)	9.3623(15)	1.6949	+2.8%
RbV_3Sb_5	5.4941(7)	9.1071(15)	1.6576	-
KV_3Sb_5	5.4260(9)	8.845(2)	1.6301	−2.8%

TABLE C.3: Lattice parameter taken from [25] and estimation of change of c-axis relative to RbV_3Sb_5.

Effects of the frequency resolution

We consider a generic oscillatory signal for any physical quantity Q periodic in $1/B$, and has three frequencies f_i:

$$Q = \left[A_1 \cos\left(\frac{2\pi f_1}{B}\right) e^{-T_{D1}/B}\right] + \left[A_2 \cos\left(\frac{2\pi f_2}{B}\right) e^{-T_{D2}/B}\right] + \ldots + \left[A_3 \cos\left(\frac{2\pi f_3}{B}\right) e^{-T_{D3}/B}\right] + (\text{noise amplitude}) \tag{C.2}$$

We consider the $f_i = 16,\ 28,\ 200\,\text{T}$ for $i = 1, 2, 3$, i.e., two low frequencies and one intermediate. The T_{Di} mimic the effects of Dingle mechanism. Finally, a noise amplitude is added to make the signal realistic. The B-window is varied between 4 T-100 T. The important results are summarized in Fig. C.2 (a-h), which show that for low frequencies such as 16, 28 T, the number of periods is approximately 3, even if measurements are made up to 100 T (the oscillations are periodic in $1/B$). Thus, the high-field measurements

cannot resolve them reliably; rather, these low frequencies can only be detected if the oscillations are present and well-resolved at low magnetic fields.

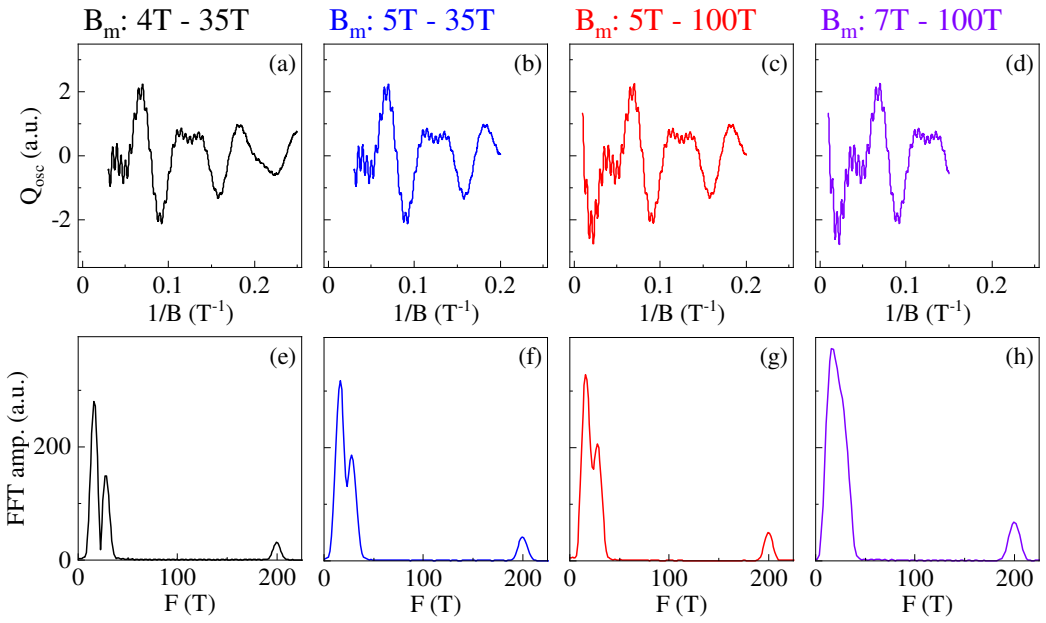

FIGURE C.2: Simulated windowing effects in quantum oscillation spectra: (a-d) Q_{osc} vs. $1/B$ generated using Eq. (C.2) for different field windows, along with their corresponding (e-h) FFTs in the same color code. (a-c) For very low frequencies, the oscillatory signal must be finite at low magnetic fields to be resolved using FFT. (d) The two low frequencies cannot be resolved, even at very high fields (mimicking pulsed facilities), due to insufficient oscillatory periods.

Masses of the low frequency orbits in CsV3Sb5

The mass extracted using the Lifshitz-Kosevich (LK) formula, $A_i(T) \approx \frac{(14.69m^*T)/B}{\sinh(14.69m^*T/B)}$, is shown in Fig. C.3. The estimated effective mass of the α, β, γ, and δ-band are $0.03m_e$, $0.03m_e$, $0.10m_e$, and $0.09m_e$ respectively. These small effective masses are in agreement with the previous reports of very low mass for these bands [50]. The effective mass ($m_s \approx 0.10$) extracted for the 72 T SdH feature does not simply match $(m_2 - m_1)$. This is consistent with elliptical or non-parabolic band dispersions, where the difference (or sum) frequency will possibly inherit a more complicated cyclotron mass that cannot be written as $|m_2 \pm m_1|$. Thus, it is quite plausible that the defect-assisted scattering between the ~ 90 T V-pocket and a faint ~ 18 T pocket generates a difference-frequency signal $\Delta F = 72$ T in SdH but not in dHvA, and that its measured mass deviates from a difference of the individual effective masses.

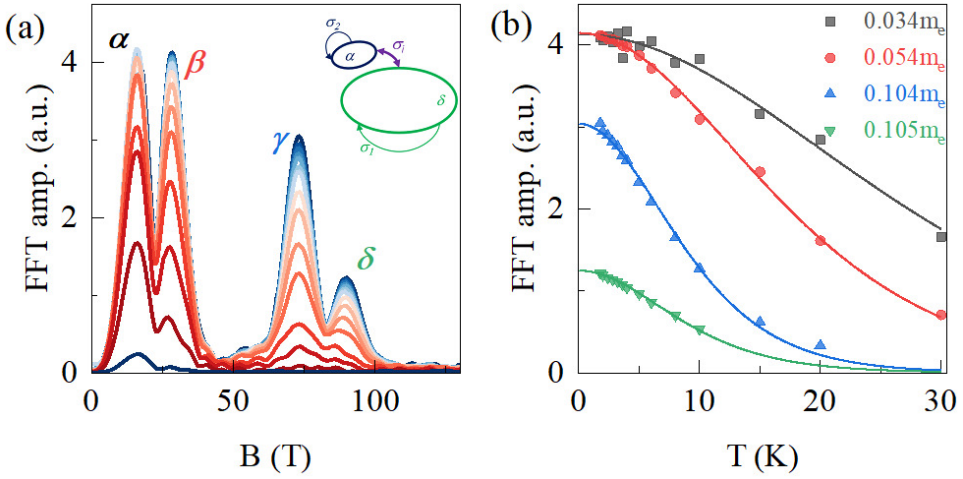

FIGURE C.3: (a) FFT amplitude vs frequency for CsV_3Sb_5 obtained from electrical transport. Inset shows the schematic of possible interband and intraband coupling. (b) FFT amplitude for the four frequencies in (a) plotted against temperature to obtain mass of the orbit. The thick lines denote the fit using LK formula.

Residual DOS and the open-question of the multi-band features

From tunneling-microscopy measurements, all AV_3Sb_5 (A = K, Rb, Cs) samples exhibit a substantial residual density of states (DOS). The low-temperature heat-capacity data [Fig. C.4] also corroborate this observation, as C_e/T remains finite within the superconducting phase. Here, we first focus on the superconducting heat capacity of CsV_3Sb_5, for which data down to $T \approx 0.4\,T_c$ are available. This compound also appears to be the cleanest among the three.

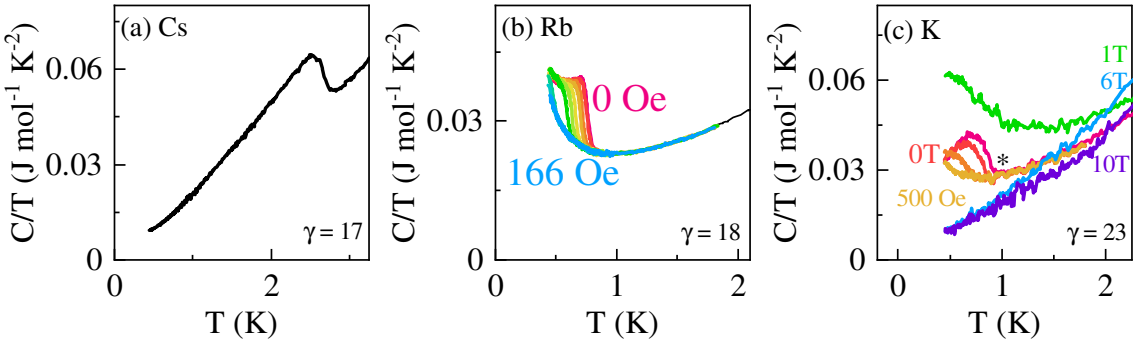

FIGURE C.4: Heat capacity C vs T for AV_3Sb_5 single crystals, where (a) A = Cs, (b) A = Rb, and (c) A = K. Sharp jumps occur at the charge density wave (CDW) transition.

Figure C.5(a) displays C/T vs T^2 for CsV_3Sb_5, highlighting the residual Sommerfeld coefficient, $\gamma_r \approx 6$ mJ mol^{-1} K^{-2}. The electronic contribution to the specific heat, normalized by the normal-state Sommerfeld coefficient, $C_e/(\gamma_N T)$, is shown in Fig. C.5(b). The black curve includes the residual DOS, whereas the dark-yellow curve excludes it. For

comparison, an ideal single-gap BCS curve is plotted as well. Once the residual DOS is subtracted, the resulting curve for Cs-based samples closely resembles the single-gap BCS behavior.

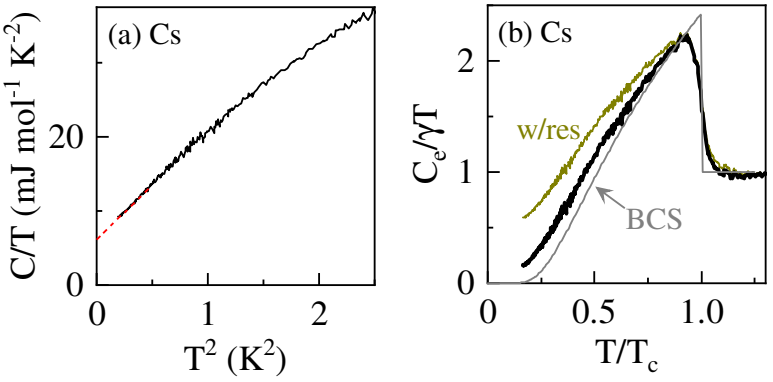

FIGURE C.5: (a) Heat capacity plotted as C/T vs T^2 for CsV_3Sb_5, illustrating the finite residual DOS, γ_r. (b) The electronic specific heat, $C_e/(\gamma_N T)$, vs T/T_c, with and without subtracting the residual DOS. For comparison, the dashed line shows the ideal BCS behavior.

In both RbV_3Sb_5 and KV_3Sb_5, the extraction of $C_e/(\gamma T)$ is complicated by large Schottky anomalies at low temperatures, as well as by relatively low superconducting transition temperatures ($T_c < 1\,\mathrm{K}$). Schottky anomalies arise from discrete low-energy excitations—often localized states or paramagnetic impurities—whose energy splitting is on the order of $k_B T$ at low temperature. For RbV_3Sb_5, a clear $1/T^3$ trend dominates the low-temperature data. In KV_3Sb_5, measurements under an applied magnetic field reveal a Schottky-like peak in C vs B at $B \approx 0.5\,\mathrm{T}$ [Fig. C.4(c)].

Frequency-resolved magnetization and magnetostriction comparison:

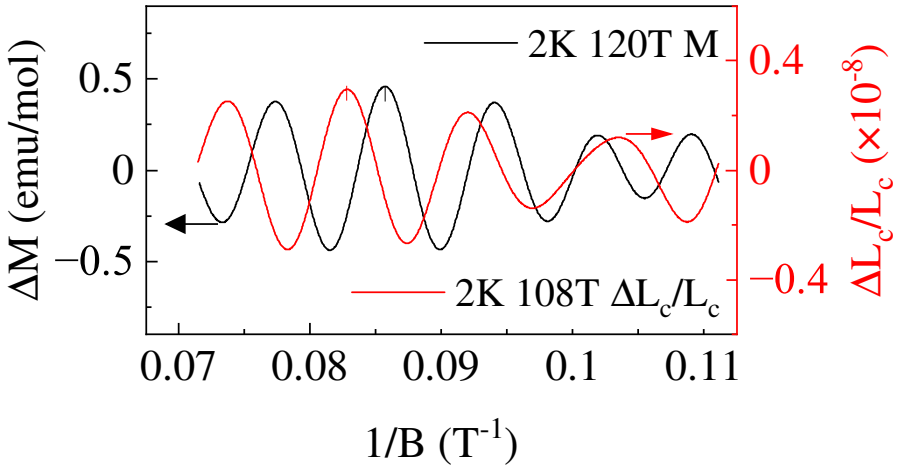

FIGURE C.6: FFT filtered oscillatory magnetization ΔM (black curve, left axis) and c-axis magnetostriction $\Delta L_c/L_c$ (red curve, right axis) in RbV3Sb5, measured at $T =$ 2 K and 2.1 K, respectively, as functions of the inverse magnetic field $1/B$.

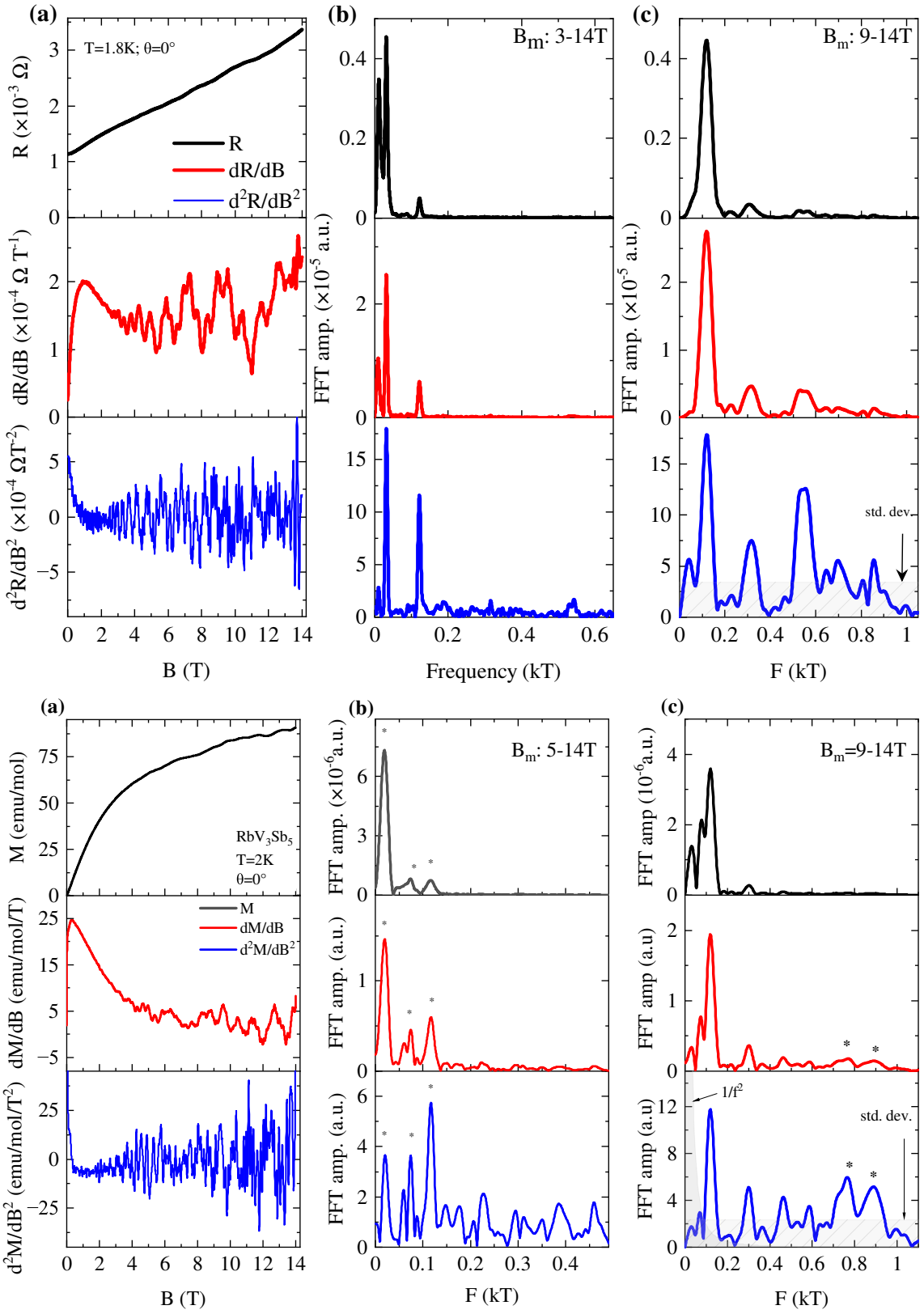

FIGURE C.7: Example determination of the frequencies in the (top) electrical transport and (bottom) magnetization of RbV_3Sb_5. The lowest temperature data was taken and its derivative and double derivative were taken. Column (b) and (c) represent different window ranges B_m.

C.1 Analysis of the quantum oscillation data

Temperature dependence for CsV_3Sb_5 transport data

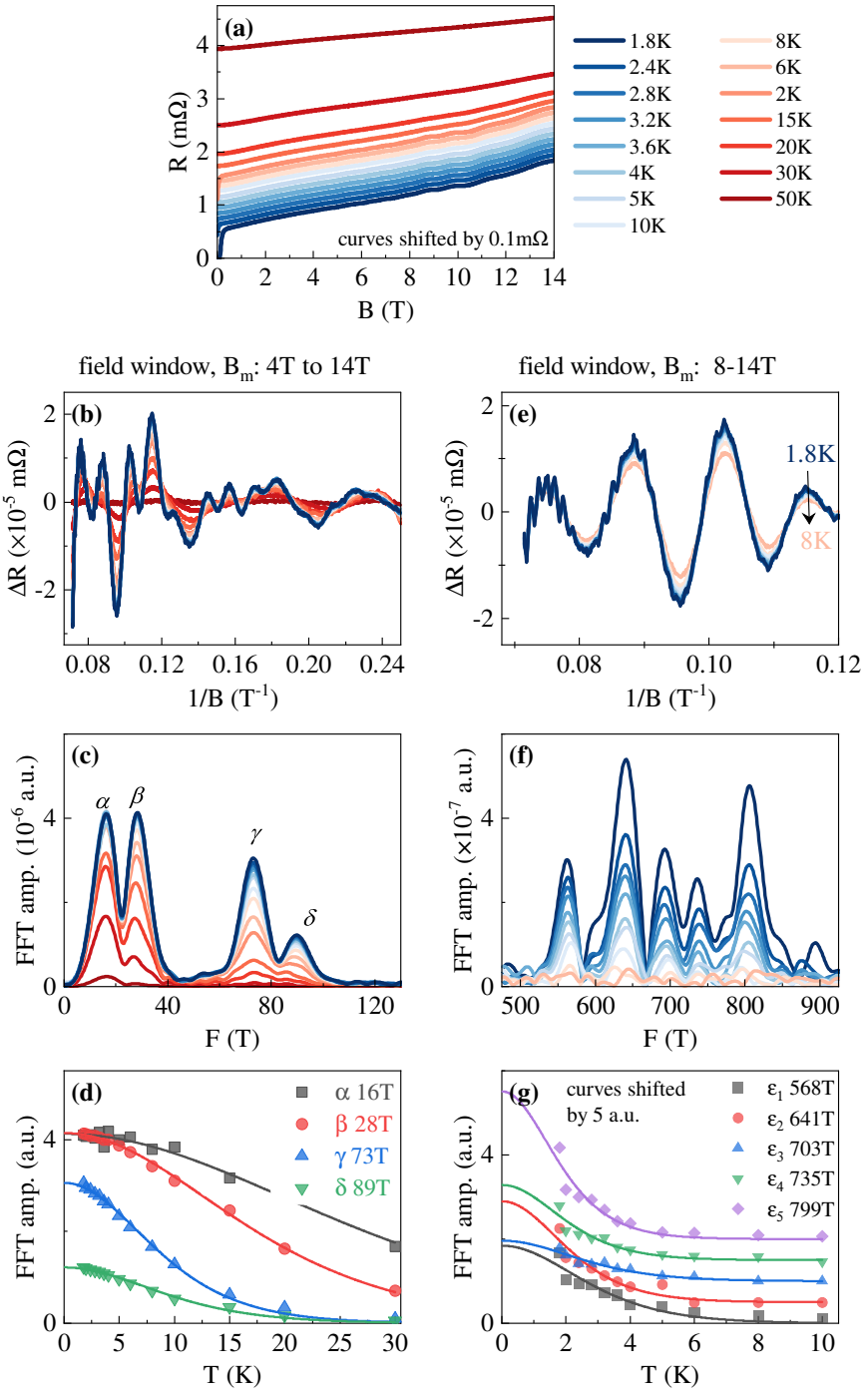

FIGURE C.8: Quantum Oscillations in *electrical transport* for CsV_3Sb_5: (a) shows the resistance vs external magnetic field along $c-$axis for different temperatures. For the 4-14 T window, panel (b-d) show the (b) oscillating part of the R extracted by subtracting a polynomial against inverse of B_{ext}, (c) the FFT of this signal and the (d) masses extracted using Eq. (1.14). Panel (e-g) show the same for 8-14 T window.

Temperature dependence for CsV_3Sb_5 magnetization data

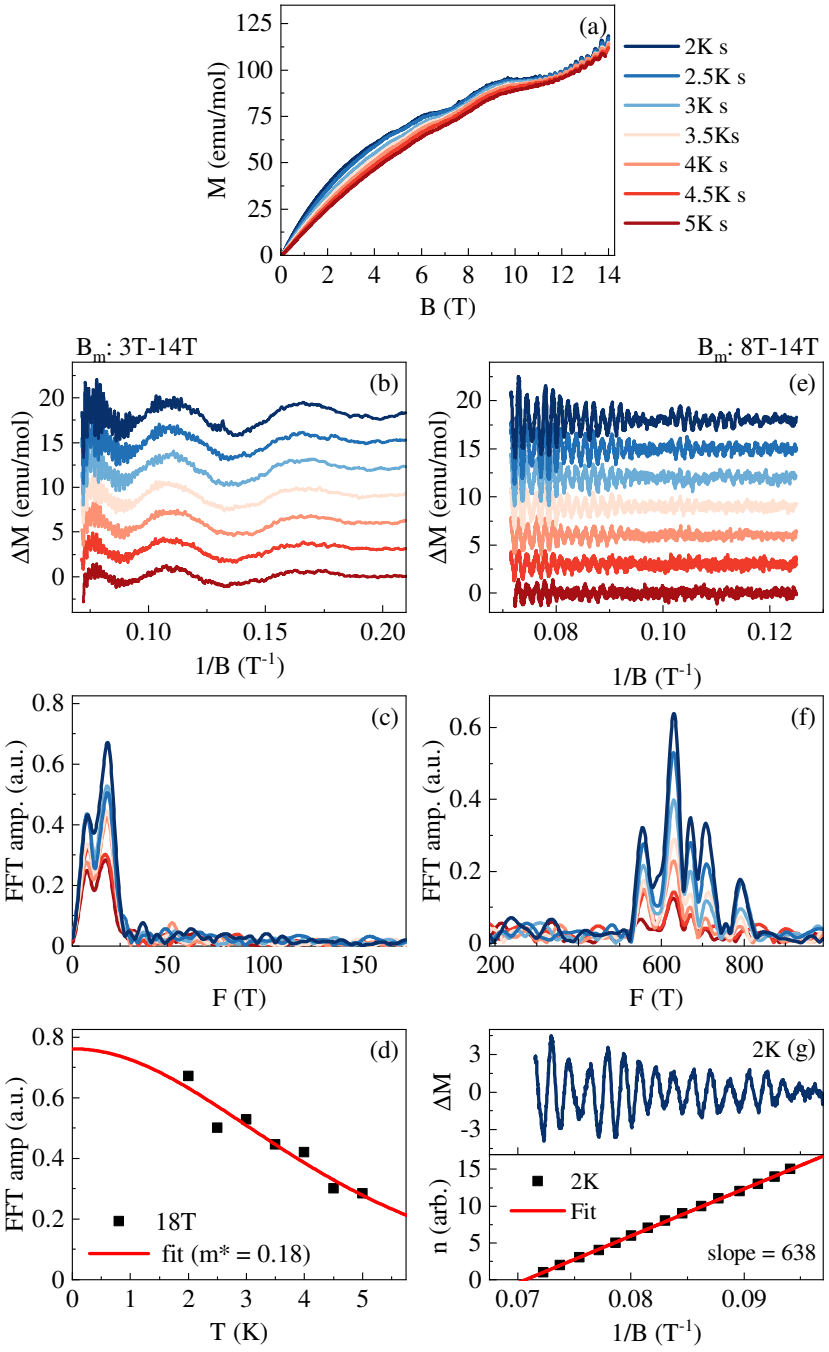

FIGURE C.9: Quantum Oscillations in *magnetization* for CsV_3Sb_5: (a) shows the magnetization vs external magnetic field along $c-$axis for different temperatures. For the 3-14 T window, panels (b-d) show the (b) oscillating part (curves shifted) of the M extracted by subtracting a polynomial against inverse of B_{ext}, (c) the FFT of this signal and the (d) masses extracted using Eq. (1.14). For the 8-14 T window, panel (e-g) show the (e) oscillating part (curves shifted) of the M, and (f) the FFT of the oscillatory part. This gives the mid-frequency spectra with 5 frequencies. (g) Shows that for the 2 K, M_{osc} has 638 T as dominant frequency which can be seen by direct index plot. The integer n here is arbitrary and is not the same as the Landau-level index used in an LL-index plot

Temperature dependence for RbV_3Sb_5 transport data

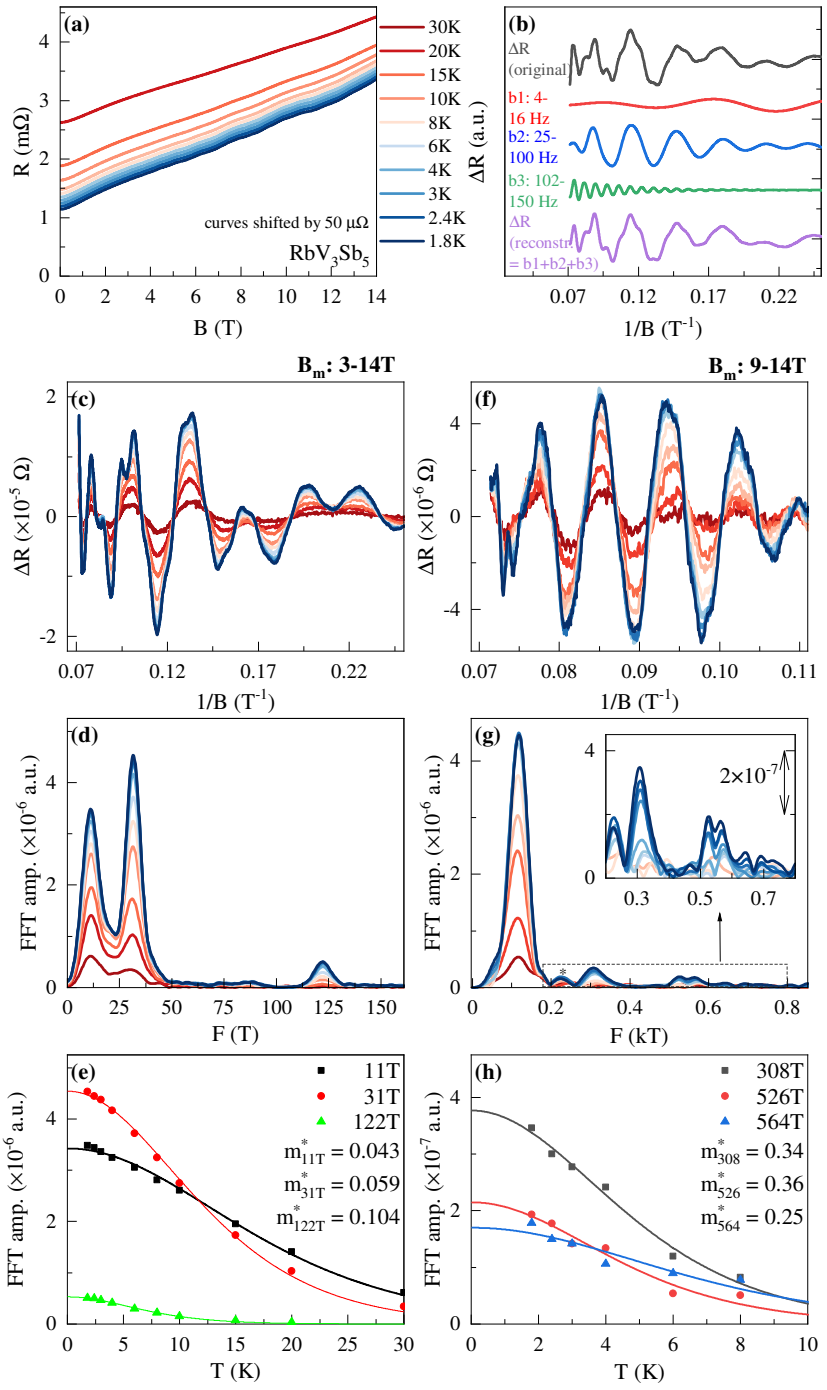

FIGURE C.10: Quantum Oscillations in *electrical transport* for RbV_3Sb_5: (a) shows the resistance vs external magnetic field along $c-$axis for different temperatures, the decomposition and the reconstruction of the raw signal at 1.8 K into different frequency components is shown in (b). For the 3-14 T window, panel (c-e) show the (c) oscillating part of the R extracted by subtracting a polynomial against inverse of B_{ext}, (d) the FFT of this signal and the (e) masses extracted using Eq. (1.14). Panel (f-h) show the same for 9-14 T window. Inset of (g) shows the mid-frequency spectrum where 3 frequencies 308 T, 526 T, 564 T are observed. These last two frequencies however are near limit in the resolution and hence not counted. Color code is same for all the figures except (b).

Temperature dependence for RbV_3Sb_5 magnetization data

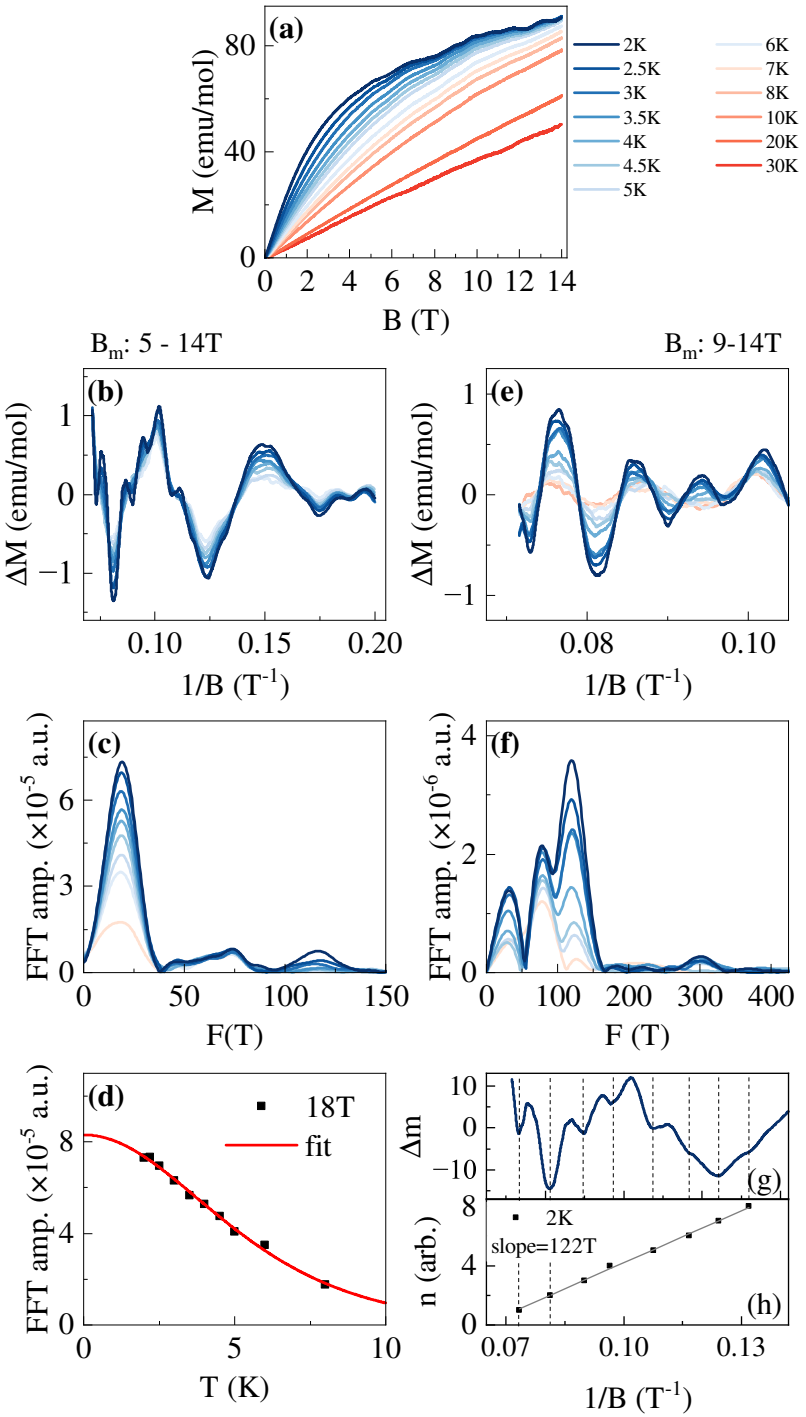

FIGURE C.11: Quantum Oscillations in *magnetization* for RbV_3Sb_5: (a) shows the magnetization vs external magnetic field along $c-$axis for different temperatures. For the 3-14 T window, panel (b-d) show the (b) oscillating part of the M extracted by subtracting a polynomial against inverse of B_{ext}, (c) the FFT of this signal and the (d) mass extracted using Eq. (1.14) for 18 T frequency. For the 9-14 T window, panel (e-g) show (e) the oscillatory component of the signal, and the corresponding (f) FFT of this signal. (g,h) show the index plot for the oscillatory signal at 2 K in 5-14 T window highlighting the dominant 122 T frequency in the spectrum.

Temperature dependence for KV_3Sb_5 transport data

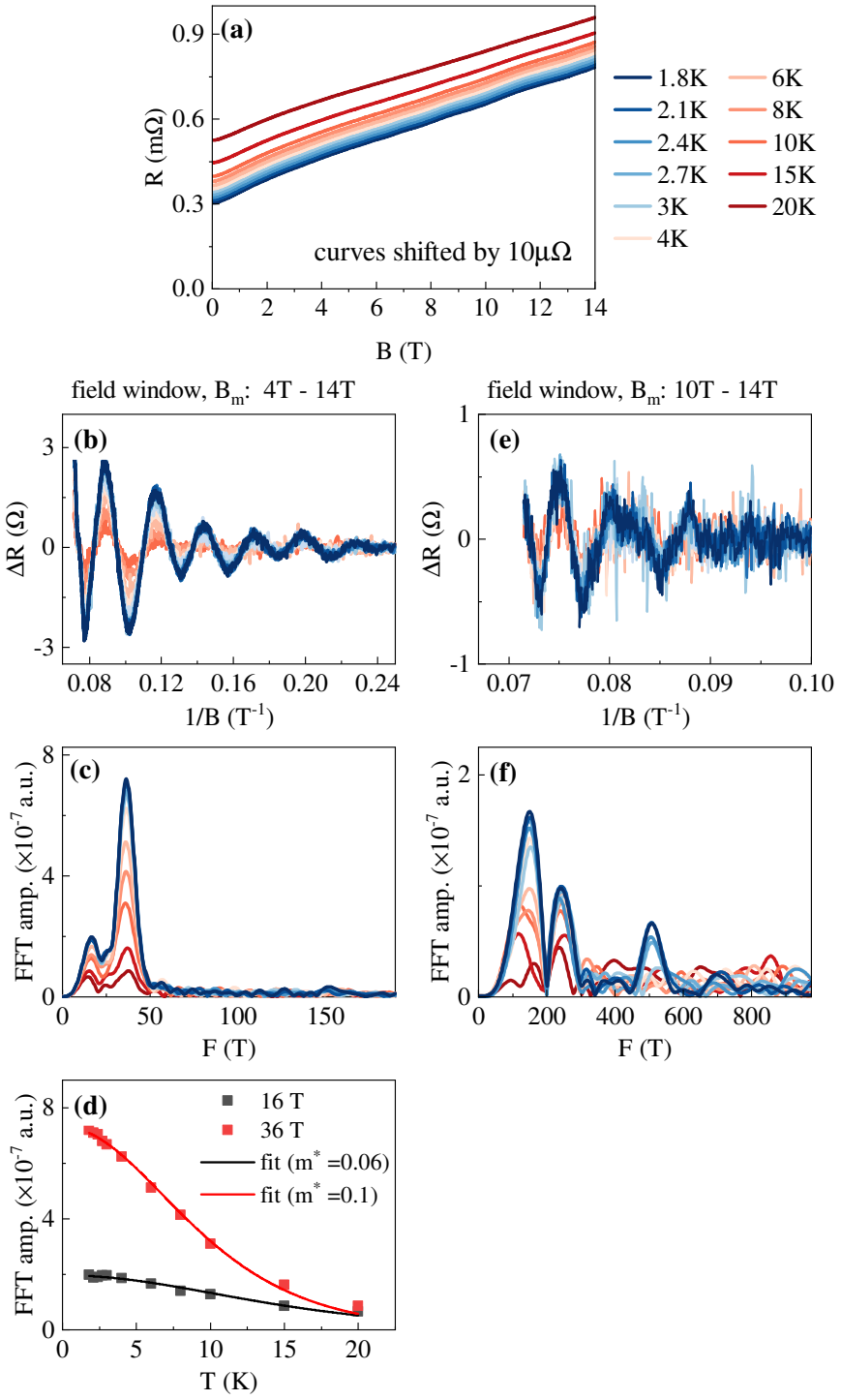

FIGURE C.12: Quantum Oscillations in *electrical transport* for KV_3Sb_5: (a) shows the resistance vs external magnetic field along $c-$axis for different temperatures. For the 4-14 T window, panel (b-d) show the (b) oscillating part of the R extracted by subtracting a polynomial against inverse of B_{ext}, (c) the FFT of this signal and the (d) masses extracted using Eq. (1.14) for 16, 36 T frequency. Panel (e,f) show the (e) oscillatory component and the (f) FFT for the 10-14 T window. No mass extraction is possible in this case as the oscillations fall below the noise baseline (not shown).

Temperature dependence for KV_3Sb_5 magnetization data

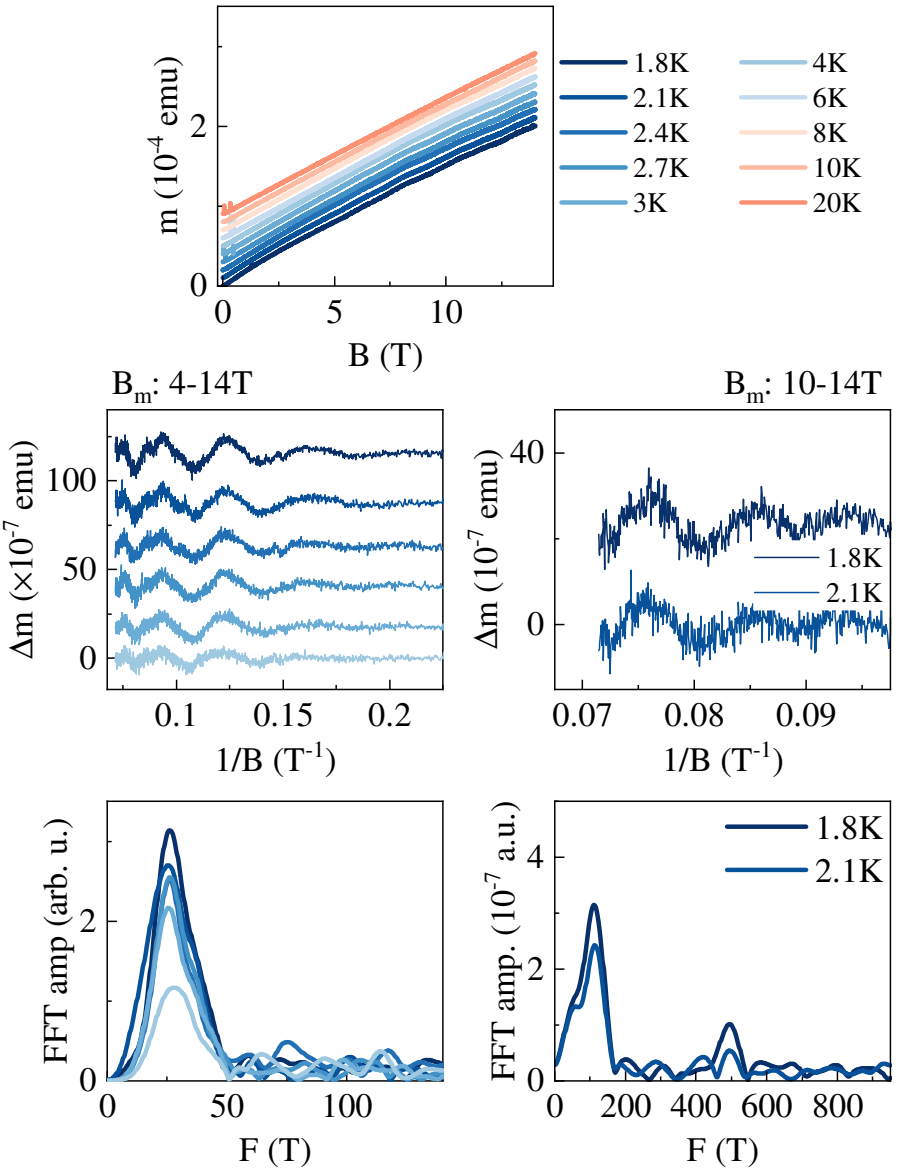

FIGURE C.13: Quantum Oscillations in *magnetization* for KV_3Sb_5: (a) shows the magnetization vs external magnetic field along $c-$axis for different temperatures. Feeble quantum oscillations are seen up to 4 K. For the 4-14 T window, panel (b-c) show the (b) oscillatory part of the M extracted by subtracting a polynomial against inverse of B_{ext}, (c) the FFT of this signal. Panel (d,e) show the (d) oscillatory component and the (e) FFT for the 10-14 T window.

Angle dependence for RbV_3Sb_5 magnetostriction data

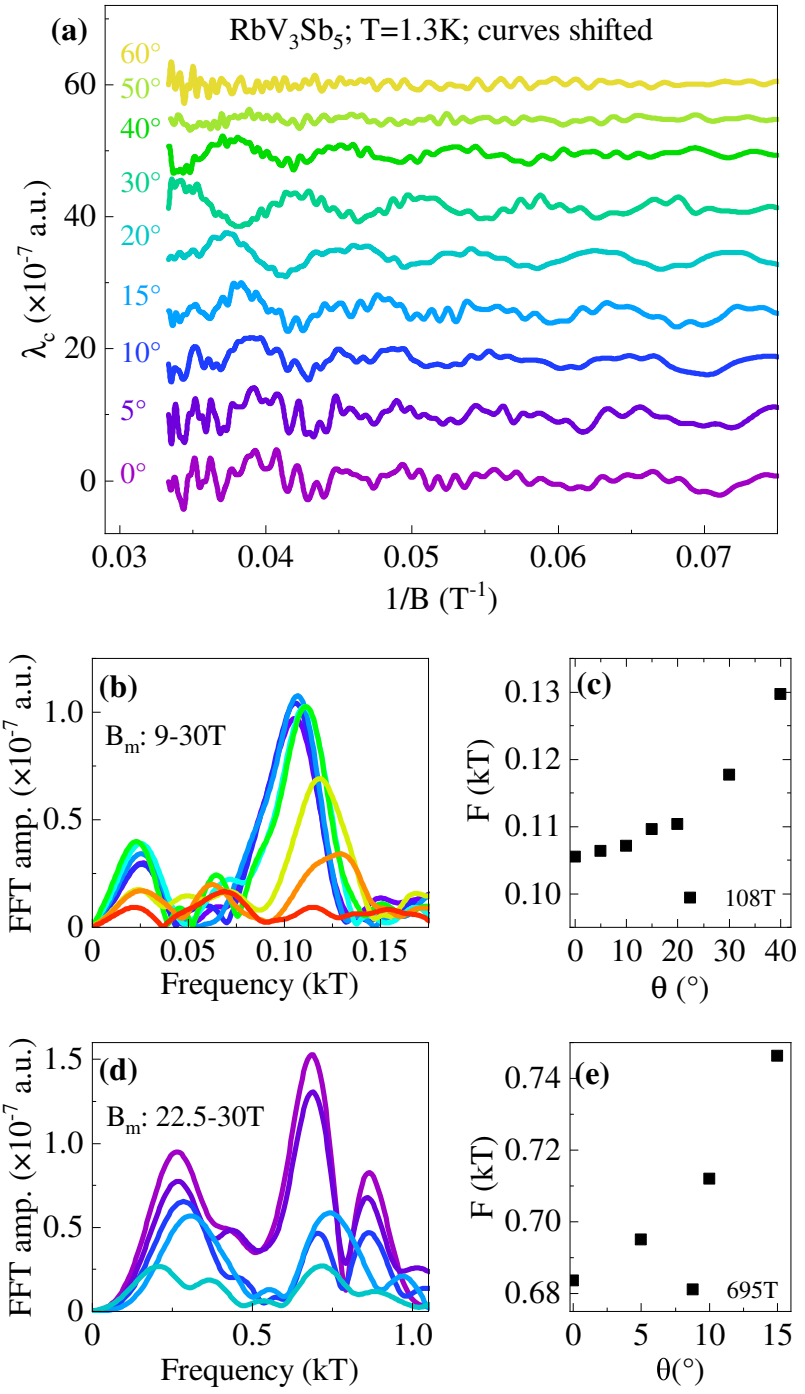

FIGURE C.14: Angle-dependent quantum-oscillations in magnetostriction in RbV_3Sb_5 at $T = 1.3\,\mathrm{K}$. (a) Oscillation amplitude versus inverse magnetic field for various tilt angles θ of the applied field from 0° to 60°, showing systematic phase shifts and changes in amplitude; curves are offset for clarity. (b, c, d, e) Extracted quantum-oscillation frequencies (in kT) plotted against magnetic field angle and/or amplitude, highlighting multiple orbits (e.g., near 108 T, 695 T). (c) 122 T frequency survives to high angles as expected and reported for these prolate elliptical orbits in case of CsV_3Sb_5 [51]. (e) In comparison, the peak amplitudes decay much more quickly for 695 T frequency

Dingle analysis for RbV_3Sb_5 magnetostriction data

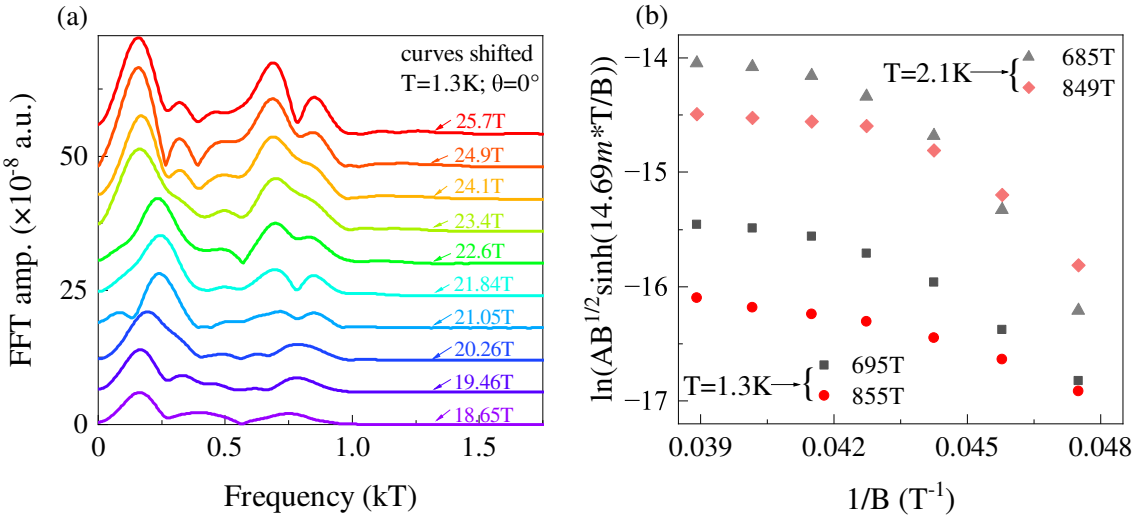

FIGURE C.15: Magnetostriction quantum-oscillation data for RbV_3Sb_5 at low temperatures: (a) Oscillation amplitude (arbitrary units) plotted versus inverse magnetic field $(1/B)$ at $T = 1.3\,\mathrm{K}$ and selected angles ($\alpha = 0°$, etc.), with curves shifted vertically for clarity. Prominent frequencies near $\sim 695\,\mathrm{T}$ and $\sim 855\,\mathrm{T}$ are visible. (b) Dingle analysis illustrating $\ln\left[\sqrt{A}\,\sinh(\dots)\right]$ versus $1/B$ at $T = 1.3\,\mathrm{K}$ and $T = 2.1\,\mathrm{K}$. The slopes extracted from these linear fits yield Dingle temperatures, allowing estimation of quasiparticle scattering rates.

The change in slope at high fields is also found in the CsV_3Sb_5 [55] and is related to the magnetic breakdown in the sample.

Bibliography

[1] Y. Kamihara, H. Hiramatsu, M. Hirano, R. Kawamura, H. Yanagi, T. Kamiya, and H. Hosono, "Iron-based layered superconductor: LaOFeP," Journal of the American Chemical Society **128**, 10012–10013 (2006).

[2] Y. Kamihara, T. Watanabe, M. Hirano, and H. Hosono, "Iron-based layered superconductor $La[O_{1-x}F_x]FeAs$ (x= 0.05-0.12) with $T_c = 26$ K," Journal of the American Chemical Society **130**, 3296–3297 (2008).

[3] J.-H. Chu, J. G. Analytis, K. De Greve, P. L. McMahon, Z. Islam, Y. Yamamoto, and I. R. Fisher, "In-plane resistivity anisotropy in an underdoped iron arsenide superconductor," Science **329**, 824–826 (2010).

[4] R. Fernandes, A. Chubukov, and J. Schmalian, "What drives nematic order in iron-based superconductors?" Nature Physics **10**, 97–104 (2014).

[5] A. I. Coldea, "Electronic nematic states tuned by isoelectronic substitution in bulk $FeSe_{1-x}S_x$," Frontiers in Physics **8**, 594500 (2021).

[6] A. E. Böhmer and C. Meingast, "Electronic nematic susceptibility of iron-based superconductors," Comptes Rendus Physique **17**, 90–112 (2016).

[7] M. He, L. Wang, F. Hardy, L. Xu, T. Wolf, P. Adelmann, and C. Meingast, "Evidence for short-range magnetic order in the nematic phase of FeSe from anisotropic in-plane magnetostriction and susceptibility measurements," Physical Review B **97**, 104107 (2018).

[8] I. Paul and M. Garst, "Lattice effects on nematic quantum criticality in metals," Physical Review Letters **118**, 227601 (2017).

[9] A. E. Böhmer, F. Hardy, F. Eilers, D. Ernst, P. Adelmann, P. Schweiss, T. Wolf, and C. Meingast, "Lack of coupling between superconductivity and orthorhombic distortion in stoichiometric single-crystalline FeSe," Physical Review B **87**, 180505 (2013).

[10] A. E. Böhmer, P. Burger, F. Hardy, T. Wolf, P. Schweiss, R. Fromknecht, M. Reinecker, W. Schranz, and C. Meingast, "Nematic susceptibility of hole-doped and electron-doped $BaFe_2As_2$ iron-based superconductors from shear modulus measurements," Physical Review Letters **112**, 047001 (2014).

[11] Z. Yin, K. Haule, and G. Kotliar, "Kinetic frustration and the nature of the magnetic and paramagnetic states in iron pnictides and iron chalcogenides," Nature Materials **10**, 932–935 (2011).

[12] M. Yi, Z. Liu, Y. Zhang, R. Yu, J.-X. Zhu, J. Lee, R. Moore, F. Schmitt, W. Li, S. Riggs, *et al.*, "Observation of universal strong orbital-dependent correlation effects in iron chalcogenides," Nature Communications **6**, 1–7 (2015).

[13] A. Chubukov, "Pairing mechanism in Fe-based superconductors," Annu. Rev. Condens. Matter Phys. **3**, 57–92 (2012).

[14] E. Abrahams and Q. Si, "Quantum criticality in the iron pnictides and chalcogenides," Journal of Physics: Condensed Matter **23**, 223201 (2011).

[15] K. Ishida, Y. Onishi, M. Tsujii, K. Mukasa, M. Qiu, M. Saito, Y. Sugimura, K. Matsuura, Y. Mizukami, K. Hashimoto, *et al.*, "Pure nematic quantum critical point accompanied by a superconducting dome," Proceedings of the National Academy of Sciences **119**, e2110501119 (2022).

[16] E. Fradkin, S. A. Kivelson, M. J. Lawler, J. P. Eisenstein, and A. P. Mackenzie, "Nematic Fermi fluids in condensed matter physics," Annu. Rev. Condens. Matter Phys. **1**, 153–178 (2010).

[17] I. Syôzi, "Statistics of kagomé lattice," Progress of Theoretical Physics **6**, 306–308 (1951).

[18] K. Momma and F. Izumi, "Vesta: a three-dimensional visualization system for electronic and structural analysis," Journal of Applied Crystallography **41**, 653–658 (2008).

[19] O. Bradley, B. Cohen-Stead, S. Johnston, K. Barros, and R. T. Scalettar, "Charge order in the kagome lattice Holstein model: a hybrid Monte Carlo study," npj Quantum Materials **8**, 21 (2023).

[20] L. Balents, "Spin liquids in frustrated magnets," Nature **464**, 199–208 (2010).

[21] H. Zhang, H. Feng, X. Xu, W. Hao, and Y. Du, "Recent progress on 2D kagome magnets: Binary T_mSn_n (T = Fe, Co, Mn)," Advanced Quantum Technologies **4**, 2100073 (2021).

[22] B. R. Ortiz, L. C. Gomes, J. R. Morey, M. Winiarski, M. Bordelon, J. S. Mangum, I. W. Oswald, J. A. Rodriguez-Rivera, J. R. Neilson, S. D. Wilson, *et al.*, "New kagome prototype materials: discovery of KV_3Sb_5, RbV_3Sb_5, and CsV_3Sb_5," Physical Review Materials **3**, 094407 (2019).

[23] S. D. Wilson and B. R. Ortiz, "AV_3Sb_5 kagome superconductors," Nature Reviews Materials **9**, 1–13 (2024).

[24] M. H. Christensen, T. Birol, B. M. Andersen, and R. M. Fernandes, "Theory of the charge density wave in AV_3Sb_5 kagome metals," Physical Review B **104**, 214513 (2021).

[25] L. Kautzsch, B. R. Ortiz, K. Mallayya, J. Plumb, G. Pokharel, J. P. Ruff, Z. Islam, E.-A. Kim, R. Seshadri, and S. D. Wilson, "Structural evolution of the kagome superconductors AV_3Sb_5 (A = K, Rb, Cs) through charge density wave order," Physical Review Materials **7**, 024806 (2023), arXiv: 2211.16602.

[26] T. Neupert, M. M. Denner, J.-X. Yin, R. Thomale, and M. Z. Hasan, "Charge order and superconductivity in kagome materials," Nature Physics **18**, 137–143 (2022).

[27] C. Zhao, L. Wang, W. Xia, Q. Yin, J. Ni, Y. Huang, C. Tu, Z. Tao, Z. Tu, C. Gong, *et al.*, "Nodal superconductivity and superconducting domes in the topological kagome metal CsV_3Sb_5," arXiv preprint arXiv:2102.08356 (2021).

[28] H. Chen, H. Yang, B. Hu, Z. Zhao, J. Yuan, Y. Xing, G. Qian, Z. Huang, G. Li, Y. Ye, *et al.*, "Roton pair density wave in a strong-coupling kagome superconductor," Nature **599**, 222–228 (2021).

[29] H.-S. Xu, Y.-J. Yan, R. Yin, W. Xia, S. Fang, Z. Chen, Y. Li, W. Yang, Y. Guo, and D.-L. Feng, "Multiband superconductivity with sign-preserving order parameter in kagome superconductor CsV_3Sb_5," Physical Review Letters **127**, 187004 (2021).

[30] C. Mu, Q. Yin, Z. Tu, C. Gong, H. Lei, Z. Li, and J. Luo, "S-wave superconductivity in kagome metal CsV_3Sb_5 revealed by 121/123Sb NQR and 51V NMR measurements," Chinese Physics Letters **38**, 077402 (2021).

[31] M. Tinkham, *Introduction to superconductivity*, Vol. 1 (Courier Corporation, 2004).

[32] F. Bouquet, Y. Wang, R. Fisher, D. Hinks, J. Jorgensen, A. Junod, and N. Phillips, "Phenomenological two-gap model for the specific heat of MgB2," Europhysics Letters **56**, 856 (2001).

[33] F. Gross, B. Chandrasekhar, D. Einzel, K. Andres, P. Hirschfeld, H. Ott, J. Beuers, Z. Fisk, and J. Smith, "Anomalous temperature dependence of the magnetic field penetration depth in superconducting UBe_{13}," Zeitschrift für Physik B Condensed Matter **64**, 175–188 (1986).

[34] E. Helfand and N. Werthamer, "Temperature and purity dependence of the superconducting critical field, H_{c2}. II," Physical Review **147**, 288 (1966).

[35] L. Gor'Kov, "The critical supercooling field in superconductivity theory," Sov. Phys. JETP **10**, 28 (1960).

[36] G. Grüner, "The dynamics of charge-density waves," Reviews of Modern Physics **60**, 1129 (1988).

[37] D. Shoenberg, *Magnetic oscillations in metals* (Cambridge University Press, 2009).

[38] W. Zhao and X. Wang, "Berry phase in quantum oscillations of topological materials," Advances in Physics: X **7**, 2064230 (2022).

[39] P. Giannozzi, S. Baroni, N. Bonini, M. Calandra, R. Car, C. Cavazzoni, D. Ceresoli, G. L. Chiarotti, M. Cococcioni, I. Dabo, *et al.*, "Quantum espresso: a modular and open-source software project for quantum simulations of materials," Journal of physics: Condensed matter **21**, 395502 (2009).

[40] M. Kawamura, "Fermisurfer: Fermi-surface viewer providing multiple representation schemes," Computer Physics Communications **239**, 197–203 (2019).

[41] P. Walmsley and I. Fisher, "Determination of the resistivity anisotropy of orthorhombic materials via transverse resistivity measurements," Review of Scientific Instruments **88**, 043901 (2017).

[42] P. W. Phillips, N. E. Hussey, and P. Abbamonte, "Stranger than metals," Science **377**, eabh4273 (2022).

[43] J. S. Hwang, K. J. Lin, and C. Tien, "Measurement of heat capacity by fitting the whole temperature response of a heat-pulse calorimeter," Review of Scientific Instruments **68**, 94–101 (1997).

[44] R. Küchler, T. Bauer, M. Brando, and F. Steglich, "A compact and miniaturized high resolution capacitance dilatometer for measuring thermal expansion and magnetostriction," Review of Scientific Instruments **83**, 095102 (2012).

[45] C. Meingast, B. Blank, H. Bürkle, B. Obst, T. Wolf, H. Wühl, V. Selvamanickam, and K. Salama, "Anisotropic pressure dependence of T_c in single-crystal $YBa_2Cu_3O_7$ via thermal expansion," Physical Review B **41**, 11299–11304 (1990).

[46] L. D. Landau *et al.*, "On the theory of phase transitions," Zh. eksp. teor. Fiz **7**, 926 (1937).

[47] P. Blaha, K. Schwarz, G. K. Madsen, D. Kvasnicka, J. Luitz, *et al.*, "wien2k," An augmented plane wave+ local orbitals program for calculating crystal properties **60**, 155–169 (2001).

[48] S. Julian, "Numerical extraction of de Haas-van Alphen frequencies from calculated band energies," Computer Physics Communications **183**, 324–332 (2012).

[49] A. Kokalj, "Xcrysden—a new program for displaying crystalline structures and electron densities," Journal of Molecular Graphics and Modelling **17**, 176–179 (1999).

[50] B. R. Ortiz, S. M. Teicher, L. Kautzsch, P. M. Sarte, N. Ratcliff, J. Harter, J. P. Ruff, R. Seshadri, and S. D. Wilson, "Fermi surface mapping and the nature of charge-density-wave order in the kagome superconductor CsV_3Sb_5," Physical Review X **11**, 041030 (2021).

[51] Y. Fu, N. Zhao, Z. Chen, Q. Yin, Z. Tu, C. Gong, C. Xi, X. Zhu, Y. Sun, K. Liu, *et al.*, "Quantum transport evidence of topological band structures of kagome superconductor CsV_3Sb_5," Physical Review Letters **127**, 207002 (2021).

[52] K. Shrestha, R. Chapai, B. K. Pokharel, D. Miertschin, T. Nguyen, X. Zhou, D. Chung, M. Kanatzidis, J. Mitchell, U. Welp, *et al.*, "Nontrivial Fermi surface topology of the kagome superconductor CsV_3Sb_5 probed by de Haas–van Alphen oscillations," Physical Review B **105**, 024508 (2022).

[53] D. Chen, B. He, M. Yao, Y. Pan, H. Lin, W. Schnelle, Y. Sun, J. Gooth, L. Taillefer, and C. Felser, "Anomalous thermoelectric effects and quantum oscillations in the kagome metal CsV_3Sb_5," Physical Review B **105**, L201109 (2022).

[54] K.-W. Chen, G. Zheng, D. Zhang, A. Chan, Y. Zhu, K. Jenkins, F. Yu, M. Shi, J. Ying, Z. Xiang, *et al.*, "Magnetic breakdown and spin-zero effect in quantum oscillations in kagome metal CsV_3Sb_5," Communications Materials **4**, 96 (2023).

[55] R. Chapai, M. Leroux, V. Oliviero, D. Vignolles, N. Bruyant, M. Smylie, D. Chung, M. Kanatzidis, W.-K. Kwok, J. Mitchell, *et al.*, "Magnetic breakdown and topology in the kagome superconductor CsV_3Sb_5 under high magnetic field," Physical Review Letters **130**, 126401 (2023), arXiv: 2208.05523.

[56] Y. Wang, Z. Chen, Y. Nie, Y. Zhang, Q. Niu, G. Zheng, X. Zhu, W. Ning, and M. Tian, "Nontrivial Fermi surface topology and large anomalous hall effect in the kagome superconductor RbV_3Sb_5," Physical Review B **108**, 035117 (2023).

[57] K. Shrestha, M. Shi, T. Nguyen, D. Miertschin, K. Fan, L. Deng, D. E. Graf, X. Chen, and C.-W. Chu, "Fermi surface mapping of the kagome superconductor RbV_3Sb_5 using de Haas-van Alphen oscillations," Physical Review B **107**, 075120 (2023).

[58] L. Wang, W. Zhang, Z. Wang, T. F. Poon, W. Wang, C. W. Tsang, J. Xie, X. Zhou, Y. Zhao, S. Wang, *et al.*, "Anomalous hall effect and two-dimensional Fermi surfaces in the charge-density-wave state of kagome metal RbV_3Sb_5," Journal of Physics: Materials **6**, 02LT01 (2023).

[59] Q. Yin, Z. Tu, C. Gong, Y. Fu, S. Yan, and H. Lei, "Superconductivity and normal-state properties of kagome metal RbV_3Sb_5 single crystals," Chinese Physics Letters **38**, 037403 (2021).

[60] S.-Y. Yang, Y. Wang, B. R. Ortiz, D. Liu, J. Gayles, E. Derunova, R. Gonzalez-Hernandez, L. Šmejkal, Y. Chen, S. S. Parkin, *et al.*, "Giant, unconventional anomalous hall effect in the metallic frustrated magnet candidate, KV_3Sb_5," Science Advances **6**, eabb6003 (2020).

[61] K. Shrestha, M. Shi, B. Regmi, T. Nguyen, D. Miertschin, K. Fan, L. Deng, N. Aryal, S.-G. Kim, D. Graf, *et al.*, "High quantum oscillation frequencies and nontrivial topology

in kagome superconductor KV_3Sb_5 probed by torque magnetometry up to 45 T," Physical Review B **107**, 155128 (2023).

[62] Z. Wang, W. Zhang, L. Wang, T. F. Poon, C. W. Tsang, W. Wang, J. Xie, S. T. Lam, X. Zhou, Y. Zhao, *et al.*, "Similarities and differences in the fermiology of kagome metals AV_3Sb_5 (A = K, Rb, Cs) revealed by Shubnikov–de Haas oscillations," Applied Physics Letters **123**, 012601 (2023).

[63] Y. Wang, H. Wu, G. T. McCandless, J. Y. Chan, and M. N. Ali, "Quantum states and intertwining phases in kagome materials," Nature Reviews Physics **5**, 635–658 (2023).

[64] P. Raybaut, "Spyder-documentation," (2009).

[65] C. R. Harris, K. J. Millman, S. J. van der Walt, R. Gommers, P. Virtanen, D. Cournapeau, E. Wieser, J. Taylor, S. Berg, N. J. Smith, R. Kern, M. Picus, S. Hoyer, M. H. van Kerkwijk, M. Brett, A. Haldane, J. F. del Río, M. Wiebe, P. Peterson, P. Gérard-Marchant, K. Sheppard, T. Reddy, W. Weckesser, H. Abbasi, C. Gohlke, and T. E. Oliphant, "Array programming with NumPy," Nature **585**, 357–362 (2020).

[66] The MathWorks Inc., "Signal Processing Documentation," (2022).

[67] A. Martinelli, A. Palenzona, M. Tropeano, C. Ferdeghini, M. Putti, M. R. Cimberle, T. D. Nguyen, M. Affronte, and C. Ritter, "From antiferromagnetism to superconductivity in $Fe_{1+y}Te_{1-x}Se_x$ ($0 \leq x \leq 0.20$): Neutron powder diffraction analysis," Physical Review B **81**, 094115 (2010).

[68] S. Li, C. de la Cruz, Q. Huang, Y. Chen, J. W. Lynn, J. Hu, Y.-L. Huang, F.-C. Hsu, K.-W. Yeh, M.-K. Wu, and P. Dai, "First-order magnetic and structural phase transitions in $FeSe_xTe_{1-x}$," Physical Review B **79**, 054503 (2009).

[69] Y. Li, N. Zaki, V. O. Garlea, A. T. Savici, D. Fobes, Z. Xu, F. Camino, C. Petrovic, G. Gu, P. D. Johnson, *et al.*, "Electronic properties of the bulk and surface states of $Fe_{1+y}Te_{1-x}Se_x$," Nature Materials **20**, 1221–1227 (2021).

[70] J. Glasbrenner, I. Mazin, H. O. Jeschke, P. Hirschfeld, R. Fernandes, and R. Valentí, "Effect of magnetic frustration on nematicity and superconductivity in iron chalcogenides," Nature Physics **11**, 953–958 (2015).

[71] Q. Wang, Y. Shen, B. Pan, X. Zhang, K. Ikeuchi, K. Iida, A. Christianson, H. Walker, D. Adroja, M. Abdel-Hafiez, *et al.*, "Magnetic ground state of FeSe," Nature Communications **7**, 12182 (2016).

[72] T. Liu, J. Hu, B. Qian, D. Fobes, Z. Q. Mao, W. Bao, M. Reehuis, S. Kimber, K. Prokeš, S. Matas, *et al.*, "From (π, 0) magnetic order to superconductivity with (π, π) magnetic resonance in $Fe_{1.02}Te_{1-x}Se_x$," Nature Materials **9**, 718–720 (2010).

[73] E. Gati, A. E. Böhmer, S. L. Bud'ko, and P. C. Canfield, "Bulk superconductivity and role of fluctuations in the iron-based superconductor FeSe at high pressures," Physical Review Letters **123**, 167002 (2019).

[74] J. Li, B. Lei, D. Zhao, L. P. Nie, D. W. Song, L. X. Zheng, S. J. Li, B. L. Kang, X. G. Luo, T. Wu, and X. H. Chen, "Spin-orbital-intertwined nematic state in FeSe," Physical Review X **10**, 011034 (2020).

[75] A. E. Böhmer, T. Arai, F. Hardy, T. Hattori, T. Iye, T. Wolf, H. v. Löhneysen, K. Ishida, and C. Meingast, "Origin of the tetragonal-to-orthorhombic phase transition in FeSe: A combined thermodynamic and NMR study of nematicity," Physical Review Letters **114**, 027001 (2015).

[76] A. V. Chubukov, M. Khodas, and R. M. Fernandes, "Magnetism, superconductivity, and spontaneous orbital order in iron-based superconductors: Which comes first and why?" Physical Review X **6**, 041045 (2016).

[77] Y. Gallais and I. Paul, "Charge nematicity and electronic Raman scattering in iron-based superconductors," Comptes Rendus Physique **17**, 113–139 (2016).

[78] J. Huang, R. Yu, Z. Xu, J.-X. Zhu, J. S. Oh, Q. Jiang, M. Wang, H. Wu, T. Chen, J. D. Denlinger, *et al.*, "Correlation-driven electronic reconstruction in $FeTe_{1-x}Se_x$," Communications Physics **5**, 29 (2022).

[79] P. Hirschfeld, M. Korshunov, and I. Mazin, "Gap symmetry and structure of Fe-based superconductors," Reports on Progress in Physics **74**, 124508 (2011).

[80] R. M. Fernandes, A. I. Coldea, H. Ding, I. R. Fisher, P. Hirschfeld, and G. Kotliar, "Iron pnictides and chalcogenides: a new paradigm for superconductivity," Nature **601**, 35–44 (2022).

[81] J. Kang, R. M. Fernandes, and A. Chubukov, "Superconductivity in FeSe: the role of nematic order," Physical Review Letters **120**, 267001 (2018).

[82] T. Watashige, Y. Tsutsumi, T. Hanaguri, Y. Kohsaka, S. Kasahara, A. Furusaki, M. Sigrist, C. Meingast, T. Wolf, H. v. Löhneysen, *et al.*, "Evidence for time-reversal symmetry breaking of the superconducting state near twin-boundary interfaces in FeSe revealed by scanning tunneling spectroscopy," Physical Review X **5**, 031022 (2015).

[83] C.-L. Song, Y.-L. Wang, P. Cheng, Y.-P. Jiang, W. Li, T. Zhang, Z. Li, K. He, L. Wang, J.-F. Jia, *et al.*, "Direct observation of nodes and twofold symmetry in FeSe superconductor," Science **332**, 1410–1413 (2011).

[84] F. Hardy, M. He, L. Wang, T. Wolf, P. Schweiss, M. Merz, M. Barth, P. Adelmann, R. Eder, A.-A. Haghighirad, and C. Meingast, "Calorimetric evidence of nodal gaps in the nematic superconductor FeSe," Physical Review B **99**, 035157 (2019).

[85] G.-Y. Chen, X. Zhu, H. Yang, and H.-H. Wen, "Highly anisotropic superconducting gaps and possible evidence of antiferromagnetic order in FeSe single crystals," Physical Review B **96**, 064524 (2017).

[86] P. O. Sprau, A. Kostin, A. Kreisel, A. E. Böhmer, V. Taufour, P. C. Canfield, S. Mukherjee, P. J. Hirschfeld, B. M. Andersen, and J. S. Davis, "Discovery of orbital-selective Cooper pairing in FeSe," Science **357**, 75–80 (2017).

[87] D. Liu, C. Li, J. Huang, B. Lei, L. Wang, X. Wu, B. Shen, Q. Gao, Y. Zhang, X. Liu, *et al.*, "Orbital origin of extremely anisotropic superconducting gap in nematic phase of FeSe superconductor," Physical Review X **8**, 031033 (2018).

[88] L. Jiao, C.-L. Huang, S. Rößler, C. Koz, U. K. Rößler, U. Schwarz, and S. Wirth, "Superconducting gap structure of FeSe," Scientific Reports **7**, 44024 (2017).

[89] P. Bourgeois-Hope, S. Chi, D. Bonn, R. Liang, W. Hardy, T. Wolf, C. Meingast, N. Doiron-Leyraud, and L. Taillefer, "Thermal conductivity of the iron-based superconductor FeSe: Nodeless gap with a strong two-band character," Physical Review Letters **117**, 097003 (2016).

[90] R. Khasanov, M. Bendele, A. Amato, K. Conder, H. Keller, H.-H. Klauss, H. Luetkens, and E. Pomjakushina, "Evolution of two-gap behavior of the superconductor $FeSe_{1-x}$," Physical Review Letters **104**, 087004 (2010).

[91] M. Li, N. Lee-Hone, S. Chi, R. Liang, W. Hardy, D. Bonn, E. Girt, and D. Broun, "Superfluid density and microwave conductivity of FeSe superconductor: ultra-long-lived quasiparticles and extended s-wave energy gap," New Journal of Physics **18**, 082001 (2016).

[92] T. Otsuka, S. Hagisawa, Y. Koshika, S. Adachi, T. Usui, N. Sasaki, S. Sasaki, S. Yamaguchi, Y. Nakanishi, M. Yoshizawa, *et al.*, "Incoherent-coherent crossover and the pseudogap in Te-annealed superconducting $Fe_{1+y}Te_{1-x}Se_x$ revealed by magnetotransport measurements," Physical Review B **99**, 184505 (2019).

[93] K. Mukasa, K. Matsuura, M. Qiu, M. Saito, Y. Sugimura, K. Ishida, M. Otani, Y. Onishi, Y. Mizukami, K. Hashimoto, *et al.*, "High-pressure phase diagrams of $FeSe_{1-x}Te_x$: correlation between suppressed nematicity and enhanced superconductivity," Nature Communications **12**, 381 (2021).

[94] K. Mukasa, K. Ishida, S. Imajo, M. Qiu, M. Saito, K. Matsuura, Y. Sugimura, S. Liu, Y. Uezono, T. Otsuka, M. Čulo, S. Kasahara, Y. Matsuda, N. E. Hussey, T. Watanabe, K. Kindo, and T. Shibauchi, "Enhanced superconducting pairing strength near a pure nematic quantum critical point," Physical Review X **13**, 011032 (2023).

[95] J. M. Tranquada, G. Xu, and I. A. Zaliznyak, "Magnetism and superconductivity in $Fe_{1+y}Te_{1-x}Se_x$," Journal of Physics: Condensed Matter **32**, 374003 (2020).

[96] Y. Sun, Z. Shi, and T. Tamegai, "Review of annealing effects and superconductivity in $Fe_{1+y}Se_{1-x}Te_x$ superconductors," Superconductor Science and Technology **32**, 103001 (2019).

[97] Y. Koshika, T. Usui, S. Adachi, T. Watanabe, K. Sakano, S. Simayi, and M. Yoshizawa, "Effects of annealing under tellurium vapor for $Fe_{1.03}Te_{0.80}Se_{0.2}$ single crystals," Journal of the Physical Society of Japan **82**, 023703 (2012).

[98] X. Jiang, M. Qin, X. Wei, L. Xu, J. Ke, H. Zhu, R. Zhang, Z. Zhao, Q. Liang, Z. Wei, *et al.*, "Interplay between superconductivity and the strange-metal state in FeSe," Nature Physics **19**, 365–371 (2023).

[99] O. Gunnarsson, M. Calandra, and J. E. Han, "Colloquium: Saturation of electrical resistivity," Rev. Mod. Phys. **75**, 1085–1099 (2003).

[100] K. R. Islam and A. Chubukov, "Unconventional superconductivity near a nematic instability in a multi-orbital system," (2023).

[101] Q. Jiang, Y. Shi, M. H. Christensen, J. J. Sanchez, B. Huang, Z. Lin, Z. Liu, P. Malinowski, X. Xu, R. M. Fernandes, *et al.*, "Nematic fluctuations in an orbital selective superconductor $Fe_{1+y}Te_{1-x}Se_x$," Communications Physics **6**, 39 (2023).

[102] M. Watson, T. Yamashita, S. Kasahara, W. Knafo, M. Nardone, J. Béard, F. Hardy, A. McCollam, A. Narayanan, S. Blake, *et al.*, "Dichotomy between the hole and electron behavior in multiband superconductor FeSe probed by ultrahigh magnetic fields," Physical Review Letters **115**, 027006 (2015).

[103] F. Hardy, L. Doussoulin, T. Klein, M. He, A. Demuer, R. Willa, K. Willa, A.-A. Haghighirad, T. Wolf, M. Merz, C. Meingast, and C. Marcenat, "Vortex-lattice melting and paramagnetic depairing in the nematic superconductor FeSe," Physical Review Research **2**, 033319 (2021).

[104] P. P. Singh, "Effects of disorder in FeSe: an ab initio study," Journal of Physics: Condensed Matter **22**, 135501 (2010).

[105] Q. Hou, W. Wei, X. Zhou, W. Liu, K. Wang, X. Xing, Y. Zhang, N. Zhou, Y. Pan, Y. Sun, *et al.*, "Bulk and surface Dirac states accompanied by two superconducting domes in FeSe-based superconductors," Proceedings of the National Academy of Sciences **121**, e2409756121 (2024).

[106] A. B. Morfoot, T. K. Kim, M. D. Watson, A. A. Haghighirad, S. J. Singh, N. Bultinck, and A. I. Coldea, "Resurgence of superconductivity and the role of dxy hole band in $FeSe_{1-x}Te_x$," Communications Physics **6**, 362 (2023).

[107] G. Pang, M. Smidman, J. Zhang, L. Jiao, Z. Weng, E. M. Nica, Y. Chen, W. Jiang, Y. Zhang, W. Xie, *et al.*, "Fully gapped d-wave superconductivity in $CeCu_2Si_2$," Proceedings of the National Academy of Sciences **115**, 5343–5347 (2018).

[108] T. Metz, S. Bae, S. Ran, I.-L. Liu, Y. S. Eo, W. T. Fuhrman, D. F. Agterberg, S. M. Anlage, N. P. Butch, and J. Paglione, "Point-node gap structure of the spin-triplet superconductor UTe_2," Physical Review B **100**, 220504 (2019).

[109] A. Chubukov and I. Eremin, "Angle-resolved specific heat in iron-based superconductors: The case for a nodeless extended s-wave gap," Physical Review B **82**, 060504 (2010).

[110] S. Graser, T. Maier, P. Hirschfeld, and D. Scalapino, "Near-degeneracy of several pairing channels in multiorbital models for the Fe pnictides," New Journal of Physics **11**, 025016 (2009).

[111] T. Nagashima, K. Ishihara, K. Imamura, M. Kobayashi, M. Roppongi, K. Matsuura, Y. Mizukami, R. Grasset, M. Konczykowski, K. Hashimoto, *et al.*, "Lifting of gap nodes by disorder in tetragonal $FeSe_{1-x}S_x$ superconductors," Physical Review Letters **133**, 156506 (2024).

[112] C. Setty, S. Bhattacharyya, Y. Cao, A. Kreisel, and P. Hirschfeld, "Topological ultranodal pair states in iron-based superconductors," Nature Communications **11**, 523 (2020).

[113] Y. Lubashevsky, E. Lahoud, K. Chashka, D. Podolsky, and A. Kanigel, "Shallow pockets and very strong coupling superconductivity in $FeSe_xTe_{1-x}$," Nature Physics **8**, 309–312 (2012).

[114] B. Zeng, G. Mu, H. Luo, T. Xiang, I. Mazin, H. Yang, L. Shan, C. Ren, P. Dai, and H.-H. Wen, "Anisotropic structure of the order parameter in $FeSe_{0.45}Te_{0.55}$ revealed by angle-resolved specific heat," Nature Communications **1**, 112 (2010).

[115] M. Bendele, A. Ichsanow, Y. Pashkevich, L. Keller, T. Strässle, A. Gusev, E. Pomjakushina, K. Conder, R. Khasanov, and H. Keller, "Coexistence of superconductivity and magnetism in $FeSe_{1-x}$ under pressure," Physical Review B **85**, 064517 (2012).

[116] S. A. Kimber, A. Kreyssig, Y.-Z. Zhang, H. O. Jeschke, R. Valentí, F. Yokaichiya, E. Colombier, J. Yan, T. C. Hansen, T. Chatterji, *et al.*, "Similarities between structural distortions under pressure and chemical doping in superconducting $BaFe_2As_2$," Nature Materials **8**, 471–475 (2009).

[117] J. Fink, S. Thirupathaiah, R. Ovsyannikov, H. Dürr, R. Follath, Y. Huang, S. De Jong, M. Golden, Y.-Z. Zhang, H. Jeschke, *et al.*, "Electronic structure studies of $BaFe_2As_2$ by angle-resolved photoemission spectroscopy," Physical Review B **79**, 155118 (2009).

[118] D. J. Singh, "Electronic structure and doping in $BaFe_2As_2$ and LiFeAs: Density functional calculations," Physical Review B **78**, 094511 (2008).

[119] L. Lauke, R. Heid, M. Merz, T. Wolf, A.-A. Haghighirad, and J. Schmalian, "Band engineering of Dirac cones in iron chalcogenides," Physical Review B **102**, 054209 (2020).

[120] Z. Wang, P. Zhang, G. Xu, L. Zeng, H. Miao, X. Xu, T. Qian, H. Weng, P. Richard, A. V. Fedorov, *et al.*, "Topological nature of the $FeSe_{0.5}Te_{0.5}$ superconductor," Physical Review B **92**, 115119 (2015).

[121] L. Wang, F. Hardy, T. Wolf, P. Adelmann, R. Fromknecht, P. Schweiss, and C. Meingast, "Superconductivity-enhanced nematicity and "s+d" gap symmetry in $Fe(Se_{1-x}S_x)$," physica status solidi (b) **254**, 1600153 (2017).

[122] T. Barron, J. Collins, and G. White, "Thermal expansion of solids at low temperatures," Advances in Physics **29**, 609–730 (1980).

[123] R. Liu, Q. Tang, C. Liu, C. Li, K. Zhou, Q. Wang, and X. Lu, "Evolution of pairing symmetry in $FeSe_{1-x}S_x$ as probed by uniaxial-strain tuning of T_c," arXiv preprint arXiv:2410.13319 (2024).

[124] M. Yoshizawa, D. Kimura, T. Chiba, S. Simayi, Y. Nakanishi, K. Kihou, C.-H. Lee, A. Iyo, H. Eisaki, M. Nakajima, *et al.*, "Structural quantum criticality and superconductivity in iron-based superconductor $Ba(Fe_{1-x}Co_x)_2As_2$," Journal of the Physical Society of Japan **81**, 024604 (2012).

[125] C. Meingast, F. Hardy, R. Heid, P. Adelmann, A. Böhmer, P. Burger, D. Ernst, R. Fromknecht, P. Schweiss, and T. Wolf, "Thermal expansion and Grüneisen parameters of $Ba(Fe_{1-x}Co_x)_2As_2$: A thermodynamic quest for quantum criticality," Physical Review Letters **108**, 177004 (2012).

[126] B. Lüthi, *Physical acoustics in the solid state*, Vol. 148 (Springer Science & Business Media, 2005).

[127] M. Yoshizawa and S. Simayi, "Anomalous elastic behavior and its correlation with superconductivity in iron-based superconductor $Ba(Fe_{1-x}Co_x)_2As_2$," Modern Physics Letters B **26**, 1230011 (2012).

[128] T. Goto, R. Kurihara, K. Araki, K. Mitsumoto, M. Akatsu, Y. Nemoto, S. Tatematsu, and M. Sato, "Quadrupole effects of layered iron pnictide superconductor $Ba(Fe_{0.9}Co_{0.1})_2As_2$," Journal of the Physical Society of Japan **80**, 073702 (2011).

[129] A. Böhmer, "Competing phases in iron-based superconductors studied by high-resolution thermal-expansion and shear-modulus measurements," Doctoral thesis, Karlsruhe Institute of Technology (2014).

[130] R. M. Fernandes, L. H. VanBebber, S. Bhattacharya, P. Chandra, V. Keppens, D. Mandrus, M. A. McGuire, B. C. Sales, A. S. Sefat, and J. Schmalian, "Effects of nematic fluctuations on the elastic properties of iron arsenide superconductors," Physical Review Letters **105**, 157003 (2010).

[131] M. Zacharias, I. Paul, and M. Garst, "Quantum critical elasticity," Physical Review Letters **115**, 025703 (2015).

[132] D. Labat and I. Paul, "Pairing instability near a lattice-influenced nematic quantum critical point," Physical Review B **96**, 195146 (2017).

[133] D. Labat, P. Kotetes, B. M. Andersen, and I. Paul, "Variation of shear moduli across superconducting phase transitions," Physical Review B **101**, 144502 (2020).

[134] M. D. Lumsden, A. D. Christianson, E. Goremychkin, S. E. Nagler, H. Mook, M. B. Stone, D. L. Abernathy, T. Guidi, G. J. MacDougall, C. de la Cruz, *et al.*, "Evolution of spin excitations into the superconducting state in $FeTe_{1-x}Se_x$," Nature Physics **6**, 182–186 (2010).

[135] D. Arčon, P. Jeglič, A. Zorko, A. Potočnik, A. Ganin, Y. Takabayashi, M. Rosseinsky, and K. Prassides, "Coexistence of localized and itinerant electronic states in the multiband iron-based superconductor $FeSe_{0.42}Te_{0.58}$," Physical Review B **82**, 140508 (2010).

[136] A. Tamai, A. Y. Ganin, E. Rozbicki, J. Bacsa, W. Meevasana, P. D. C. King, M. Caffio, R. Schaub, S. Margadonna, K. Prassides, M. J. Rosseinsky, and F. Baumberger, "Strong electron correlations in the normal state of the iron-based $FeSe_{0.42}Te_{0.58}$ superconductor observed by angle-resolved photoemission spectroscopy," Physical Review Letters **104**, 097002 (2010).

[137] J. Maletz, V. B. Zabolotnyy, D. V. Evtushinsky, S. Thirupathaiah, A. U. B. Wolter, L. Harnagea, A. N. Yaresko, A. N. Vasiliev, D. A. Chareev, A. E. Böhmer, F. Hardy, T. Wolf, C. Meingast, E. D. L. Rienks, B. Büchner, and S. V. Borisenko, "Unusual band renormalization in the simplest iron-based superconductor $FeSe_{1-x}$," Physical Review B **89**, 220506 (2014).

[138] L. Zhu, M. Garst, A. Rosch, and Q. Si, "Universally diverging Grüneisen parameter and the magnetocaloric effect close to quantum critical points," Physical Review Letters **91**, 066404 (2003).

[139] M. Garst and A. Rosch, "Sign change of the Grüneisen parameter and magnetocaloric effect near quantum critical points," Physical Review B **72**, 205129 (2005).

[140] Y. Schattner, S. Lederer, S. A. Kivelson, and E. Berg, "Ising nematic quantum critical point in a metal: A Monte Carlo study," Physical Review X **6**, 031028 (2016).

[141] X. Huang, C. Guo, C. Putzke, M. Gutierrez-Amigo, Y. Sun, M. G. Vergniory, I. Errea, D. Chen, C. Felser, and P. J. Moll, "Three-dimensional Fermi surfaces from charge order in layered CsV_3Sb_5," Physical Review B **106**, 064510 (2022), arXiv: 2201.07780.

[142] H. Li, D. Oh, M. Kang, H. Zhao, B. R. Ortiz, Y. Oey, S. Fang, Z. Ren, C. Jozwiak, A. Bostwick, *et al.*, "Small Fermi pockets intertwined with charge stripes and pair density wave order in a kagome superconductor," Physical Review X **13**, 031030 (2023).

[143] H. Tan, Y. Li, Y. Liu, D. Kaplan, Z. Wang, and B. Yan, "Emergent topological quantum orbits in the charge density wave phase of kagome metal CsV_3Sb_5," npj Quantum Materials **8**, 39 (2023).

[144] C. Broyles, D. Graf, H. Yang, X. Dong, H. Gao, and S. Ran, "Effect of the interlayer ordering on the Fermi surface of kagome superconductor CsV_3Sb_5 revealed by quantum oscillations," Physical Review Letters **129**, 157001 (2022).

[145] F. Stier, A.-A. Haghighirad, G. Garbarino, S. Mishra, N. Stilkerich, D. Chen, C. Shekhar, T. Lacmann, C. Felser, T. Ritschel, *et al.*, "Pressure-dependent electronic superlattice in the kagome superconductor CsV_3Sb_5," Physical Review Letters **133**, 236503 (2024).

[146] Q. Stahl, D. Chen, T. Ritschel, C. Shekhar, E. Sadrollahi, M. C. Rahn, O. Ivashko, M. v. Zimmermann, C. Felser, and J. Geck, "Temperature-driven reorganization of electronic order in CsV_3Sb_5," Physical Review B **105**, 195136 (2022).

[147] M. Frachet, L. Wang, W. Xia, Y. Guo, M. He, N. Maraytta, R. Heid, A.-A. Haghighirad, M. Merz, C. Meingast, *et al.*, "Colossal c-axis response and lack of rotational symmetry breaking within the kagome planes of the CsV_3Sb_5 superconductor," Physical Review Letters **132**, 186001 (2024).

[148] R. Dynes, "McMillan's equation and the T_c of superconductors," Solid State Communications **10**, 615–618 (1972).

[149] H. Tan, Y. Liu, Z. Wang, and B. Yan, "Charge density waves and electronic properties of superconducting kagome metals," Physical Review Letters **127**, 046401 (2021).

[150] M. N. Hasan, R. Bharati, J. Hellsvik, A. Delin, S. K. Pal, A. Bergman, S. Sharma, I. Di Marco, M. Pereiro, P. Thunström, *et al.*, "Magnetism in AV_3Sb_5 (A = Cs, Rb, and K): Origin and consequences for the strongly correlated phases," Physical Review Letters **131**, 196702 (2023).

[151] L. Zheng, Z. Wu, Y. Yang, L. Nie, M. Shan, K. Sun, D. Song, F. Yu, J. Li, D. Zhao, *et al.*, "Emergent charge order in pressurized kagome superconductor CsV_3Sb_5," Nature **611**, 682–687 (2022).

[152] N. Wang, K. Chen, Q. Yin, Y. Ma, B. Pan, X. Yang, X. Ji, S. Wu, P. Shan, S. Xu, *et al.*, "Competition between charge-density-wave and superconductivity in the kagome metal RbV_3Sb_5," Physical Review Research **3**, 043018 (2021).

[153] E. T. Ritz, R. M. Fernandes, and T. Birol, "Impact of Sb degrees of freedom on the charge density wave phase diagram of the kagome metal CsV_3Sb_5," Physical Review B **107**, 205131 (2023).

[154] C. Guo, C. Putzke, S. Konyzheva, X. Huang, M. Gutierrez-Amigo, I. Errea, D. Chen, M. G. Vergniory, C. Felser, M. H. Fischer, *et al.*, "Switchable chiral transport in charge-ordered kagome metal CsV_3Sb_5," Nature **611**, 461–466 (2022).

[155] C. Guo, M. R. van Delft, M. Gutierrez-Amigo, D. Chen, C. Putzke, G. Wagner, M. H. Fischer, T. Neupert, I. Errea, M. G. Vergniory, *et al.*, "Distinct switching of chiral transport in the kagome metals KV_3Sb_5 and CsV_3Sb_5," npj Quantum Materials **9**, 20 (2024).

[156] Y. Xiang, Q. Li, Y. Li, W. Xie, H. Yang, Z. Wang, Y. Yao, and H.-H. Wen, "Twofold symmetry of c-axis resistivity in topological kagome superconductor CsV_3Sb_5 with in-plane rotating magnetic field," Nature Communications **12**, 6727 (2021).

[157] S. D. Sarma and Y. Liao, "Know the enemy: 2D Fermi liquids," Annals of Physics **435**, 168495 (2021).

[158] Z. Liu, Y. Shi, Q. Jiang, E. W. Rosenberg, J. M. DeStefano, J. Liu, C. Hu, Y. Zhao, Z. Wang, Y. Yao, *et al.*, "Absence of E2g nematic instability and dominant A1g response in the kagome metal CsV_3Sb_5," Physical Review X **14**, 031015 (2024).

[159] C. Guo, G. Wagner, C. Putzke, D. Chen, K. Wang, L. Zhang, M. Gutierrez-Amigo, I. Errea, M. G. Vergniory, C. Felser, *et al.*, "Correlated order at the tipping point in the kagome metal CsV_3Sb_5," Nature Physics **20**, 579–584 (2024).

[160] K. Jiang, T. Wu, J.-X. Yin, Z. Wang, M. Z. Hasan, S. D. Wilson, X. Chen, and J. Hu, "Kagome superconductors AV_3Sb_5 (A = K, Rb, Cs)," National Science Review **10**, nwac199 (2023).

[161] Y. Gan, W. Xia, L. Zhang, K. Yang, X. Mi, A. Wang, Y. Chai, Y. Guo, X. Zhou, and M. He, "Magneto-seebeck effect and ambipolar nernst effect in the CsV_3Sb_5 superconductor," Physical Review B **104**, L180508 (2021).

[162] F. Yu, T. Wu, Z. Wang, B. Lei, W. Zhuo, J. Ying, and X. Chen, "Concurrence of anomalous hall effect and charge density wave in a superconducting topological kagome metal," Physical Review B **104**, L041103 (2021).

[163] W. Zhang, L. Wang, C. W. Tsang, X. Liu, J. Xie, W. C. Yu, K. T. Lai, and S. K. Goh, "Emergence of large quantum oscillation frequencies in thin flakes of the kagome superconductor CsV_3Sb_5," Physical Review B **106**, 195103 (2022).

[164] G. Athas, J. Brooks, S. Klepper, S. Uji, and M. Tokumoto, "Tunnel diode oscillator application to high sensitivity de Haas-van Alphen and superconducting critical field

studies of anisotropic organic conductors," Review of Scientific Instruments **64**, 3248–3251 (1993).

[165] T. Coffey, Z. Bayindir, J. DeCarolis, M. Bennett, G. Esper, and C. Agosta, "Measuring radio frequency properties of materials in pulsed magnetic fields with a tunnel diode oscillator," Review of Scientific Instruments **71**, 4600–4606 (2000).

[166] V. Leeb and J. Knolle, "Theory of difference-frequency quantum oscillations," Physical Review B **108**, 054202 (2023).

[167] N. Huber, V. Leeb, A. Bauer, G. Benka, J. Knolle, C. Pfleiderer, and M. A. Wilde, "Quantum oscillations of the quasiparticle lifetime in a metal," Nature **621**, 276–281 (2023).

[168] H. Deng, H. Qin, G. Liu, T. Yang, R. Fu, Z. Zhang, X. Wu, Z. Wang, Y. Shi, J. Liu, *et al.*, "Chiral kagome superconductivity modulations with residual Fermi arcs," Nature **632**, 775–781 (2024).

[169] T. Kato, Y. Li, T. Kawakami, M. Liu, K. Nakayama, Z. Wang, A. Moriya, K. Tanaka, T. Takahashi, Y. Yao, *et al.*, "Three-dimensional energy gap and origin of charge-density wave in kagome superconductor KV_3Sb_5," Communications Materials **3**, 30 (2022).

[170] H. Li, T. T. Zhang, T. Yilmaz, Y. Y. Pai, C. E. Marvinney, A. Said, Q. Yin, C. Gong, Z. Tu, E. Vescovo, *et al.*, "Observation of unconventional charge density wave without acoustic phonon anomaly in kagome superconductors AV3Sb5 (A = Rb, Cs)," Physical Review X **11**, 031050 (2021).

[171] Y.-X. Jiang, J.-X. Yin, M. M. Denner, N. Shumiya, B. R. Ortiz, G. Xu, Z. Guguchia, J. He, M. S. Hossain, X. Liu, *et al.*, "Unconventional chiral charge order in kagome superconductor KV_3Sb_5," Nature Materials **20**, 1353–1357 (2021).

[172] Z. Liu, N. Zhao, Q. Yin, C. Gong, Z. Tu, M. Li, W. Song, Z. Liu, D. Shen, Y. Huang, *et al.*, "Charge-density-wave-induced bands renormalization and energy gaps in a kagome superconductor RbV_3Sb_5," Physical Review X **11**, 041010 (2021).

[173] D. Shoenberg and B. Watts, "The effect of tension on the Fermi surfaces of the noble metals," Philosophical Magazine **15**, 1275–1288 (1967).

[174] R. Chambers, "Magnetic breakdown in real metals," Proceedings of the Physical Society **88**, 701 (1966).

[175] W. Zhang, X. Liu, L. Wang, C. W. Tsang, Z. Wang, S. T. Lam, W. Wang, J. Xie, X. Zhou, Y. Zhao, *et al.*, "Nodeless superconductivity in kagome metal CsV_3Sb_5 with and without time reversal symmetry breaking," Nano Letters **23**, 872–879 (2023).

[176] R. Chapai, A. E. Koshelev, M. P. Smylie, D. Y. Chung, A. Kayani, K. Bhatt, G. Rimal, M. G. Kanatzidis, W.-K. Kwok, J. Mitchell, *et al.*, "Origin of the unusual temperature dependence of the upper critical field of kagome superconductor CsV_3Sb_5: Multiple Bands or van Hove Singularities?" arXiv preprint arXiv:2411.16625 (2024).

[177] Y. Wang, S.-Y. Yang, P. K. Sivakumar, B. R. Ortiz, S. M. Teicher, H. Wu, A. K. Srivastava, C. Garg, D. Liu, S. S. Parkin, *et al.*, "Anisotropic proximity-induced superconductivity and edge supercurrent in kagome metal, $K_{1-x}V_3Sb_5$," Science Advances **9**, eadg7269 (2023).

[178] S. Ni, S. Ma, Y. Zhang, J. Yuan, H. Yang, Z. Lu, N. Wang, J. Sun, Z. Zhao, D. Li, *et al.*, "Anisotropic superconducting properties of kagome metal CsV_3Sb_5," Chinese Physics Letters **38**, 057403 (2021).

[179] Z. Wang, Y.-X. Jiang, J.-X. Yin, Y. Li, G.-Y. Wang, H.-L. Huang, S. Shao, J. Liu, P. Zhu, N. Shumiya, *et al.*, "Electronic nature of chiral charge order in the kagome superconductor CsV_3Sb_5," Physical Review B **104**, 075148 (2021).

[180] Z. Liang, X. Hou, F. Zhang, W. Ma, P. Wu, Z. Zhang, F. Yu, J.-J. Ying, K. Jiang, L. Shan, *et al.*, "Three-dimensional charge density wave and surface-dependent vortex-core states in a kagome superconductor CsV_3Sb_5," Physical Review X **11**, 031026 (2021).

[181] Z. Guguchia, C. Mielke III, D. Das, R. Gupta, J.-X. Yin, H. Liu, Q. Yin, M. H. Christensen, Z. Tu, C. Gong, *et al.*, "Tunable unconventional kagome superconductivity in charge ordered RbV3Sb5 and KV_3Sb_5," Nature Communications **14**, 153 (2023).

[182] W. Duan, Z. Nie, S. Luo, F. Yu, B. R. Ortiz, L. Yin, H. Su, F. Du, A. Wang, Y. Chen, *et al.*, "Nodeless superconductivity in the kagome metal CsV_3Sb_5," Science China Physics, Mechanics & Astronomy **64**, 107462 (2021).

[183] B. R. Ortiz, P. M. Sarte, E. M. Kenney, M. J. Graf, S. M. Teicher, R. Seshadri, and S. D. Wilson, "Superconductivity in the Z2 kagome metal KV_3Sb_5," Physical Review Materials **5**, 034801 (2021).

[184] Y. Zhong, J. Liu, X. Wu, Z. Guguchia, J.-X. Yin, A. Mine, Y. Li, S. Najafzadeh, D. Das, C. Mielke III, *et al.*, "Nodeless electron pairing in CsV_3Sb_5-derived kagome superconductors," Nature **617**, 488–492 (2023).

[185] G. Wagner, C. Guo, P. J. Moll, T. Neupert, and M. H. Fischer, "Phenomenology of bond and flux orders in kagome metals," Physical Review B **108**, 125136 (2023).

[186] H.-T. Liu, J. Huang, T. Zhou, and W. Huang, "Constraints on the orbital flux phase in AV_3Sb_5 from polar Kerr effect," arXiv preprint arXiv:2406.16398 (2024).

Acknowledgements

Here, I thank everyone who made my life *easier* during these past years as a PhD student. First and foremost thanks to Prof. Le Tacon and Dr. Meingast, who accepted me into the PhD. I received a lot of support from Prof. Le Tacon in numerous aspects. He offered valuable suggestions for improving the visual presentation of the figures and provided thorough and important corrections throughout the thesis. Over the years, whether with the registrations, extensions, visas and what not, he was always supportive and understanding.

Dr. Christoph Meingast and Dr. Frédéric Hardy supervised my day to day work at IQMT. Majority of instrument operation and data analysis was taught to me by Fred. He also read through the whole thesis and gave a thorough feedback. While the thesis contains the study on Fe(Se,Te) and AV3Sb5 compounds - I got to work on several other compounds over the years. My first project was the P-doped BaNi2As2. As I was in the lab removing one of the FeSe samples from PPMS, Christoph came and gave me the sample to measure the heat capacity. I was able to resolve the orthorhombic anomaly in it which was almost at the instrument limit! I also performed the transport on these samples. Later, in perhaps a very similar way, Fred came in the lab and told me to do the magnetization on a Cr substituted CsFe2As2. I performed a lot of measurements on these samples and this became my second successful project.

I spent the *majority* of my time studying Fe(Se,Te). The aim was to explore the Se-rich part of the phase diagram, the high quality single crystals in this part is extremely difficult to grow. Dr Amir A Haghighirad made a great deal of effort to grow these samples. Part of the complication was also the *kind* of measurements we performed - heat capacity requires the sample to be large enough and thermal expansion requires the sample to be thick enough. Amir optimized the growth and made the largest samples compared to the reported literature. He also gave me an iron based spinel sample to measure the heat capacity and magnetization. While most of my time was spent measuring metals, measuring this insulating compound with extraordinary magnetism was indeed interesting. Coming back to the Fe(Se,Te), I thank Dr. Liran Wang for measuring the thermal expansion on some of the thinnest samples! These extremely important measurements would not have been possible without her steady hands.

The AV_3Sb_5 Kagome study was a project initiated by Fred, in collaboration with Mingquan He (Jason). Here also, Fred gave me the sample to measure the magnetization and I obtained quantum oscillations in it. He then gave all the three compounds in the series to me to study the basic properties and the quantum oscillations. Prof. Le Tacon then arranged my secondment at the University of Oxford with Prof. Amalia Coldea. This was most useful mainly because there only I learned how to relate the band structure studies in kagome (which are a lot in the literature) with the quantum oscillation data (which are also a lot in the literature). I thank her a lot for this.

Another important person to me in the lab was Dr. Santanu Pakhira. While he stayed only for a year in the lab, he initiated a study of a novel intermetallic and I got to do all the measurements on it. He had exceptional command on magnetism and I benefited a lot from his presence. He also arranged for the neutron measurement with Dr. Weber. In the lab, Dr. Kristin Willa helped me a lot in the initial days explaining the measurements and more importantly - the paperwork. Similarly, Dr. Mehdi Frachet notably gave me valuable suggestions on the transport measurements - thanks a lot to both of you. With Fred, I performed the torque and magnetostriction measurements at the magnet labs in Grenoble and Nijmegen respectively. I thank Dr. Ilya Shekin (LNCMI Grenoble) and Prof Wiedmann (Nijmegen) for their valuable support during these measurements. I thank Dr. Michael Merz and Dr. Nour Maraytta for the XRD measurements on several compounds.

This doctoral work was carried out within the QUSTEC project, which received funding from the European Union's Horizon 2020 research and innovation programme under the Marie Skłodowska-Curie grant agreement No. 847471. I also thank Prof. Schmalian for acting as a co-referee for the thesis and providing valuable feedback.

I thank my colleagues at IQMT: Dr. Stefan Schuppler, Dr. Roland Hott, Dr. Robert Eder, Dr. Kai Grube, Dr. Rolf Heid, Arun, Tom Lacmann, Paolo, Fabian, Shruti, Tristan, and Indu. I would like to thank my close friends for their constant support through all these years. I would like to thank my parents and siblings for the support through all these years. Finally, I want to thank my wife, Dr. Deeksha Gupta, for being the calm in my ever-chaotic life.

Anmol Shukla